

**Growth, Transport and Functionalization of Noble Metal Nanoparticles
Inside and Outside a Gas Aggregation Cluster Source:
Uncovered by in-situ Diagnostics**

Dissertation

by

Jonas Drewes

born in Walsrode

*Submitted to obtain the degree of
Doctor of Engineering (Dr.-Ing.)
at the
Faculty of Engineering, Kiel University
Institute of Materials Science*

First Supervisor: Prof. Dr. Franz Faupel
Chair for Multicomponent Materials
Faculty of Engineering, Kiel University

Second Supervisor: Prof. Dr. Jan Benedikt
Chair for Experimental Plasma Physics
Faculty of Mathematics and Natural Sciences, Kiel University

Third Supervisor: Prof. Ing. Andrey Shukurov
Department for Macromolecular Physics
Faculty of Mathematics and Physics, Charles University

Date of Disputation

April 27th 2023

Danksagung

Diese Seite möchte ich allen widmen, die durch ihr Wirken und ihre Unterstützung auf unterschiedliche Weise zum Gelingen dieser Arbeit beigetragen haben.

Beginnen möchte ich mit meinem Doktorvater Franz Faupel, der mir die Chance gegeben hat diese Dissertation in seiner Arbeitsgruppe anzufertigen. Ich bedanke mich für sein Vertrauen, die Möglichkeit der eigenen Entfaltung und all die Dinge die ich von ihm lernen durfte. Außerdem danke ich ihm dafür, dass er mir die Vereinbarung von Beruf und Familie in vielerlei Hinsicht erleichtert hat.

An zweiter Stelle möchte ich mich bei Alexander Vahl bedanken. Er hatte stets ein offenes Ohr für die Diskussion von Ergebnissen und der Planung und Durchführung von neuen Experimenten. Außerdem hat er mich vielfältig beim Schreiben der Veröffentlichungen unterstützt und mir die Möglichkeit gegeben vieles von ihm zu lernen. Auch über die wissenschaftliche Arbeit hinaus bin ich dankbar ihn einen Freund nennen zu können, der mir den Arbeitsalltag stets angenehm gemacht hat.

Oleksandr Polonskyi bin ich dankbar, da er mich in das Thema eingearbeitet hat und mich auch für das Thema begeistern konnte. Ihn in Richtung USA zu verabschieden, war nicht einfach. Aber es freut mich, dass wir trotz der Distanz den Kontakt halten konnten.

Ein besonderer Dank geht auch an das ganze Department for Macromolecular Physics an der Charles University in Prague. Während meines Aufenthalts konnte ich viel lernen und habe viele neue Freundschaften geknüpft. Ein besonderer Dank gilt Hynek Biederman, Andrei Choukourov, Daniil Nikitin, Suren Ali-Ogly und Artem Shelemin für die erfolgreichen Kollaborationen auf vielen verschiedenen Ebenen.

Auch bei Jan Benedikt und Oguz Han Asnaz möchte ich mich herzlich für die Zusammenarbeit im gemeinsamen Projekt und die warme und herzliche Arbeitsatmosphäre während meiner Zeit an der Physik bedanken. Auch Holger Kersten bin ich für die Kooperation und die Leihgabe von Forschungsgeräten für meine Arbeit zu Dank verpflichtet.

Ganz besonders möchte ich mich auch bei unserem Laboringenieur Stefan Rehders für all seine Hilfe und Geduld bedanken. Auch für unsere Freundschaft über die Arbeit hinaus bin ich zutiefst dankbar. Ohne ihn wäre diese Arbeit nicht möglich gewesen.

Auch bei dem gesamten Lehrstuhl für Materialverbunde möchte ich mich für die wunderbare Atmosphäre, den freundschaftlichen Umgang und die Hilfsbereitschaft bedanken. Besonders möchte ich mich auch bei meinen Bürokollegen Alex, Stefan, Niko und Thomas für die stets von Humor geprägte Atmosphäre und die offenen Ohren für meine wissenschaftlichen und nicht wissenschaftlichen Probleme bedanken.

Des Weiteren möchte ich mich bei Klaus, Thomas, Kristian und Alex für die Durchsicht und die Hilfe bei der Strukturierung dieser Dissertation bedanken.

Zu guter Letzt danke ich meiner gesamten Familie. Meinen Eltern möchte ich dafür danken, dass sie immer an mich geglaubt haben und mir das Studium ermöglicht haben. Ihr Vertrauen, ihre Zuneigung und ihre Unterstützung haben mich durch das Studium und die Promotion getragen. Außerdem möchte ich mich bei meiner Frau Anna bedanken, dafür dass sie mir zwei wundervolle Kinder geschenkt hat und mich während der Promotionszeit, trotz all der damit verbundenen Anstrengungen, stets mit ihrer Liebe und Zuneigung unterstützt hat.

Abstract

Over the last decades nanoparticles (NPs) attracted the interest of many researchers, because they show properties which differ from their bulk counterparts. This work is focused on the synthesis of Ag NPs, AgAu alloy NPs and Ag@SiO₂ core-shell NPs. The properties of such NPs can be influenced by tuning their size, composition, the filling factor and the surrounding medium in case of core-shell NPs. Therefore, a synthesis process which enables precise control over such properties of NPs is in high demand. The Haberland type gas aggregation cluster source (HGAS), which was invented in 1992 by Haberland et al., provides the opportunity to synthesize different types of NPs and tailor their properties by adjusting the operating parameters of the HGAS. Although nowadays the HGAS is used by many groups for the synthesis of NPs, the processes inside the HGAS are not fully understood until today. Therefore, the aim of this dissertation is to increase the understanding of the ongoing processes inside the HGAS, because this opens the way for new fields of applications. In order to gain a better understanding of the HGAS, in-situ diagnostics with a good spatial and temporal resolution are essential. Five different in-situ methods were used, which together contribute to a better understanding of growth, transport and functionalization of NPs inside a HGAS.

In-situ small angle X-ray scattering (SAXS) measurements at a synchrotron have shown that Ag NPs are trapped in the close vicinity of the target. Additionally, the size and density of NPs in the trapping zone were oscillating. That could be caused by periodic expelling from the trapping zone, when a critical size is reached, or a rotation of the NP cloud around the magnetron axis. Both explanations could not be verified because of the low spatial resolution of the method. To further investigate the trapping of NPs, UV-Vis spectroscopy was used, because it is better accessible than a synchrotron. Due to the localized surface plasmon resonance (LSPR) of Ag NPs, they absorb light in the visible spectrum. This can be exploited to relate the absorption strength to the relative density of NPs and the wavelength of the LSPR peak to the size of the NPs. Thereby the trapping of NPs in the HGAS as a function of different gas flows and pressures can be studied. However, the SAXS and UV-Vis measurements have only a 1-dimensional resolution, which made it impossible to find the exact position of the trapped NPs inside the HGAS. Therefore, laser light scattering (LLS) was utilized, which provides 2-dimensional resolution. Due to Rayleigh scattering the NPs scatter light, which could be imaged by a camera and finally enables NP imaging. The LLS results have shown that different gas inlets strongly influence the regions in which NPs can be trapped.

Furthermore, the variety of possible applications of a synthesis method also plays a crucial role, e.g. the synthesis of alloy NPs or core-shell NPs. Therefore, an interesting option of the HGAS is the ability to tailor the composition of alloy NPs in-situ, when the multicomponent target approach is used, which was reported by Vahl et al. in 2017. In this dissertation it turned out that the target lifetime has a strong influence on the resulting composition of the NPs. By applying optical emission spectroscopy (OES) as an in-situ diagnostic, it was possible to predict the composition of the NPs. Furthermore, in this thesis a novel combined method for the production of core-shell NPs was invented, which combines a HGAS with a second RF discharge. The confinement and coating of the NPs was confirmed by in-situ UV-Vis spectroscopy and in-situ Fourier-transform infrared spectroscopy (FTIR) measurements.

By combining different in-situ methods it was possible to investigate dynamic processes in a HGAS and thereby gain new insights into growth, transport and trapping of NPs. Furthermore, the reliability of the multicomponent target approach could be enhanced, which makes it an excellent tool for the fabrication of alloy NPs with tailored composition. Finally, a new approach for the production of core-shell NPs in the gas phase was developed, which is expected to open up new applications for core-shell NPs because of its outstanding flexibility in terms of material combinations and reliability.

Kurzfassung

In den letzten Jahrzehnten haben Ag-Nanopartikel (NP), NP aus AgAu-Legierungen und Ag@SiO₂-Kern-Schale-NP das Interesse vieler Forscher auf sich gezogen, da sie Eigenschaften aufweisen, die sich von ihren großen Gegenstücken unterscheiden. Die Eigenschaften solcher NP können durch Anpassung ihrer Größe, Zusammensetzung, des Füllfaktors und des umgebenden Mediums im Falle von Kern-Schale-NP beeinflusst werden. Daher ist ein Syntheseverfahren, das eine genaue Kontrolle über diese Eigenschaften der NP ermöglicht, sehr gefragt. Die Gasaggregationsclusterquelle (HGAS) vom Typ Haberland, die 1992 von Haberland et al. erfunden wurde, bietet die Möglichkeit, verschiedene Arten von NP zu synthetisieren und ihre Eigenschaften durch Variation der Prozessparameter der HGAS anzupassen. Obwohl die HGAS heute von vielen Gruppen für die Synthese von NP verwendet wird, sind die Prozesse im Inneren der HGAS bis heute nicht vollständig verstanden. Ziel dieser Dissertation ist es daher, das Verständnis für die ablaufenden Prozesse innerhalb der HGAS zu verbessern, da dies den Weg für neue Anwendungsfelder eröffnet. Um die HGAS besser zu verstehen, sind in-situ Diagnostiken mit einer guten räumlichen und zeitlichen Auflösung unerlässlich. Es wurden fünf verschiedene in-situ Methoden verwendet, die zusammen zu einem besseren Verständnis des Wachstums, des Transports und der Funktionalisierung von NP in einer HGAS beitragen.

In-situ Messungen mit Kleinwinkel-Röntgenstreuung (SAXS) an einem Synchrotron haben gezeigt, dass die Ag-NP in unmittelbarer Nähe des Targets gefangen sind. Außerdem schwankten die Größe und Dichte der NP in der Einfangzone. Dies könnte durch ein periodisches Ausstoßen aus der Einfangzone, wenn eine kritische Größe erreicht wird, oder durch eine Rotation der NP-Wolke um die Magnetronachse verursacht werden. Beide Erklärungen konnten aufgrund der geringen räumlichen Auflösung der Methode nicht verifiziert werden. Um das Einfangen der NP weiter zu untersuchen, wurde die UV-Vis-Spektroskopie verwendet, da sie besser zugänglich ist als ein Synchrotron. Aufgrund der lokalisierten Oberflächenplasmonenresonanz (LSPR) von Ag-NP absorbieren sie Licht im sichtbaren Spektrum. Dies kann ausgenutzt werden, um die Absorptionsstärke mit der relativen Dichte der NP und die Wellenlänge des LSPR-Maximums mit der Größe der NP in Beziehung zu setzen. Auf diese Weise kann das Einfangen von NP in der HGAS in Abhängigkeit von verschiedenen Gasflüssen und Drücken untersucht werden. Die SAXS- und UV-Vis-Messungen haben jedoch nur eine eindimensionale Auflösung, was es unmöglich macht die genaue Position der gefangenen NP in der HGAS zu bestimmen. Daher wurde die Laserlichtstreuung (LLS) eingesetzt, die eine zweidimensionale Auflösung bietet. Aufgrund der Rayleigh-Streuung streuen die NP Licht, das von einer Kamera abgebildet werden kann und schließlich die Darstellung der NP ermöglicht. Die LLS-Ergebnisse haben gezeigt, dass unterschiedliche Gaseinlässe einen starken Einfluss auf die Regionen haben, in denen NP eingefangen werden können.

Darüber hinaus spielt auch die Vielfalt der möglichen Anwendungen einer Synthesemethode eine entscheidende Rolle. Beispiele sind die Synthese von Legierungs-NP oder Kern-Schale-NP. Eine interessante Option des HGAS ist daher die Möglichkeit, die Zusammensetzung von Legierungs-NP in-situ zu ändern, wenn der Multikomponenten-Target-Ansatz verwendet wird, wie Vahl et al. 2017 berichteten. In dieser Dissertation stellte sich heraus, dass die Lebensdauer des Targets einen starken Einfluss auf die resultierende Zusammensetzung der NP hat. Durch die Anwendung der optischen Emissionsspektroskopie (OES) als in-situ-Diagnose war es möglich die Zusammensetzung der NP vorherzusagen. Darüber hinaus wurde in dieser Arbeit eine neuartige, kombinierte Methode zur Herstellung von Kern-Schale-NP entwickelt, die eine HGAS mit einer zweiten HF-Entladung kombiniert. Das Einfangen und die Beschichtung der NP wurde durch in-situ-UV-Vis-Spektroskopie und in-situ-Fourier-Transformations-Infrarotspektroskopie (FTIR)-Messungen bestätigt.

Durch die Kombination verschiedener in-situ-Methoden war es möglich dynamische Prozesse in einer HGAS zu untersuchen und dadurch neue Erkenntnisse über das Wachstum, den Transport und das Einfangen von NP zu gewinnen. Darüber hinaus konnte die Zuverlässigkeit des Multikomponenten-Target-Ansatzes verbessert werden, was ihn zu einem hervorragenden Werkzeug für die Herstellung von Legierungs-NP mit maßgeschneiderter Zusammensetzung macht. Schließlich wurde ein neuer Ansatz für die Herstellung von Kern-Schale-NP in der Gasphase entwickelt, von dem erwartet wird, dass er neue Anwendungen für Kern-Schale-NP eröffnet, da er sehr zuverlässig ist und in Bezug auf Materialkombinationen äußerst flexibel ist.

Declaration of Authenticity

I hereby declare that this thesis and the respective research was independently composed and authored by myself.

This work complies with the DFG recommendations for safeguarding good scientific practice. All content and ideas drawn directly or indirectly from external sources are clearly indicated.

This thesis has not been published or been submitted to any other examining body and all related research items that have been composed and published in peer-review journals are clearly indicated as such.

I declare that no academic degree has been withdrawn from me.

Kiel, 06.02.2023

Publications in the Context of this Dissertation

The publications are presented in the order, how they are appearing in this cumulative thesis. The publications are abbreviated with letters from A-F. These letters are used in the entire thesis to refer to these publications. First or equally contributing authors are underlined. The experimental data in publication C was partially obtained during my master thesis in 2017.

[A] Shelemin, A., Pleskunov, P., Kousal, **J.**, **Drewes, J.**, Hanuš, J., Ali-Ogly, S., Nikitin, D., Solař, P., Kratochvíl, J., Vaidulych, M., Schwartzkopf, M., Kylián, O., Polonskyi, O., Strunskus, T., Faupel, F., Roth, S. v., Biederman, H., & Choukourov, A. (2020). Nucleation and Growth of Magnetron-Sputtered Ag Nanoparticles as Witnessed by Time-Resolved Small Angle X-Ray Scattering. *Particle and Particle Systems Characterization*, 37(2), 1–11. <https://doi.org/10.1002/ppsc.201900436>

[B] Nikitin, D., Hanuš, J., Ali-Ogly, S., Polonskyi, O., **Drewes, J.**, Faupel, F., Biederman, H., & Choukourov, A. (2019). The evolution of Ag nanoparticles inside a gas aggregation cluster source. *Plasma Processes and Polymers*, 16(10), 1–7. <https://doi.org/10.1002/ppap.201900079>

[C] **Drewes, J.**, Ali-Ogly, S., Strunskus, T., Polonskyi, O., Biederman, H., Faupel, F., & Vahl, A. (2022). Impact of argon flow and pressure on the trapping behavior of nanoparticles inside a gas aggregation source. *Plasma Processes and Polymers*, 19(1), 2100125. <https://doi.org/10.1002/ppap.202100125> (**Front Cover**)

[D] **Drewes, J.**, Rehders, S., Strunskus, T., Kersten, H., Faupel, F., & Vahl, A. (2022). In Situ Laser Light Scattering for Temporally and Locally Resolved Studies on Nanoparticle Trapping in a Gas Aggregation Source. *Particle & Particle Systems Characterization*, 2200112. <https://doi.org/10.1002/ppsc.202200112>

[E] **Drewes, J.**, Vahl, A., Carstens, N., Strunskus, T., Polonskyi, O., & Faupel, F. (2020). Enhancing composition control of alloy nanoparticles from gas aggregation source by in operando optical emission spectroscopy. *Plasma Processes and Polymers*, October, 1–11. <https://doi.org/10.1002/ppap.202000208> (**Front Cover**)

[F] Asnaz, O. H., **Drewes, J.**, Elis, M., Strunskus, T., Greiner, F., Polonskyi, O., Faupel, F., Kienle, L., Vahl, A., & Benedikt, J. (2023). A novel method for the synthesis of core–shell nanoparticles for functional applications based on long-term confinement in a radio frequency plasma. *Nanoscale Advances*. <https://doi.org/10.1039/D2NA00806H>

Further Publications within PhD period

The publications are presented in chronological order. The publications I and P are also related to the NP synthesis with the GAS.

[G] Gensch, M., Schwartzkopf, M., Ohm, W., Brett, C. J., Pandit, P., Vayalil, S. K., Bießmann, L., Kreuzer, L. P., **Drewes, J.**, Polonskyi, O., Strunskus, T., Faupel, F., Stierle, A., Müller-Buschbaum, P., & Roth, S. v. (2019). Correlating Nanostructure, Optical and Electronic Properties of Nanogranular Silver Layers during Polymer-Template-Assisted Sputter Deposition. *ACS Applied Materials and Interfaces*, 11(32), 29416–29426. <https://doi.org/10.1021/acsami.9b08594>

- [H] Veziroglu, S., Ullrich, M., Hussain, M., **Drewes, J.**, Shondo, J., Strunskus, T., Adam, J., Faupel, F., & Aktas, O. C. (2020). Plasmonic and non-plasmonic contributions on photocatalytic activity of Au-TiO₂ thin film under mixed UV–visible light. *Surface and Coatings Technology*, 389. <https://doi.org/10.1016/j.surfcoat.2020.125613>
- [I] Veziroglu, S., Hwang, J., **Drewes, J.**, Barg, I., Shondo, J., Strunskus, T., Polonskyi, O., Faupel, F., & Aktas, O. C. (2020). PdO nanoparticles decorated TiO₂ film with enhanced photocatalytic and self-cleaning properties. *Materials Today Chemistry*, 16. <https://doi.org/10.1002/pssa.201800898>
- [J] Lupan, C., Khaledialidusti, R., Mishra, A. K., Postica, V., Terasa, M. I., Magariu, N., Pauporté, T., Viana, B., **Drewes, J.**, Vahl, A., Faupel, F., & Adelung, R. (2020). Pd-Functionalized ZnO:Eu Columnar Films for Room-Temperature Hydrogen Gas Sensing: A Combined Experimental and Computational Approach. *ACS Applied Materials and Interfaces*, 12(22), 24951–24964. <https://doi.org/10.1021/acsami.0c02103>
- [K] Schwartzkopf, M., Wöhnert, S. J., Waclawek, V., Carstens, N., Rothkirch, A., Rubeck, J., Gensch, M., **Drewes, J.**, Polonskyi, O., Strunskus, T., Hinz, A. M., Schaper, S. J., Körstgens, V., Müller-Buschbaum, P., Faupel, F., & Roth, S. v. (2021). Real-time insight into nanostructure evolution during the rapid formation of ultra-thin gold layers on polymers. *Nanoscale Horizons*, 6(2), 132–138. <https://doi.org/10.1039/d0nh00538j>
- [L] Burk, M. H., Langbehn, D., Hernández Rodríguez, G., Reichstein, W., **Drewes, J.**, Schröder, S., Rehders, S., Strunskus, T., Herges, R., & Faupel, F. (2021). Synthesis and Investigation of a Photoswitchable Copolymer Deposited via Initiated Chemical Vapor Deposition for Application in Organic Smart Surfaces. *ACS Applied Polymer Materials*, 3(3), 1445–1456. <https://doi.org/10.1021/acsapm.0c01312>
- [M] Postica, V., Lupan, O., Gapeeva, A., Hansen, L., Khaledialidusti, R., Mishra, A. K., **Drewes, J.**, Kersten, H., Faupel, F., Adelung, R., & Hansen, S. (2021). Improved Long-Term Stability and Reduced Humidity Effect in Gas Sensing: SiO₂ Ultra-Thin Layered ZnO Columnar Films. *Advanced Materials Technologies*, 6(5). <https://doi.org/10.1002/admt.202001137>
- [N] Liang, S., Chen, W., Yin, S., Schaper, S. J., Guo, R., **Drewes, J.**, Carstens, N., Strunskus, T., Gensch, M., Schwartzkopf, M., Faupel, F., Roth, S. v., Cheng, Y. J., & Müller-Buschbaum, P. (2021). Tailoring the Optical Properties of Sputter-Deposited Gold Nanostructures on Nanostructured Titanium Dioxide Templates Based on in Situ Grazing-Incidence Small-Angle X-ray Scattering Determined Growth Laws. *ACS Applied Materials and Interfaces*, 13(12), 14728–14740. <https://doi.org/10.1021/acsami.1c00972>
- [O] Gensch, M., Schwartzkopf, M., Brett, C. J., Schaper, S. J., Kreuzer, L. P., Li, N., Chen, W., Liang, S., **Drewes, J.**, Polonskyi, O., Strunskus, T., Faupel, F., Müller-Buschbaum, P., & Roth, S. v. (2021). Selective Silver Nanocluster Metallization on Conjugated Diblock Copolymer Templates for Sensing and Photovoltaic Applications. *ACS Applied Nano Materials*, 4(4), 4245–4255. <https://doi.org/10.1021/acsanm.1c00829>
- [P] Pleskunov, P., Košutová, T., Vaidulych, M., Nikitin, D., Krtouš, Z., Ali-Ogly, S., Kishenina, K., Tafiichuk, R., Biederman, H., Gordeev, I., **Drewes, J.**, Barg, I., Faupel, F., Cieslar, M., Yatskiv, R., Pihosh, Y., Nandal, V., Seki, K., Domen, K., & Choukourov, A. (2021). The sputter-based synthesis of tantalum oxynitride nanoparticles with architecture and bandgap controlled by design. *Applied Surface Science*, 559. <https://doi.org/10.1016/j.apsusc.2021.149974>

- [Q] Gensch, M., Schwartzkopf, M., Brett, C. J., Schaper, S. J., Li, N., Chen, W., Liang, S., **Drewes, J.**, Polonskyi, O., Strunskus, T., Faupel, F., Müller-Buschbaum, P., & Roth, S. v. (2021). Correlating Optical Reflectance with the Topology of Aluminum Nanocluster Layers Growing on Partially Conjugated Diblock Copolymer Templates. *ACS Applied Materials & Interfaces*, 13(47), 56663–56673. <https://doi.org/10.1021/acsami.1c18324>
- [R] Schröder, S., Ababii, N., Lupan, O., **Drewes, J.**, Magariu, N., Krüger, H., Strunskus, T., Adelung, R., Hansen, S., & Faupel, F. (2022). Sensing performance of CuO/Cu₂O/ZnO:Fe heterostructure coated with thermally stable ultrathin hydrophobic PV3D3 polymer layer for battery application. *Materials Today Chemistry*, 23, 100642. <https://doi.org/10.1016/j.mtchem.2021.100642>
- [S] Liang, S., Guan, T., Yin, S., Krois, E., Chen, W., Everett, C. R., **Drewes, J.**, Strunskus, T., Gensch, M., Rubeck, J., Haisch, C., Schwartzkopf, M., Faupel, F., Roth, S. v., Cheng, Y.-J., & Müller-Buschbaum, P. (2022). Template-Induced Growth of Sputter-Deposited Gold Nanoparticles on Ordered Porous TiO₂ Thin Films for Surface-Enhanced Raman Scattering Sensors. *ACS Applied Nano Materials*, 5(5), 7492–7501. <https://doi.org/10.1021/acsanm.2c01481>
- [T] Lupan, C., Mishra, A. K., Wolff, N., **Drewes, J.**, Krüger, H., Vahl, A., Lupan, O., Pauporté, T., Viana, B., Kienle, L., Adelung, R., de Leeuw, N. H., & Hansen, S. (2022). Nanosensors Based on a Single ZnO:Eu Nanowire for Hydrogen Gas Sensing. *ACS Applied Materials and Interfaces*. <https://doi.org/10.1021/acsami.2c10975>
- [U] Marxen, M. L., Hansen, L., Reimers, A., Tjardts, T., Saure, L. M., Greve, E., **Drewes, J.**, Schütt, F., Adelung, R., & Kersten, H. (2022). On the plasma permeability of highly porous ceramic framework materials using polymers as marker materials. *Plasma Processes and Polymers*. <https://doi.org/10.1002/ppap.202200118>
- [V] Li, J., Reimers, A., Dang, K. M., Brunk, M. G. K., **Drewes, J.**, Hirsch, U. M., Willems, C., Schmelzer, C. E. H., Groth, T., Nia, A. S., Feng, X., Adelung, R., Sacher, W. D., Schütt, F., & Poon, J. K. S. (2023). 3D printed neural tissues with in situ optical dopamine sensors. *Biosensors and Bioelectronics*, 222, 114942. <https://doi.org/10.1016/j.bios.2022.114942>

Scientific contributions to conferences

Talks

J. Drewes, A. Vahl, O. Polonskyi, T. Strunskus and F. Faupel, Controlled composition tuning of alloy nanoparticles in a gas aggregation source monitored by in-situ UV-Vis, 4th German-Czech Workshop on Nanomaterials, Budweis/Czech Republic 2018

J. Drewes, A. Vahl, T. Strunskus, H. Kersten and F. Faupel, In-Situ Diagnostic Methods for the Growth and Transport of Nanoparticles in a Gas Aggregation Source, Gaseous Electronics Symposium 3 (GES3), Ljubljana/Slovenia 2020

J. Drewes, A. Vahl, O. Polonskyi, E. Miteva, F. Ziegler, T. Strunskus, H. Kersten and F. Faupel, In-Situ Diagnostic Methods for the Growth and Transport of Nanoparticles in a Gas Aggregation Source (GAS), 5th German-Czech Workshop on Nanomaterials, Dresden/Germany 2021 (Online)

J. Drewes, A. Vahl, O. Polonskyi, E. Miteva, F. Ziegler, T. Strunskus, H. Kersten and F. Faupel, In-Situ Diagnostic Methods for the Growth and Transport of Nanoparticles in a Gas Aggregation Source (GAS), NanoWorkshop 2021, Varese/Italy 2021

Posters

J. Drewes, O. Polonskyi, A. Vahl, T. Strunskus and F. Faupel, Nanoparticle Growth of Different Metals in a Gas Aggregation Source Investigated by in-situ UV-Vis, 8th International Workshop on polymer Metal Nanocomposites, Prague/Czech Republic 2017

J. Drewes, A. Vahl, O. Polonskyi, T. Strunskus and F. Faupel, Controlled composition tuning of alloy nanoparticles in a gas aggregation source monitored by in-situ UV-Vis, Materials Science and Engineering (MSE), Darmstadt/Germany 2018

Supervised and Co-supervised Theses

Bachelor

[B1] Florian Ziegler in 2019

Influence of a magnetron with an adjustable magnetic circuit on growth of nanoparticles inside a gas aggregation cluster source

[B2] Michael Morisch in 2020

Einfluss der Veränderung des Magnetfeldes auf die Deposition von Cu und CuNi Nanopartikeln mithilfe einer Gasaggregationsquelle

[B3] Görkem Bilgin in 2021

Diagnostik von Kenngrößen einer GAS-Magnetronentladung

Master

[M1] Momme Thomsen in 2019

ZrN Nanoparticles for plasmonics produced by gas aggregation cluster source

[M2] Syeda Fatima Bukhari in 2019

Deposition of Titanium Nitride nanoparticles via GAS (Gas Aggregation Source)

- [M3] Radka Stefanikova in 2020
Heterogeneous metal-plasma polymer nanoparticles prepared by means of gas aggregation sources
- [M4] Eva Emilova Miteva in 2020
Synthese von Nanokompositmaterialien in einer kombinierten HF-Entladung mit Gas-Aggregationsquelle
- [M5] Dominik Stefan in 2021
Synthesis of Metal Nanoparticles via Gas Aggregation Source for Ultra-Thin Broadband Absorbers
- [M6] Felix Pohl in 2022
Multilayer broad band solar absorber based on plasmonic nanoparticles
- [M7] Martin Hicke in 2022
Gas phase synthesis of hybrid nanoparticles for potential photocatalytic applications
- [M8] Kevin Rogall in 2022
Fabrication of broadband solar selective absorbers based on Cu nanoparticles in an Al₂O₃ matrix using Co-Sputtering
- [M9] Florian Ziegler in 2022
In-Flight Trapping of Metal Nanoparticles and Formation of Core-Shell Nanoparticles

Table of Contents

Danksagung	I
Abstract	II
Kurzfassung	III
Declaration of Authenticity	V
Publications in the Context of this Dissertation	VI
Further Publications within PhD period	VI
Scientific contributions to conferences.....	IX
Talks.....	IX
Posters.....	IX
Supervised and Co-supervised Theses	IX
Bachelor.....	IX
Master	IX
1 Introduction.....	1
2 Theoretical Background.....	4
2.1 Synthesis of Nanoparticles	4
2.1.1 Definition of Nanotechnology	4
2.1.2 Different Nanoparticle Synthesis Methods	5
2.1.3 Different Types of Cluster Sources	6
2.1.4 Magnetron Sputtering.....	8
2.1.5 The Haberland Type Gas Aggregation Cluster Source (HGAS)	10
2.1.6 In-situ Composition Tuning Inside a HGAS.....	15
2.2 Particle Holding Inside a Dusty Plasma	15
2.3 Plasmonic Properties of Nanoparticles	18
2.4 Computational Fluid Dynamic (CFD) Simulations.....	21
2.5 In-situ Diagnostic Methods Inside and Outside the HGAS	24
2.5.1 In-situ UV-Vis Spectroscopy	25
2.5.2 In-situ Optical Emission Spectroscopy (OES).....	25
2.5.3 In-situ Small Angle X-ray Scattering (SAXS)	26
2.5.4 In-situ Laser Light Scattering (LLS).....	28
2.5.5 In-situ Fourier-Transform Infrared Spectroscopy (FTIR)	29
2.6 Ex-situ Characterization Methods of Nanoparticles.....	31
2.6.1 Scanning Electron Microscopy (SEM).....	31
2.6.2 Transmission Electron Microscopy (TEM)	32

2.6.3	Energy-Dispersive X-ray Spectroscopy (EDX)	33
2.6.4	X-ray Photoelectron Spectroscopy (XPS).....	33
3	Results and Discussion	36
3.1	Summary, Motivation and Interconnection of the Different Publications	38
3.2	Publication A: Nucleation and Growth of Magnetron-Sputtered Ag Nanoparticles as Witnessed by Time-Resolved Small Angle X-Ray Scattering	40
3.3	Publication B: The Evolution of Ag Nanoparticles Inside a Gas Aggregation Source	68
3.4	Publication C: Impact of Argon Flow and Pressure on the Trapping Behavior of Nanoparticles Inside a Gas Aggregation Source.....	79
3.5	Publication D: In-situ Laser Light Scattering for Temporally and Locally Resolved Studies on Nanoparticle Trapping in a Gas Aggregation Source.....	100
3.6	Publication E: Enhancing Composition Control of Alloy Nanoparticles from Gas Aggregation Source by in-operando Optical Emission Spectroscopy	118
3.7	Publication F: A Novel Method for the Synthesis of Core-Shell Nanoparticles for Functional Applications Based on the Long-Term Confinement in a Radio Frequency Plasma	138
4	Conclusion	153
5	Outlook.....	157
6	List of Figures.....	i
7	Bibliography.....	ii
8	Declaration of Authorship	ix

1 Introduction

In the last decades, metal nanoparticles (NPs) gained huge attention in many research areas, because they show properties which differ from their bulk counterparts. These properties of NPs open up their application in many areas such as catalysis [1], photocatalysis [2–6], resistive switching [7–12], optics [13] and sensors [14–18]. Recently we used Cu NPs to fabricate a thin-film broadband absorber, which shows once more how manifold the applications for noble metal NPs are in general [19]. For many of these applications it is important to control properties of NPs such as size, size distribution, purity, alloy composition and surrounding medium. For the thin-film broad band absorber we showed that, e.g. the size distribution and the inter-particle distance strongly impacts the position and the width of the absorption in the electromagnetic spectrum [19]. Therefore, a good control over the synthesis of NPs is essential for a variety of possible applications. Thus, the focus of this thesis is the synthesis and the understanding of the formation of NPs.

An interesting technique for the synthesis of NPs with high purity in the gas phase is a so-called gas aggregation cluster source (GAS) which is compatible to a broad range of vacuum-based deposition techniques and typically allows a good control over the size of the NPs. Different kinds of cluster sources were developed from the early 1970s on. The different types of GAS rely on, e.g. erosion techniques, effusive methods and supersonic jet expansion [20–22]. In 1992, Haberland et al. invented another PVD based gas phase synthesis method based on high pressure sputtering, which is called a Haberland type gas aggregation source (HGAS) [23]. In the HGAS, direct current (DC) magnetron sputtering is used to vaporize a target material, which creates a supersaturated vapor in which NPs are formed by condensation in the presence of an inert gas. This is a highly dynamic process in which growth and transport of NPs are coupled to each other. Since its initial description by Haberland in 1992, a theoretical framework has been developed that qualitatively describes the nanoparticle formation in a HGAS:

- Formation of nuclei: For the nucleation, a three-body collision of two sputtered atoms and one gas atom is needed. Therefore, a high concentration of sputtered atoms and gas molecules is needed [24].
- Growth of particles: The nuclei formation enables further attachment of sputtered atoms while the heat of condensation is transferred by collisions to the inert gas, which stabilizes the particles.
- Transport and nanoparticle beam formation: The gas flow also guides the NPs by the drag force into the direction of the orifice. Along this way from the target to the orifice (aggregation length) the NPs can grow further by attachment of sputtered atoms or coalescence [25] with other NPs. After they exit the orifice a NP beam is formed. Then the NPs can be deposited onto various substrates [23].

In such a HGAS, the particle size and deposition rate can be tuned by various parameters like ratio of sputter and buffer gas, gas flow, the operating pressure, the magnetron power and aggregation length. A detailed qualitative description on how different parameters affect the size and deposition rate theoretically can be found in Chapter 2.1.5.2.

However, mechanisms of growth and transport are interlinked and not completely understood yet. This is expressed by the fact that in experimental studies even contradictory trends for parameter studies have been observed. To illustrate this, in the following part literature examples for the power dependency and the aggregation length dependency of the NP size distribution will be presented:

On the one hand, Liu et al. [26] found that the NP size decreases with increasing sputter power. On the other hand, Stranak et al. [27] observed a decrease of the NP diameter for high powers (larger than 130 W). But Polonskyi et al. [28] found out that the NP size is increasing with increasing power. An additional parameter, which is not completely understood so far, is the aggregation length. It was reported several times and consistently in the literature that a longer aggregation length increases the NP size simply because the time for growth by sputtered atom attachment increases [29–32]. Nevertheless, Kousal et al. [33] found by in-situ small angle X-ray scattering (SAXS) measurements that a high density of big NPs (diameter larger than 70 nm) is found close to the target. It was also observed that the diameter and the density of NPs decreases with increasing distance to the target. This is contradictory to the simple description of the influence of the aggregation length. Therefore, the current description of the working principle of the HGAS has to be extended.

Furthermore, the HGAS approach has another issue despite the not fully understood influence of different parameters on the size of the NPs. Sanzone et al. [34] reported that the typical nanoparticle throughput is in the order of 1 µg/h which is not adequate to fulfill the requirements for industrial usage. This originates partially from redeposition of atoms and NPs onto the target as well as deposition of NPs onto the walls of the HGAS. Most probably also the trapping of NPs inside the HGAS reduces the efficiency. Therefore, increasing the deposition rate is in high demand. To optimize the nanoparticle throughput and to tailor the size distribution of NPs, a deeper understanding of fundamental processes inside the HGAS has to be accomplished.

However, for the application of any NP source not only the efficiency is important. Another important question is, which NP properties can be achieved with the synthesis method. If special properties can be obtained by functionalization of NPs only with the HGAS, a non-ideal efficiency of the source may be tolerated. Therefore, new methods must be developed to produce functional NPs with unique and tailored properties with the HGAS to increase the scope of applications of this approach. Because of the above-mentioned issues and the high demand for functional NPs, the main research question of this cumulative dissertation is the following:

How can the fundamental understanding of the HGAS be increased to extend the scope of applications of the HGAS?

The main research question can be divided into three sub-questions:

- 1) Which in-situ diagnostic techniques can be utilized to investigate the growth, transport and functionalization of Ag NPs inside and outside the HGAS to increase the understanding of the method?**
- 2) Which known and unknown parameters can be used to increase the efficiency of the NP synthesis inside the HGAS?**
- 3) How is it possible to functionalize NPs inside and outside the HGAS to extend the scope of applications of the HGAS?**

To answer these questions, different in-situ diagnostics were utilized. However, none of the in-situ techniques is able to answer all the questions alone. For that reason, a combination of different in-situ diagnostics was used to investigate the growth, transport and functionalization of NPs. All techniques have used electromagnetic radiation which has the big advantage that these methods are not invasive for the synthesis process of NPs inside the HGAS. One approach to study the growth and transport of NPs inside the GAS is in-situ small angle X-ray scattering (SAXS) [35]. In the framework of this thesis, with this method it was possible to observe that the growth of NPs inside the HGAS is highly dynamic and that especially big NPs are trapped in the close vicinity of the target. Details can be found in

Chapter 3.2. Another approach to study the growth and transport of NPs for fixed or different Ar gas flows and pressures is in-situ UV-Vis spectroscopy [36,37]. In this thesis this method provided information about the trapping of NPs and that the trapping location and deposition rate highly depends on the gas flow and pressure inside the HGAS. To increase the understanding of the trapping mechanism and of the drag force, which is acting on the NPs, computational fluid dynamic simulation (CFD) were conducted. Here it turned out that the velocity distribution inside the HGAS is extremely inhomogeneous and that also regions are existing, where the velocity is close to 0 m/s. The velocity distribution is highly dependent on the HGAS geometry, which was only rarely investigated so far. Details of these studies can be found in Chapter 3.3 and 3.4. It turned out that in-situ small angle X-ray scattering (SAXS) [35] and in-situ UV-Vis spectroscopy [36,37] give good insights into the growth and transport of Ag NPs inside the HGAS and the trapping of NPs. However, they only provide 1-dimensional resolution which is not adequate to fully describe the dynamics in the processes. Therefore, in-situ laser light scattering (LLS) [38] measurements were conducted providing 2-dimensional resolution. Motivated by the CFD simulations, different gas inlet designs were developed and measured with the LLS technique. Although all parameters are kept constant except the gas inlet design, a strong impact on the deposition rate and the NP size distribution could be observed. This has shown once more how important the HGAS geometry is and it also indicates that new designs can help significantly to increase the deposition rate of the HGAS. The details are presented in Chapter 3.5.

Photon-based in-situ diagnostics can not only be used to investigate growth, transport and trapping. Photon-based methods can also be used to study the properties of functional NPs, e.g. the composition of alloy nanoparticles or to study the shell growth of core-shell NPs. Furthermore, the in-situ diagnostics can be used to develop or optimize new or known methods for the synthesis of functional NPs which extends the scope of applications of the HGAS. Here optical emission spectroscopy measurements (OES) were used to study the impact of redeposition on the alloy composition in the multicomponent target approach. Vahl et al. [39] showed in 2017 that the alloy composition of NPs produced with the HGAS can be tuned in-situ with the usage of only one target with a special geometry. However, at that time the high dynamics inside the HGAS and the high amount of redeposition onto the target were unknown. Therefore, no long-term experiments and in-situ diagnostics were applied during the synthesis of functional NPs in their study. In the framework of this thesis, it turned out that especially the redeposition effect brings its own challenge for the multicomponent target approach, which is a target lifetime dependent composition. However, it was possible to enhance the composition control of alloy NPs from the HGAS by applying in-situ OES [40]. This showed once more how helpful in-situ diagnostics are not only for the fundamental understanding of a method but also to increase the reliability of a method. The details on this study can be found in Chapter 3.6.

In addition, a novel method for the production of functional core-shell NPs was developed as part of this thesis using photon-based in-situ diagnostics. This study is a perfect example on how in-situ diagnostics can enhance the development of new synthesis approaches. In this study a HGAS was mounted to a vacuum chamber in which the Ag NPs can be confined by an RF plasma for an extended time period [41]. To proof that NPs can be hold in the RF plasma, UV-Vis measurements were used. There it was shown that the NPs can be hold for 1 h without losing NPs. This enabled treatments with Silane (SiH_4) as a precursor gas. UV-Vis and FTIR measurements were used to monitor the coating of the NPs with SiO_2 . Over the course of experiments, nearly no losses of NPs were observed. This and the possibility to hold the NPs nearly for an infinite time inside the plasma makes this novel combination of a HGAS and an RF discharge an excellent tool for the gas phase synthesis of core-shell NPs. The details on this study are provided in Chapter 3.7.

2 Theoretical Background

In this chapter the theoretical background of this thesis will be presented. Firstly, the reader is guided through different types of synthesis methods of NPs. Afterwards the HGAS will be explained in detail because it is important for all publications inside this cumulative dissertation. Therefore, magnetron sputtering will be introduced before the parameters, which affect the growth and transport of NPs in the HGAS, will be explained. Afterwards the composition tuning of alloy NPs in the multicomponent target approach will be described because it is essential for **Publication E**. Then the holding or trapping of NPs inside dusty plasmas will be described, which is important for **Publication F**, where particles are held in an RF discharge. Afterwards, the plasmonic properties of NPs will be introduced, which is highly relevant for **Publication B, C and F**, where UV-Vis spectroscopy is used to monitor the absorption caused by the plasmon resonance. Next, computational fluid dynamic simulations will be discussed, because they are used in **Publication C** to determine the gas velocity distribution inside the HGAS. In the last two chapters the in-situ and ex-situ methods, which were used for the investigations of the NPs inside and outside the HGAS will be introduced.

2.1 Synthesis of Nanoparticles

In this chapter, first a short definition of Nanotechnology will be given, which contains the aim and the difficulties in the research field. Afterwards, different NP synthesis methods and especially different kinds of cluster sources will be introduced to place the GAS in the context of different synthesis approaches. Furthermore, the magnetron sputtering and the GAS will be introduced.

2.1.1 Definition of Nanotechnology

Nanotechnology is an interdisciplinary field and a comparable young research discipline. Although NPs or even nanocomposites are known and used for centuries they attracted high attention in the last decades. Before different synthesis routes of NPs will be discussed in detail, in the following sub chapters, it has to be defined what NPs and nanotechnology are.

The Definition from the U.S. National Nanotechnology Initiative (NNI) is as follows:

“Nanotechnology is the understanding and control of matter at dimensions of roughly 1 to 100 nm, where unique phenomena enable novel applications. (...) . At this level, the physical, chemical, and biological properties of materials differ in fundamental and valuable ways from the properties of individual atoms and molecules or bulk matter (Nanoscale Science Engineering and Technology Subcommittee 2004).” [42]

This definition already shows, on the one hand the aim of nanotechnology and on the other hand it addresses the biggest difficulties in the research field. The aim is to synthesize NPs or nanocomposite which have beneficial properties, which their bulk counterparts do not have. But the biggest problem for the nanotechnology is to control matter at dimensions of roughly 1 to 100 nm.

The control of matter at the nanoscale inside a HGAS is the motivation of this thesis. Only when all processes inside the HGAS are reasonably understood, it can be used to create new nanocomposites with unique properties. Before the HGAS will be discussed in detail in Chapter 2.1.5. A general overview about NPs synthesis methods will be given in following Chapter 2.1.2. afterwards magnetron sputtering will be introduced in Chapter 2.1.4 to create the basis for the discussion on the HGAS.

2.1.2 Different Nanoparticle Synthesis Methods

Before the different synthesis approaches of NPs will be introduced, it is important to clarify what the demands on an ideal NP deposition process are. These important demands are illustrated in Figure 2-1.

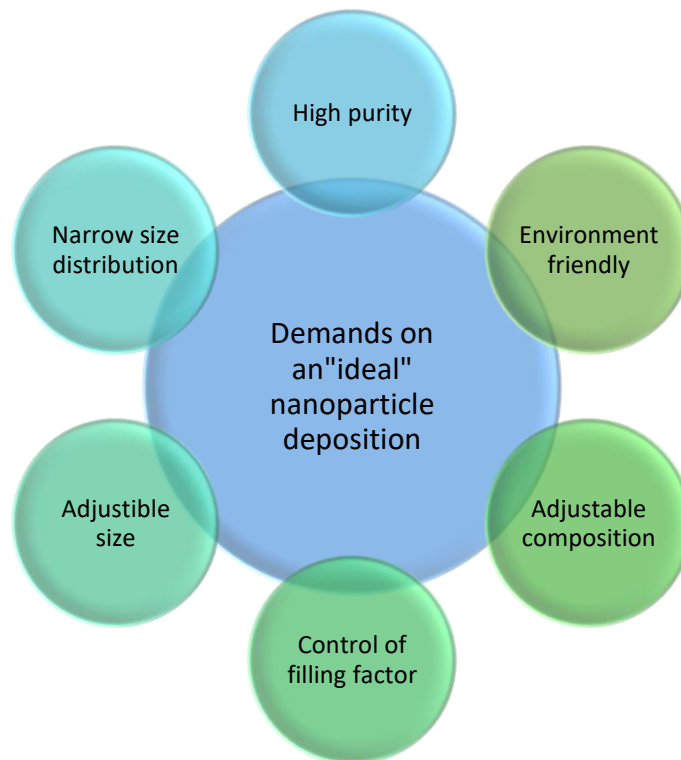


Figure 2-1: Demands on an ideal nanoparticle deposition process.

High purity of NPs can be extremely important for applications in health science. The size distribution, the size in general and the composition (in case of alloys) of noble metal NPs is very important for their optical properties. If nanocomposites should be produced it is important to choose a method, which enables to tune the filling factor of the composite in the desired range. The impact on the environment is also important and should be considered during the selection of the best suited NP synthesis method.

Depending on the desired application of the NPs, different synthesis methods of NPs are available, which all have different advantages and disadvantages. These methods range from biological, over chemical to physical approaches [43–45]. In Figure 2-2 different NP synthesis methods are shown and the color indicates to which disciplines the methods are assigned best. Not all methods will be described in detail here, because the main focus of this thesis is the inert gas condensation method, which is a physical process. This leads to the inert gas condensation approach, where NPs are produced in the gas phase, which enables the combination with different vacuum thin film deposition techniques. Nanoparticle sources based on the inert gas condensation are also called gas aggregation cluster sources. Different types are existing and an overview will be given in the next chapter.

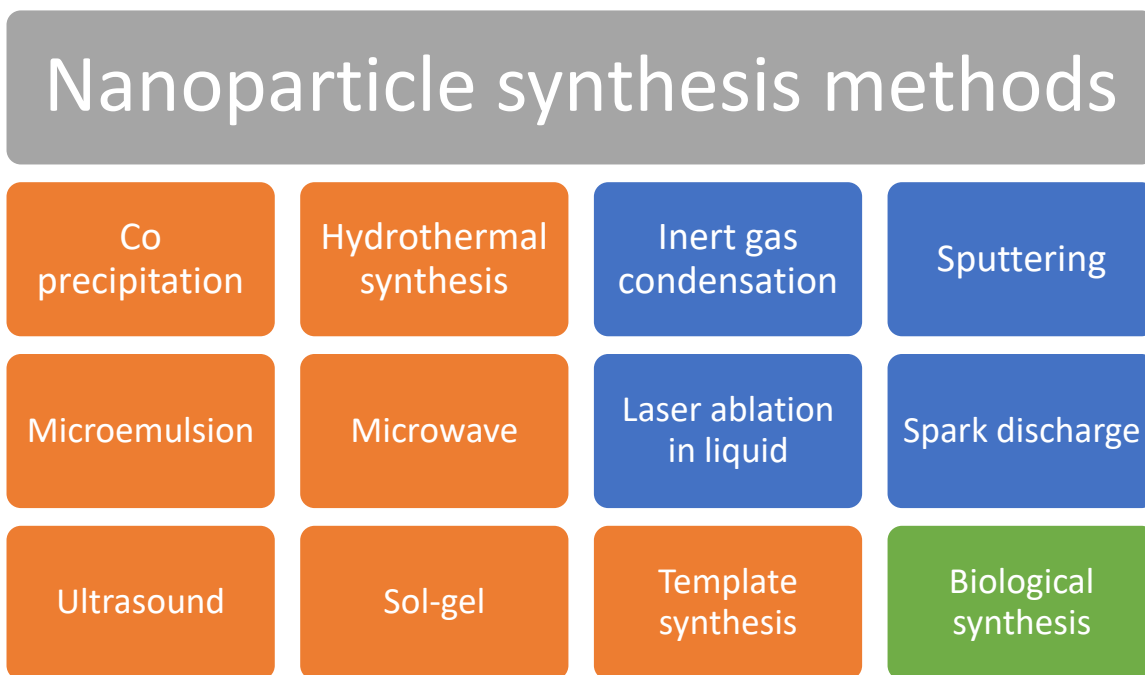


Figure 2-2: Different NP synthesis methods ranging from biological (green) over chemical (orange) to physical processes (blue).[46]

2.1.3 Different Types of Cluster Sources

Different types of cluster sources were invented over the last decades, which are listed in Figure 2-3. The basic principle of cluster formation is similar for all types of cluster sources but the differences are, e.g. in the vaporization method of the raw material, the cluster process and in the gas delivery. Some sources are operated continuously and others are pulsed. In this chapter a short overview about the different cluster sources will be given to place the sputter GAS or HGAS in the context of other PVD NP synthesis methods. In the last part of this chapter the unique advantage of the HGAS over the other GAS methods will be presented. Furthermore, the in-situ diagnostics which are used in this thesis to investigate the growth and transport inside a HGAS may have the potential to be transferred to other GAS types.

The **seeded supersonic nozzle source** produces high fluxes of low melting point metals like alkali metals. In this source the solid metal is heated in a furnace to temperatures that result in a vapor pressure in the region between 10 and 100 mbar. This vapor is mixed or seeded into an inert gas which is introduced into the furnace with a pressure of several atmospheres. The hot mixture of inert gas and vapor expands into vacuum through a small orifice. The rapid cooling behind the orifice leads to the condensation of the metal into clusters. A drawback of the method is the limited temperature in which the source can be operated, which restricts the choice of material. On the other hand, the advantage is a relative high production rate of clusters. [47–49]

In the **thermal GAS** the metal vapor is produced by thermal heating of the raw material inside a Knudsen cell. In comparison to molecular beam epitaxy the required vapor pressure for a cluster source is 10^{-3} mbar, which is three orders of magnitude higher. Therefore, higher temperatures are needed inside the Knudsen cell. In comparison to the seeded supersonic nozzle source, the expansion is weaker. Because a Knudsen cell is used, only a small volume must be heated, which makes it possible to reach 2000 K, which increases the variety of possible materials. [47,48,50]

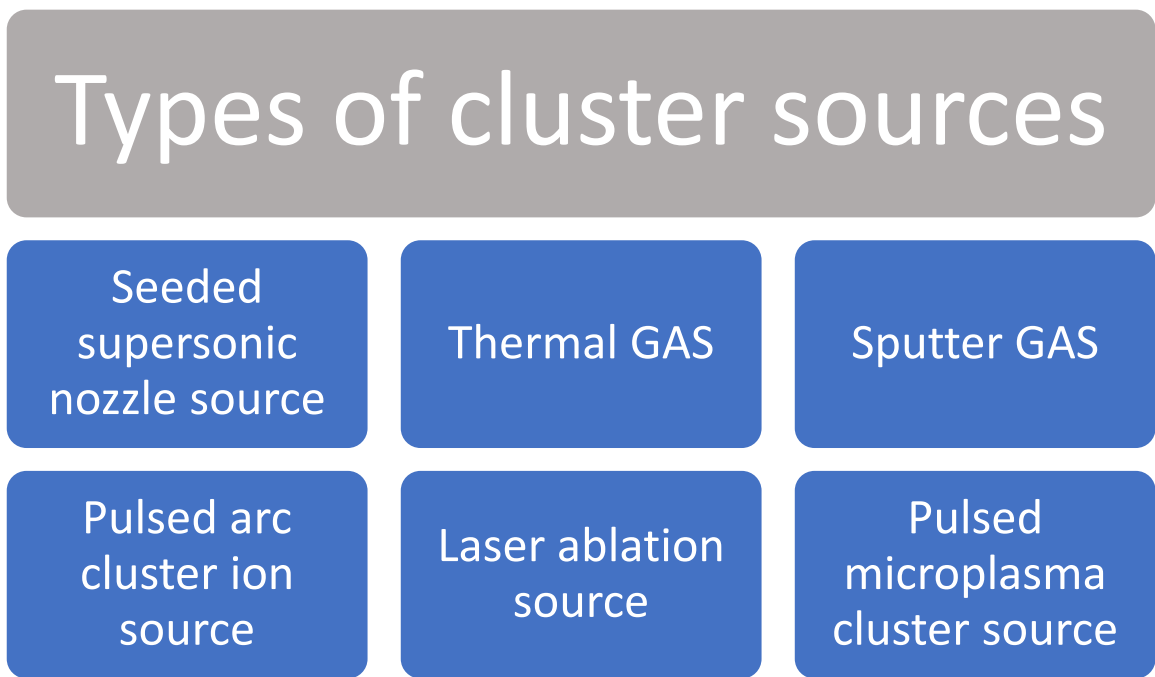


Figure 2-3: Different kinds of cluster sources.

In the **laser ablation source**, the material is vaporized by laser pulses of high power. This is combined with inert gas pulses of high pressure. The clusters are produced when the inert gas and the vaporized material are mixed. During the expansion through a nozzle, which rapidly cools down the mixture, the clustering is accelerated. A possible drawback is the high cost for the laser equipment. On the other hand, high cluster fluxes are possible with this kind of source. [47,48,51]

In the **pulsed microplasma cluster source**, the inert gas is injected with a pressure of several hundreds of Pascals, but the valve is only open for short subsecond timepulses. The gas flux is directed onto a target cathode, where a pulsed plasma is ignited. Due to the high pressure in the close vicinity to the target cathode, the sputter yield is increased. The high-pressure sputtering leads to the direct sputtering of clusters, which can work as cluster seeds for further growth. [47,52]

The **pulsed arc cluster ion source** shows similarities to the laser ablation source in terms of the clustering process. In general, the material is vaporized in the pulsed arc cluster ion source by a pulsed arc. The high current of the arc vaporizes the target material, which together with a gas pulse of an inert gas, starts the clustering process. Due to the vaporization method by arcing, a big portion of around 10 % of clusters are charged. Therefore, it is possible to use charged-particle analyzers to tailor the sizes of the deposited NPs. [47,48,53]

In the **sputter gas aggregation source**, the material is vaporized by magnetron sputtering. This type of GAS was originally developed by the group of Haberland in Freiburg and is nowadays used by many groups all over the world [23]. The biggest advantage is that nearly every material can be sputtered and can therefore be also used inside a HGAS. Additionally, the ionized portion of clusters produced in a HGAS can be $\approx 50\%$. This enables even more efficient mass selection in comparison to the pulsed arc cluster ion source, because the portion of not ionized clusters is lower, which leads finally to less waste of raw material [47,48]. The HGAS has also the advantage in comparison to the other methods, to in-situ control the composition of alloy NPs by applying the multicomponent target approach [39,40].

In the following chapter, magnetron sputtering will be described in detail, because it is the initial step for the cluster production in the HGAS. Afterwards, in Chapter 2.1.5 the working principle of the cluster formation inside the HGAS will be described in details.

2.1.4 Magnetron Sputtering

In this chapter the magnetron sputtering will be introduced, which creates the basis for the discussion on the HGAS in the next chapter. The main difference in the operation of a magnetron for the purpose of thin film production in comparison to the operation inside the HGAS for cluster production, is the operating pressure. In this section the magnetron sputtering will be described classically with the purpose of thin film production.

Magnetron sputtering is a widely used technique for the production of thin films. The fundamental process of sputtering is the impact of energetic ions onto a target material, where atoms are removed (sputtered) due to the momentum transfer of the energetic ions onto the target atoms. The sputtered atoms are deposited onto a substrate material afterwards. [47,54,55]

For DC magnetron sputtering, a noble gas like Ar is used to ignite a plasma. For that purpose, a negative bias voltage is applied to the target that also accelerates the inert gas ions onto the target surface. A schematic of a magnetron and the sputtering process is shown in Figure 2-4. The main components of a magnetron are: [47,54,55]

1. The target, which is set to a negative potential during sputtering.
2. A ground cap, which acts as a counter electrode.
3. Gas inlet.
4. Permanent magnets.
5. Water cooling, which prevents target melting and demagnetization of the magnets.

Typically, a voltage between -150 to -400 V is applied to the target. The inert gas is injected to the vacuum chamber through a small channel between the magnetron and the ground cap. The width of the channel is smaller than 1 mm to prevent plasma ignition in this area. The permanent magnets behind the target are used to generate a magnetic field above the target, which traps electrons in a circular motion due to the Lorentz force. This area is called race track. The trapping of electrons above the target increases the electron density, which increases the ionization probability of neutral gas atoms. Finally, this leads to an increased ion density and an increased sputter rate in this area. Therefore, much more material is removed in the race track region, where the synonymous name erosion zone originates from. The pressure can be reduced by using permanent magnets without decreasing the ion flux. This increases the mean free path of sputtered atoms, which increases the deposition rate and the energy of the arriving atoms on the substrate. The formation of the erosion zone is a disadvantage, because the target has to be exchanged before the whole material was used for sputtering. This can be prevented with the usage of full-face-erosion-zone magnetrons [56]. Their magnetic field is not constant but is manipulated in a way, which enables to sputter nearly the whole target material, without the formation of an erosion trench. Not the whole applied power to the magnetron is transferred into the sputtering process. A significant portion is transferred into heat. This can cause cracks or melting of the target. To prevent this, a magnetron is water cooled. [47,54,55]

In this chapter the basic concept of sputtering was described. In the next chapter, the HGAS will be discussed. There also magnetron sputtering is used to knock out atoms from a target, but in comparison to the formation of thin films, the operating pressure during magnetron sputtering is in the range of hundreds of pascals in comparison to fractions of pascals.

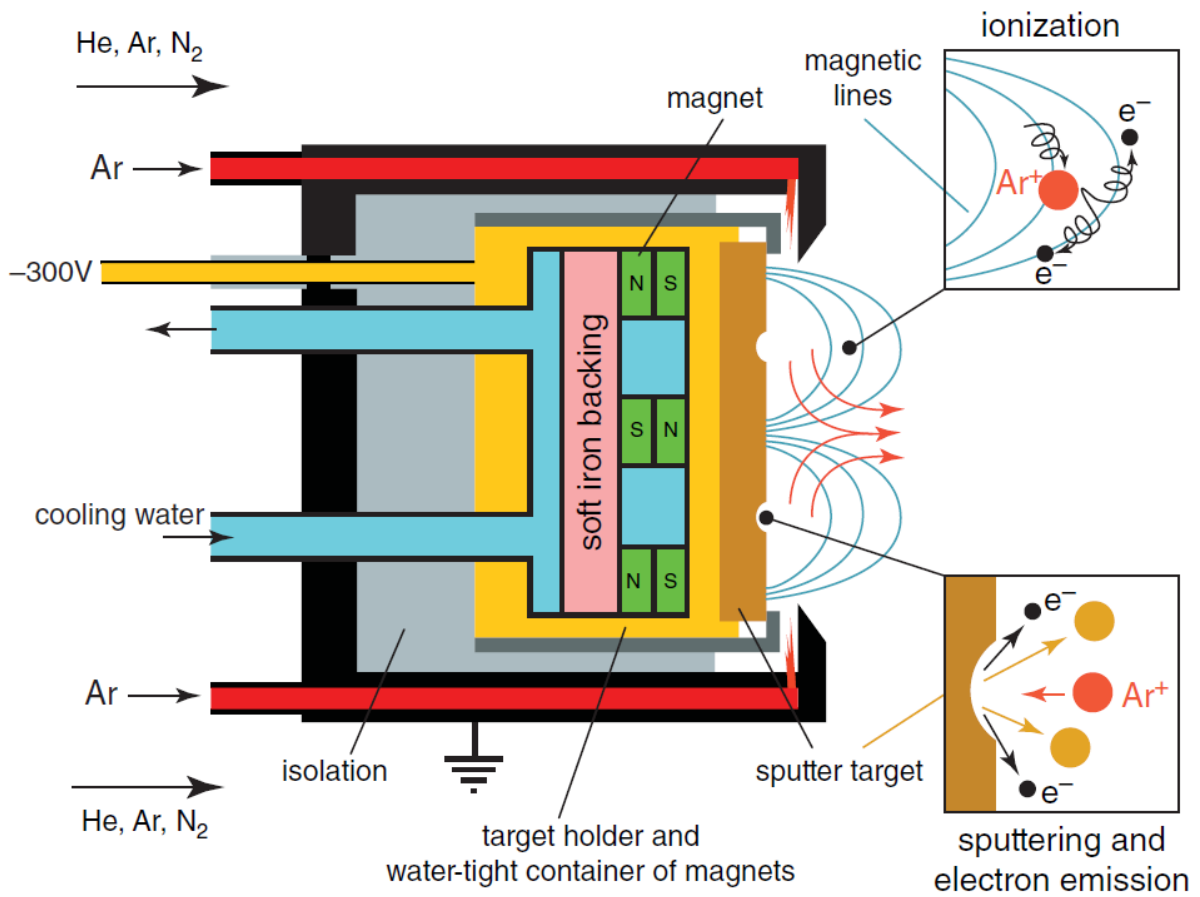


Figure 2-4: Schematic cross section of a planar magnetron. Shown are the target, the ground cap, the gas inlet, the permanent magnets and the water cooling. Additionally, the sputtering process and the ionization process are schematically depicted. The figure is reprinted from the book from Huttel et al. [47].

2.1.5 The Haberland Type Gas Aggregation Cluster Source (HGAS)

In this chapter the working principle of a HGAS will be introduced. The chapter is structured into two parts. In the first part, the setup of a HGAS and the nucleation and growth processes inside the HGAS will be discussed. In the second part the working parameters, which are affecting the HGAS, will be introduced.

2.1.5.1 Nucleation and Growth

As it was mentioned before in Chapter 2.1.3, the HGAS is a sputter GAS. It consists of a magnetron, where the target material is vaporized. A small orifice (1-5 mm) connects the HGAS and the deposition chamber. The setup of a HGAS and the NP growth is schematically shown in Figure 2-5. To enable condensation of sputtered atoms and to form NPs, a high pressure (tens or hundreds of Pa) compared to sputter deposition for thin films is needed. Since the inert gas, usually Ar, is inserted inside the HGAS and only the deposition chamber is pumped, a higher pressure in the HGAS is created, because the gas flow conductance through the orifice is low. The process of NP formation inside the HGAS can be divided into six steps, which are also shown in Figure 2-5: [47]

1. Vaporization of target material
2. Irreversible nuclei formation
3. Growth of NPs by condensation
4. Coalescence of different NPs
5. Sintering of NPs
6. Transport through orifice and deposition onto the target

In the following section, all steps will be described and all of these steps are schematically presented additionally in Figure 2-5.

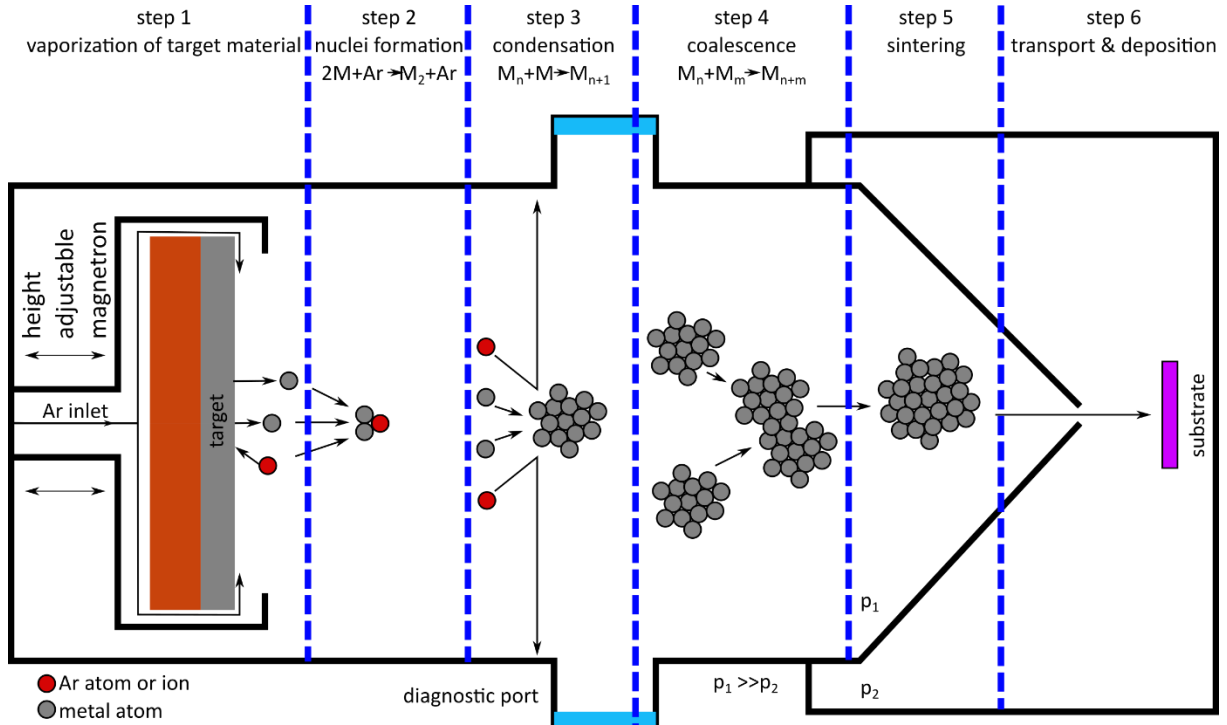


Figure 2-5: Schematic of a HGAS and the growth of NPs. The HGAS consists of a height adjustable magnetron with an Ar inlet, diagnostic ports for in-situ investigations and an orifice, which is connected to the deposition chamber. Important is that the pressure in the HGAS (p_1) is much higher than in the deposition chamber (p_2). The 6 steps sputtering, nuclei formation, condensation, coalescence, sintering, transport & deposition are also shown.

Step 1 is the vaporization of the target material or sputtering, which was already described in details in Chapter 2.1.4.

Step 2 is the nuclei formation, which can be described partially with the classical nucleation theory (CNT) [47]. The free enthalpy of formation of a nucleus consists out of two counteracting terms. One term is the surface contribution to the enthalpy ΔG_{surf} and the other term the volume contribution to the enthalpy ΔG_{vol} . If the solid face is the stable face ΔG_{vol} is negative, thus energy is gained by forming the nuclei. Then ΔG_{surf} is positive and represents the cost of energy for the creation of the surface. Both terms are shown below:[47]

$$\Delta G_{surf} = 4 \pi R^2 \Delta g_{surf} \quad (2-1)$$

$$\Delta G_{vol} = -\frac{4}{3} \pi R^3 \Delta g_{vol} \quad (2-2)$$

Here R is the radius of the growing nuclei and Δg represents the enthalpies per unit surface or volume. The sum of both terms is the overall free enthalpy: [47]

$$\Delta G = \Delta G_{surf} + \Delta G_{vol} \quad (2-3)$$

If the first derivative of ΔG equals zero, the radius is called the critical radius R^* . If the critical radius is reached, the particles are stable and can grow further: [47]

$$R^* = \frac{2 \sigma v}{k_B T \log(S)} \quad (2-4)$$

Here σ is the surface energy, v is the atomic volume, S is the supersaturation ratio between the vapor pressure in the gas phase and the vapor pressure over a flat surface of the corresponding solid. In a HGAS, the supersaturation ratio is usually much higher than one. However, the CNT is too much simplified, because it assumes that the small NPs have the same properties as their bulk counterparts. [47]

Therefore, another theory was developed: The kinetic nucleation theory. It uses a steady state approximation to describe the formation of nuclei. The basic assumption is that the nucleus is stable, if the probability for evaporation and condensation of one atom from or on the nucleus is the same. The following equation can be written, where X corresponds to the growing nuclei: [47]



When this reaction is extended by an intermediate step between the reactant, which is the gas, and the product, which is the solid, the Rice-Ramsberger-Kassel-Marcus (RRKM) theory is formed. The transition state in the following formula corresponds to the energy barrier ΔG from the CNT: [47]



Here $k_f(N)$ is probability of complex formation (condensation of an atom on the nuclei), $k_d(N)$ is the complex destruction and $p_s(N)$ is the probability for stabilization. The first step of this reaction is a bimolecular reaction and the second step is a unimolecular reaction. In the unimolecular reaction, the nucleus is stabilized by the sputter gas or the buffer gas, which takes up the released energy. As a buffer gas typically He is used, because it has a high mean velocity, which enables fast energy exchange between the nuclei and the chamber walls. Nevertheless, in this thesis no buffer gas is used, but the sputter gas Ar can also serve as a buffer gas. The interested reader can find more details on this topic in the text book of Yves Huttel. [47]

After the nucleation process was described, now **step 3**, the condensation, will be discussed. When the formed nucleus is stable, it can grow further by collision and condensation of single atoms. The condensation energy is distributed across the internal degrees of freedom of the particle, which heats up the particle. At this step the buffer gas becomes important, because it transfers the energy from the particles to the side walls of the HGAS. Therefore, many HGAS sources are equipped with water or liquid nitrogen cooled walls [28,57]. A faster cooling rate of the particles leads to less re-evaporation of atoms from the particles and finally increases the growth speed. At this point of growth, most NPs are in a liquid stage because of the melting point depression of small NPs [58–60].

The high flow of buffer gas inside the HGAS from the magnetron to the orifice builds up a laminar flow. Due to the increasing size of the NPs, the collision rate between the gas molecules and the clusters is increased. The resulting drag force transports the NPs in the direction to the orifice. During the transport of the NPs more and more atoms condense on the NPs reducing the atom density along the path to the orifice. At some point no free atoms are left which can bound to the NP and the growth stops. Nevertheless, some NPs cannot follow the gas flow and diffuse to the side walls of the HGAS, where they get lost. [47]

After the growth by condensation stopped, **step 4** (coalescence) takes place. Coalescence is the formation of two NPs to one large NP. This process takes place close to the orifice, because in the cone region the NPs are focused to the orifice, which increases the collision probability of two NPs. This process depends also on the inert gas pressure, the free atom density and the aggregation length. [47]

Another effect is the charging of NPs inside the HGAS due to the plasma environment. The NPs collide with ions and electrons that charges the NPs either positive or negative. This can increase the coalescence probability, because the individual NPs are attracted by the Coulomb force, if they have opposing charges. The general assumption for charging of NPs in plasmas is that they will charge up negatively, because of the higher mobility of electrons compared to ions in the plasma. However, in the HGAS the particle density is so high that many electrons are bound to the NPs disrupting the quasi neutrality of the plasma locally. Furthermore, the ion and electron densities far away from the magnetron are much lower in comparison to a region closer to the magnetron. Therefore, NPs can charge up positively far away from the magnetron by collecting ions or by photo-electron emission. Thus, NPs can charge both positively and negatively, but the larger the NPs, the more likely they are to charge negatively due to the larger cross-sectional area. The charging of the NPs can also be utilized for mass selection in quadrupole mass filters, which can be installed behind the HGAS. There the particles can be deflected in dependence to their mass and charge. This enables the extraction of NPs with a narrow size distribution on the cost of deposition rate. [28,61]

If the melting point of the NPs is low enough or the temperature is high enough, the coalesced particles can rearrange or sinter (**Step 5**) to minimize the surface energy.

Step 6 is the last step and is the transport and deposition of the NPs onto the substrate. The pressure in the deposition chamber is usually smaller than 1 Pa. Therefore, the collision with gas molecules is rare and the NPs form a linear beam from the orifice to the substrate. The speed of the particles can reach 200 m/s depending on their size and process parameters of the HGAS[28]. Since the kinetic energy of the NPs is low, they do not damage the substrate or get damaged due to the impact. Therefore, the NPs are deposited in the so-called soft-landing regime.

2.1.5.2 Parameters Affecting the Growth and the Deposition Rate

After the setup of a HGAS was described and the different formation steps of NPs inside the HGAS were introduced, in this chapter the working parameters of the HGAS, which are affecting the NP growth will shortly be described. These parameters are shown in Figure 2-6.

One factor, which influences the size distribution of nanoparticles, is the **power** applied to the magnetron. On the one hand Liu et al. [26] found that the NP size decreases with increasing sputter power. They attributed this effect to the higher ionization degree of sputtered atoms with higher powers. Therefore, more positively and negatively charged ions are present for higher powers, which increases the nucleation rate, because of the attraction of ions with opposite charges [26]. On the other hand, Stranak et al. observed a decrease of NP size for powers bigger than 130 W and attributed this effect to the evaporation of atoms from the NPs as a result of the increasing temperature [27]. Nevertheless, Polonskyi et al. found out that the NP size is increasing with increasing power, without giving an explanation, because the focus of the work was not on the size dependence [28]. It can be concluded that the power dependency of NPs from the NP source is not fully understood until now, but it is confirmed that the power influences the NPs growth. Therefore, in-situ diagnostics for the processes inside the HGAS are in high demand. To find a suitable in-situ diagnostics for the HGAS is one aim of this thesis.

Another influencing parameter of the NP size is the pulse frequency and duty cycle of the magnetron, if the applied **power is pulsed**. It was found that the relaxation time, which is the plasma off time, is an important factor. If the relaxation time becomes longer, the cooling of NPs is more efficient and they can grow larger. At frequencies below 1 kHz and low duty cycles the discharge is operated in the so called High-power impulse magnetron sputtering (HIPIMS) mode. Here the ionization of sputtered atoms becomes high and the positive ions are attracted back to the cathode [27].

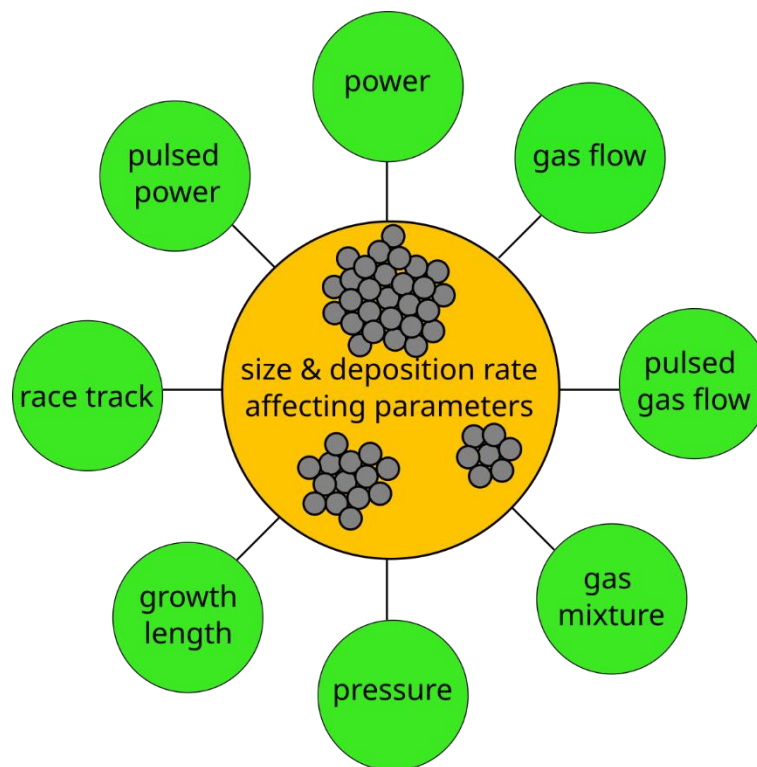


Figure 2-6: Working parameters of the HGAS which are affecting the size and the deposition rate of the resulting NPs.

Four more size affecting parameter are related to the gas. Critical parameters are the gas flow, pulsing of gas flow, the resulting pressure in the HGAS and the gas mixture. In general, a higher **gas flow** leads to a higher drag force on the particles and therefore to a higher velocity of the NPs. Hence, an increasing gas flow with constant pressure would lead to smaller NPs, because the time for condensation of atoms on the NPs becomes shorter. Experimentally this is difficult to test, because usually the orifice has a fixed size and therefore an increase of the gas flow always leads to a higher pressure. Batková et al. measured the size of NPs for constant pressures with different flows by using different orifice diameters. They were able to confirm that an increase in flow leads to smaller particles, due to the reduced residence time [62]. Additionally, a higher gas flow often leads to a higher deposition rate, because the NPs are dragged more efficiently towards the orifice and less particles get lost to the chamber walls.

The **Ar pressure** in the HGAS influences also the NP growth. The Ar pressure influences on the one hand the sputtering rate and on the other hand the appearance of condensation nuclei. Therefore, a higher Ar pressure leads to more nuclei and increases the deposition rate. Nevertheless, the higher pressure is usually achieved by increasing the Ar flow and so the drag force on the NPs is increased. Therefore, generally the higher Ar flow at a higher pressure reduces the residence time which reduces the NP size. [29,63]

Another impacting factor on the NP growth is the **admixture of He** as a buffer gas in addition to the Ar flow. It was found that the He does not influence the sputtering process and the nucleation process so much. On the other hand, the He influences mainly the NP velocity. Therefore, a higher He flow terminates the growth of NPs faster, because the NPs are swept out of the growing region inside the HGAS faster. [29,63]

The **gas flow can also be pulsed** in a HGAS like it is done, e.g. in a pulsed arc cluster ion source or laser ablation source. The gas pulsing in the HGAS will also influence the NP size and deposition rate. When the gas flow is pulsed, the pressure inside the HGAS is oscillating around an average pressure. During the low-pressure period in the beginning of the gas pulse, more atoms are sputtered in comparison to continuous operation. During the high-pressure period the particles are more effectively cooled due to sufficient energy transfer which produces larger NPs. Drache et al. found 8 times higher NP mass flux for pulsed operation in comparison to continuous operation. Here the constant pressure was the same like the mean pressure during pulsed operation. [64]

The **aggregation length** of a HGAS can often be adjusted by the use of a height adjustable magnetron, like it was shown in Figure 2-5. Here the distance between the magnetron and the exit orifice can be adjusted easily. It was found that an increase in aggregation length leads to an increase in the NPs size. This is related to the increased residence time of NPs in the strongly supersaturated sputtered metal vapor environment [29,63]. But Kousal et al. [33] found trapping of NPs in the close vicinity of the target and also that larger NPs are found close to the target as far away from the target. Therefore, the simple picture that NPs grow along their whole way through the HGAS to the orifice seems to be more complex. This shows once more, how important in-situ diagnostics are to fully understand the growth and transport inside the HGAS.

The last size and deposition rate affecting parameter is the shape of the **race track**. It could also be said that the target lifetime influences the growth process, because a strongly used target shows more erosion than a recently installed target. Ganeva et al. [65] found that with increasing lifetime or increasing erosion the NP deposition rate and the size is firstly increasing. After a maximum, the size and the deposition rate drops under the initial values. If the target is used even longer, the formation of NPs stopped abruptly. Ganeva et al. attributed this finding to the angular dependence of the sputter

yield. With increasing erosion, the impact angle of the Ar ions in respect to the target surface changes. With increasing angle, the sputter yield increases until a maximum is reached at around 60°. Then the sputter yield drops quickly. It was found that this angle was reached at the point, where the size distribution changed significantly. Therefore, the target lifetime is a critical parameter, which has to be considered during the operation of a HGAS. [65]

Other factors, which are not discussed here are the influence of the gas velocity distribution inside the HGAS, the gas inlet configuration, redeposition onto the target and trapping of NPs. These factors were partially not considered in literature before the start of this thesis in 2018. Details about these additional factors can be found in Chapter 3.4 and 3.5, where the publications dealing with these subjects are presented.

2.1.6 In-situ Composition Tuning Inside a HGAS

To enable the application of the HGAS in the industry, not only the efficiency and deposition rate are important. Moreover, the ability of the HGAS to produce special NPs, e.g. alloy NPs with tailored composition, can be a selling argument against other synthesis methods, which do not have this option. In 2017 Vahl et al. [39] found a method where inside a HGAS the composition of AgAu NPs could be varied in-situ without changing the target. They used a customized target, where a trench was milled inside a pure Ag target first and three gold wires were embossed into this trench afterwards. They found out that by adjustment of the operation pressure of the HGAS from 36 Pa to 191 Pa the resulting NP composition could be varied from ≈ 60 at% to ≈ 73 at% of Au measured with XPS. They attributed the composition change to a change in the mean free path of the Ar ions with a change in the pressure. A higher pressure results in a shorter mean free path and, therefore, in a narrower erosion zone. Since the Au wires are embossed into the center of the erosion zone, the narrower erosion zone leads to a higher Au content in the NPs. [39]

Nevertheless, in this publication the influence of redeposition of sputtered material for a longer target lifetime was not investigated. Therefore, in this thesis the multicomponent target approach was investigated in more detail in terms of target lifetime. Here in-situ optical emission spectroscopy was applied to identify the sputtered atoms inside the HGAS and relate this to the resulting composition. More details on this subject can be found in the **Publication E**.

2.2 Particle Holding Inside a Dusty Plasma

A plasma is often called the fourth fundamental state of matter and is characterized by its electrical conductivity. This conductivity is caused by it being a partially or fully ionized gas, thus consisting of ions, electrons and neutral atoms and molecules. If particles with a size from nm to μm are present as well, the plasma is called a dusty plasma. The particles can either grow by different mechanisms inside the plasma or can be injected into the plasma. In this thesis in **Publication F** a dusty plasma is created by the injection of Ag NPs from a HGAS aggregation source into a second RF plasma discharge. There the particles got trapped and were coated. In this chapter the mechanism which enables the trapping of NPs inside a dusty plasma will be described. Additionally, the forces which are discussed here can potentially also act on NPs inside the HGAS which is most probably the reason for the trapping inside the HGAS.

In dusty plasmas the dust grains get charged primarily because they are collecting electrons and positive ions. In a plasma, electrons have a higher mobility in comparison to the ions, because they have a much lower mass but hold one elementary charge as well. For that reason, dust particles are usually charged negatively. Due to the charging of the particles, different forces are acting on the

particles inside a dusty plasma which are finally able to trap particles inside a plasma. These forces are: [66,67]

1. Gravity
2. Electric field force
3. Ion drag force
4. Thermophoresis
5. Neutral drag

In the following section these forces will be shortly described and their dependence on the size of the particles will be described.

The gravitational force is:

$$F_g = m_d g = \frac{4}{3} \pi a^3 \rho_d g \quad (2-7)$$

With g is the gravitational acceleration, ρ_d is the mass density of the dust particle, a is the radius of a spherical dust particle. The gravitational force plays only an important role for particles in the micrometer range and becomes negligible for particles in the nanometer range, because it scales with a^3 . [66,67]

The electric field force is:

$$F_E = Q_d E = 4 \pi \varepsilon_0 a \phi_{fl} E \quad (2-8)$$

Where Q_d is the charge of the dust particle, ε_0 is the dielectric permittivity of vacuum, a particle radius, ϕ_{fl} is the floating potential of the dust particle and E is the electric field. The equation shows that the electric field force scales linearly with the size of the particle, which is derived from the orbit-limited (OML) model. In the plasma volume (outside the sheath region) only a small electric field is present. Therefore, the electric field is only able to overcome the gravitational force for small particles inside the nanometer range. [66–68]

The ion drag force is:

$$F_{ion} = F_{col} + F_{orb} \quad (2-9)$$

The ion drag force consists of two different forces. One is the collection force F_{col} and the other one is the orbit force F_{orb} . This model was introduced by Barnes et. al. [69]. The collection force is present because a charged dust particle collects ions and these ions are transferring momentum to the particle. The collection force depends with a^2 on the radius of the particle. The orbit force has to be considered, because if an ion is deflected in the field of a dust particle, the momentum of the ion changes the direction, but the magnitude is conserved. The orbit force depends in the end with a^2 on the particle size. Therefore, the ion drag force depends with a^2 on the size of the particle. For more details on this theory the reader is referred to the original model by Barnes et al. [66,67]

The neutral drag force is:

$$F_{drag} = -\delta \frac{4}{3} \pi a^2 m_n v_{th,n} n_n v_d \quad (2-10)$$

Here m_n is the mass of the neutral gas atom, n_n is the density of the neutral gas atom and $v_{th,n}$ is the thermal velocity of the neutral gas atoms. The momentum transfer of the neutral gas onto the dust particle depends on how the gas atoms are reflected from the particle. The gas can be reflected in different ways, e.g. diffuse, specular, etc. The parameter δ accounts for the different types of reflections and lies between 1 for specular reflection and 1.44 for diffuse reflections. The neutral drag force can be understood as a friction force due to the neutral gas atoms, which are impinging on the

dust particle and slow the dust particle down, when it is moving. The neutral drag force depends with a^2 on the size of the particle. [66,67]

In the HGAS this force enables the transport of NPs from the HGAS to the deposition chamber.

The thermophoretic force is:

$$F_{th} = -\frac{32}{15} \frac{a^2 k_n}{v_{th,n}} \nabla T_n \quad (2-11)$$

Here ∇T_n is the temperature gradient of the neutral gas and k_n the thermal conductivity of the gas. The thermophoretic force originates from a temperature gradient in the neutral gas. In a simple picture, the neutral gas atoms hitting a particle from a side with a higher temperature transfer a larger momentum than gas atoms from a colder side. Therefore, the force acting on the particle from the side with the higher temperature exceeds the force from the colder side. The thermophoretic force is especially important for nanometer sized particles inside a plasma. This force is present in a dusty plasma, because a plasma discharge is heating the gas. The thermophoretic force depends with a^2 on the particle size. [66,67]

After the most important forces, which can act on particles inside a plasma, are discussed, in the following section the interplay of these forces which can finally lead to particle holding or trapping will be discussed.

In Figure 2-7 the forces acting on a dust particle in a typical low power RF Ar discharge are calculated for different particle radii. The neutral drag is not included, because it is only of interest for moving particles. It is also important to note that the electric field is assumed to be constant for the calculation, even though this is not the case in a real discharge. It is well visible that for low radii in the nanometer range the dominating forces are the electric field force and the ion drag force. The thermophoretic force for a gradient of 200 K/m is already noticeable. The gravitational force for particles in the nanometer range is negligible. The dust will move to a point where the electrical field force balance out the other forces. For small particles the gravitational force is low, thus smaller electric fields are able to levitate and trap the particles in the entire plasma volume. Nevertheless, so called "voids" are existing in plasmas, where no particles can be found. These voids are also associated to the interplay of electric field forces and ion drag forces. In the plasma center the electric fields are always small for geometrical reasons. Therefore, the ion flow velocity is small, too. However, the electrical field force is smaller in the center than the ion drag force. This leads finally to an empty space, the void, where no dust is found. [66,67]

The holding and trapping of dust in a plasma is utilized in **Publication F** to confine NPs, which are synthesized in a HGAS, to coat them by the introduction of precursors into the RF plasma.

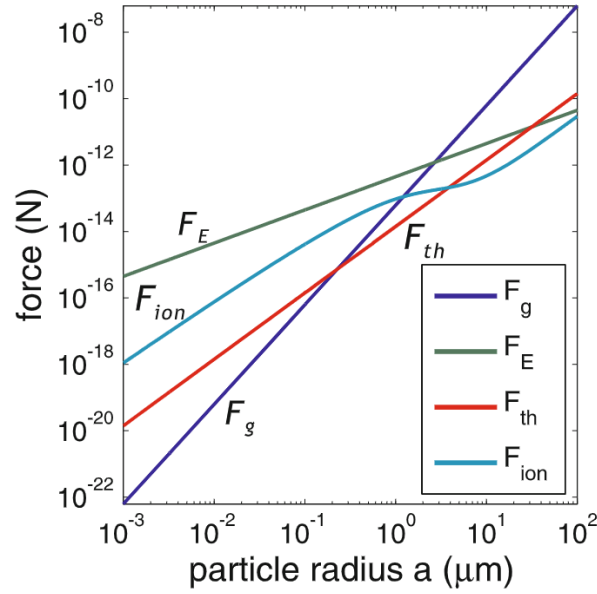


Figure 2-7: Shown are the forces acting on dust particles for the parameters: $\rho_d = 1500 \text{ kg/m}^3$, $T_e = 2 \text{ eV}$, $\phi_{fl} = -4 \text{ V}$, $E = 1000 \text{ V/m}$, $n_i = 10^{15} \text{ m}^{-3}$, $v_{th,n} = v_{th,i} = 400 \text{ m/s}$, $\nabla T_n = 200 \text{ K/m}$, $k_n = 0.016 \text{ kg m s}^{-3} \text{ (Ar)}$. The figure is reprinted from [67].

2.3 Plasmonic Properties of Nanoparticles

The plasmonic properties of noble metal NPs are responsible for their unique optical characteristics. In this thesis, the optical properties of NPs are used to detect them inside the HGAS with in-situ UV-Vis spectroscopy (**Publication B & C**). Therefore, it is important to discuss the origin of the plasmonic properties of NPs which will be done in this chapter.

Plasmon resonances can be defined as collective oscillations of conduction electrons in response to an electric field, e.g. a light wave. In general, three different kinds of plasmon resonances are existing: Bulk plasmons, surface plasmons and localized surface plasmons.

Bulk plasmons are the result of an electromagnetic wave which are propagating through a material. The field polarizes the medium and excites a physical movement of the charges. Therefore, the excitation field and the displacement of the charges are coupled. Such a coupled excitation is called Polariton. In this thesis, the main focus is on the plasmonic properties of NPs. Therefore, the understanding of surface plasmons and localized surface plasmons is much more important. For those reasons bulk plasmons won't be treated in detail. [70–72]

The interested reader can find a good overview about bulk plasmons and plasmonic properties in general in the textbook of Enoch et al. [70].

Surface plasmon polaritons (SPPs) can be described as surface charge density waves which are propagating along a metal-dielectric interface. An exemplary dispersion curve for SPPs (blue-dashed line) can be found in Figure 2-8. From the dispersion curves of light in vacuum (black-solid line) and the curve of the SPP follows that light cannot couple directly to a plasmon excitation of a flat semi-infinite surface, because energy and momentum cannot be conserved at the same time. Nevertheless, light can also excite SPPs when additional momentum is provided. Different options are possible. One option is to modify the surface of the metal by gratings. Such gratings can provide lattice momentum. Another option is to pass the light through a block of glass. This increases the wavenumber and the momentum so that the light can couple to the SPPs. [70–72]

Two configurations are possible. One is the Otto configuration and the other the Kretschmann configuration [73]. In the Otto configuration, the light illuminates the wall of a glass prism and is reflected totally internally. On the other side of the wall a thin metal film is positioned close to the prism wall. If the distance between the prism and the metal film is close enough, an evanescent wave can interact with the metal surface and excite the SPP. In the Kretschmann configuration, the metal is directly evaporated onto the prism wall. In this case the evanescent wave penetrates through the metal film. Therefore, the SPP is excited on the outer side of the metal film. [73]

In contrast to the SPP of a flat semi-infinite surface, the plasmon is not propagating in a metallic NP. Due to the small dimensions and the closed geometry, the surface charge density can oscillate locally (Figure 2-8), which is called localized surface plasmon (LSP). If the electron cloud of a metal NP is moved away from its original position, a restoring force arises from the attraction of nuclei and electrons due to Coulomb forces. Due to this restoring force, the electron cloud is oscillating. The finite geometry does not only allow the coupling to external light, it also enables to tune the energies of the plasmon excitation. Therefore, a good control over the size of metal NPs is important to adjust the optical properties of these NPs precisely. Nevertheless, different other factors besides the size of NPs are affecting the plasmon resonance, which will be described in the following section. [70–72]

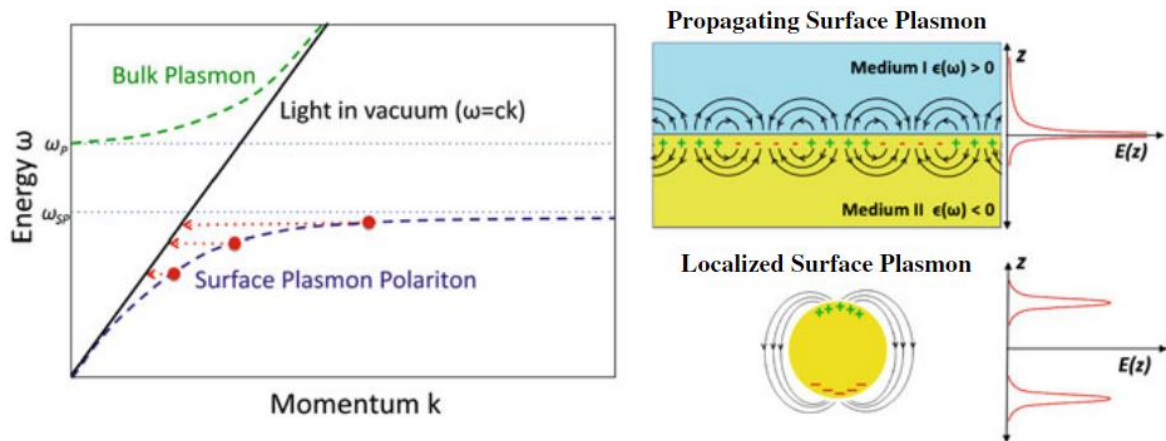


Figure 2-8: The plot on the left side shows the dispersion curve of the bulk plasmon (green-dashed line) and surface plasmon polariton (blue-dashed line). Additionally, the curve of light in vacuum is displayed (black-solid line). The red dots and red-dashed lines show schematically the additional momentum, which is needed for effective coupling. On the top right, a schematic drawing of a propagating surface plasmon polariton is shown together with a plot for the electric field strength in dependence to the distance to the interface. On the bottom right, the schematic drawing of the surface charge density of a localized surface plasmon together with the electric field strength plot in dependence to the distance to the center of the particle is shown. The figure is reprinted from [70].

Factors affecting the LSP are:

1. Size of NPs
2. Shape of NPs
3. Dielectric surrounding of NPs
4. Inter particle distance between NPs (Plasmonic coupling)

To understand how the size and the surrounding medium are affecting the LSP, the polarizability of a spherical particle has to be introduced. The optical response of the LSP in a metallic NP can be described with the polarizability which links the incoming electric field with the electric dipole moment. In the quasi static approach, the dipolar polarizability α_{sph} of a spherical particle can be described with the following equation: [70–72]

$$\alpha_{sph} = 4 \pi \varepsilon_0 a^3 \frac{\varepsilon_{sph} - \varepsilon_{med}}{\varepsilon_{sph} + 2 \varepsilon_{med}} \quad (2-12)$$

Here ε_{sph} is the dielectric function of the sphere, ε_{med} is the dielectric function of the surrounding medium, a is the radius of the NP and ε_0 is the vacuum permittivity. A spherical metal NP can be treated as a kind of optical antenna, because it converts effectively electromagnetic radiation from the far-field into the near-field and vice versa. To describe the scattering and absorption by NPs, the scattering and absorption cross-sections have to be introduced. These cross-sections can be used to relate the energy, which is sent back to the far-field (scattering), to the energy, which is dissipated within the NP (absorption). The scattering cross-section and the absorption-cross section are related to the incident power I_{inc} , the scattered power I_{scat} and the absorbed power I_{abs} .as follows: [70]

$$C_{scat} \propto \frac{I_{scat}}{I_{inc}} \quad (2-13)$$

$$C_{abs} \propto \frac{I_{abs}}{I_{inc}} \quad (2-14)$$

For spherical NPs with a radius a , which is smaller than the incident wavelength, retardation does not play a role and the scattering and absorption cross sections are defined by the following formulas: [70]

$$C_{scat} = \frac{k^4}{6 \pi} |\alpha_{sph}|^2 = \frac{8 \pi}{3} k^4 a^6 \left| \frac{\varepsilon_{sph} - \varepsilon_{med}}{\varepsilon_{sph} + 2 \varepsilon_{med}} \right| \Rightarrow C_{scat} \propto \frac{a^6}{\lambda^4} \quad (2-15)$$

$$C_{abs} = k \text{Im}\{\alpha_{sph}\} = 4 \pi k a^3 \text{Im}\left\{ \frac{\varepsilon_{sph} - \varepsilon_{med}}{\varepsilon_{sph} + 2 \varepsilon_{med}} \right\} \Rightarrow C_{abs} \propto \frac{a^3}{\lambda} \quad (2-16)$$

Here k is the wavevector, which is related to the frequency ω and the speed of light in vacuum c by the following formula: [70]

$$k = \frac{\omega}{c} \quad (2-17)$$

From the equations (2-15) and (2-16) follows that with increasing size of the NPs the relative contribution of scattering to the total extinction increases because of the a^6 and a^3 dependence of the scattering and absorption cross-sections. It has to be mentioned that the quasistatic approximation does not consider any size dependence of the spectral position of the LSPR. Thus, this approach cannot explain the size dependence of the LSPR spectral position, but it explains how the scattering and absorption contributions are changing. Additionally, it explains how the **surrounding medium** around the NPs influences the LSPR. Therefore, e.g. thin shells of a dielectric material around metal NPs can be used to tune the spatial position of the LSPR of core-shell NPs. [70–72]

In the following sub section, the **size dependence** of the LSPR will be shortly discussed. For particles which are much smaller than the incoming wavelength, the incoming fields are nearly constant across the NP. With increasing size of NPs, the quasistatic approach is no longer valid and a full solution of Maxwell's equations is necessary to obtain the correct spectral position and intensity of the LSPR. The solution of the modes in a spherical NP was obtained by Gustav Mie [74]. Here retardation in the electro-magnetic interaction is considered. The solution of scattering and absorption was obtained by an expansion of the fields in spherical harmonics. Here the scattering and absorption cross-sections are showing maxima at a specific resonance frequency, which depends on the size of the NPs. In general, the spatial position of the LSPR gets red shifted (higher wavelength), when the size of the NPs is increasing. [70–72]

After the size dependence of the LSPR was discussed, in this section the influence of the **shape** will be described exemplary with an elliptical NP. The maximum of the polarizability defines the resonance condition of a metallic NP. For a sphere the polarizability α is isotropic and given by the formula (2-12). In the case of an elliptical particle the polarizability becomes anisotropic and shows different optical responses along the different directions. In the case of an elliptical NP, the polarizability is defined by a tensor that addresses the optical response along several directions. For an elliptical NP elongated along the z-axis within the electrostatic approximation, the polarizabilities along its symmetry axes is as follows: [70–72]

$$\alpha_{x,y,z} = \frac{4}{3} \pi L_x L_y L_z \frac{\varepsilon_{ell} - \varepsilon_{med}}{\varepsilon_{med} + P_{x,y,z} (\varepsilon_{ell} - \varepsilon_{med})} \quad (2-18)$$

Where $P_{x,y,z}$ are the depolarization factors in the different directions, L_x, L_y, L_z are the different lengths of the ellipsoid, ε_{ell} is the dielectric function of the ellipsoid and ε_{med} is the dielectric function of the surrounding medium. In the end, two different solutions of the dipolar LSPR are possible. One solution for the long axis polarizability and one for the short axis polarizability. It follows that an extinction cross-section plot vs. wavelength for an elliptical NP shows two maxima: One maximum for the short axis is found, which is commonly referred to as transversal LSP and is located at a lower wavelength. The second maximum is found for the long axis. This LSP is called longitudinal LSP and is located at a higher wavelength. Nowadays, lithography methods have enabled complex shapes of NP, e.g. nanocubes, nanoshells, nanorings, nanocups, nanostars, nanotriangles and others. Such modifications in the shape of the NPs can be used to tune the location of the LSPR. [70–72]

The last important factor affecting the LSPR is the **coupling of different NPs**. If two or more NPs are approaching each other, the localized modes of each single particle couple to each other via Coulomb interaction. This results in a strongly localized symmetric surface plasmon mode and originates from the hybridization of the single dipolar surface plasmons from each particle. The field in the gap between the particles is enhanced strongly and is called “hot spot” sometimes. [70–72]

The arrangement of NPs in respect to the propagation direction of the incoming light is important for the spectral response of the LSPR. Two different arrangements are possible, which are longitudinally aligned (NPs are aligned in front of each other parallel to the incoming light) and transversally aligned dipoles (NPs are aligned orthogonal to the incoming light beam). With decreasing separation distance, the LSPR gets red-shifted for the longitudinal coupling. However, transversally coupled dipoles exhibit a blue-shift when the inter particle distance is reduced. The effect of the longitudinal coupling is usually much stronger in comparison to the transversal coupling. Thus, red shifts are usually observed in experiments exhibiting decreasing interparticle distances. [70–72]

2.4 Computational Fluid Dynamic (CFD) Simulations

Nowadays virtual prototyping is the standard method to develop new products. CFD simulations are used to design, e.g. new cars or aircraft with the aim to reduce their fuel consumption. Virtual prototyping is cost effective and saves the environment, because less material and energy is needed than building real prototypes [36,75]. Nevertheless, CFD simulations can be used in science to design new chemical reactors or HGAS sources as well. In this thesis, CFD simulations were conducted by Suren Ali-Ogly from the Charles University in Prague to determine the gas velocity distribution inside an existing HGAS. Since the simulations are not performed by myself, this chapter will give an overview about CFD simulations and will not discuss all the details of the approach.

In general, for CFD simulations it is helpful to separate the properties of the fluid and the flow. The properties of fluids are viscosity, density, surface tension, diffusivity and heat conduction, which are intrinsic properties depending on the temperature, pressure and composition. Some properties are

depending on the flow, e.g. pressure, turbulence and turbulent viscosity. In CFD simulations the flows can be categorized into laminar-turbulent, steady-transient and single-phase-multiphase [75]. For the HGAS under experimental conditions the flow was expected to be a steady, viscous laminar, single-phase flow [36].

To determine if a flow can be treated as a continuum or if the flow behaves like, a molecular flow or as a transitional flow, the Knudsen number can be used which is determined by the following equation: [75]

$$Kn = \frac{\lambda_{MFP}}{L} \quad (2-19)$$

Where λ_{MFP} is the mean free path and L is a characteristic length of the geometry, e.g. a diameter of a pipe. For $Kn < 0.01$ the flow can be treated as continuum, for Kn between 0.01 and 0.1 the flow can be treated as transitional flow and for $Kn > 0.1$ the flow can be treated as molecular flow. For the simulations in this thesis, mostly continuous flow is expected and only at the regions close to the orifice, where L becomes small, transitional flow is expected. In these regions corrections must be applied. [75]

To determine whether a flow is turbulent or laminar, the Reynolds number can be used. The Reynolds number Re for a flow through a pipe is defined by the following equation:

$$Re = \frac{\langle U \rangle L}{\nu} \quad (2-20)$$

Where $\langle U \rangle$ is the average velocity in a pipe, L is the characteristic length (the inner diameter for a pipe) and ν is the kinematic viscosity of the fluid. It was determined experimentally that for $Re > 2100$ a transition from laminar to turbulent flow occurs in a pipe [75]. The Re is the ratio of inertial force to viscous force. When the Re increases it is related to a relative increase in the inertial force in relation to the viscous force. If a flow changes from laminar to turbulent, this is related to a disturbance in the flow field and its amplification. For a high viscosity of a fluid, a disturbance can be damped effectively and the flow stays laminar. If the disturbance is not damped, it will be amplified and the flow changes to turbulent [75]. In this study, the flow in the HGAS can be treated as laminar in the cylindrical part of the HGAS [36].

After it was shown with the help of the Knudsen number and the Reynolds number that the flow can be treated as laminar continuous flow, in the following part the roadmap for simulations will be briefly described. The CFD simulation as a method is not in the focus of this thesis, but the results from the CFD simulations were extremely helpful to understand the processes inside the HGAS. The interested reader can find a detailed overview about the CFD method in the textbook from Bengt Andersson "*Computational fluid dynamics for engineers*" [75].

The roadmap of a CFD simulation is shown in Figure 2-9. All CFD simulations start with a 2D or 3D model of the geometry of a system. Usually any CAD program can be used to draw the initial design. In this study, the geometry was predefined by the existing HGAS. [75]

The next step is the grid generation or meshing of the model. In CFD simulations the equations of momentum transport have to be solved. Therefore, the computational volume has to be discretized, because the equations are nonlinear. The meshing is really important, because improper meshing can produce inaccurate results. Often the mesh is refined after preliminary results are obtained. [75]

After the meshing is done, the model can be defined. For single-phase laminar flow, the Navier-Stokes equations can be solved directly. If turbulent flow or multiphase flows shall be simulated, more complex models are needed. [75]

In the next step, the physical properties of the fluid must be defined. These properties are, e.g. viscosity, density, temperature, composition and pressure dependence. Many commercial software includes material libraries containing the physical properties. [75]

The last step, before the CFD simulations can be executed, is setting the boundary conditions and the inlet conditions. Here, e.g. the pressure or the flow into the system at the inlet and outside the system at the outlet must be defined. Additionally, also the wall condition has to be applied. [75]

Then the solver has to be chosen, e.g. segregated or coupled solver. A segregated solver solves the equations first for one variable for all cells before it solves for the next variable. A coupled solver solves for all variables and includes all of the coupling between the variables at once. Additionally, the acceptable quality of the solution has to be defined by the convergence criteria. [75]

During the post-processing of the CFD results, the quality of the results has to be determined. Therefore, it is necessary to check if the solution is independent of, e.g. the grid size and the convergence criterion. If one has checked the quality of the results, the final plots and information can be created and extracted from the software. One can create plane cuts, which are showing the velocity distributions through this cut. Also streamlines from the inlet to the outlet can be drawn. Some software also offers to insert small particles at specific points in the volume and track their position over time. [75]

In this thesis, velocity distribution plots were obtained which helped to localize the loss and trapping regions of NPs inside a HGAS. More details on the used software and the simulations settings can be found in Chapters 3.3 and 3.4. [36,37]

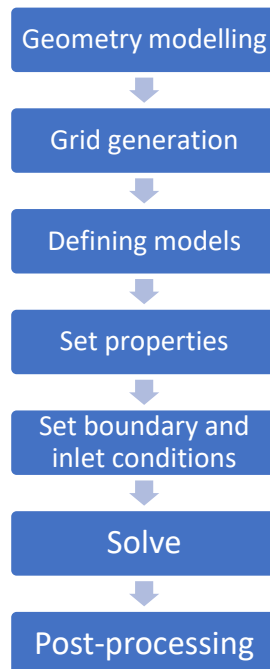


Figure 2-9: Roadmap for CFD simulations [75].

2.5 In-situ Diagnostic Methods Inside and Outside the HGAS

It was already reported that not all processes inside the HGAS are completely understood, e.g. effect of aggregation length and power on the NP size. Furthermore, Kousal et al. [33] reported the trapping of NPs inside the HGAS, which was the result of in-situ SAXS measurements. Additionally, it was reported that the biggest challenge for the implementation of the HGAS in industrial applications is the low deposition rate. Therefore, the key for the optimization of the HGAS is the understanding of all relevant processes inside the HGAS. Since the NP synthesis in the HGAS is a highly dynamic process, spatial and time resolved in-situ diagnostics are needed to increase the understanding of the NP formation inside the HGAS. Therefore, in this chapter the five different in-situ diagnostic techniques which were used in this thesis to characterize the growth and transport of NPs inside the source and the functionalization outside the source will be introduced. To each technique a pictogram is attributed, which is shown in Figure 2-10.

All techniques are using electromagnetic radiation to probe the growth, transport and functionalization of NPs inside the HGAS. In the following section the motivation to use each technique in this thesis will be mentioned shortly before all techniques will be described in detail in the following sub-chapters.

In the **SAXS** measurements, X-rays scatter with the NPs inside the GAS. The scattering signal contains information about the NP density and size distribution in 1-dimensional resolution.

In the **UV-Vis** spectroscopy, the NPs absorb light in the UV-Vis region of the electromagnetic spectrum due to their LSPR. The LSPR depends on the size of the NPs and the absorption is related to the NP density. This method provides 1-dimensional resolution.

The **LLS** technique utilizes Rayleigh scattering of NPs. The scattered light is detected by a camera. The signal contains 2-dimensional information about the location of NPs inside the HGAS.

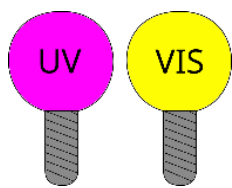
The **OES** uses the light emission of atoms inside a plasma, like it is present during magnetron sputtering inside a HGAS. Therefore, the strength of the different atomic lines in the OES signal are related to the amount of sputtered species from the target. This is useful to control the composition of atoms in the plasma during the synthesis of alloy NPs with the multicomponent target approach.

The **FTIR** can be used to identify chemical bonds, which is used in this thesis during the coating of Ag NPs with SiO₂. In this study, the increase in the coating thickness during the synthesis of core-shell NPs was monitored with the FTIR.



Figure 2-10: The five different in-situ diagnostic methods used are named and shown with their attributed pictogram. From left to right the pictograms for small angle X-ray scattering (SAXS), UV-Vis spectroscopy (UV-Vis), laser light scattering (LLS), optical emission spectroscopy (OES) and Fourier transform infrared spectroscopy (FTIR) are shown.

2.5.1 In-situ UV-Vis Spectroscopy



The electromagnetic spectrum is divided into different regions, e.g. X-rays, ultraviolet (UV), visible (Vis) and infrared (IR) radiation. In UV-Vis spectroscopy only the UV (starting at about 200 nm) and Vis (ending at about 690 nm) regions of the electromagnetic spectrum are probed. The energy of electromagnetic radiation or photons E is given by the following equation:

$$E = h \nu \quad (2-21)$$

Where h is Planck's constant and ν is frequency. Because radiation acts as a wave, it can be described by wavelength or frequency. Wavelength and frequency are related to each other by the following equation:

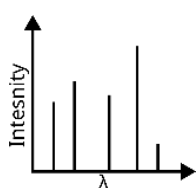
$$\nu = \frac{c}{\lambda} \quad (2-22)$$

Where c is the speed of light and λ is wavelength. From equation (2-21) and the above-mentioned equation it follows that the shorter the wavelength the higher the energy.

In a classical UV-Vis spectroscopy setup in transmission mode, a sample is placed between the incoming UV-Vis radiation and a detector. When the light passes through the sample several processes can occur, e.g. reflection, scattering, absorption, fluorescence/phosphorescence and photochemical reactions. Ideally during an UV-Vis measurement only absorption takes place. Since in this thesis mainly plasmonic noble metal NPs are probed, only absorption due to plasmonic interaction is observed in most cases [76]. Details on the interaction between photons and plasmon resonances of NPs can be found in Chapter 2.3. This chapter is named in-situ UV-Vis spectroscopy, because the UV-Vis is mounted to a HGAS or another plasma chamber, during the synthesis or functionalization of NPs. Usually the transmittance is measured, which is the ratio between transmitted and incident light intensity. In practice, prior to the experiment and without NPs in the light path a reference spectrum is taken. This is then used as the incident radiation spectrum.

The technical information on the UV-Vis detector, the UV-Vis light source and the measurement parameters used in this thesis are given in the corresponding **Publications B, C and F**.

2.5.2 In-situ Optical Emission Spectroscopy (OES)



Optical emission spectroscopy (OES) is a well-known method to monitor the compositional changes of thin films in conventional sputter deposition processes. The intensity in an OES spectrum is related to the number of excited atoms of a specific element in the gas phase. Therefore, the resulting elemental composition of the thin film is closely related to the OES signal. [77–80]

The principal of OES relies on the excitation of gas and sputtered atoms by different energetic collisions. Inside a plasma plenty of electrons have sufficient energy to excite gas and sputtered atoms. Also other plasma species, e.g. fast gases or ions, can excite sputtered atoms. Some of these excited atoms decay by emission of characteristic lines, which are monitored during OES measurements. The intensity of a specific emission line for an element depends on the supply rate of the element into the plasma (sputter rate), the emission process and the instrumental detection efficiency. The emission process depends on the number of photons emitted per sputtered atom and on the absorption of these photons. [81]

Since in this thesis OES is used to determine the concentration of alloy NPs in-situ in the gas phase of a HGAS, some differences to the use of OES in comparison to conventional low pressure magnetron sputtering for thin film production occur. One cannot be sure that all sputtered atoms, which are contributing to the OES signal, also contribute with the same fraction into the formation of NPs. It is possible that one element preferentially contributes to the particle growth and the other gets preferentially lost to chamber walls. More details can be found in the Chapter 3.6.

2.5.3 In-situ Small Angle X-ray Scattering (SAXS)



In the Chapter 3.2 small angle X-ray scattering (SAXS) was used to in-situ measure the size distribution and the density of NPs inside a HGAS. Therefore, a vacuum chamber equipped with a HGAS was installed at the Deutsches Elektronen Synchrotron (DESY) in Hamburg at PETRA 3. SAXS is a well-known technique to investigate structural properties of nanomaterials. The first textbooks on the SAXS technique were published in the 1950s, but the technique became more widespread with the development of synchrotron radiation, because the intensity of conventional X-ray tubes was too low. [82]

Since X-rays have typical wavelength smaller than 1 nm, they are ideal for the characterization of nanoparticles. A big advantage of SAXS is that the obtained information is already statistically relevant, because the results are averaged over a large number of NPs. In contrast to that, many SEM or TEM images have to be taken to get statistically relevant information about, e.g. size distributions of NPs. The drawback of SAXS is that the obtained results must be analyzed in the reciprocal space, because no real space image is formed. Therefore, the results have to be fitted or modelled to extract the relevant information. [82]

In a typical SAXS setup a parallel and monochromatic X-ray beam goes through a material, which is inhomogeneous at the nanoscale (Figure 2-11). This material can be a suspension of NPs or NPs distributed in vacuum, as it is the case in the HGAS. Some portion of the X-ray beam is scattered in the forward direction around the direct beam with a small angle, typically smaller than 5 degrees. From this fact the name small angle X-ray scattering originates. In the case of randomly distributed nanoparticles, the scattering pattern at the detector is independent of the azimuthal angle. This allows for a circular integration over the scattering pattern, allowing the scattered intensity to be obtained as a function of the scattering angle. Practically a beamstop is used to prevent that the direct beam approaches the detector. This allows to measure with higher X-ray intensities or with higher detector integration times without reaching the maximum count rate of the detector, which would damage the device. This leads to a better signal to noise ratio of the SAXS pattern and only requires some masking prior to the circular integration of the detector scattering pattern. [82]

Because the scattering depends on the kinetic energy of the X-rays and so on the wavelength of the X-rays, the scattered intensity is usually not analyzed as a function of wavelength, but as a function of momentum transfer. The equation for the momentum transfer is: [82]

$$q = \frac{4 \pi}{\lambda \sin \theta} = \frac{4 \pi}{h c E_{ph} \sin \theta} \quad (2-23)$$

Where λ is wavelength of X-ray photons, θ is half of the scattering angle, h is the Planck constant, c is the speed of light and E_{ph} is the Energy of the X-ray photons. [82]

For SAXS measurements high intensity, monochrome and collimated X-ray beams with a small beam size are needed, which can be found at synchrotrons. Especially the high intensity at synchrotrons enables fast measurements, which increases the temporal resolution of in-situ measurements. [82]

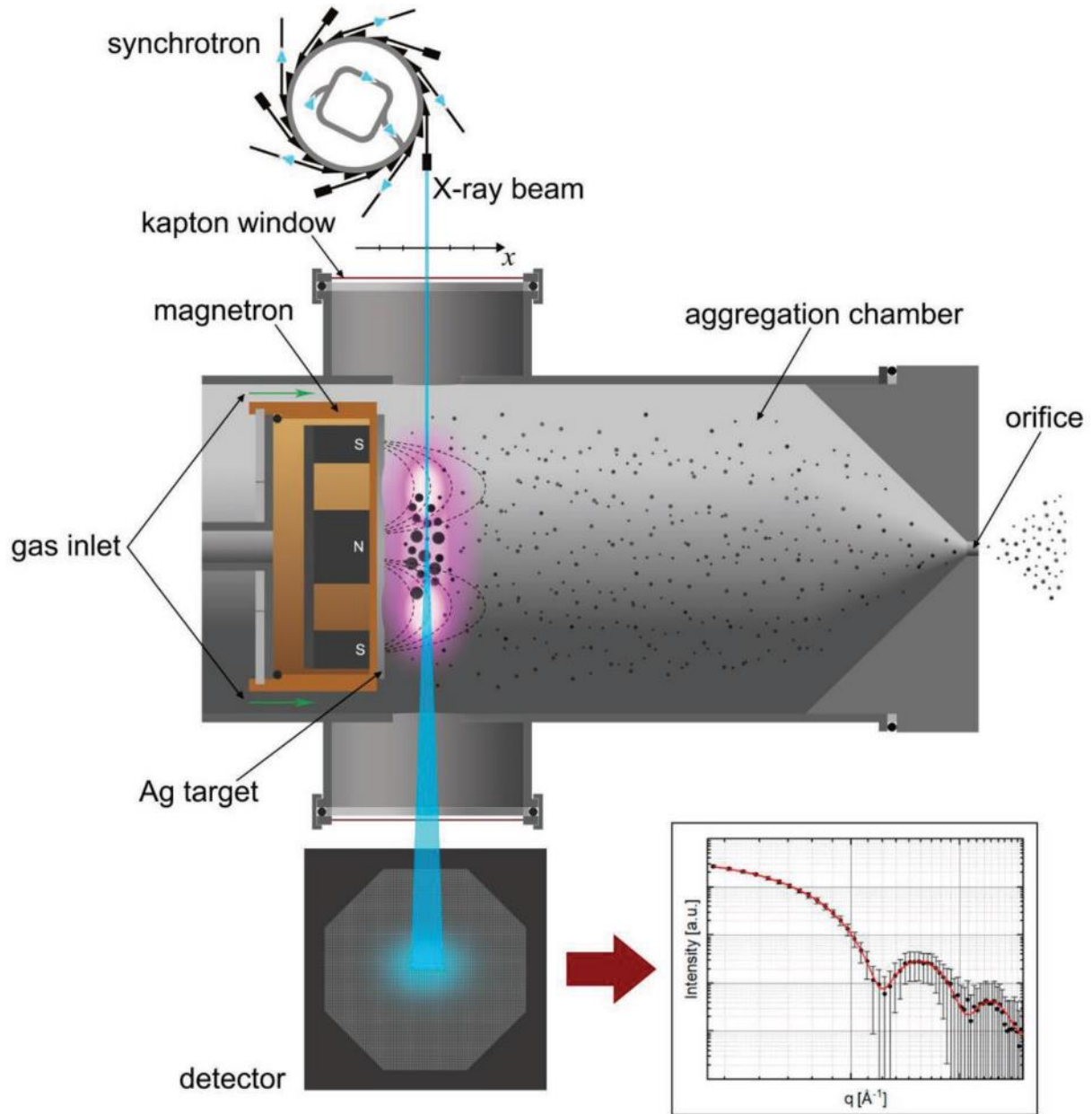


Figure 2-11: Experimental setup of the SAXS measurements at DESY. The path of the X-ray beam through the HGAS, the SAXS scattering at the NPs and the X-ray detection at the detector is shown. Additionally, the resulting scattering intensity vs. q plot for Ag NPs inside the HGAS is shown. The Figure is reprinted from [83].

Figure 2-11 shows an exemplary scattered intensity vs. q plot of Ag NPs in the HGAS. To obtain the particle size, the q -axis needs to be calibrated. Like equation (2-23) shows, q only depends on scattering angle and the photon energy. Therefore, only the sample to detector distance has to be measured accurately and the pixel size of the detector must be known. At beamlines the calibration can be performed with materials with a known d -spacing (distance between parallel planes of atoms). In this thesis collagen with a d -spacing of 65 nm was used to calibrate the sample detector distance. If the concentration of NPs should be determined additionally, scattered intensities normalized to the incident intensity are required. This can be done, e.g. by using calibrated detectors to measure the incoming photon flux and an area detector to register the scattering pattern. Here it is important that the quantum efficiency of the detector is known. [82]

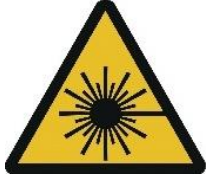
To obtain the size distribution from the scattered intensity vs. q plots, the commercial software “Irena” is available, which is able to calculate the intensity of small-angle scattering from particles in multiple populations of scatterers, based on the theory of Guinier & Fournet [84]. The formula for the intensity calculation is the following:

$$I(q) = \sum_k |\Delta\rho_k|^2 S_k(q) \sum_{ik} |F_k(q, D_{ik})|^2 V_k(D_{ik}) f_k(D_{ik}) \Delta D_{ik} \quad (2-24)$$

Where the subscript i includes all bins in the size distribution and ΔD_i is the width of bin i . The subscript k represents different populations. Each of these populations has its own binning index ik . D is the dimension of particle, which is in this thesis the radius of the NPs. The scattering contrast is $|\Delta\rho_k|^2$, the structure factor is $S_k(q)$, the form factor is $F_k(q, D_{ik})$, the particle volume is $V_k(D_{ik})$ and the volume size distribution is $f_k(D_{ik})$. Because the NP concentration inside the HGAS can be assumed as relatively low, the structure factor was considered to be unity. [82,83,85]

More details on the modeling of SAXS data can be found in **Publication A** [35] and in the supplementary information of this publication.

2.5.4 In-situ Laser Light Scattering (LLS)



After in-situ UV-Vis spectroscopy and in-situ SAX were introduced as possible methods to analyze the growth and transport of NPs inside a HGAS, in this chapter the laser light scattering (LLS) technique will be introduced. Different LLS techniques were already applied in dusty plasmas to investigate the growth and transport of NPs. Some methods rely on Rayleigh scattering [86–89] and others on Mie scattering [90–92]. With Mie scattering techniques NPs of radii between 80–200 nm can be detected and by evaluation of the polarization, also the size distribution of the NPs can be analyzed, e.g. inside a dusty plasma [90–92]. Since the limit between Mie scattering and Rayleigh scattering is 1/10 of the wavelength of the incoming light, for a HGAS typically only Rayleigh scattering is applicable. Since the typical size of NPs synthesized by a HGAS is below 50 nm and the most widely used and affordable laser sources have a wavelength of 532 nm. Therefore, in this thesis also a laser with a wavelength of 532 nm is used and so only Rayleigh scattering is applicable.

In this thesis a laser plane through the HGAS is created and a camera with a color filter is mounted in a 90° configuration to the laser plane. The color filter is necessary to prevent that too much emitted light from the plasma, which was discussed in Chapter 2.5.2, can enter the camera. The setup is shown in Figure 2-12. The scattered light by NPs can be detected with a good temporal and spatial resolution. This method is common in conventional RF dusty plasmas [86–89] but not in a HGAS. This method was utilized for the first time for the investigation of NPs inside a HGAS [38]. In contrast to in-situ SAX or in-situ UV-Vis, the LLS based on Rayleigh scattering can provide good spatial resolution but cannot provide a precise information about the size of NPs. This is related to the general Rayleigh scattering formula:

$$I = \frac{8 \pi^4 a^6 n_{med}^4 I_0}{d^2 \lambda_0^4} \left| \frac{m^2 - 1}{m^2 + 1} \right|^2 (1 + \cos^2\theta) \quad (2-25)$$

The scattering Intensity I depends on the particle size a , the refractive index of the medium n_{med} , the intensity of the incident light I_0 , the distance from the scattering object to the detector d , the wavelength of laser light in vacuum λ , the particle relative refractive index m and the test angle ϑ [93]. Accordingly, the scattering intensity depends on the particle size to the power of six. Because the formula holds for the scattering intensity for one particle, the scattering intensity depends linearly on

the particle density. Since the intensity depends on the size and the density simultaneously, no precise information about the size and density of NPs can be obtained.

The technical information about the LLS setup and on the data processing in this thesis are given in **Publication D** [38].

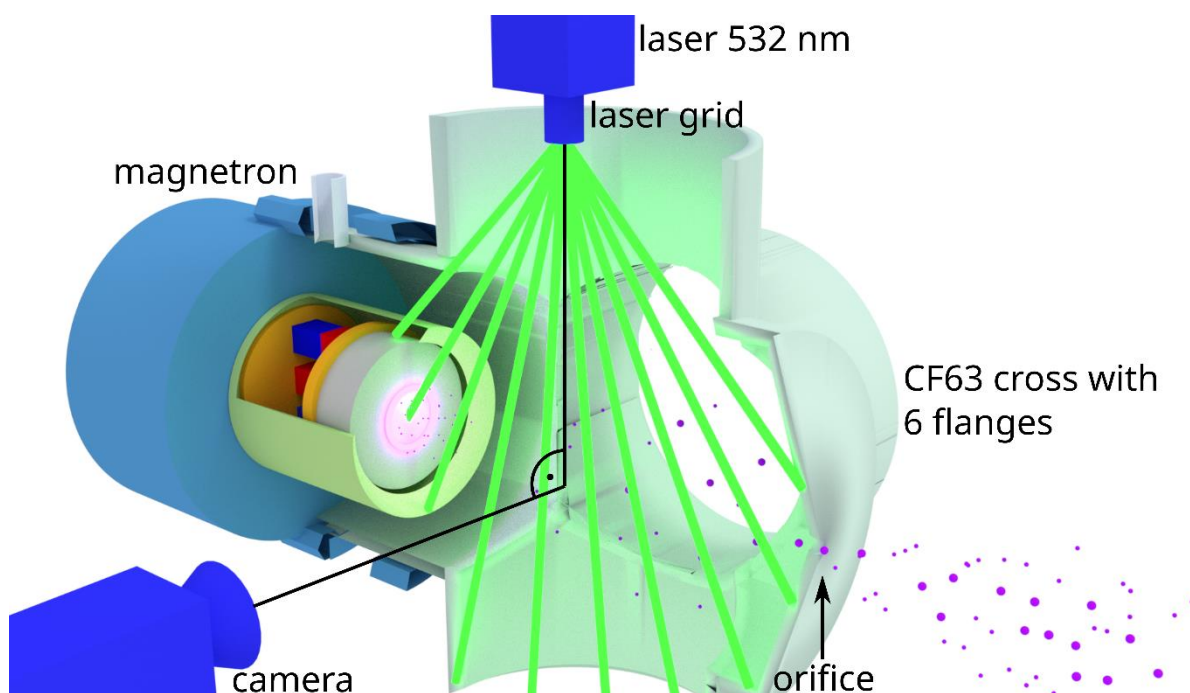
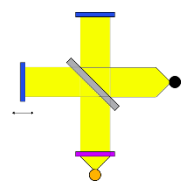


Figure 2-12: Schematic representation of the LLS setup on the HGAS. The setup consists of a magnetron, a CF63 cross with 6 flanges, an orifice, a laser, a laser grid and a camera. The figure is reprinted from [38].

2.5.5 In-situ Fourier-Transform Infrared Spectroscopy (FTIR)



In **Publication F**, in-situ Fourier-transform infrared spectroscopy (FTIR) is used to analyze the functionalization of Ag NPs with a SiO₂ shell. Therefore, in this chapter the method will be introduced. FTIR is used to obtain information about the chemical bonding types inside a sample. It can be performed for solid materials as well as for liquid or gaseous samples. Usually, in dispersive spectroscopy methods the wavelength must be changed gradually to obtain a spectrum over the whole range. However, during a FTIR measurement photons over the whole spectral range of the IR source are sent to the sample at the same time and the absorption is measured. When the radiation interacts with the probed material, some specific wavelength is absorbed because transitions between vibrational energy states are occurring. The molecular vibrations can range from coupled motion of two atoms in a diatomic molecule to complex motion of each atom in large molecules with diverse functional groups. All different kinds of functional groups show specific absorption bands in an infrared spectrum. Therefore, from an FTIR spectrum one can figure out which types of bondings are present in a measured sample. An FTIR spectrometer consists out of: [94]

1. Radiation source (heated black body)
2. Beam path (different kinds of mirrors for focusing and defocusing)
3. Interferometer (consists of beam splitter, mirror drive, laser)
4. Detector (black body which transfers the incoming photons into electrical signals)
5. Computer (running measurement and Fourier-Transformation)

The most important part is the interferometer which is often a Michelson interferometer, as depicted schematically in Figure 2-13. In such an interferometer, the incoming beam is splitted into two beams. One beam is directed onto a fixed mirror and the other one onto a moveable mirror. After both light beams are reflected, they merge again and interfere. This creates an interferogram where the maximum is located at the position where the mirror-beam splitter distance between both mirrors is the same (constructive interference). The obtained interferogram can be transferred into a spectrogram by a Fourier-transformation. The interaction of the IR radiation inside the sample originates from different IR absorption of chemical bonds. The IR frequencies are recorded in units of wavenumber (cm^{-1}) and located in the range between 700 and 5000 cm^{-1} . In this energy range usually, no bond breaking occurs but the energy is sufficient to induce vibrations like stretching or bending of bonds. [94]

In this thesis, the FTIR is mounted to a RF plasma chamber where Ag NPs are trapped and coated with SiO_2 by injection of SiH_4 . Here it was possible to measure in-situ the amount of SiO_2 bonds, which could then be used to monitor the shell thickness of core-shell NPs in-situ.

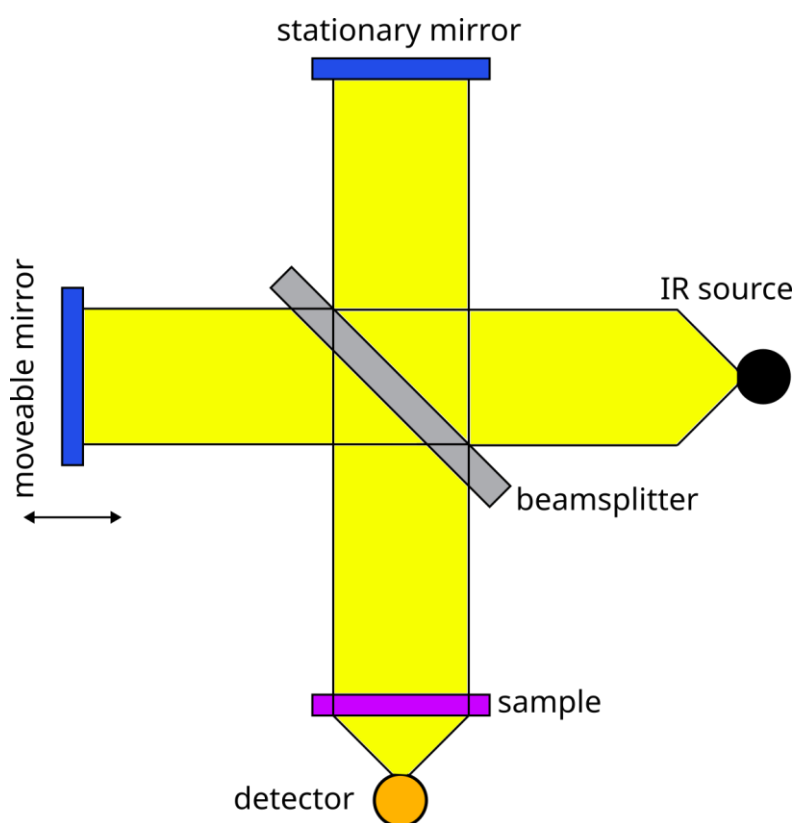


Figure 2-13: Schematic representation of a Michelson interferometer.

2.6 Ex-situ Characterization Methods of Nanoparticles

The insights from in-situ diagnostics are complemented by ex situ methods, such as SEM, TEM, EDX and XPS, which are important for the verification of the in-situ diagnostic results. In this thesis SEM and TEM investigations of NPs were performed to determine their size and shell thickness in case of core-shell NPs. Additionally, EDX measurements were performed with the TEM to determine the chemical composition of core-shell NPs. The target surface of a multicomponent target was studied with an SEM in combination with EDX to determine the surface morphology and composition of the target surface. In addition, XPS measurements were performed to analyze the chemical composition of alloy NPs. Therefore, first the electron microscopes and the EDX technique will be introduced and afterwards the XPS method.

2.6.1 Scanning Electron Microscopy (SEM)

Visible light microscopes have a limited resolution, which is caused by the wavelength of the photons in the visible range. To increase the resolution, electron microscopes were developed. In contrast to conventional light microscopes, the accelerated electrons in a SEM have much lower wavelengths. Since in this thesis mainly nanoparticles are investigated, only electron microscopy techniques are feasible for the measurements. The electron microscopes are frequently used in this thesis to investigate the size distributions of nanoparticles synthesized by the HGAS.

In a scanning electron microscope (SEM) electrons from a thermionic, Schottky or field-emission gun are accelerated through an electric field to an energy between 1 and 50 keV. This electron beam is focused by electromagnetic lenses to a probe size of ≈ 1 nm and is scanned over the sample. An image can be created by detecting time and position synchronized the electrons emitted from the sample. The main portion of emitted electrons are originating from secondary electron emission and elastic backscattering. The primary electron beam ionizes and excites atoms due to high energy of the electrons on its way through the sample. During these processes, free electrons are created which are called secondary electrons. These secondary electrons are moving randomly through the sample and are less energetic compared to the primary electrons of around 10 eV. Due to the low energy of the secondary electrons their mean free path is short. This is the reason, why these electrons can only escape from the sample, when they are created in the first few atomic layers of the sample. Thus, the secondary electrons provide a good topographic contrast and good lateral resolution. The interaction volume of the primary electron beam is shown in Figure 2-14. It is well visible that the detectable secondary electrons are originating close to the sample surface and that the interaction area is defined by the spot size of the primary electron beam. For that reason, the resolution limit for secondary electron detection depends mainly on the spot size of the primary electron beam and the escape depth of the secondary electrons. [95]

Another important source of sample information is in the backscattered electrons. Due to the high energy of the backscattered electrons, the mean free path and so the interaction volume of these electrons is much larger in comparison to the secondary electrons. Due to the multiple elastic scattering events and the big interaction volume, the lateral resolution is smaller in comparison to the backscattered electrons. The big advantage of the backscattered electrons is that their intensity is a function of the atomic number Z . Therefore, the backscattered electrons can be used to some extent to distinguish between different materials. [95]

Also, other electron interactions can take place which either produce Auger electrons or X-rays. Auger electrons are released if the primary electron beam excites an electron from an inner shell of a sample atom. Then another electron from an outer shell occupies the empty position and releases the energy of this transition. This free energy can then emit an electron from a higher shell, which is called an

Auger electron. The energy of an Auger electron depends not on the energy of the primary electron beam. The energy depends only on the energy of the electron transition and the binding energy of the orbital from which it was released. For that reason, the energy of Auger electrons is in the order of hundreds of eV, which cause a small mean free path in the range of 1 to 10 nm comparable to secondary electrons. If an electron energy analyzer is used, the energy of the Auger electrons can be used to identify the chemical species inside the sample. [95]

Furthermore, the energy difference of an electron changing from an outer to an inner shell, can be released as characteristic X-rays. Because the interaction of electrons with matter is much stronger compared to X-rays, the escape depth of X-rays is much bigger compared to electrons. If the energy of the X-rays is detected, the method is called energy-dispersive X-ray spectroscopy (EDX). This method will be discussed in detail in Chapter 2.6.3. [95,96]

The technical information on the SEM device and the measurement parameters used in this thesis are given in the corresponding publications.

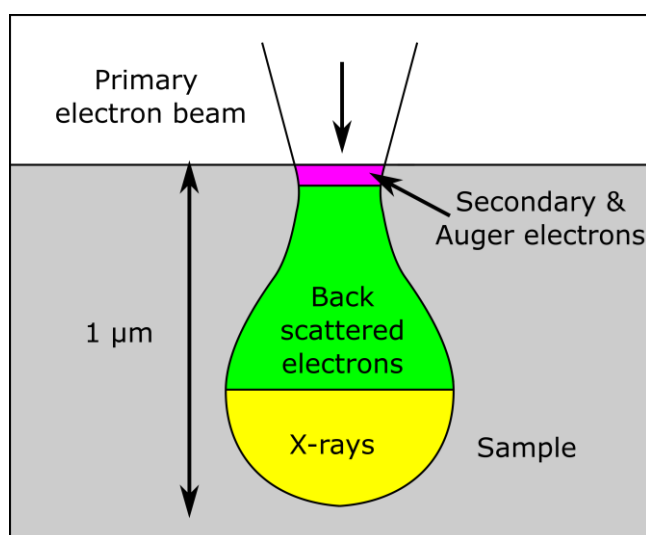


Figure 2-14: Interaction volume of the primary electron beam. The different regions are indicating the origin of detectable electrons and photons. Secondary and Auger electrons are escaping only close to the sample surface. Backscattered electrons are originating from a deeper volume than the secondary or Auger electrons. X-rays are also able to leave the sample from even deeper regions.[55]

2.6.2 Transmission Electron Microscopy (TEM)

In this thesis, SEM investigations are often used to measure the size distributions of nanoparticles synthesized with the HGAS. The SEM is often sufficient for this purpose and the sample preparation for the SEM is much easier in comparison to TEM investigations. Nevertheless, an SEM is not capable to give information about the crystal structure and the coating thickness of core shell particles. Therefore, TEM investigations are in high demand. The TEM is used in this thesis to investigate the coating thickness of core-shell nanoparticles and their crystal structure.

In contrast to an SEM, in a TEM the electrons which have passed the sample are used for imaging. This has high requirements on the sample preparation. Depending on the used sample material, a thickness between 10 and 200 nm can be already thick enough to absorb all electrons. Therefore, for TEM investigations the sample thickness has to be really small. Since in this thesis mainly core-shell

nanoparticles are investigated by TEM, this requirement was easily fulfilled, because the NP diameter is in the range of ≈ 20 nm. As substrate material, copper grids with a thin carbon film on top are used. These grids allow for sufficient electron transmission. [96]

The electron beam is created similarly to an SEM, which was described earlier in Chapter 2.6.1. The beam is accelerated to energies between 100 keV and 3 MeV. The beam is focused by electrostatic lenses onto the sample. During the interaction of the electron beam with the sample, the electrons can be scattered, they can excite secondary electrons, X-rays and Auger electrons. [96]

After the electrons have passed the sample, different detection modes can be chosen in a TEM. One mode is the bright field mode. In this case the beam is magnified onto a detector. The produced image shows a contrast depending on the atomic number and the sample thickness at every point. Another possibility is to investigate the diffraction pattern instead of an image of the sample. This is useful if, one wants to investigate the crystal structure of the sample. [96]

In this thesis, only the bright field mode is used to find out how big the shell of core-shell nanoparticles are. The technical information on the TEM device and the measurement parameters used in this thesis are given in the corresponding sections.

2.6.3 Energy-Dispersive X-ray Spectroscopy (EDX)

Energy-dispersive X-ray spectroscopy (EDX) can be used either in a SEM or a TEM to determine the chemical composition of a sample. This method is used in the **Publications E and F** to investigate e.g., the redeposited material on the surface of a multicomponent sputter target or to identify the elements present in the core and the shell of core-shell nanoparticles. [96]

In an EDX measurement the characteristic X-rays that are emitted from a sample are investigated to identify and quantify the elements present in a sample. Like described in the previous sections, if the primary electron beam of an SEM or EDX excites an electron from an inner shell of a sample atom, the energy of an outer shell to an inner shell transition can be released in the form of characteristic X-rays. These X-rays are detected by the EDX detector. Different detector types are existing such as Si(Li) detectors or silicon drift detectors (SDD). The general concept of the detectors is similar. An X-ray photon creates electrons and holes inside a semiconductor. The amount of electron hole pairs is proportional to the X-ray energy. Inside the detector, the electrons and holes are separated and an electron pulse can be measured. Since the size of the band gap of the semiconductor is known, the energy of the incoming X-rays can be calculated from the number of generated electrons. By this method an EDX spectrum can be created. From such a spectrum the different elements inside a sample can be identified and quantified. [96]

2.6.4 X-ray Photoelectron Spectroscopy (XPS)

To analyze the chemical structure of a sample surface and to quantify the elements present in a sample surface X-ray photoelectron spectroscopy is a commonly used technique. In this thesis, XPS was used to quantify the Au and Ag concentration in alloy nanoparticles in **Publication E**. Especially for nanoparticles the technique is useful because of the high surface sensitivity. In comparison to EDX, the signal originates only out of the first nanometers. [97]

The measurement principle and all necessary instruments for an XPS system are shown in Figure 2-15.

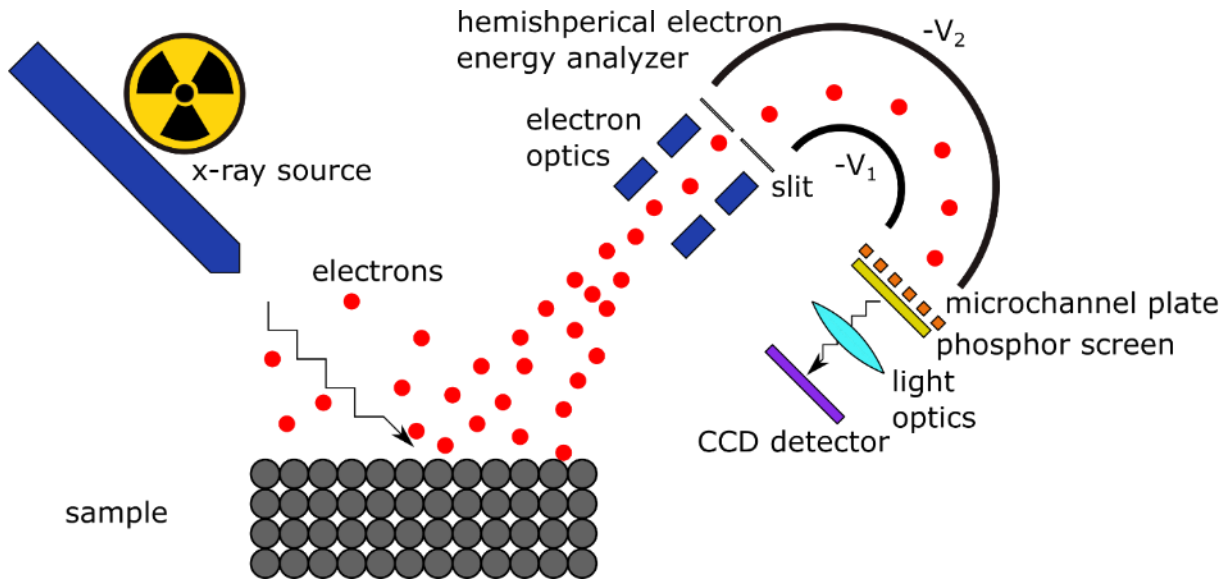


Figure 2-15: Working principle of an XPS measurement system.

A typical XPS system consists of X-ray tube, where X-rays are generated. Frequently used anode materials are aluminum with the main emission on the K_{α} line at 1486.6 eV and magnesium with the K_{α} line at 1253.6 eV. The X-ray radiation can be filtered with a monochromator, which reduces the intensity of the X-ray beam but increases the energy resolution. Another important part of an XPS system is the hemispherical electron energy analyzer. This analyzer is able to measure the energy of the incoming electrons. During an XPS measurement at a first stage, X-rays are generated and sent onto the sample. When the X-rays are interacting with the sample, they can excite electrons. The electrons can travel through the sample and excite other electrons, get scattered or can leave the sample. Also Auger electrons can be produced like it was discussed before in section 2.6.1. The kinetic energy of the electrons E_{kin} which are excited from the X-ray beam depends on the X-ray energy $h\nu$, the work function of the sample Φ and the binding energy of the original state of the electron E_B [97]:

$$E_{kin} = h\nu - \Phi - E_B \quad (2-26)$$

The kinetic energy of the excited electrons is in the order of hundreds of eV resulting in a short mean free path in the order of nanometers. This is the origin of the high surface sensitivity of the XPS method. In most cases one is interested in the binding energy of the electrons. Because the measured energy depends highly on the work function of the sample and the charging, the binding energy scale has to be calibrated with a known line of an element. Here often the C 1s peak of aliphatic carbon is used. It is often used because every sample which is not directly produced in vacuum or sputter cleaned, shows aliphatic carbon. Therefore, it is well suitable as reference. [97]

Charging of the sample is observed, if insulating samples are investigated. Since the X-ray irradiation continuously removes electrons from the sample, the sample charges up positively if the sample is an insulator. The electric field which evolves due to the charging decreases the kinetic energy of all electrons leaving the sample in the same manor. Therefore, the binding energy seems to be higher than it is. Nevertheless, a calibration can easily fix this issue. [97]

In the system used for the thesis, no monochromated X-ray source was installed, which will cause satellite peaks in the measurement spectrum. They are originating because the second weaker radiation lines of the anode material are also irradiating the sample at the same time. Therefore, every peak in the spectrum has a smaller peak with a fixed binding energy difference, which is called satellite peak. These satellite peaks do not cause problems in most cases, because they can be easily identified.

Nevertheless, sometimes the satellite peak overlaps with a main peak of another element. In such cases the quantification is difficult, because it is not clear how much of the intensity of the peak originates from the main peak or the satellite peak. [97]

If a measurement is charge calibrated and satellite peaks are not an issue, peaks can be identified and also a quantification can be performed. For a quantification, the area under one peak for each element after background subtraction has to be calculated. The area of each line has to be divided by an element specific line and system specific intensity calibration factor. A good reference for such values is the book from Moulder [98] and the database from the national institute of standards and technology[99].

One of the biggest advantages of an XPS in comparison to an EDX system is the additional investigation of the chemical bonding states of the elements present in the sample. The binding energy of an atom is affected by its chemical surrounding. Especially the binding energy of atoms which are bound to elements with a high electronegativity, e.g. O or F are shifted strongly by some eV. But also other bonding partners can be identified. Therefore, the peak of an element of interest has to be deconvoluted into the portions of different types of bonding. [97]

These give the option to distinguish easily between, e.g. pure metals and their respective oxides. [97]

3 Results and Discussion

In this thesis the following main question with its included sub-questions concerning the growth and transport of NPs inside a HGAS will be addressed:

How can the fundamental understanding of the HGAS be increased to extend the scope of applications of the HGAS?

- 1) Which in-situ diagnostic techniques can be utilized to investigate the growth, transport and functionalization of Ag NPs inside and outside the HGAS to increase the understanding of the method?**
- 2) Which known and unknown parameters can be used to increase the efficiency of the NP synthesis inside the HGAS?**
- 3) How is it possible to functionalize NPs inside and outside the HGAS to extend the scope of applications of the HGAS?**

These questions are of high importance, because growth, transport and trapping of NPs are coupled to each other inside a HGAS. If, e.g. the particles are trapped, they have most probably more time to grow and the transport of NPs outside the source is limited. If, e.g. the transport of NPs is increased by a higher gas flows, the residence time in the HGAS is reduced, which decreased the time to grow. Therefore, it is not enough to investigate the deposited NPs or the NP beam outside the HGAS. In-situ diagnostics are unavoidable to increase the understanding of the processes inside the HGAS. Depending on the in-situ diagnostic approach different findings can be obtained, e.g. UV-Vis spectroscopy and SAXS measurements can provide information about the size distribution and the relative density of NPs with 1-dimensional resolution. LLS can provide 2-dimensional resolution but no information about density and size of the NPs. For that reason, a combination of different in-situ diagnostic methods was used to investigate the growth, transport and functionalization of NPs inside and outside the HGAS.

In connection with the first sub-question, the goal is to find out:

- In what period of time do the particles grow?
- Is there a spatial distribution of NP growth within the HGAS?
- How big do the NPs grow at different places within the HGAS?
- Where are the NPs transported to and can all NPs exit the HGAS through the orifice?
- Are the NPs trapped or not inside the HGAS and how can the trapping be controlled?
- What in-situ diagnostic methods can be used to answer these questions?

Therefore, five different in-situ diagnostic methods were used to investigate the growth, transport and functionalization of NPs. To investigate the growth and transport inside the HGAS the following methods were used: in-situ SAXS, UV-Vis spectroscopy and LLS. The in-situ measurements revealed that NPs are trapped inside the HGAS at different locations because of a complicated interplay of electromagnetic forces and the drag force originating from the inert gas flow. The in-situ SAXS and UV-Vis spectroscopy techniques have provided helpful information about the size and density of the NPs at different distances to the magnetron but showed only 1-dimensional resolution. Therefore, it was not possible to fully comprehend the complex dynamics inside the HGAS. That became possible with the LLS technique, which finally provided 2-dimensional resolution. With the LLS technique it was possible for the first time to image NPs trapped in vortices inside the HGAS. Especially the LLS images obtained for different gas inlet configurations show together with CFD simulation that the gas velocity distribution inside the HGAS plays a crucial role for the growth, transport and trapping of NPs inside the HGAS.

This leads to the second sub-question regarding the operational parameters of the HGAS and how they influence the efficiency of the HGAS. The velocity distribution depends on the gas flow, the pressure and to a high degree on the geometry of the HGAS. Geometrical factors, like the gas inlet location, bottle necks between the gas inlet and the orifice and the diameter of the magnetron and the HGAS itself, highly impact the gas velocity distribution. The impact of such parameters on the processes inside the HGAS were only rarely investigated so far. However, they are most likely one reason why contradicting parameter studies on the size of NPs in dependence on, e.g. the power can be found in the literature. Since the HGAS is not standardized, different research groups are using different geometries, which results in different gas velocity distributions and finally leads to different growth, transport and trapping behaviors. Nevertheless, the results for different gas inlets have shown a strong dependence of the deposition rate on the gas inlet configuration. Therefore, the HGAS can most probably be optimized further by the development of a new HGAS design with the help of CFD simulations to prevent trapping and the loss of NPs in low velocity regions.

The in-situ diagnostics are not limited to investigate the growth, transport and trapping of NPs inside the HGAS, they can also contribute to the development of new methods for the production of functional NPs or to solve problems with time dependent composition changes during the synthesis of alloy NPs. Therefore, in-situ diagnostics can help to answer the last sub-question. The multicomponent target approach, which enables in-situ adjustment of the composition of alloy NPs, turned out to be highly dependent on the target lifetime. In the context of this thesis, this issue was solved by in-situ OES. The OES lines of the different atomic species inside the plasma can be used to predict the composition of the alloy NPs during the deposition.

To extend the scope of applications of the HGAS further, a novel method for the production of core-shell NPs was developed in the context of this thesis. Here, the in-situ diagnostic methods UV-Vis spectroscopy and FTIR enabled the fast development of the process. The diagnostics were used to find optimal conditions for the confinement of NPs and the coating without the necessity of sample extraction and analysis. In comparison to other approaches, where NPs from the HGAS are coated, in our approach the shell thickness can be tuned in a nearly unlimited range. In our approach the NPs are confined inside a second RF plasma discharge for an extended time period which enables to tailor the shell thickness really precisely independent of the initial velocity of the NPs or the speed of the coating process.

In the following chapters the results during the PhD period will be presented in the form of 6 publications. First, one chapter which points out the interconnection between the different publications will be presented. Afterwards, for each publication one page in front of the publication can be found in which the main aspects of the publication are summarized. Additionally, the own contributions to the publication are briefly mentioned. A detailed declaration of authorship can be found in Chapter 8.

3.1 Summary, Motivation and Interconnection of the Different Publications

In this chapter the interconnections between the different publications of the thesis will be presented. Furthermore, it will be shown how the results from earlier publications motivated subsequent publications. The interconnections are also shown graphically in Figure 3-1.

Trapping of NPs inside a HGAS was reported the first time by Kousal et al. [33] for Cu NPs. They used in-situ SAXS measurements to investigate the growth and transport of Cu NPs inside a HGAS. In **Publication A** [35], the SAXS measurements were extended to the investigations of Ag NPs inside the HGAS to examine if Ag NPs show a similar behavior as Cu NPs. The SAXS method was chosen, because it provides a good temporal resolution and information about the NPs size distribution. During this study a confinement, i.e. trapping, of NPs was found in the close vicinity of the target. Additionally, fluctuations in the growth and transport of NPs were observed. However, to determine the origin of the fluctuations, other in-situ diagnostics with a better spatial resolution had to be found. Furthermore, a lot of redeposited material on the target center was detected after long operation of the HGAS.

Similar experiments can be performed with lab scale equipment if UV-Vis spectroscopy is applied instead of SAXS. In **Publication B** [37] in-situ UV-Vis spectroscopy was utilized for investigations of the growth and transport of NPs inside a HGAS. This has the advantage that the experiments are independent of a synchrotron. It was shown that trapping of NPs inside the HGAS occurs. In this study also redeposition in the central region of the target was observed.

In **Publication B** the trapping of NPs was investigated successfully with UV-Vis spectroscopy for a fixed gas flow and pressure. To learn more about the trapping of Ag NPs inside the HGAS in dependence on the gas flow and pressure a new series of UV-Vis measurements were conducted in **Publication C** [36].

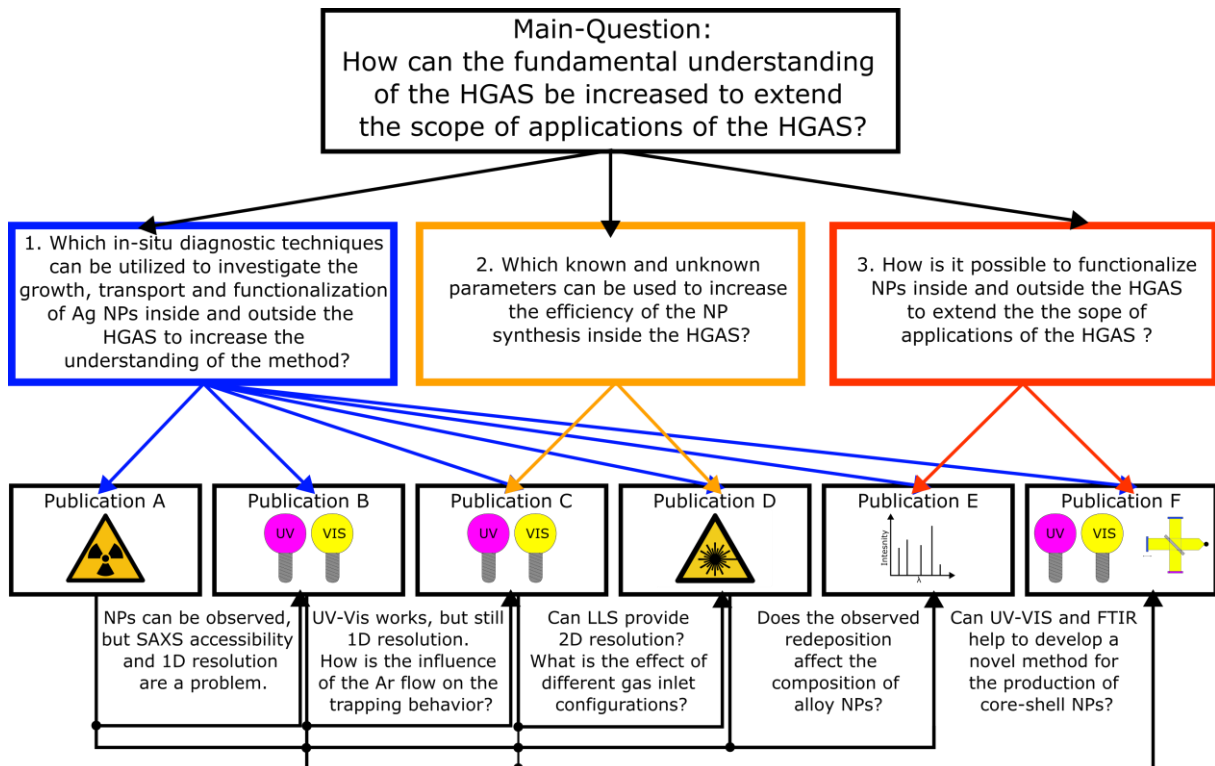


Figure 3-1: Schematic of the structure of the thesis. On the top is the main research question, which was structured into three sub-questions. The arrows from the sub-questions to the publications are indicating which publications have partially answered which sub-questions. The publications are connected also with arrows to show how the publications are connected.

By comparing the LSPR observed experimentally with simulations it was found out that large NPs with a diameter of up to 70 nm are present in the HGAS. Although, such large NPs were never observed outside the source. Furthermore, it was found that the deposition rate and the trapping highly depend on the gas flow and pressure. To learn more about the growth and transport of NPs inside the HGAS, computational fluid dynamic (CFD) simulations were performed. It turned out that the gas velocity distribution is highly inhomogeneous and depends on the geometry of the HGAS and the location of the gas inlet.

This motivated **Publication D** [38] in which three different gas inlets with different gas flows and pressures were tested. The previous publications (**Publication A-C**) have used in-situ SAXS and UV-Vis spectroscopy as diagnostic techniques. One drawback of both techniques is the poor spatial resolution (1-dimensional), because the information is always obtained from the whole interaction volume of the photon beam. Therefore, in **Publication D** laser light scattering (LLS) was applied to the HGAS. LLS uses a laser beam which is expanded by a grid to a plane through the HGAS. Rayleigh scattering causes NPs to scatter light which can be monitored by a camera. Therefore, the obtained information results from one plane or cut through the HGAS, which gives in comparison to SAXS and UV-Vis measurements 2-dimensional information in comparison to 1-dimensional information. It was found out that the type of gas inlet heavily impacts the location where NPs were observed or trapped. The LLS also provides a suitable temporal resolution which has shown the formation of vortices in which NPs are trapped. Furthermore, the deposition rate and the size distributions were impacted by the gas inlet configuration even though the pressure and gas flow were the same.

In-situ diagnostics are not only interesting for fundamental research inside the HGAS, but they can be also used to investigate and develop the synthesis of functional NPs, e.g. alloy or core-shell NPs. In the case of alloy NPs, the composition plays an important role, because, e.g. the plasmonic properties depend on the composition. In the multicomponent target approach developed by Vahl et al., alloy NPs with tailored composition can be synthesized. In the approach a special target geometry is used which enables composition tuning by adjustment of the operating pressure in the HGAS. However, the other publications have indicated that extensive redeposition can occur on the target surface. Therefore, in **Publication E** [40] the resulting composition of the multicomponent target approach was investigated with in-situ OES for longer operation times compared to the study by Vahl et al. It was found that the composition of the NPs was not only dependent on the pressure, but also on the target lifetime. This issue was solved by the in-situ OES measurements, because it was possible to predict the composition of the NPs in-situ.

Furthermore, the synthesis of core-shell NPs can be investigated with in-situ methods too. Hence in **Publication F** [41], a HGAS was combined with a vacuum chamber in which the Ag NPs can be confined by an RF plasma for long durations. This is similar to the trapping of NPs inside the HGAS with the big difference that here the trapping is intended. The experience from the previous publications on the UV-Vis spectroscopy was used here to proof that NPs can be hold in the RF plasma for long times without any losses. This enables the coating of NPs with, e.g. SiO₂ by the injection of a precursor gas like Silane (SiH₄). The UV-Vis spectroscopy was used to monitor the coating process. To get better insight into the chemistry of the coating process, in-situ Fourier-transform infrared spectroscopy (FTIR) measurements were performed additionally. The publication is a perfect example on how in-situ diagnostics can speed up the development of novel synthesis methods. Because without the in-situ diagnostics, much more time would be needed to find conditions where NPs can be confined, coated and extracted.

3.2 Publication A: Nucleation and Growth of Magnetron-Sputtered Ag Nanoparticles as Witnessed by Time-Resolved Small Angle X-Ray Scattering

For this publication in-situ time resolved SAXS measurements were performed during the synthesis of Ag NPs inside a HGAS at the “Deutsches Elektronen-Synchrotron” (DESY) in Hamburg. The aim of the experiments was to investigate the growth and transport of Ag NPs inside the HGAS at different distances to the magnetron surface.

In this publication capturing or trapping of NPs inside the HGAS was observed because of a force interplay of electromagnetic forces, thermophoretic force, the gravitational force, the neutral drag force from the gas flow and the ion drag force. Furthermore, the time dependence of the NP growth inside the capture zone was investigated. Additionally, large NPs with diameters of ≈ 80 nm could be rarely found outside the HGAS on the substrate, although SAXS measurements confirmed their existence inside the HGAS. But these NPs could be found on substrates placed inside the HGAS. From these observations it was concluded that smaller NPs have a better chance to escape from the capture zone than large NPs. SEM investigations of the Ag target after the SAXS measurements have shown NPs with a diameter of 90 nm in the central region of the target. Additionally, a hill of NPs in the center of the target was measured with a profilometer. This confirmed the theory that NPs trapped in the capture zone get preferentially deposited onto the target surface or the outside walls and only rarely escape from the HGAS.

These results, have drawn the attention onto two phenomena, which were further investigated in this thesis. One phenomenon is the trapping of NPs and the other one the redeposition of NPs onto the target. The SAXS measurement have the option to give not only information about the relative volume fraction of NPs inside the X-ray beam but also about the size distribution of NPs inside the X-ray beam. The biggest drawback of the method, is that it gives only 1-dimensional information, because the data originate from the whole X-ray path through the source. Therefore, techniques which would enable spatial resolved information about the NP growth and transport are highly needed. Furthermore, SAXS measurements at a synchrotron cannot be performed routinely and the effort for the measurements is extremely high.

Own contributions to this work partially include the data processing and evaluation of the SAXS measurement, the data interpretation, as well as writing of the manuscript.

This chapter is a reprint from the following publication:

Shelemin, A., Pleskunov, P., Kousal, J., **Drewes**, J., Hanuš, J., Ali-Ogly, S., Nikitin, D., Solař, P., Kratochvíl, J., Vaidulych, M., Schwartzkopf, M., Kylián, O., Polonskyi, O., Strunskus, T., Faupel, F., Roth, S. v., Biederman, H., & Choukourov, A. (2020). Nucleation and Growth of Magnetron-Sputtered Ag Nanoparticles as Witnessed by Time-Resolved Small Angle X-Ray Scattering. *Particle and Particle Systems Characterization*, 37(2), 1–11. <https://doi.org/10.1002/ppsc.201900436>

Nucleation and Growth of Magnetron-Sputtered Ag Nanoparticles as Witnessed by Time-Resolved Small Angle X-Ray Scattering

Artem Shelemin, Pavel Pleskunov, Jaroslav Kousal, Jonas Drewes, Jan Hanuš, Suren Ali-Ogly, Daniil Nikitin, Pavel Solař, Jiř Kratochvíl, Mykhailo Vaidulych, Matthias Schwartzkopf, Ondřej Kylián, Oleksandr Polonskyi, Thomas Strunskus, Franz Faupel, Stephan V. Roth, Hýnek Biederman, and Andrei Choukourov*

Kinetic aspects of the synthesis of Ag nanoparticles (NPs) by magnetron sputtering are studied by in situ and time-resolved small angle X-ray scattering (SAXS). Part of the NPs are found to become confined within a capture zone at 1–10 mm from the surface of the target and circumscribed by the plasma ring. Three regimes of the NP growth are identified: 1) early growth at which the average NP diameter rapidly increases to 90 nm; 2) cycling instabilities at which the SAXS signal periodically fluctuates either due to expelling of large NPs from the capture zone or due to the axial rotation of the NP cloud; and 3) steady-state synthesis at which stable synthesis of the NPs is achieved. The NP confinement within the capture zone is driven by the balance of forces, the electrostatic force being dominant. On reaching the critical size, large NPs acquire an excessive charge and become expelled from the capture zone via the electrostatic interactions. As a result, significant NP deposits are formed on the inner walls of the aggregation chamber as well as in the central area of the target.

1. Introduction

Synthesis of metal nanoparticles (NPs) by magnetron sputtering with subsequent condensation in a cold buffer gas has been attracting strong scientific interest for years.^[1] This approach benefits from the vaporization of metals via the bombardment by energetic ions, rather than by purely thermal means, which allows virtually any metal to be sputtered and its atomic vapors to be supplied into the gas phase. Sputtered atoms escape from the target with hyperthermal energy and are forced to thermalize upon the interaction with the atoms of the cold inert gas, resulting in the spontaneous nucleation and formation of NPs. The inert gas flow is typically created to drag the NPs from the aggregation zone into another vacuum chamber where they can be collected on substrates.

The employment of highly nonequilibrium conditions favors tailoring the morphology of resultant NPs which strongly depends on the rate with which NPs equilibrate themselves with the ambient gas.^[2–5] Furthermore, mixing of two or more metals can be realized either simultaneously or sequentially giving rise to a wealth of homogeneous or heterogeneous nanoalloys, unattainable by conventional means.^[6–18] Despite great progress in laboratory synthesis of novel NPs with advanced functionalities, commercial applications of magnetron-sputtered NPs are still far from being at hand. A major obstacle for the commercialization is commonly seen in the uncompetitively low rate of the NP deposition on surfaces which is related to a generally recognized issue of the loss of the NPs inside the aggregation chamber before they leave it. Solving this problem is still quite challenging because of the knowledge gap that exists between the understanding of the atomistic processes of sputtering and the processes of the NP formation, growth and transport under the conditions of the magnetron discharge.

In our previous works, the new findings on the mechanisms of the gas phase formation of Cu NPs were revealed by in situ small angle X-ray scattering (SAXS) analysis^[19] and ultraviolet–visible spectroscopy.^[20] As was shown, Cu NPs are


Dr. A. Shelemin, P. Pleskunov, Dr. J. Kousal, Dr. J. Hanuš, S. Ali-Ogly, Dr. D. Nikitin, Dr. P. Solař, J. Kratochvíl, Dr. M. Vaidulych, Prof. O. Kylián, Prof. H. Biederman, Prof. A. Choukourov
 Department of Macromolecular Physics
 Faculty of Mathematics and Physics
 Charles University

V Holesovickach 2, 18000 Prague, Czech Republic
 E-mail: choukourov@kmf.troja.mff.cuni.cz

J. Drewes, Dr. O. Polonskyi, Dr. T. Strunskus, Prof. F. Faupel
 Chair for Multicomponent Materials
 Faculty of Engineering
 Kiel University
 Kiel, Germany

Dr. M. Schwartzkopf, Dr. S. V. Roth
 Deutsches Elektronen-Synchrotron (DESY)
 Notkestr. 85, D-22607 Hamburg, Germany

Dr. S. V. Roth
 KTH Royal Institute of Technology
 Department of Fibre and Polymer Technology
 Teknikringen 56-58, SE-100 44 Stockholm, Sweden

 The ORCID identification number(s) for the author(s) of this article can be found under <https://doi.org/10.1002/ppsc.201900436>.

DOI: 10.1002/ppsc.201900436

formed at a very short distance from the magnetron target; moreover, their average size and the relative volume fraction demonstrate strong nonlinear distribution along the aggregation zone. This effect was the most pronounced at a distance of 1–10 mm from the target where untypically large Cu NPs with the average diameter of 80 nm were detected.

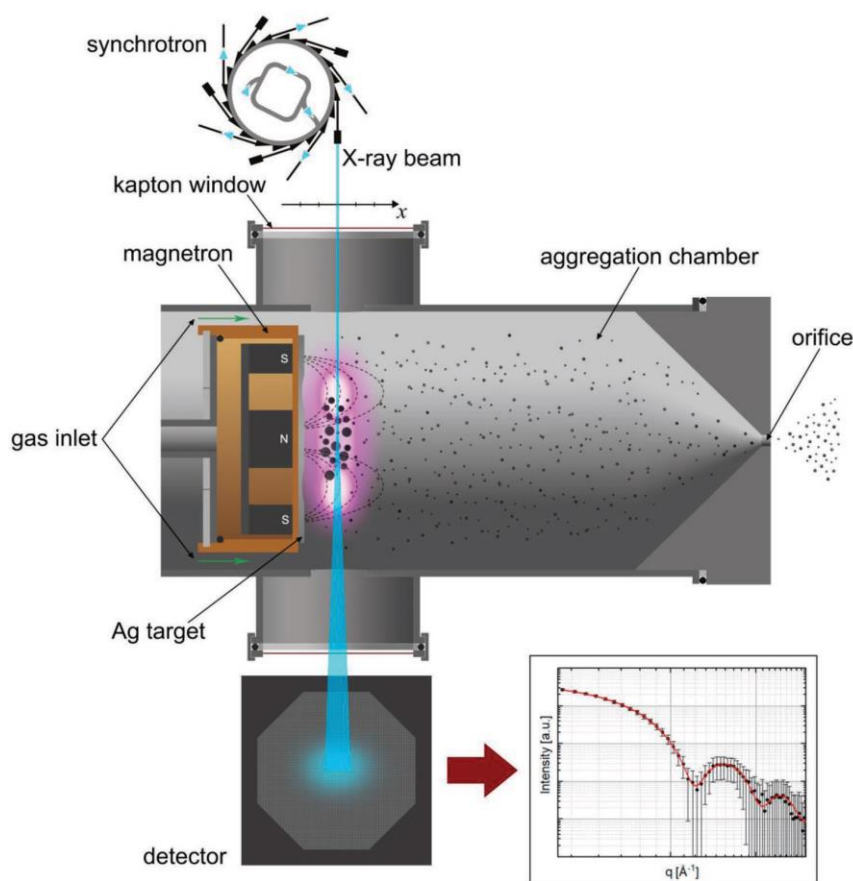
The present work investigates the synthesis of Ag NPs with the purpose to highlight the common features between the two metals. We utilize the similar SAXS diagnostics, yet at a more sophisticated level. In situ SAXS measurements are employed in a time-resolved mode to unveil the kinetic aspects of the Ag NP formation, growth, and transport, and to address the issue of the NP loss within the aggregation chamber.

2. Experimental Section

A custom gas aggregation cluster source (GAS) was built to ensure arbitrary X-ray probing positions within the inner volume of the aggregation chamber (Scheme 1, for the experimental details see Supporting Information). The GAS consisted

of a 100 mm diameter stainless steel chamber cooled by water and terminated by a conical lid with an exit orifice of 2.0 mm in diameter. A moveable 3 in. magnetron with a 3 mm thick silver target (Safina, A. C. 99.99% purity) was installed in the GAS. The magnetron was run by a DC power supply (Advanced Energy MDX500) operated in a constant current regime with the current set to 600 mA and the corresponding voltage of 313 V. A toroidal-shaped plasma ring with a diameter of 40 mm was maintained by a circuit of permanent neodymium magnets installed inside the magnetron. A pair of transversal 100 mm viewports with 125 μm thick Kapton windows provided an access for the X-ray beam to the interior of the GAS.

The GAS was mounted onto a main deposition chamber evacuated by scroll and turbomolecular pumps to a base pressure of 10^{-4} Pa. Quartz crystal microbalance (QCM) was positioned inside the deposition chamber in front of the exit orifice to monitor the deposition rate of the NPs measured in terms of the QCM frequency shift. Argon was used as a buffer gas at a pressure of 133 Pa and a flow rate of 18 sccm. The entire assembly was installed at the P03 beamline of PETRA III, DESY, Hamburg, Germany.^[21] An electrically actuated



Scheme 1. Experimental setup. The gas aggregation cluster source is moveable with respect to the X-ray beam along the x-axis, which allows for probing Ag NPs at different axial distances from the magnetron target, acquiring SAXS signal at the detector, reconstructing the scattering intensity as a function of the magnitude of the wave vector q and fitting these curves to obtain the NP size distribution and relative volume fraction.

mobile platform was used to allow for the axial positioning of the entire experimental setup with respect to an X-ray beam (photon energy is 13.01 keV, elliptically microfocused to $22 \times 32 \mu\text{m}$, $V \times H$ axes). SAXS measurements with variable x were performed, where x is the axial distance from the magnetron target. In this configuration, the X-ray beam passes above the target and crosses its entire diameter so that the probed space involves two regions of the plasma ring and the central region. Time-resolved measurements were performed with a frequency of 10 Hz, with 95 ms acquisition time followed by 5 ms read-out time per image using a Pilatus 300 K detector (Dectris Ltd., pixel size $172 \mu\text{m}$) in a distance of (5642 ± 8) mm to the center of the GAS. The data were processed using the software DPDAK,^[22] a customizable code for the analysis of large SAXS data, as described in the Supporting Information.

Scanning electron microscopy (SEM) measurements of the target were performed using a microscope Supra55VP-Carl Zeiss equipped with an in-lens detector. The acceleration voltage was 5 kV. Series of the experiments were performed with silicon substrates ($\langle 100 \rangle$ Si, one-side polished, $525 \pm 15 \mu\text{m}$ thick, ON Semiconductor, Czech Republic) positioned inside the aggregation zone at different distances from the target. These samples were analyzed by a Tescan Mira III SEM microscope equipped with an in-beam SE detector with acceleration voltage of 20 kV.

The profilometry measurements were performed with a Bruker DektakXT profilometer. The applied force on the stylus was 1 mg and the obtained resolution was $0.46 \mu\text{m}$.

A fluid flow analysis inside the aggregation chamber was performed using a computational fluid dynamics software (Siemens STAR CCM+ 13.04.010). The analysis was done in a steady-state mode employing a segregated flow solver with 2nd order convection. Semi-implicit method for pressure linked equations (SIMPLE) pressure–velocity coupling algorithm was used. The boundary conditions were set to be as follows: the system pressure is 133 Pa, the inlet gas flow is 18 sccm, and the Ar temperature is 20°C . For more detail, see the Supporting Information.

3. Results

Time-averaged SAXS curves were processed to obtain the axial dependence of the average diameter d of Ag NPs and their relative volume fraction f_{rel} (the parameter directly proportional to the ratio of the volume occupied by all the NPs to the sampled volume defined by the beam size), which are shown in **Figure 1** along with the earlier reported data for Cu NPs. Similar trends were confirmed: both parameters grow fast in the close proximity to the magnetron target, reach maximal values, and then decay to constant levels at farther distances. Designated earlier as the capture zone, the range of $x = 2\text{--}5$ mm is characterized by the presence of large NPs with the average size reaching 80 nm. Nevertheless, the NPs of this size were found only sporadically on the substrates placed outside the GAS.

Time-resolved SAXS measurements were performed to obtain the kinetic information about the NPs in the vicinity of the magnetron target. The discharge was turned on for 60 s and the SAXS data were acquired with a time step of 100 ms. **Figure 2a,b** shows the time dependence of the average NP

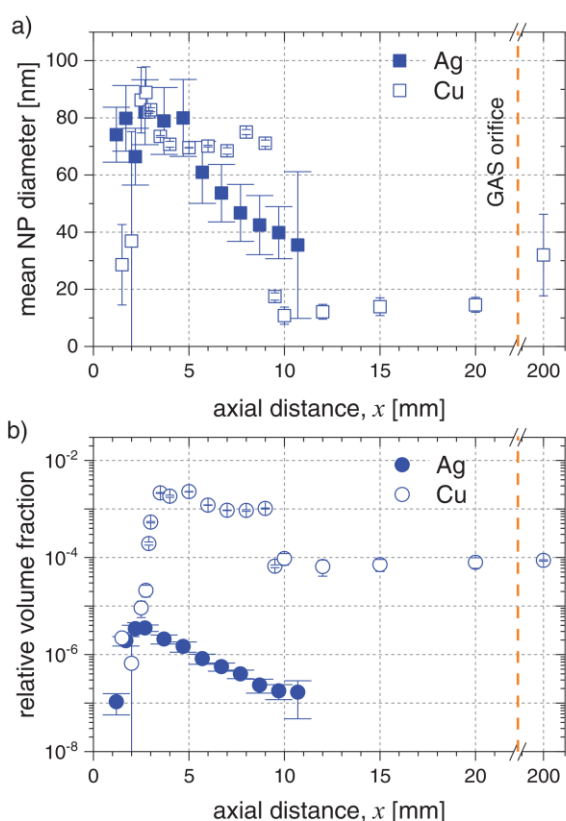


Figure 1. a) Average diameter and b) relative volume fraction of Ag and Cu NPs (data used from ref. [19]) in dependence on the axial distance in the GAS with the radial distance fixed at $\gamma = 0.0$ mm. The position $x = 0.0$ mm corresponds to the surface of the target. The vertical dotted line shows the position of the exit orifice of the GAS at $x = 120.0$ mm. Error bars are standard deviation obtained from fitting of 90 individual scattering curves at each spatial position.

diameter and the relative volume fraction obtained in this manner for the position $x = 2.2$ mm where the scattering intensity was maximum. For reference, Figure 2c shows the time dependence of the deposition rate of the NPs measured outside the GAS at $x = 200.0$ mm in terms of the QCM frequency shift. Three periods can be identified.

- 1) In the early regime (0–2 s), both the NP diameter and the relative volume fraction rapidly increase, yet QCM does not detect any deposition rate.
- 2) In the second regime (2–16 s), significant fluctuations of the scattering signal are observed, although none are present in the QCM signal, which starts increasing after an initial lag. The scattering curves periodically deviate from the shape characteristic for the monomodal NP size distribution. At these phases, bimodal size distribution is introduced to fit the data and two sets of the average size and the relative volume fraction are shown for two populations of the NPs (for more detail, see Supporting Information).

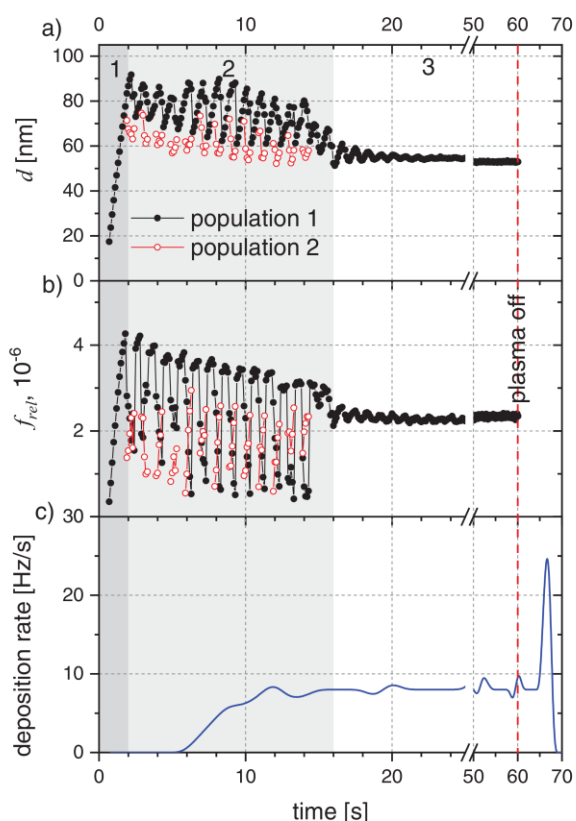


Figure 2. Evolution of a) the average diameter d , b) the relative volume fraction f_{rel} of Ag NPs produced in the GAS at $x = 2.2$ mm, and c) the deposition rate (in terms of QCM frequency shift) outside the GAS at $x = 200.0$ mm. The values of time $t = 0$ and 60 s correspond to turning the discharge on and off. The second population of the NPs (open symbols) was added to the fit of the scattering curves whenever the monomodal size distribution was not sufficient to fit the data correctly (for details see Supporting Information). Three periods of the NP formation in the GAS are identified: 1) nucleation and early growth; 2) cycling instabilities; 3) steady-state synthesis.

3) In the third regime (16–60 s), the fluctuations subside and a steady-state generation of the NPs is reached which is accompanied by a constant deposition rate. It is worth noting that the SAXS signal disappears very fast after turning off the discharge at $t = 60$ s, although QCM demonstrates a lag of the same duration as in the beginning. The lag is finished by an abrupt burst of the deposition rate followed by its decrease to zero.

Peculiarities of the three regimes are scrutinized separately in the subsequent sections.

3.1. Early Growth

The time dependencies of the average NP diameter and the relative volume fraction were calculated for 12 axial positions

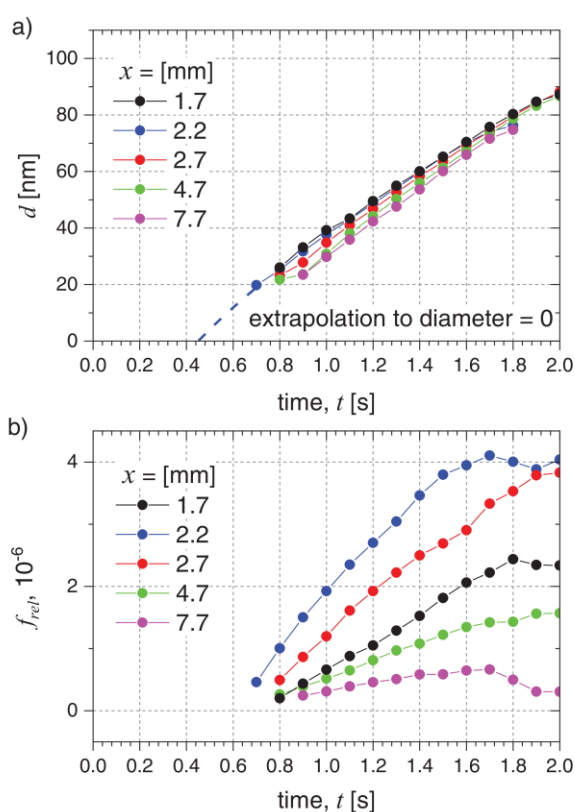


Figure 3. Time dependence of a) the average Ag NP diameter d and b) the relative volume fraction f_{rel} measured at different axial positions. Time $t = 0$ corresponds to the ignition of the discharge. The dotted line shows the example of the linear extrapolation of the data to the NP diameter $d = 0$ nm, the time point taken as the moment at which the smallest NPs are born (the NP appearance time).

in the vicinity of the magnetron target. **Figure 3** shows selected data for clarity. The NP diameter increases almost linearly with time for the entire set of x . The relative volume fraction also increases close to the linear time dependence. This parameter is directly proportional to the total volume occupied by all NPs within the sampling volume and hence is proportional to the molar concentration of Ag atoms bound within the NPs $[Ag_{NP}]$. If a simplistic condensation scheme is considered in which Ag atoms pass from the vapor to the bound state $[Ag_{vapor}] \rightarrow [Ag_{NP}]$, the linear character of the function $[Ag_{NP}] = kt$ points to the realization of this scheme via a zero-order scenario: the reaction rate does not apparently depend on the concentrations of reactants and is equal to the reaction constant k . In our case, this means that the concentration of atomic Ag vapor state remains to be in large excess and that it cannot be a limiting factor for the formation of Ag NPs for the entire set of x .

The rate of the condensation $d[Ag_{NP}]/dt$ shows a complex dependence on the axial position (Figure 3). At small x , it increases with the axial distance and reaches the maximum for $x = 2.2$ mm. At farther distances from the magnetron target, the rate starts decaying and drops to very low values at $x = 10.7$ mm.

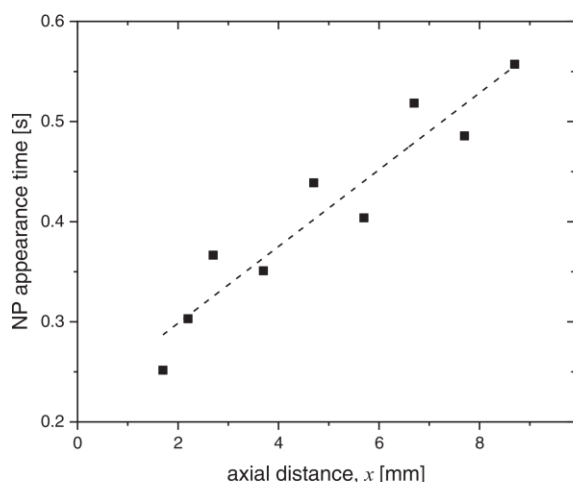


Figure 4. Time at which NPs start to appear (the NP appearance time) at different axial distances from the magnetron target. The data are obtained by extrapolating the curves of Figure 3a to the NP diameter $d = 0$ mm. The dotted line corresponds to the linear fit of the data.

Such complex behavior will be analyzed later in Section 4. Here, we stress that f_{rel} retains close-to-linear time dependence for all x and therefore the concentration of atomic Ag vapors remains sufficiently high not to limit the NP formation and growth. This conclusion also agrees with a concept of supersaturation, which is required to induce spontaneous nucleation of NPs and which implies that supersaturated (high) metal vapor pressure is continually replenished. Thus, the nucleation of Ag NPs occurs in the entire axial range in question.

Low concentration of the NPs in the gas phase does not allow for the reliable processing of the scattering curves in the high- q region, and the detection of the NPs with the average size <20 nm is impeded at the present experimental configuration. This shortcoming explains the fact that the NP size dependencies start with the values of about 20 nm and do not show smaller NPs. The extrapolation of the $d \approx f(t)$ data can be performed to the point of $d = 0$ mm and thus-obtained values of t can be used to estimate the moment at which the first nuclei are formed after the ignition of the discharge (we will designate this moment as the NP appearance time, t_a). Despite seemingly overlapping, the curves in Figure 3a provide different values of t_a , which align into a linear dependence if plotted as a function of the axial distance (Figure 4). The linear fit to the data gives the value of 26 ± 3 mm s^{-1} , which is consistent with the linear velocity of the gas flow in the GAS.

Several important conclusions can be drawn at this point. The first NPs appear within a fraction of a second after the ignition of the discharge, the lag being larger at farther distances from the magnetron target. Once created, the NPs increase in size equally fast at different x and their growth is not limited by the partial pressure of atomic Ag vapors. These findings imply that nucleation is efficient in the entire range of axial positions studied (0–11 mm) and that the lag in the onset of the NP formation is given by the lag in the supply of atomic metal vapors from the target surface after the ignition of the discharge.

3.2. Cycling Instabilities

After reaching the maximum size and concentration within ≈ 2 s after turning on the discharge, NPs enter the regime of instabilities in which the NP parameters start to change in an oscillating manner. The regime of cycling instabilities is analyzed in more detail in Figure 5 where the average NP diameter d , the relative volume fraction f_{rel} and the relative number of NP N_{rel} (normalized to NP diameter) are shown for the axial position of maximal scattering intensity ($x = 2.2$ mm) in dependence on time at a zoomed timescale. The relative number of NPs was calculated by dividing the relative volume fraction by the average NP volume ($N_{rel} = f_{rel} / \left(\frac{\pi}{6} d^3\right)$); it represents the quantity which is directly proportional to the concentration of the NPs within the volume sampled by the X-ray beam.

In the beginning of the cycle, the scattering curves are readily fitted by the monomodal lognormal size distribution (see Supporting Information). The average NP diameter increases, the

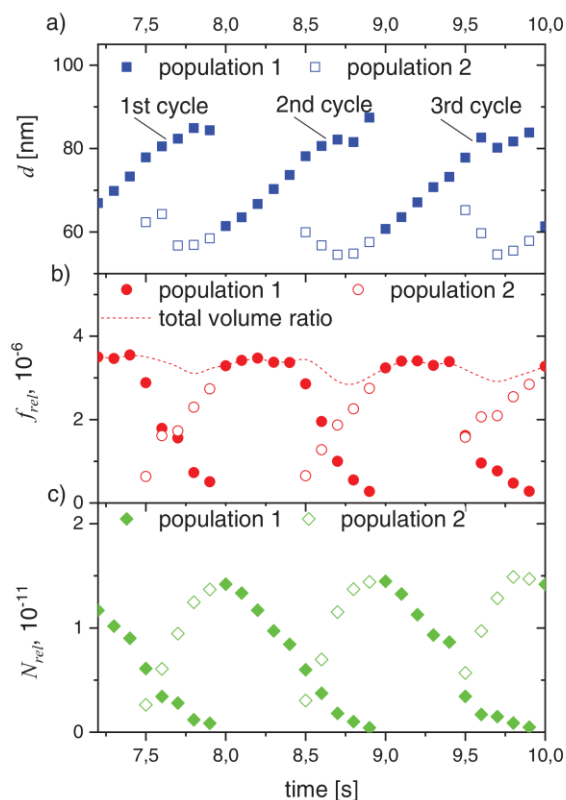


Figure 5. Cycling fluctuations of a) the average diameter d , b) relative volume fraction f_{rel} , and c) relative number N_{rel} of Ag NPs occurring in the GAS at $x = 2.2$ mm during the period of instabilities (period 2). The second population of the NPs (open symbols) was added to the fit of the scattering curves whenever the monomodal size distribution was not sufficient to fit the data correctly (for details see Supporting Information). Serial numbers designate the N th cycle ($N = 1, 2, 3, \dots$). The dotted line shows the sum of the relative volume ratios for the NP population 1 and 2.

relative volume ratio remains constant and the number of NPs decreases. At a certain moment, the monomodal size distribution becomes insufficient to fit the data satisfactorily. The introduction of the second population of smaller NPs solves the problem (see also Supporting Information). Hereafter, the first population of NPs proceeds in the growth but the volume they occupy and their number decrease. The NPs of the second population demonstrate the opposite behavior: they decrease in size but occupy the larger volume and increase in number. At the extremum, the average size of the first population reaches 85 nm whereas the average size of the second population decreases to 55 nm (here, we stress that these numbers are average values of lognormal size distributions with different values of dispersity). Then, the larger NPs disappear suddenly or, at least, they become undetectable by SAXS. Only smaller NPs are detected at this moment and the cycle is repeated. The scattering curves can be fitted with a monomodal size distribution again, the average NP diameter increases, the relative volume ratio remains constant and the number of NPs decreases until differentiation into other two populations of NPs occurs. The period of the described fluctuations is 1 s. For better visualization, an animation showing the evolution of the Ag NP size distribution was added to the Supporting Information. A more detailed reasoning about the interpretation of these oscillations follows in Section 4.

3.3. Steady-State Synthesis and Extinction of the Discharge

After the period of fluctuations, the generation of Ag NPs arrives to the steady-state regime at which the NP size and concentration do not change in time. An interesting phenomenon was observed when switching off the discharge: QCM detected stable deposition of NPs for a certain time followed by its sudden increase and then a decrease to zero (Figure 1). A pulsing approach was applied to investigate this effect in more detail. The discharge was pulsed with time-on $t_{\text{on}} = 10$ s and time-off $t_{\text{off}} = 5$ s, and the deposition rate was monitored by QCM positioned outside the GAS at $x = 200.0$ mm (Figure 6). It was confirmed that for each pulse no deposition occurs during the first 3 s after turning the discharge on, then the deposition rate starts increasing and reaches the stable value at about 5 s, it remains stable at this level even after turning the discharge off at 10 s, then it sharply proliferates, but only for a short duration followed by a decrease to zero at 15 s, the time at which the next pulse is initiated. The time lag between the discharge turning on/off and the QCM response is readily explained by the time needed for NPs to travel along the GAS. When the distance of 120 mm between the magnetron target and the orifice is divided by the average linear gas velocity of 29 mm/s, the time of about 4 s is obtained that roughly matches the QCM lag (the 80 mm distance between the QCM and the orifice is neglected because NPs travel at much higher velocity in this region).

The phenomenon of a manifold burst of the deposition rate with the discharge off can be analyzed by performing the time-resolved SAXS measurements in the pulsed discharge regime. Figure 7 shows the changes observed in the average NP size, the relative volume fraction and the relative number of

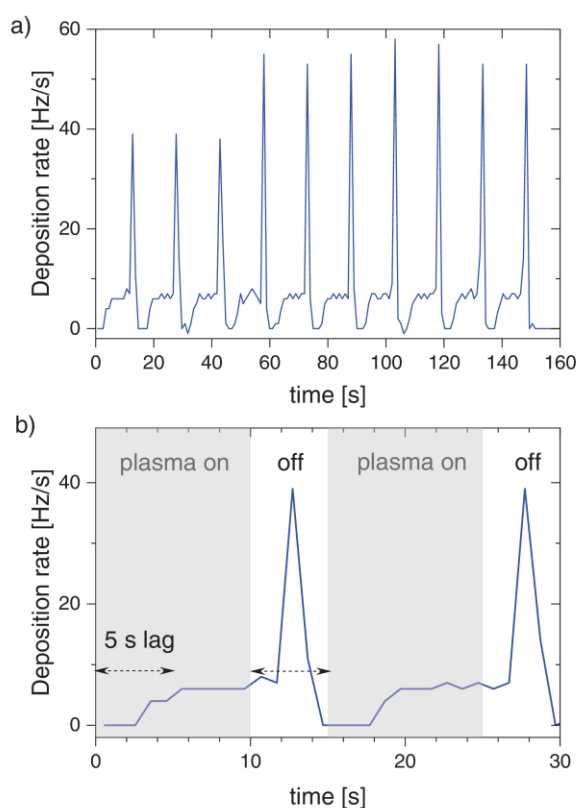


Figure 6. The deposition rate of Ag NPs measured by QCM outside the GAS at $x = 200.0$ mm during pulsing the discharge with $t_{\text{on}} = 10$ s and $t_{\text{off}} = 5$ s. a) At longer timescale. b) The same dependence at shorter timescale.

NPs after turning the discharge off at $t = 10.0$ s at different axial positions in the GAS. For the position of the highest scattering intensity at $x = 2.2$ mm, the NPs disappear within 0.2 s and the scattering intensity decreases to the background level. However at a farther distance of $x = 9.7$ mm, all the NP parameters show an increase for a fraction of second and then the intensity drops down as well. Markedly, the position closest to the magnetron target at $x = 0.2$ mm also demonstrates an interesting feature. The size of the NPs is too small for the detection at this position and the SAXS signal remains at the background level during the operation of the discharge. However, large 80 nm sized NPs become detectable for a short period of 0.1 s after the discharge is turned off and then they also disappear. The short detection period explains the presence of only two data points for $x = 0.2$ mm in Figure 7.

Thus, the following mechanism can be suggested. Part of the NPs becomes trapped in the capture zone when the discharge is on. The trapping results in a longer time that NPs spend in this region and, as a consequence, in an increase of their average diameter to the larger values. After turning the discharge off, the trapped NP cloud collapses and the large amount of NPs escape from the capture zone. After the time lag determined by the linear gas flow, the released multitude of NPs arrives to QCM and induces the short-time burst in the deposition rate.

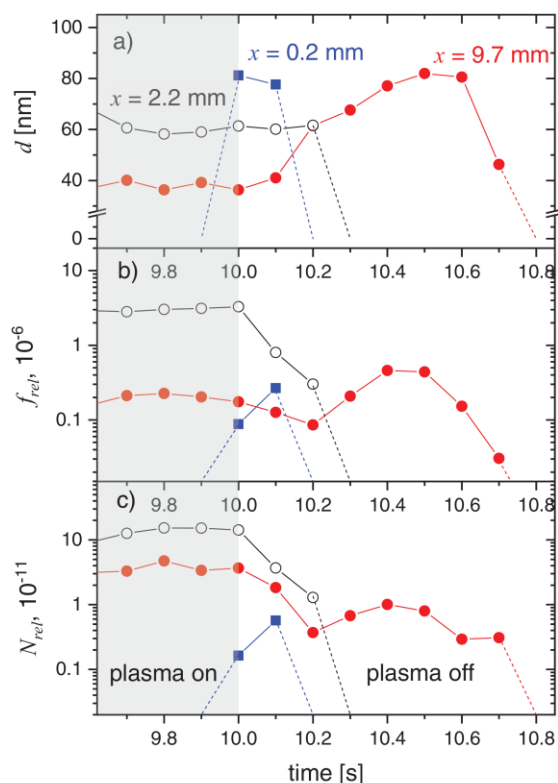


Figure 7. Evolution of a) the NP diameter d , b) the relative volume fraction f_{rel} , and c) the relative number N_{rel} after the discharge is turned off at $t = 10.0$ s for the position closest to the magnetron target ($x = 0.2$ mm), in the capture region with maximal scattering intensity ($x = 2.2$ mm) and outside the capture region ($x = 9.7$ mm). Dotted lines are guide to eyes showing the decrease of the scattering intensity to the background level.

Markedly, the NPs escape from the capture zone in the direction toward the magnetron target as well, that is against the gas flow (see the simulations of Ar velocity vectors in the Supporting Information). **Figure 8** shows the photos of the target surface taken after 1 week of the experimental campaign. A macroscopic deposit of the NPs is formed in the central area of the target. The SEM images demonstrate that the deposit consists of coalesced NPs and a rough estimation shows that, although strongly coalesced, they have the average diameter of about 90 nm. This finding confirms that the NPs become trapped above the target in the region circumscribed by the magnetron plasma ring.

Two sets of the experiments were performed with placing 0.5×0.5 cm Si substrates directly onto the inner wall of the aggregation chamber at different distance from the magnetron target. After installing the substrates, the GAS was evacuated, the experimental parameters were adjusted, the discharge was turned on for 10 s and then the sputtering was stopped. The substrates were extracted from the GAS and analyzed by SEM. The second set was performed in a similar manner, yet with the 60 s operation. The SEM analysis of the resultant deposits is shown in **Figure 9**. Similar to the earlier notation, the position

$x = 0$ mm corresponds here to the position of the target plane so that $x = -3$ mm corresponds to the substrate shifted by 3 mm behind the magnetron target.

Even after 10 s of sputtering, we observe the accumulation of NPs on the walls all along the aggregation chamber, the amount of the deposit being larger closer to the magnetron. Markedly, the NPs are effectively deposited even at the positions behind the target plane. The morphology of the deposits also changes. Closer to the magnetron at $x < 3$ mm, the deposit consists of spherical NPs arriving as-formed in the gas phase. A strong contribution from the large NPs can be seen here. At $3 < x < 39$ mm, irregularly shaped nanoislands dominate the deposits although spherical NPs are also present to a lesser extent. The nanoislands strongly resemble the structure typically formed as a result of atomic silver deposition onto weakly interacting substrates.^[23–25] At remote distances with $x > 39$ mm, spherical NPs start dominating again, yet the total NP number becomes smaller.

These findings are further supported by the longer 60 s deposition. At $x < 3$ mm, large amount of large NPs is deposited on the substrate forming a mesoporous deposit. The NPs are strongly coalesced similar to those found on the target surface, although their size is smaller. The strong coalescence may serve as evidence that the NPs have a temperature, which is above or not very far below the melting point during their deposition onto the substrate. At $3 < x < 39$ mm, the formation of a discontinuous film with inclusions of spherical NPs is observed whereas the film growth is suppressed at $x > 39$ mm. Here, only spherical NPs are collected on the substrates and their coalescence becomes less obvious, suggesting that the NPs effectively thermalize on their travel along the aggregation chamber.

The analysis of the deposits confirms that Ag NPs escape from the capture zone both in the axial and in the radial direction. The sputtered atomic metal flux is in sufficient excess to be consumed in the gas phase for the NP formation as well as to reach the walls near about the magnetron and to contribute to the growth of films thereon. As a consequence, non-negligible amount of sputtered material is lost at the walls of the GAS instead of being transported in the form of a NP beam into the deposition chamber.

4. Discussion

After the ignition of the discharge, the NPs nucleate and grow in size to the average value of about 90 nm in the near-to-magnetron region, with the NP concentration reaching maximum at $x = 2.2$ mm. The NPs of this size can be found, yet only sporadically, on substrates positioned outside the GAS in the main deposition chamber; however, they can be found more abundantly on substrates positioned inside the GAS close to the magnetron as well as on the magnetron target itself, in its central area. The behavior agrees with the earlier reported concept of the capture zone which is created at the several mm distance above the magnetron and circumscribed by a plasma ring. Smaller NPs have a higher probability to escape the capture zone and to constitute a beam of NPs travelling along the GAS with the gas flow. Larger NPs are trapped more effectively and therefore proceed growing further until they reach a critical

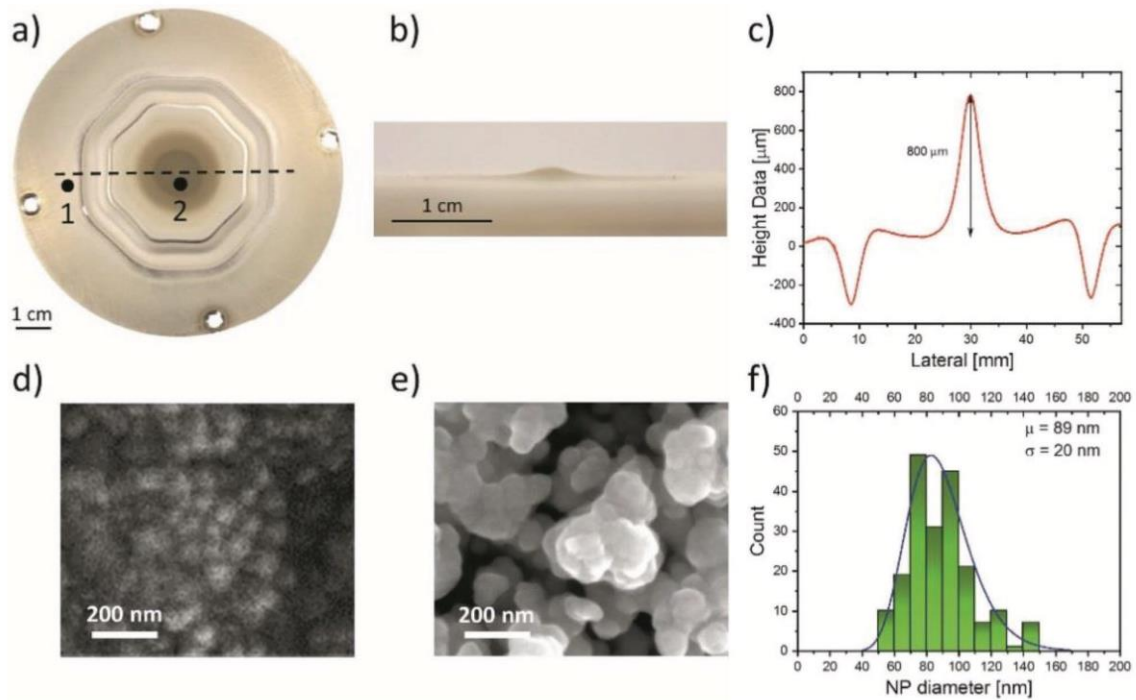


Figure 8. Characterization of the target surface. a,b) Top view and side view photos of the target showing the macroscopic redeposit of Ag NPs in the central area (taken after 1 week of the experimental campaign). c) Profilometry height profile of the redeposit of NPs corresponding to the dotted line on the top view image. d,e) SEM images of the target surface acquired at the periphery (spot 1) and in the center (spot 2) after 10 s of sputtering of fresh target. f) Size distribution of the NPs redeposited in the central area of target, the curve corresponds to the lognormal fit to the data, average NP diameter is $\mu = 89$ nm, standard deviation is $\sigma = 20$ nm.

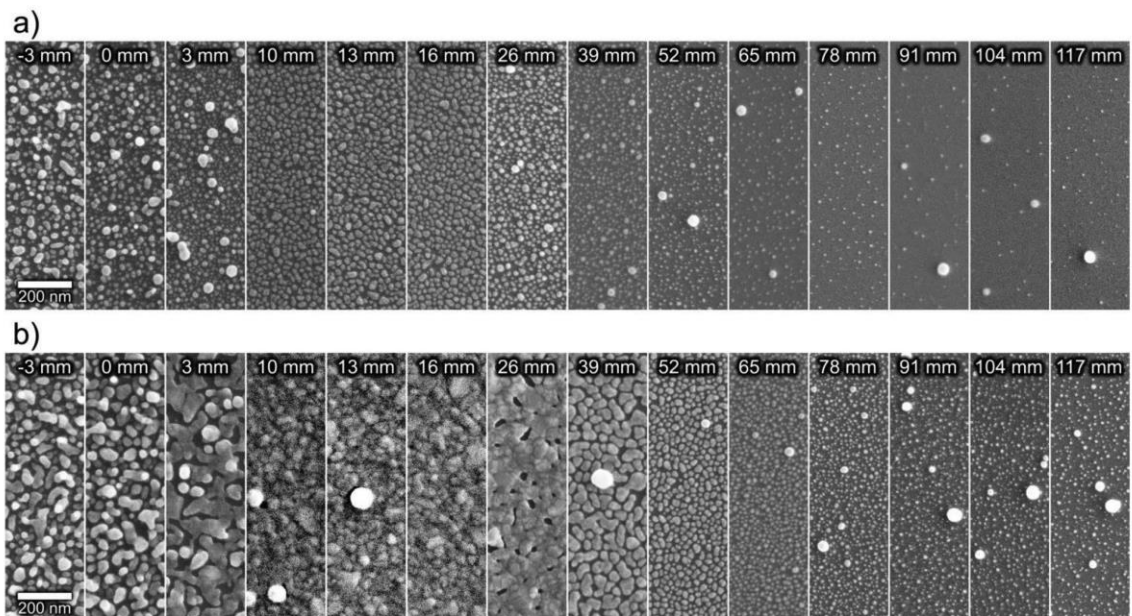


Figure 9. Top view SEM images of Ag NPs collected on Si substrates placed onto the GAS wall at different axial positions from the magnetron target. a) The deposition time $t = 10$ s, and b) the deposition time $t = 60$ s.

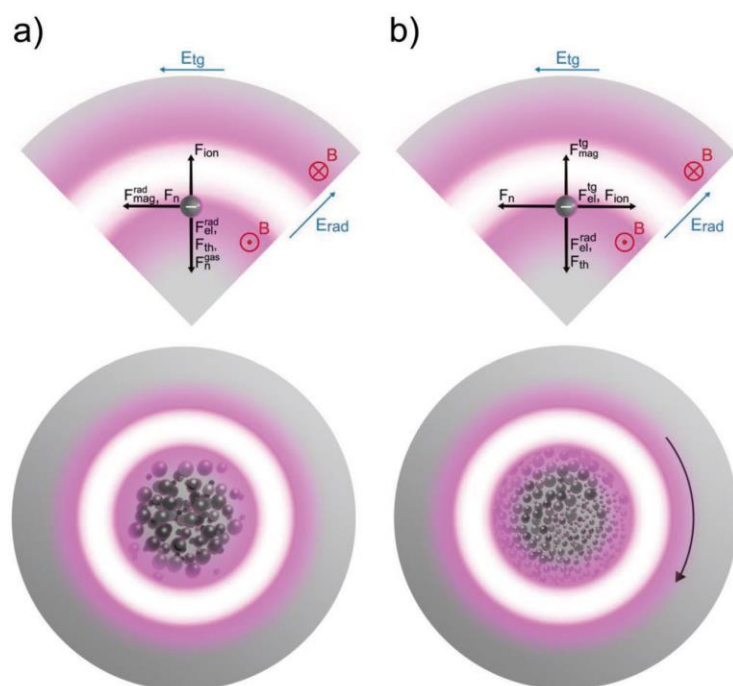
size at which they become expelled from the capture zone and deposit on the adjacent surfaces.

The phenomenon of capturing/expelling is evidently governed by the balance of forces acting on the NPs, and this balance can be shifted depending on the NP size. Given that the majority of the NPs are negatively charged in the plasma, the following forces should be taken into account: the electromagnetic force (with the electric and magnetic components of the Lorentz force describing the movement of the NP upon the action of the electric and the magnetic field), the thermophoretic force (given by the temperature gradient if such exists in the space surrounding the NPs), the gravity, the neutral drag force (the force produced onto the NP by the momentum transfer from the neutral atoms constituting the gas flow), and the ion drag force (the force induced onto the NP by the momentum transfer from directed fluxes of ions). Scheme 2a demonstrates these forces acting on a negatively charged NP located at the inner periphery of the plasma ring and at the edge of the capture zone. The schemes were constructed on the basis of the simulations of the gas flow in the GAS as well as on the previous results of the Langmuir probe measurements (see Supporting Information).

The collective action of the forces onto NPs may give rise to instabilities often observed in dusty plasmas.^[26] The oscillations of the SAXS signal with the frequency of 1 Hz reported here strongly remind the so-called heartbeat instabilities that occur with the several Hz frequency in low-temperature dusty plasmas and comprise the cycling contractions and expansions of a particle-free region called a void.^[27–29] The underlying physics involves the formation and collapse of a sheath at the void boundary, the phenomenon given by the cycling accumulation of charge by dust particles and subsequent electrostatic expelling of critically charged NPs from the void.^[30] In non-magnetized discharges with the parallel-plate electrode configuration, the particle-free void is formed in the central region of the particle cloud.^[29] Our findings, both shown here and reported earlier,^[19] indicate that the reverse is true for the magnetron discharge: the NPs concentrate in the central region and become periodically expelled therefrom (Scheme 2b).

Another possible explanation for the observed instabilities may include the rotation of the NP cloud about the magnetron axis. Such rotation may become possible if the tangential electric field appears within the circular plane of the cloud due to an inhomogeneous distribution of the NP charge (proportional to the NP size). This tangential component of the electric field may propel the NPs into a circular motion. If we interpret the time dependence of Figure 5 as the rotation of the trapped NP cloud, we can see that there is a sharp decrease of number density of the biggest NPs followed by a multitude of smaller NPs. This would correspond to the situation shown in Scheme 2b where the NP cloud is characterized by the tangential gradient of the NP size/charge. The cloud rotates about the magnetron axis, with the front of large NPs traversing the X-ray beam twice per period of the rotation.

At present, we are not able to distinguish which of the mechanisms (cycling growth/expelling or rotation of the NP cloud) is responsible for the observed instabilities. In fact, they need not be necessarily mutually exclusive and may probably coexist to a certain extent. The NPs can definitely grow from 20 to 80 nm in 1 s as witnessed during the initial stages of the process (Figure 3). This growth dynamics manifests itself at the time-scale comparable to the period of the oscillations observed later (Figure 5). Actually, local spontaneous inhomogeneity in the NP growth can be a starting point for the instabilities to occur. Since the material must be arriving into the trapped cloud region during the entire power-on period, the NPs must grow inside the cloud at least to some extent. As a result, the apparent periodic changes in the NP size and density can be a superposition of the physical movement of the NPs with their (quasi)continuous growth. The smallest NPs are continuously replenished



Scheme 2. Illustration of two mechanisms that may be responsible for cycling instabilities observed by SAXS. a) Cycling growth and expelling of NPs (larger NPs accumulate closer to the magnetron axis). b) Axial rotation of the NP cloud (the NPs are tangentially separated by their size/charge, the entire cloud rotating clockwise). Top pictures show forces acting on a negatively charged NP that is located at the inner periphery of the plasma ring and at the outer edge of the capture zone (only a quarter of the target is shown for simplicity), F_{el}^{rad} and F_{el}^{tg} are radial and tangential components of the electric force, F_{mag}^{rad} and F_{mag}^{tg} are radial and tangential components of the magnetic force, F_{th} is the thermophoretic force, F_n is the neutral drag force, and F_{ion}^{rad} and F_{ion}^{tg} are radial and tangential components of the ion drag force. The gravitational force is not shown for simplicity.

into the capture zone from the area above the erosion track and the biggest NPs continuously escape from the trap (Figure 8). We can name this process a growth-transport instability. Such “coupled processes” instability can be actually an interesting analogue of the ionization-movement instabilities observed as fast “spokes” in closed-drift ($E \times B$ drift) devices such as magnetrons^[31–33] or Hall thrusters^[34,35] but at a much longer timescale. However, we should admit that details of these phenomena remain unclear at present and require further investigation.

The cycling instabilities eventually subside and the system enters the steady-state regime. It is worth mentioning that the phenomenon of the postponed stabilization of the generation of NPs does not seem to be unique. It bears similar features to the earlier reported uncontrollable drift of the heartbeat frequency that occurred with sub-micrometer particles in dusty plasma at longer time intervals even though the experimental parameters were carefully maintained constant.^[30]

5. Conclusion

The kinetic processes of the synthesis of Ag NPs in the magnetron-based gas aggregation cluster source were analyzed by in situ and time-resolved SAXS measurements. The existence of the capture zone was confirmed in which the charged NPs are held mainly by electrostatic interactions. The capture zone is localized at 1–10 mm distance from the surface of the target and circumscribed by the magnetron plasma ring. The first NPs are found to appear within tenths of a second after the ignition of the discharge. The partial pressure of atomic Ag vapors does not limit the growth of the NPs, and they increase in size similarly fast at different axial distances from the target. After the initial period of the fast growth, the SAXS measurement detected the regime of cycling oscillations of the NP size and number which can be given by the combination of two mechanisms: 1) periodic expelling of NPs from the capture zone after they reach the critical size and 2) the rotation of the NP cloud about the magnetron axis. The oscillations of the SAXS signal eventually subside and the synthesis of the NPs enters the steady-state regime. Here, a constant amount of the NPs escape the capture zone and travel along the aggregation chamber with the velocity of the carrying gas. On their way to the exit orifice, a part of the NPs becomes lost on the inner walls of the chamber while another part becomes redeposited from the capture zone back onto the surface of the target. The significant loss of the material within the aggregation chamber suggests that optimization of magnetron-based cluster sources is the question of high importance.

Supporting Information

Supporting Information is available from the Wiley Online Library or from the author.

Acknowledgements

This work was supported by grant GACR 17–22016S from the Grant Agency of the Czech Republic., P.P., S.A.-O., D.N., and M.V. also

appreciate the support from the student grant SVV 260444/2019 of Charles University. This research was carried out at the synchrotron light source PETRA III at DESY, a member of the Helmholtz Association (HGF).

Conflict of Interest

The authors declare no conflict of interest.

Keywords

gas aggregation cluster source, magnetron sputtering, silver nanoparticles, small angle X-ray scattering

Received: November 4, 2019
Published online:

- [1] *Gas-Phase Synthesis of Nanoparticles* (Ed: Y. Huttel), Wiley-VCH, Weinheim, Germany **2017**.
- [2] J. Zhao, E. Baibuz, J. Vernieres, P. Grammatikopoulos, V. Jansson, M. Nagel, S. Steinhauer, M. Sowwan, A. Kuronen, K. Nordlund, F. Djurabekova, *ACS Nano* **2016**, *10*, 4684.
- [3] L. Xing, G. H. ten Brink, B. J. Kooi, G. Palasantzas, *J. Appl. Phys.* **2017**, *121*, 024305.
- [4] M. Schwartzkopf, A. Hinz, O. Polonskyi, T. Strunskus, F. C. Löhner, V. Körstgens, P. Müller-Buschbaum, F. Faupel, S. V. Roth, *ACS Appl. Mater. Interfaces* **2017**, *9*, 5629.
- [5] O. Polonskyi, T. Peter, A. Mohammad Ahadi, A. Hinz, T. Strunskus, V. Zaporozhchenko, H. Biederman, F. Faupel, *Appl. Phys. Lett.* **2013**, *103*, 033118.
- [6] Y.-H. Xu, J.-P. Wang, *Adv. Mater.* **2008**, *20*, 994.
- [7] D. Llamasa, M. Ruano, L. Martínez, A. Mayoral, E. Roman, M. García-Hernández, Y. Huttel, *Nanoscale* **2014**, *6*, 13483.
- [8] J.-G. Mattei, P. Grammatikopoulos, J. Zhao, V. Singh, J. Vernieres, S. Steinhauer, A. Porkovich, E. Danielson, K. Nordlund, F. Djurabekova, M. Sowwan, *Chem. Mater.* **2019**, *31*, 2151.
- [9] J. Vernieres, S. Steinhauer, J. Zhao, P. Grammatikopoulos, R. Ferrando, K. Nordlund, F. Djurabekova, M. Sowwan, *Adv. Sci.* **2019**, *6*, 1900447.
- [10] T. Kretková, J. Hanuš, O. Kylián, P. Solař, M. Dopita, M. Cieslar, I. Khalakhan, A. Choukourov, H. Biederman, *J. Phys. D: Appl. Phys.* **2019**, *52*, 205302.
- [11] G. E. Johnson, R. Colby, J. Laskin, *Nanoscale* **2015**, *7*, 3491.
- [12] P. Mukherjee, B. Balamurugan, J. E. Shield, D. J. Sellmyer, *RSC Adv.* **2016**, *6*, 92765.
- [13] A. Vahl, J. Strobel, W. Reichstein, O. Polonskyi, T. Strunskus, L. Kienle, F. Faupel, *Nanotechnology* **2017**, *28*, 175703.
- [14] J. Vernieres, S. Steinhauer, J. Zhao, A. Chapelle, P. Menini, N. Dufour, R. E. Diaz, K. Nordlund, F. Djurabekova, P. Grammatikopoulos, M. Sowwan, *Adv. Funct. Mater.* **2017**, *27*, 1605328.
- [15] J. Hanuš, M. Vaidulych, O. Kylián, A. Choukourov, J. Kousal, I. Khalakhan, M. Cieslar, P. Solař, H. Biederman, *J. Phys. D: Appl. Phys.* **2017**, *50*, 475307.
- [16] S. Gauter, F. Haase, P. Solař, O. Kylián, P. Kúš, A. Choukourov, H. Biederman, H. Kersten, *J. Appl. Phys.* **2018**, *124*, 073301.
- [17] Y. Huttel, L. Martínez, A. Mayoral, I. Fernández, *MRS Commun.* **2018**, *8*, 947.
- [18] A. Mayoral, L. Martínez, J. M. García-Martín, I. Fernández-Martínez, M. García-Hernández, B. Galiana, C. Ballesteros, Y. Huttel, *Nanotechnology* **2019**, *30*, 065606.

- [19] J. Kousal, A. Shelemin, M. Schwartzkopf, O. Polonskyi, J. Hanuš, P. Solař, M. Vaidulych, D. Nikitin, P. Pleskunov, Z. Krtouš, T. Strunskus, F. Faupel, S. V. Roth, H. Biederman, A. Choukourov, *Nanoscale* **2018**, *10*, 18275.
- [20] D. Nikitin, J. Hanuš, S. Ali-Ogly, O. Polonskyi, J. Drewes, F. Faupel, H. Biederman, A. Choukourov, *Plasma Process. Polym.* **2019**, *16*, 1900079.
- [21] A. Buffet, A. Rothkirch, R. Döhrmann, V. Körstgens, M. M. Abul Kashem, J. Perlich, G. Herzog, M. Schwartzkopf, R. Gehrke, P. Müller-Buschbaum, S. V. Roth, *J. Synchrotron Radiat.* **2012**, *19*, 647.
- [22] G. Benecke, W. Wagermaier, C. Li, M. Schwartzkopf, G. Flucke, R. Hoerth, I. Zizak, M. Burghammer, E. Metwalli, P. Müller-Buschbaum, M. Trebbin, S. Förster, O. Paris, S. V. Roth, P. Fratzl, *J. Appl. Crystallogr.* **2014**, *47*, 1797.
- [23] S. Baba, A. Kinbara, M. Adachi, *Vacuum* **1991**, *42*, 279.
- [24] G. Santoro, S. Yu, M. Schwartzkopf, P. Zhang, S. Koyiloth Vayalil, J. F. H. Risch, M. A. Rübhausen, M. Hernández, C. Domingo, S. V. Roth, *Appl. Phys. Lett.* **2014**, *104*, 243107.
- [25] S. Yu, G. Santoro, Y. Yao, D. Babonneau, M. Schwartzkopf, P. Zhang, S. K. Vayalil, P. Wessels, R. Döhrmann, M. Drescher, P. Müller-Buschbaum, S. V. Roth, *J. Phys. Chem. C* **2015**, *119*, 4406.
- [26] P. K. Shukla, B. Eliasson, *Rev. Mod. Phys.* **2009**, *81*, 25.
- [27] J. Goree, G. E. Morfill, V. N. Tsytovich, S. V. Vladimirov, *Phys. Rev. E* **1999**, *59*, 7055.
- [28] M. Mikikian, L. Couëdel, M. Cavarroc, Y. Tessier, L. Boufendi, *New J. Phys.* **2007**, *9*, 268.
- [29] M. Schwabe, S. Zhdanov, C. Rath, *IEEE Trans. Plasma Sci.* **2018**, *46*, 684.
- [30] M. Y. Pustynnik, A. V. Ivlev, N. Sadeghi, R. Heidemann, S. Mitic, H. M. Thomas, G. E. Morfill, *Phys. Plasmas* **2012**, *19*, 103701.
- [31] M. Panjan, S. Loquai, J. E. Klemberg-Sapieha, L. Martinu, *Plasma Sources Sci. Technol.* **2015**, *24*, 065010.
- [32] M. Panjan, A. Anders, *J. Appl. Phys.* **2017**, *121*, 063302.
- [33] A. Hecimovic, A. von Keudell, *J. Phys. D: Appl. Phys.* **2018**, *51*, 453001.
- [34] J.-P. Boeuf, *J. Appl. Phys.* **2017**, *121*, 011101.
- [35] K. Matyash, R. Schneider, S. Mazouffre, S. Tsikata, L. Grimaud, *Plasma Sources Sci. Technol.* **2019**, *28*, 044002.

Copyright WILEY-VCH Verlag GmbH & Co. KGaA, 69469 Weinheim, Germany, 2019.

Particle

& Particle Systems Characterization

Supporting Information

for *Part. Part. Syst. Charact.*, DOI: 10.1002/ppsc.201900436

Nucleation and Growth of Magnetron-Sputtered Ag Nanoparticles as Witnessed by Time-Resolved Small Angle X-Ray Scattering

*Artem Shelemin, Pavel Pleskunov, Jaroslav Kousal, Jonas Drewes, Jan Hanuš, Suren Ali-Ogly, Daniil Nikitin, Pavel Sola, Jiří Kratochvíl, Mykhailo Vaidulych, Matthias Schwartzkopf, Ondej Kylián, Oleksandr Polonskyi, Thomas Strunskus, Franz Faupel, Stephan V. Roth, Hynek Biederman, and Andrei Choukourov**

Supporting information

Nucleation and growth of magnetron-sputtered Ag nanoparticles as witnessed by time-resolved small angle X-ray scattering

A. Shelemin,^a P. Pleskunov,^a J. Kousal,^a J. Drewes,^b J. Hanuš,^a S. Ali-Ogly,^a D. Nikitin,^a P. Solar,^a J. Kratochvíl,^a M. Vaidulych,^a M. Schwartzkopf,^c O. Kylián,^a O. Polonskyi,^b T. Strunskus,^b F. Faupel,^b S. V. Roth,^{c,d} H. Biederman,^a A. Choukurov^{a*}

^aDepartment of Macromolecular Physics, Faculty of Mathematics and Physics, Charles University, V Holesovickach 2, 18000 Prague, Czech Republic

^b Chair for Multicomponent Materials, Faculty of Engineering, Kiel University, Kiel, Germany

^c Deutsches Elektronen-Synchrotron (DESY), Notkestr. 85, D-22607 Hamburg, Germany

^dKTH Royal Institute of Technology, Department of Fibre and Polymer Technology, Teknikringen 56-58, SE-100 44 Stockholm, Sweden

1. Experimental details

The GAS consisted of a cylindrical vacuum chamber (100 mm in diameter) with water-cooled walls. A moveable 3-inch magnetron with a silver target was installed at one side of the GAS whereas the opposite side ended with an orifice which was 4 mm long and 2.0 mm in diameter. The distance from the magnetron to the orifice was 12 cm. The magnetron was equipped with a set of permanent magnets that provided a closed plasma ring with the radius of 20 mm above the target. The profile of the magnetic field was measured and is shown in Figure S 1.

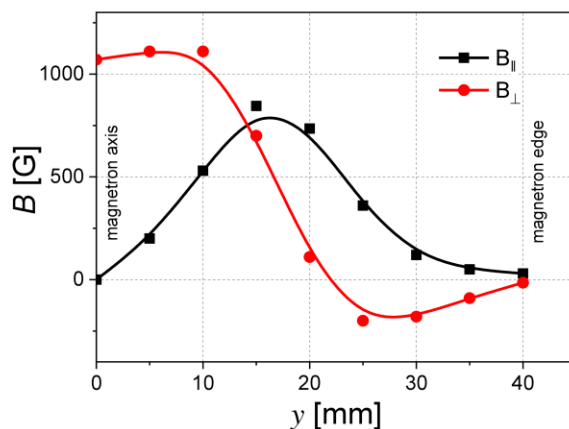


Figure S 1 Intensity of the magnetic field B measured in the parallel ($B_{||}$) and the normal (B_{\perp}) direction to the target plane from the magnetron axis, across its radius and to the magnetron edge. The zero distance corresponds to the magnetron axis.

Two opposing windows (100 mm in diameter, made of 125- μm thick KaptonTM foils) were placed on transversal ports of the GAS. The ports were equipped with rectangular baffles (25x85 mm in diameter) to minimize the deposition of NPs on the inner side of the windows. The GAS was connected *via* its orifice to another vacuum chamber through which pumping with rotary and turbomolecular pumps was performed.

The setup was installed at the P03 beamline of PETRA III, DESY, Hamburg, Germany.¹ The synchrotron provides a brilliance exceeding 10^{21} photons/(s mm² mrad²). The storage ring operates at 99.5 ± 0.5 mA beam current in a top-up mode keeping the stability of the photon flux at 1%. The X-ray was focused to an ellipsoidal beam of $22.0 \times 32.0 \pm 0.5$ μm (V \times H axes) and passed through the transversal ports of the GAS and to reach a Pilatus 300K detector (Dectris Ltd., pixel size 172 μm) which was placed 5642.0 ± 8 mm away from the axis of the GAS chamber with an evacuated pathway in between. The GAS and the pumping system were fixed at a goniometer table (HUBER Diffraktionstechnik GmbH) that allowed horizontal positioning with respect to the X-ray beam. It allowed changing of the axial position within the range 0 – 10 mm in 0.5 mm step. Constant Ar pressure of 133 Pa and the flow rate of 18 sccm were used. The magnetron was run by a DC generator (Advanced Energy MDX500) with the current and voltage set at 600 mA and 313 V, respectively.

2. SAXS calibration

The collagen (from chicken tendon) with known d-spacing 65 nm were used to calibrate the sample-to-detector distance. The calibration sample was placed inside the aggregation chamber at the position corresponding to the axis of the magnetron and under atmospheric pressure. The X-ray scattering patterns were acquired with the photon energy in the primary beam of 13.01 keV and the wavelength of 0.955 nm. The calibration was done using a SAXS/WAXS calibration tool in DPDAK.² The beam centre was defined as $x = 267.7 \pm 0.5$ pixel and $y = 228.7 \pm 0.5$ pixel; the detector tilt and rotation were at $0 \pm 0.01^\circ$. The obtained sample-to-detector distance was 5642.0 ± 8 mm.

The transmission coefficient $T = I_1/I_0 = 0.99$ was calculated for the cases with maximal scattering intensity where I_1 is the intensity of the beam after the calibration sample insertion and I_0 is the intensity of the primary beam, both measured at the beam stop.

3. SAXS data acquisition and processing

3.1. Data acquisition

For each of the spatial position inside the GAS, time-resolved measurements were performed, with the detector scanning routine being synchronized with the DC source (Figure S 2 and Figure S 3). The discharge was repeatedly run for 10 s followed by the 5 s off-time, giving the pulse period of 15 s. The diffraction images were acquired along the axis of the aggregation chamber ($y = 0.0$ mm) at different positions from the magnetron target. The diffraction images were obtained with a frequency of 10 images per second, with 0.095 s of the acquisition time followed by 0.005 s of the read-out time per image. The background signal was recorded for 1 s before and 5 s after each of the plasma runs (Figure S 4). It was found to be identical (Figure S 5), thus confirming the absence of the NP deposition on the Kapton windows.

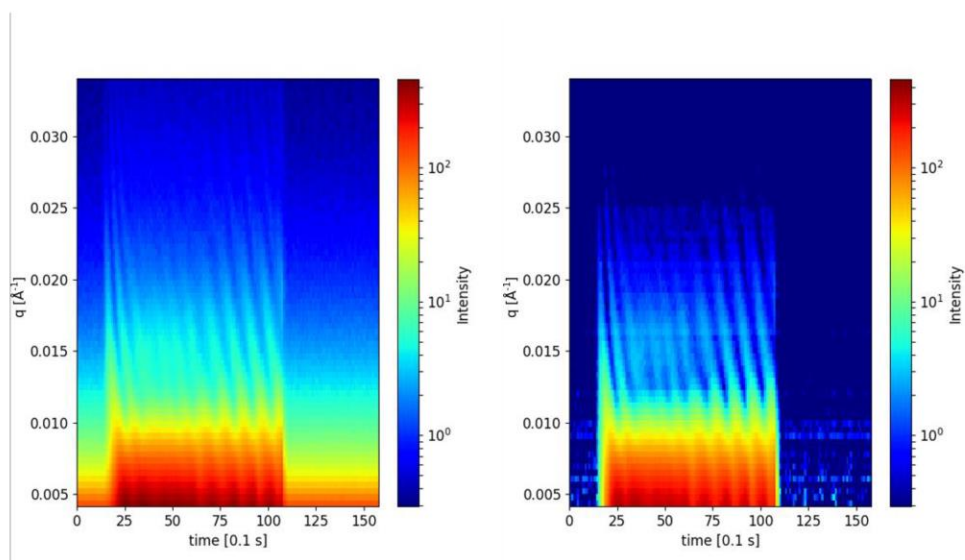


Figure S 2 2D colour map of time resolved data including background scans (left image) and after background subtraction (right image).

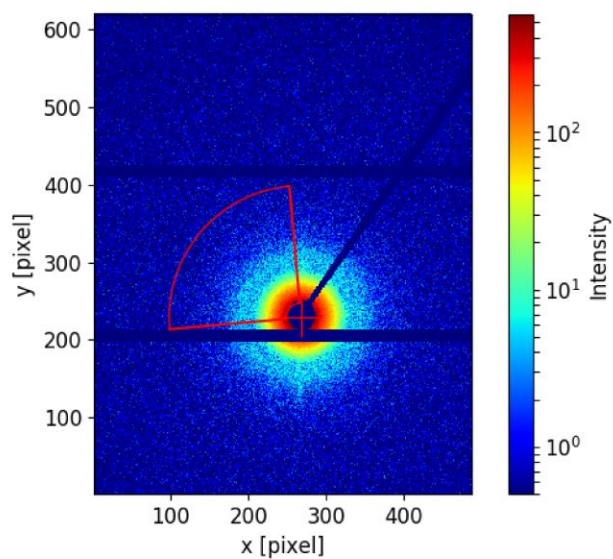


Figure S 3 Full scattering pattern on the detector with the integration sector used in DPDAK for the data processing. The mask allowing for the compensation of blank pixels, the beam stop and the residual direct beam scattering was applied.

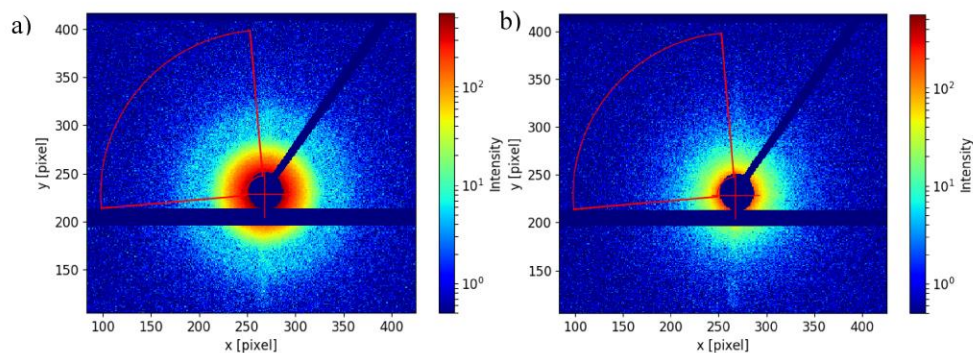


Figure S 4 Two-dimensional diffraction images from the SAXS detector sampled at the axial distance of $x = 2.2$ mm (flow of Ar – 18 sccm; pressure - 133 Pa) and at the radial distance of $y = 0.0$ mm: a) during the NP production when the discharge is on; b) background signal obtained when the discharge is off.

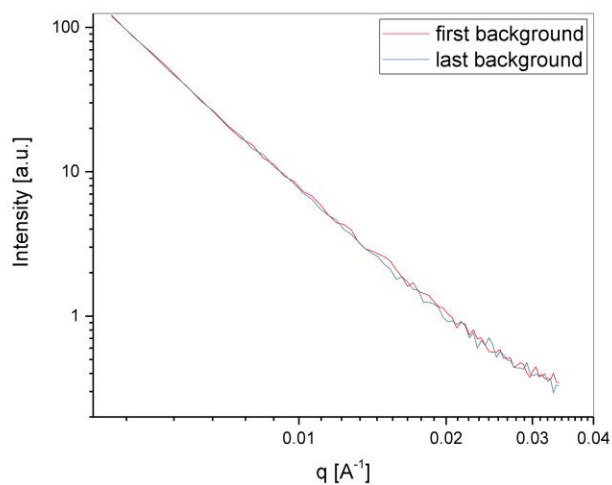


Figure S 5 The first and last background signal (in terms of integrated scattered intensity I vs. scattering wave vector q , see below) acquired before and after the SAXS measurement at the same spatial position with the axial distance of $x = 2.2$ mm and with the radial distance of $y = 0.0$ mm.

The calibration of raw data, their reduction and integration was performed using the software DPDAK, a customizable code for the analysis of large SAXS data. For each of the spatial position (x, y) , the data diffraction images and background images were integrated within the range of $q = 0.00414 - 0.03398 \text{ \AA}^{-1}$, where $q = 4\pi \sin(\theta)/\lambda$ is the magnitude of the scattering vector, θ is the scattering angle and λ is the wavelength of the X-rays. After that the background was subtracted from data sequence. Thus, the integrated scattered intensity I vs. scattering wave vector q curves were obtained. The examples of the curves for the data, for the background and for the difference between them are shown in Figure S 6.

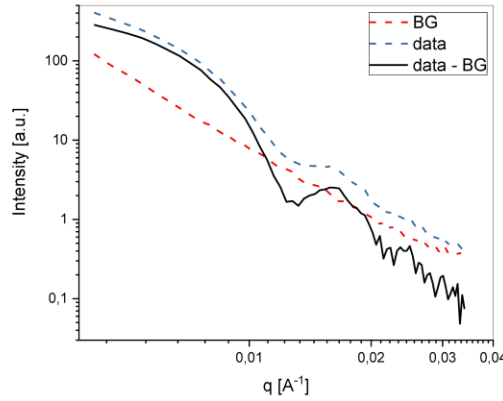


Figure S 6 Integrated scattered intensity I as a function of scattering wave vector q at $x = 2.2$ mm and $y = 0.0$ mm: a) examples obtained from one data and background (BG) acquisition when the discharge is on and off, respectively, and the difference between the two.

3.2. Fitting of the scattering curves

The scattering curves for each of the axial positions were fitted in the IRENA software using a Modelling tool.³ This tool allows the calculation the intensity of small-angle scattering from particles in multiple populations of scatterer:

$$I(q) = \sum_k |\Delta\rho_k|^2 S_k(q) \sum_{ik} |F_k(q, D_{ik})|^2 V_k(D_{ik}) f_k(D_{ik}) \Delta D_{ik} ,$$

The subscript i includes all bins in the size distribution and ΔD_i is the width of bin i . Subscript k represents different populations; each population has its own binning index ik . D is the dimension of particle (in our case radius); $|\Delta\rho_k|^2$ is scattering contrast; $S_k(q)$ denotes the structure factor, $F_k(q, D_{ik})$ the form factor, $V_k(D_{ik})$ the particle volume, and $f_k(D_{ik})$ the volume size distribution. The scattering contrast was calculated as difference between

scattering length density of the bulk silver and argon medium at pressure 133 Pa. Taking into account relatively low concentration of the nanoparticles inside GAS, the structure factor was not included into the calculation. The form factor of the full sphere was implemented as follow:

$$F(q, r)^2/V = \left[3 \frac{\sin(qr) - qr \cos(qr)}{(qr)^3} \right]^2$$

Fourier transformation of a full sphere in polar coordinates yields:

$$F(\vec{q}) = \iiint_{000}^{R \ 2\pi \ \pi} \rho_0 e^{-i\vec{q}\vec{r}} r^2 \sin(\theta) d\theta d\varphi dr = 4\pi R^3 \rho_0 \frac{(\sin(qR) - qR \cos(qR))}{(qR)^3}$$

To obtain the average size and standard deviation of NPs the lognormal size distribution was adopted:

$$\psi_{j,j=1..4}(D) = \frac{\phi_{jtotal}}{\left\{ 2\pi \left(\frac{D_{jmed} - D_{jmin}}{D_{jmode} - D_{jmin}} \right) \right\}^{0.5}} \left(\frac{1}{D - D_{jmin}} \right) \exp \left\{ \frac{- \left[\ln \left(\frac{D - D_{jmin}}{D_{jmed} - D_{jmin}} \right) \right]^2}{2 \ln \left(\frac{D_{jmed} - D_{jmin}}{D_{jmode} - D_{jmin}} \right)} \right\}$$

Figure S 7 shows the examples of the scattering curves fitted with the monomodal NP size distribution at the time of 8.4 and 9.0 s.

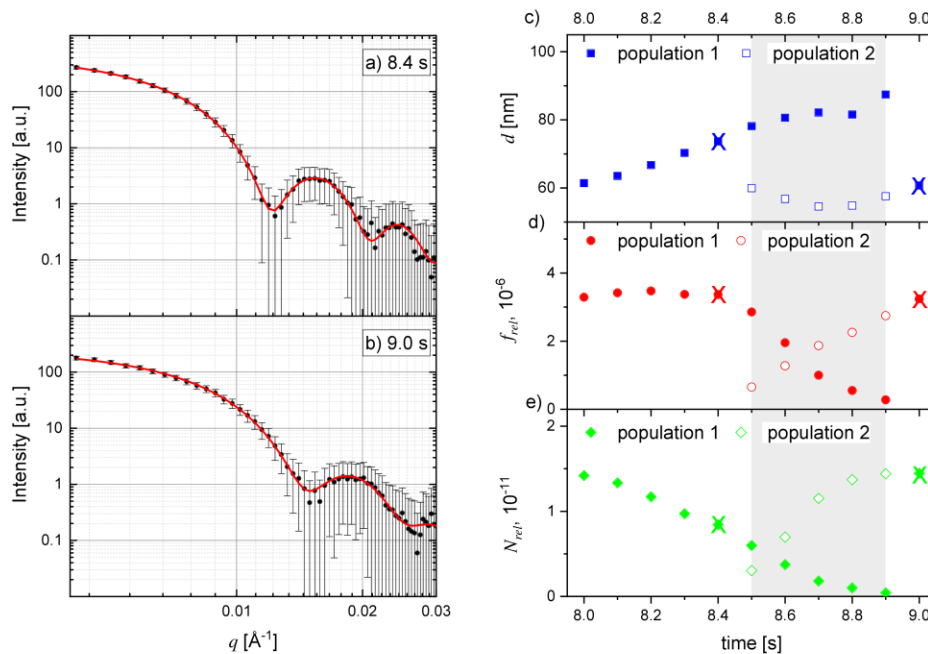


Figure S 7 Examples of the time-resolved X-ray scattering curves (background subtracted) acquired during the oscillation period at $x = 2.2$ mm and fitted with the monomodal NP size distribution: a) $t = 8.4$ s; b) $t = 9.0$ s. The dots correspond to the experimental data; the colored curves correspond to the model fit. The NP parameters obtained from the fits are shown by X for: c) the mean NP diameter d ; d) the relative volume fraction f_{rel} and e) the relative number N_{rel} .

At the intermediate values of time, however, it was not possible to obtain a satisfactory fit with the monomodal size distribution. Compare the scattering curves within the interval of 8.5 s $< t < 9.0$ s (Figure S 8). The monomodal fits deviate significantly from the experimental data whereas the introduction of the bimodal size distribution overcomes the problem.

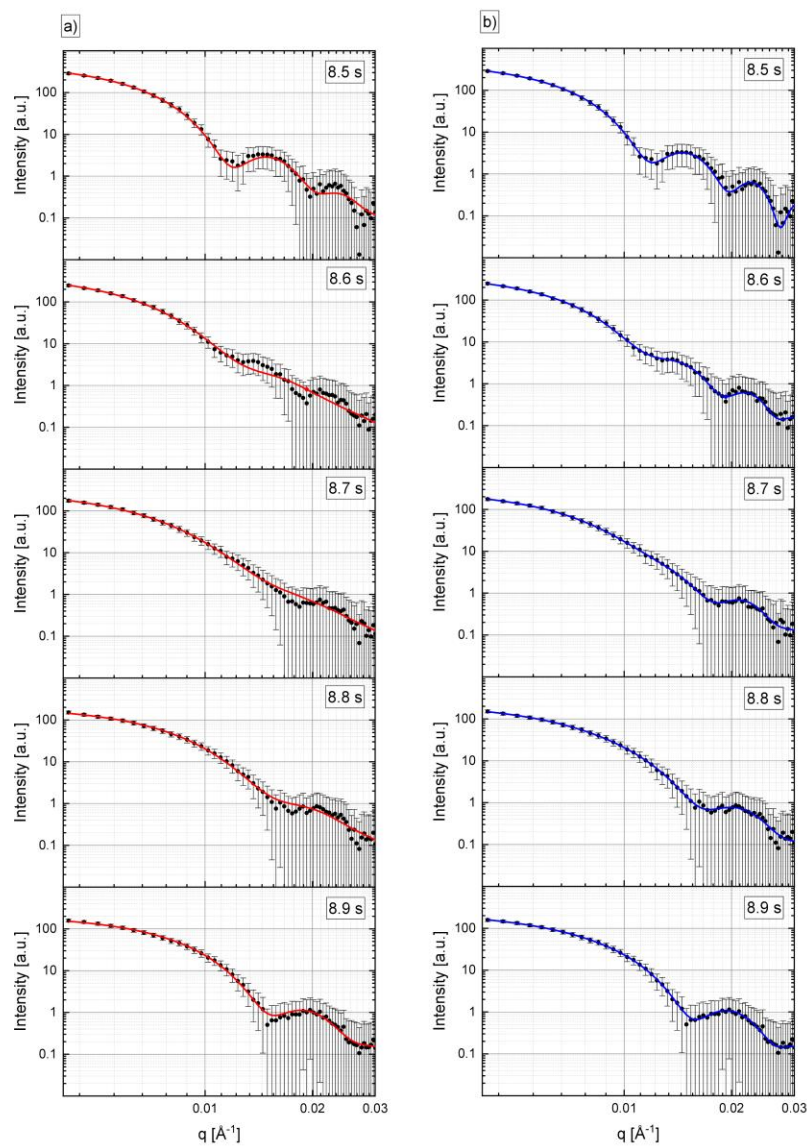


Figure S 8. Examples of the time-resolved X-ray scattering curves (background subtracted) acquired during the oscillation period at $x = 2.2$ mm and fitted with a) the monomodal NP size distribution; b) the bimodal size distribution. The dots correspond to the experimental data; the colored curves correspond to the model fit. The monomodal size distribution does not provide the satisfactory fitting in the high- q region whereas the bimodal size distribution does.

For the quantitative decision on when the scattering data must be fitted with the monomodal or bimodal NP size distribution, the normalized residuals were taken into account. If the difference between the maximum and minimal normalized residuals value exceeds 1.5, the fitting model was changed from the monomodal to the bimodal NP size distribution. Figure S 9 shows the difference between the maximum and minimal value of the normalized residuals above 1.5 for 8.5 s and the monomodal size distribution. This is the reason why the model was changed to bimodal distribution exactly at this time. The normalized residuals for the bimodal distribution shows already that the fit is more precisely, but it can be seen also in Figure S 9 directly.

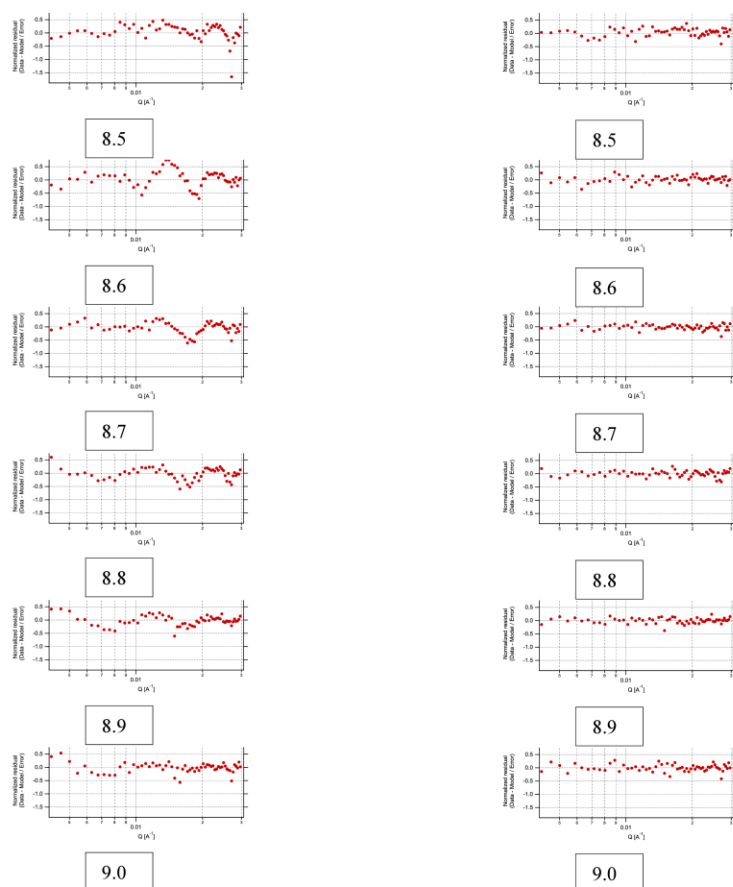


Figure S 9. The normalized residuals for all fits with the monomodal NP size distribution (left) and the bimodal size distribution (right) for the time interval from 8.5 s to 9.0 s.

To decide when the model has to be changed again to the monomodal distribution is more complex. The residuals plot for 8.6 s shows that the monomodal distribution difference is below our threshold value of 1.5 but the fit with a bimodal distribution is still much better. That is why also a different parameter is needed to decide if the monomodal or bimodal distribution is better. The decision to change back to the monomodal distribution was therefore done from the physical point of view. That means as long as the overall time dependence of the mean diameter and the relative volume fraction of both distributions make physically sense, the data is fitted bimodal. At 9 s the data was fitted again monomodal because on one hand the fit quality of monomodal and bimodal distribution do not differ much, which follows also out of the residual plots, and on the other hand the relative volume fraction of population 1 has vanished nearly like shown in Figure S 7.

Based on the results of the fitting, an animation was prepared showing the evolution of the NP size distribution with time (see the animation in a separate video file).

4. Computational Fluid Dynamics

The aggregation chamber with 100 mm inner diameter, filled with argon under the pressure of 133 Pa and temperature of 20 °C is characterized by the Knudsen number $K_n = 0.0005$, which allows to assume the fluid (gas) flow as a continuum. Hence, fundamental laws of mechanics can be used including conservation of mass, conservation of linear and angular momenta, and conservation of energy.

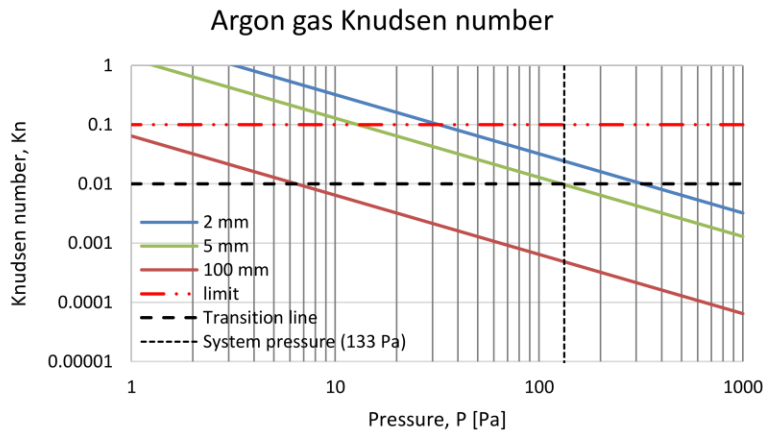


Figure S 10 Dependence of the Knudsen number on Ar pressure for $T = 20\text{ °C}$, the inner diameter of the chamber is 100 mm, the gap between the magnetron housing and the chamber wall is 5 mm, the diameter of the exit orifice is 2 mm. The fluid can be considered as a continuum at $K_n < 0.01$.

The fluid flow analysis inside the aggregation chamber was performed using the CFD software (Siemens STAR CCM+ 13.04.010 or Ricardo Vectis 2018.1). The following assumptions were made:

- The fluid was assumed to be an ideal and incompressible gas;
- No other species except for argon are present in the model;
- No slip on the chamber walls was expected, except for the magnetron housing, walls and at the exit orifice, where a Maxwell partial slip model was used;
- The flow was assumed to be laminar;
- No electromagnetic model was used.

Referring to the mentioned assumptions, it was decided to use the steady state analysis, employing a segregated flow solver with the 2nd order convection. A SIMPLE (Semi-Implicit Method for Pressure Linked Equations) pressure-velocity coupling algorithm was used. The boundary conditions included the system pressure of 133 Pa, the inlet Ar flow of 18 sccm and the Ar temperature of 20 °C. Figure S 11 shows how the model converged with the number of iterations and Figure S 12 shows the map of the gas velocity vectors inside the GAS.

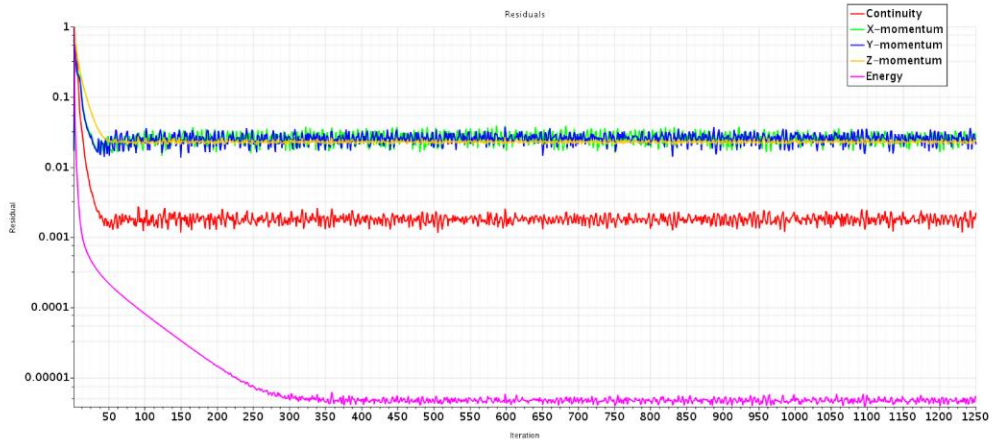


Figure S 11 Convergence of the model of the gas flow.

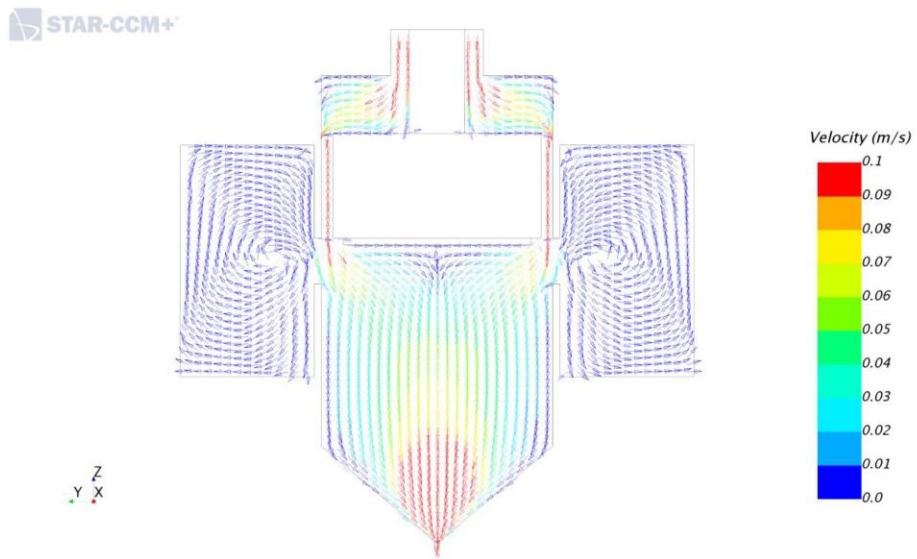


Figure S 12 Simulations of the Ar flow in the GAS. The directions of the gas velocity vectors are shown by arrows, the magnitude is colored in accordance with the shown colour bar.

5. Langmuir probe measurements

Our earlier Langmuir probe measurements unveiled that the electric field has an inhomogeneous profile above the magnetron target.⁴ At the axial distance far beyond the sheath, the plasma potential was characterized by a strong radial gradient, and the electric field of hundreds of V/cm was directed from the center towards the plasma ring (Figure S 13). The potential gradient in the axial direction was found to be much smaller; the electric field ranged from units to tens of V/cm here. Although a distance of several mm from the magnetron target was not assessed in those measurements, we believe that the difference between the radial and axial electric field is even larger in the capture zone and that the distribution of the plasma potential is qualitatively the same for the synthesis of Ag NPs presented in this work.

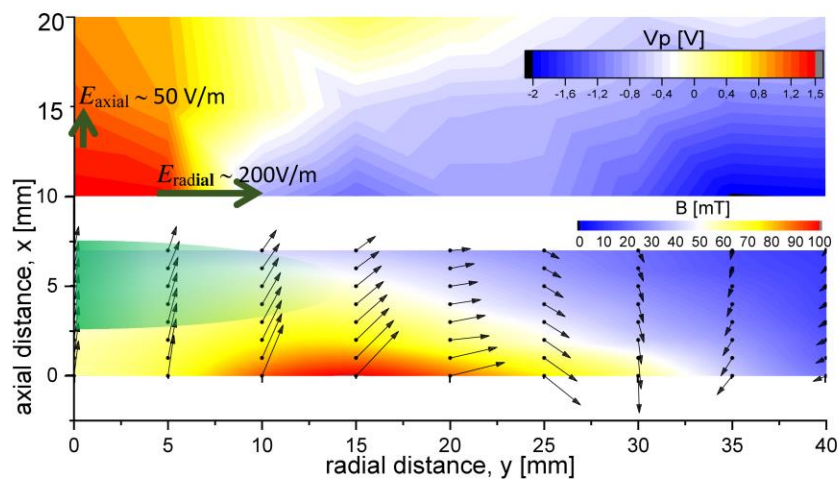


Figure S 13 Map of plasma potential (V_p) in the vicinity of the magnetron target as measured by Langmuir probes (adopted from⁴). Vectors of the electric field are shown in the direction parallel (E_{radial}) and normal (E_{axial}) to the target plane. Green semitransparent area shows approximate location of the trapped cloud of NPs.

References

- 1 A. Buffet, A. Rothkirch, R. Döhrmann, V. Körstgens, M. M. Abul Kashem, J. Perlich, G. Herzog, M. Schwartzkopf, R. Gehrke, P. Müller-Buschbaum and S. V. Roth, *J. Synchrotron Radiat.*, 2012, **19**, 647–653.

- 2 G. Benecke, W. Wagermaier, C. Li, M. Schwartzkopf, G. Flucke, R. Hoerth, I. Zizak, M. Burghammer, E. Metwalli, P. Müller-Buschbaum, M. Trebbin, S. Förster, O. Paris, S. V. Roth and P. Fratzl, *J. Appl. Crystallogr.*, 2014, **47**, 1797–1803.
- 3 J. Ilavsky and P. R. Jemian, *J. Appl. Crystallogr.*, 2009, **42**, 347–353.
- 4 J. Kousal, A. Kolpaková, A. Shelemin, P. Kudrna, M. Tichý, O. Kylián, J. Hanuš, A. Choukourov and H. Biederman, *Plasma Sources Sci. Technol.*, 2017, **26**, 105003.

3.3 Publication B: The Evolution of Ag Nanoparticles Inside a Gas Aggregation Source

In this publication, in-situ UV-Vis spectroscopy was used to investigate the growth and transport of Ag NPs inside the HGAS. The method utilized the plasmon resonance of Ag NPs to determine at which position in the HGAS the maximum absorption due to NPs could be found.

In the publications it was found that NPs are captured or trapped close to the magnetron, which is in good agreement with the findings from Publication A. Additionally, Si substrates pointing into the direction to the magnetron and also pointing into the direction of the orifice were placed in the central region of the HGAS along the way from the magnetron to the orifice. By SEM investigations of the substrates, it was found that big NPs with sizes of up to 100 nm were present close to the target and their amount decreases with increasing distance to the magnetron. These particles may grow in the capture zone from where they get either deposited onto the target or get lost on their way to the orifice to the side walls of the chamber. Surprisingly, NPs were also found on the substrates pointing into the direction of the orifice. Therefore, CFD simulations were performed to see if the samples affect the gas flow in a way that the NPs are pushed onto the substrates. That was not the case and indicates that an additional force must be acting on the NPs. Furthermore, it was found that the trapped particles must be hold in the trapping zone because of electromagnetic forces originating from the plasma discharge.

The results from this publication have shown that UV-Vis spectroscopy is a suitable diagnostic method to monitor the processes inside the HGAS as well.




Own contributions to the work are partially the conductance of the experimental work, data processing, evaluation and interpretation.

This chapter is a reprint from the following publication:

Nikitin, D., Hanuš, J., Ali-Ogly, S., Polonskyi, O., **Drewes, J.**, Faupel, F., Biederman, H., & Choukourov, A. (2019). The evolution of Ag nanoparticles inside a gas aggregation cluster source. *Plasma Processes and Polymers*, 16(10), 1–7. <https://doi.org/10.1002/ppap.201900079>

FULL PAPER

The evolution of Ag nanoparticles inside a gas aggregation cluster source

Daniil Nikitin^{1,2}  | Jan Hanuš¹  | Suren Ali-Ogly¹ | Oleksandr Polonskyi³ | Jonas Drewes³ | Franz Faupel³ | Hynek Biederman¹ | Andrei Choukourov¹ 

¹Department of Macromolecular Physics, Faculty of Mathematics and Physics, Charles University, Prague, Czech Republic

²Laboratory of Chemistry of Carbohydrate Coordination Compounds and Supermolecular Systems, G. A. Krestov Institute of Solution Chemistry of the Russian Academy of Sciences, Ivanovo, Russia

³Faculty of Engineering, Chair for Multicomponent Materials, Kiel University, Kiel, Germany

Correspondence

Daniil Nikitin, Department of Macromolecular Physics, Faculty of Mathematics and Physics, Charles University, V Holešovičkách 2, 18000 Prague, Czech Republic.
Email: daniilnikitin92@gmail.com

Funding information

Grantová Agentura České Republiky, Grant/Award Number: GACR 17-22016S; Univerzita Karlova, Grant/Award Number: SVV 260 444/2019; Grantová Agentura, Univerzita Karlova, Grant/Award Number: 1186217

Abstract

In-situ UV–Vis spectroscopy was used for investigating the evolution of silver nanoparticles (NPs) inside the gas aggregation cluster source (GAS). The light beam probed the interior of the GAS at different distances from the magnetron. Plasmon resonance was detected at 365 nm, with the highest intensity found close to the magnetron due to the NP trapping. Time-resolved measurements revealed that after the discharge switch off the majority of trapped NPs fly out of the GAS. Part of them is redeposited onto the center of the target due to the electrostatic force. NPs collected at the distance of 20 mm and further from the magnetron demonstrate gradual decrease of the size, pointing to the loss of bigger NPs on the walls.

KEYWORDS

gas aggregation cluster source, growth, nucleation, particles, UV–Vis spectroscopy

1 | INTRODUCTION

Metal nanoparticles (NPs) can be synthesized using various approaches that spread from wet chemistry to vacuum techniques, the latter including low- or high-pressure processes. Gas condensation (aggregation) may be advantageous because vapors of virtually any metal can be supplied into the gas phase either by simple vacuum evaporation or by magnetron sputtering. If cold inert gas is introduced into a zone with atomized metal, spontaneous condensation of atomic metal vapors can be achieved with the formation of NPs. Haberland was first to place planar magnetron into a

gas aggregation chamber working at a pressure range from 10 to 100 Pa. This equipment became popular as a gas aggregation cluster source (GAS).^[1,2] Afterwards, GASes were successfully applied for the production of semiconductor, insulator, and plasma polymer NPs.^[3–6] The application of two or even three magnetrons in the same aggregation chamber^[7,8] enabled the production of heterogeneous NPs. In spite of the huge number of studies that dealt with the gas phase preparation of metal NPs and their applications,^[9–16] little concern has been raised with regard to the processes occurring inside the aggregation chamber. A number of works dealing with modeling of the NP

trajectories have been performed,^[17,18] although the experimental approaches are scarce. Only recently, our group has managed to utilize Langmuir probe^[19] and in situ synchrotron small angle X-ray scattering^[20] measurements for monitoring the nucleation and growth of NPs within the aggregation zone. In case of plasmonic NPs, a much simpler and readily available technique UV-Vis spectroscopy may be used for the in-flight diagnostics.^[21] This became a great advantage in the work presented below as this technique could have been applied along with direct observations of NPs collected in different positions inside the aggregation zone of the GAS. In other words, the goal of the presented work has been to unveil the mechanisms of the NPs travel and loss inside the aggregation chamber using UV-Vis spectroscopy and then directly show by the scanning electron microscopy (SEM) the evolution of NPs from the magnetron target on the way to the exit orifice and beyond it.

2 | EXPERIMENTAL SECTION

The experiments were performed in an ultra-high vacuum system pumped by scroll and turbomolecular pumps to the base pressure of 4×10^{-5} Pa. The main deposition chamber was equipped with a GAS of the Haberland type which was mounted in the vertical configuration (Figure 1). The GAS consisted of a water-cooled aggregation chamber 100 mm in diameter and 220 mm long with two quartz windows, a glass window for the discharge observation and a port for the sample-holder. Sputtering of a 3-mm thick Ag target (99.99% purity) was realized by a movable 3-inch magnetron. The magnetron was powered by a direct current generator MDX-500 (Advanced Energy, Fort Collins, CO). The discharge current of 500 mA was kept constant during all experiments. The aggregation chamber was ended by a conical lid with an orifice 1.9 mm in diameter. The aggregation length (the distance between the magnetron target and the orifice) could be varied by the movement of the magnetron. The flow and pressure of Ar were kept at 18 sccm and 126 Pa. Quartz crystal microbalance (QCM, Inficon, Bad Ragaz, Switzerland) was used to control the deposition rate in the main chamber.

Figure 1 also shows schematically the passage of the UV-Vis light for the in situ spectroscopy characterization of Ag NPs in the aggregation zone. The measurements were performed using an Ocean Optics STS Microspectrometer with operating wavelength range of 190–600 nm in a complex with a light source Ocean Optics DH2000 BAL (Ocean Optics, Inc., Ostfildern, Germany). Fiber optic cables from the light source and spectrometer were mounted onto quartz windows. A special optical system

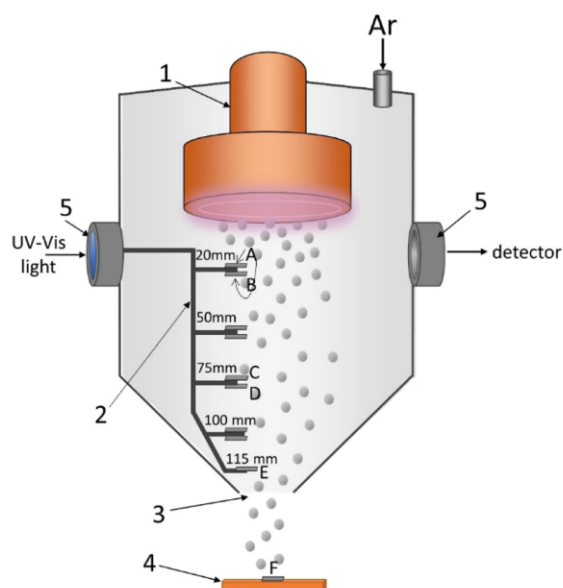


FIGURE 1 The GAS configuration used for the deposition of Ag NPs on the substrates inside (a–e) and outside (f) of the aggregation zone: 1 - height adjustable magnetron with Ag target; 2 - sample holder; 3 - orifice; 4 - sample holder behind the orifice; and 5 - quartz window for UV-Vis light measurements. GAS, gas aggregation cluster source; NPs, nanoparticles

was used to produce the parallel light beam with a diameter of 1 cm. The background was collected without plasma. The UV-Vis spectra were recorded with an integration time of 10 ms.

A special construction of the sample-holder was designed for the analysis of Ag NPs. Silicon substrates were fixed onto thin stainless steel wires positioned at different distances from the target below the erosion track of the magnetron. The substrates were precleaned using acetone and isopropanol. The NPs were also collected onto the substrates positioned outside the GAS at the distance of 20 cm behind the orifice. The deposition time was 10 s. The morphology and size of Ag NPs were determined using SEM (Supra55VP-Carl Zeiss, Oberkochen, Germany). The data for a minimum of 150 NPs were taken into account for each sample. A gas flow modeling inside the aggregation chamber was performed using a Computational Fluid Dynamics (CFD) software (Siemens STAR CCM + 13.04.010). The input parameters were similar to the experimental ones.

3 | RESULTS AND DISCUSSION

The UV-Vis spectrum was acquired when the discharge was off and it is shown as the background leveled at 100% of transmittance (Figure 2). A distinct absorption band

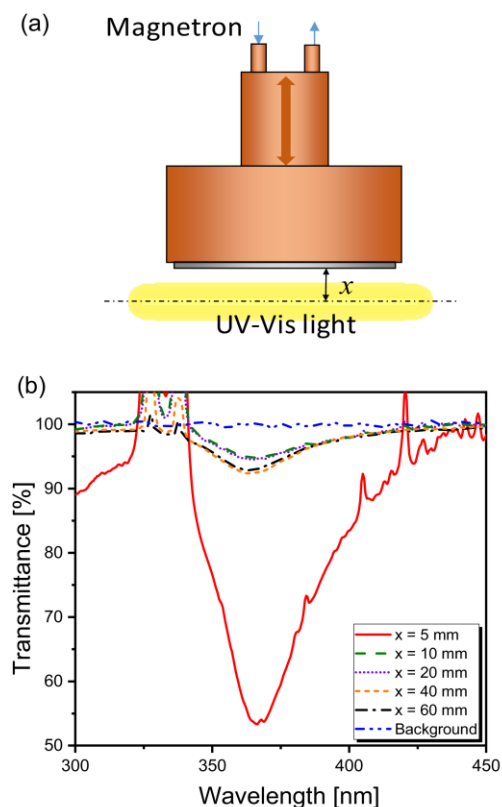


FIGURE 2 (a) Scheme of the light beam probing the space in the vicinity of the magnetron; (b) UV-Vis spectra measured at different distances from the target. The distance is taken from the light beam axis to the target plane

appears in the spectrum when the discharge is turned on. The position of this band at $\lambda = 365$ nm fits with the position of localized surface plasmon resonance (LSPR) of Ag NPs.^[22] The strongest LSPR is observed in the closest position of 5 mm between the light beam axis and the target plane (here, the light beam with a diameter of 10 mm is just about to touch the target by its lateral side, see also Figure 2). Even a small shift of the magnetron to the position of 10 mm leads to a significant decrease, yet to a detectable level, of the absorption intensity which remains approximately constant at farther distances from the magnetron. The results indicate that the concentration of Ag NPs does not change significantly along the GAS, except for the region nearest to the magnetron target where the amount of NPs is substantially higher. This finding agrees with a concept of the so-called “capture zone” that exists at the several mm distance from the target and where NPs become “trapped,” as discovered by our recent in situ SAXS measurements on Cu NPs.^[20]

Further evidence about the existence of the capture zone can be obtained from the time-resolved UV-Vis measurements performed after switching off the discharge. In this experiment, the magnetron was positioned at 20 mm from the light beam axis, leaving a 15 mm gap between the target plane and the lateral side of the light beam. The discharge was turned on and the acquisition of the spectra was started with periodicity of 0.1 s and the acquisition time of 100 ms. After the stabilization of the parameters, the discharge was turned off but the acquisition of the spectra proceeded. Figure 3 shows the spectrum acquired just before and after the discharge was turned off. The plasma-on spectrum is distinct from

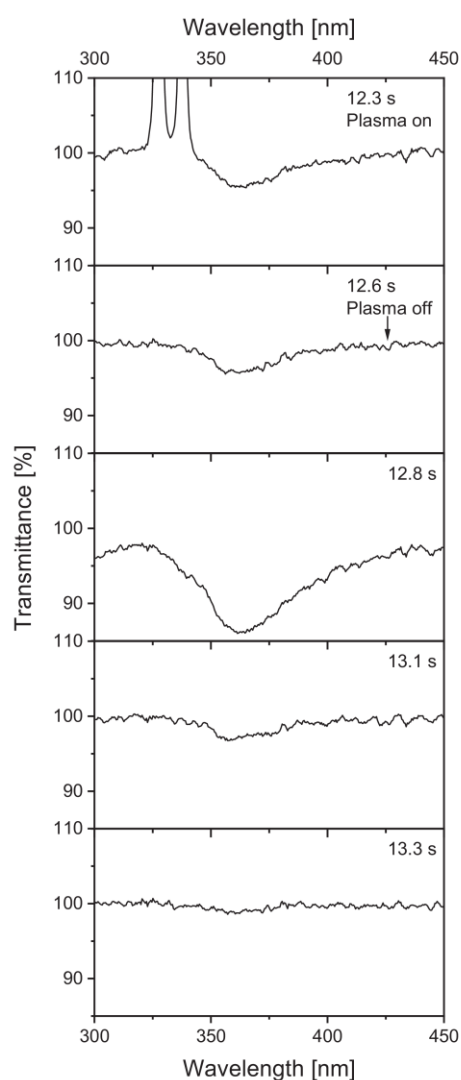


FIGURE 3 Optical transmission spectra acquired at $x = 15$ mm when the discharge is on (time 12.3 s) and after turning off the discharge (time > 12.3 s)

the other spectra by the presence of Ag atomic emission lines. After the extinction of the discharge, the Ag lines immediately disappear but the LSPR band demonstrates a noteworthy evolution. Not only does it remain detectable but also it even increases in intensity for about 0.5 s, abruptly disappearing afterwards.

The phenomenon can also be related to the existence of high amounts of NPs trapped in the capture zone which exists at the distance < 15 mm from the magnetron target. The trapped Ag NPs become released after the extinction of the discharge and start traveling with the gas flow along the aggregation chamber to the exit orifice. Under the chosen Ar flow rate, a fraction of a second is required for the gas to bring the cloud of the NPs from the capture zone to the light beam axis and this agrees with the 0.5 s time lag at which the intensification of the LSPR band was observed. At later time, the NP cloud leaves the space probed by the light beam and travels towards the orifice. This leads to a decrease of the LSPR band intensity to the background level.

After the target was sputtered for 20 hr in 100 deposition runs, we found a huge deposit in the target center which was in the form of a macroscopic hill of 800 μm height (Figure 4a). To analyze the structure of the deposit, we used a fresh Ag target and sputtered it only for 10 s. The SEM analysis was performed at the target center corresponding to point 1 (Figure 4b) and outside the erosion track corresponding to point 2 (Figure 4c). The central spot is characterized by the presence of agglomerates of NPs, with the mean size of individual NPs reaching 89 nm. Markedly, the 10 s sputtering is sufficiently long for the deposition of the amount of the NPs which exceeds the monolayer coverage in the central area. A smaller amount of NPs is detected outside the erosion track.

The observed effect of the backward deposition of the NPs onto the target surface is quite remarkable,

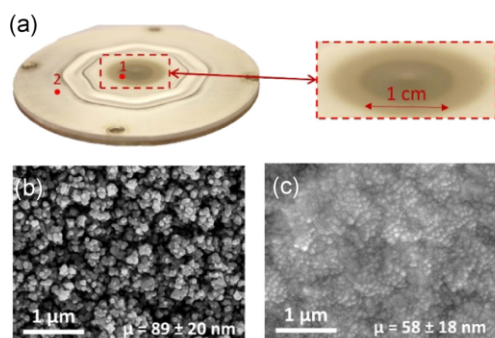


FIGURE 4 (a) Photos of Ag target after 20 hr of depositions; (b) SEM image of the fresh target after 10 s in operation measured in point 1 and (c) in point 2. SEM, scanning electron microscopy

especially taking into account that NPs have to overcome the neutral drag force (i.e., the force produced by momentum transfer from the neutral atoms of the flowing gas onto the NPs) and the gravity force to reach the target. For example, the simulations of the Ar flow (Figure 5a) indicate that the gas velocity vectors have a strong co-axial component directed downward to the exit orifice, except for the space closest to the target, where the radial component dominates and is directed from the target edges towards the center. In the region of interest (several mm from the target), the gas flow therefore tends to push the NPs radially from the periphery towards the center and then axially downward towards the orifice. This contributes to the localization of the NPs in the central part below the target. Nevertheless, there is no velocity component that would drag the NPs from the capture zone in the upward direction. It is known that NPs become electrically charged when formed in the plasma. Our earlier in situ SAXS measurements confirmed that charged Cu NPs can be held close to the magnetron by electrostatic interactions.^[20] These may force part of the NPs to travel against the gas flow and the gravity and reach the target. Therefore, we believe that electrostatic interactions are also responsible for the phenomena observed here for Ag NPs, although the detailed mechanisms are yet to be discovered.

Taking advantage of the GAS equipped with the side ports for diagnostics, we placed a special cascade substrate holder inside the aggregation zone. This enabled simultaneous collection of the NPs at 20, 50, 75, 100, and 115 mm distance from the target. The simulations of the gas flow confirmed that the gas velocity map changes in the proximity of the substrates but remains qualitatively similar close to the target (Figure 5b). Hence, we believe that the introduction of the substrates does not change significantly the phenomena related to sputtering itself as well as to nucleation and growth of the NPs.

The SEM images of the deposited samples are shown in Figure 6, where the NPs collected on the substrates facing the target (top – (a), (b), and (c)) are compared with those collected on the substrates facing the orifice (rear – (d) and (e)) as well as with those deposited outside the GAS (f). The reason for the observations from the rear side was to limit the deposition of Ag atoms and minimize the formation of nanoislands from them. Indeed, the sample deposited at the closest distance of 20 mm and facing the target is characterized by a complex structure. It consists of a discontinuous film (most probably grown as a result of atomic sputter-deposition) and individual spherical NPs incorporated into it. The rear side sample is characterized by the absence of the film and by the presence of the NPs of a spherical as well as an irregular shape. The formation of the

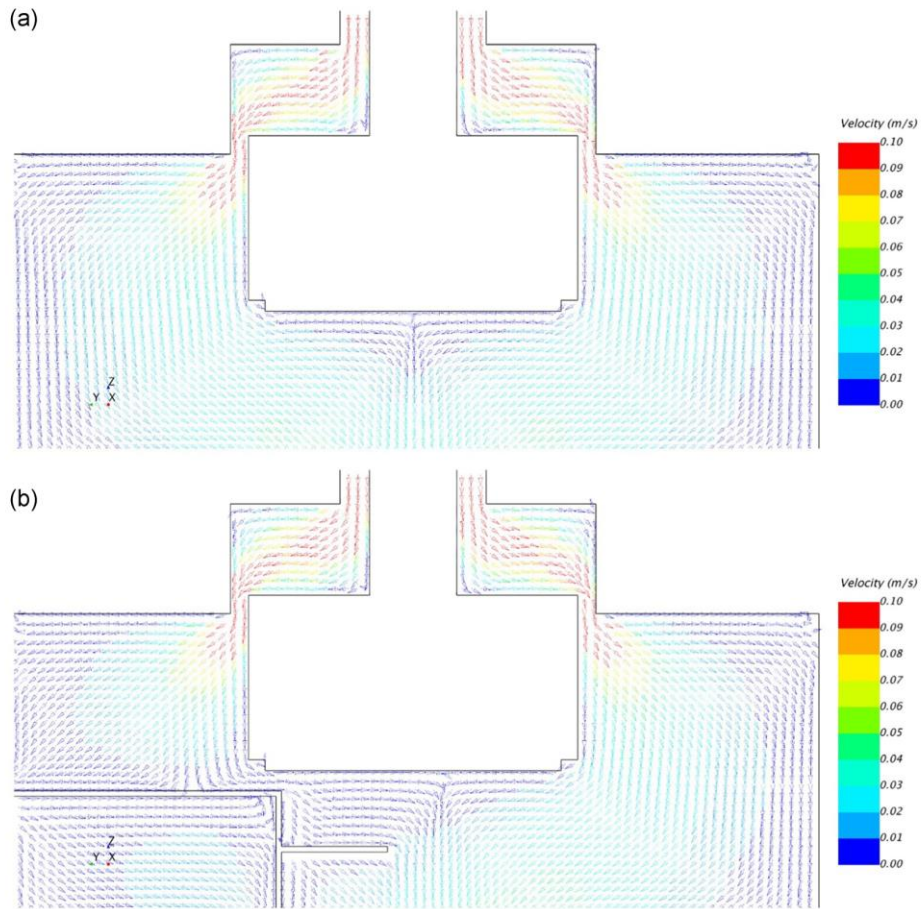


FIGURE 5 Simulation of the Ar flow in the vicinity of magnetron (a) without sample holder; (b) with sample holder inside

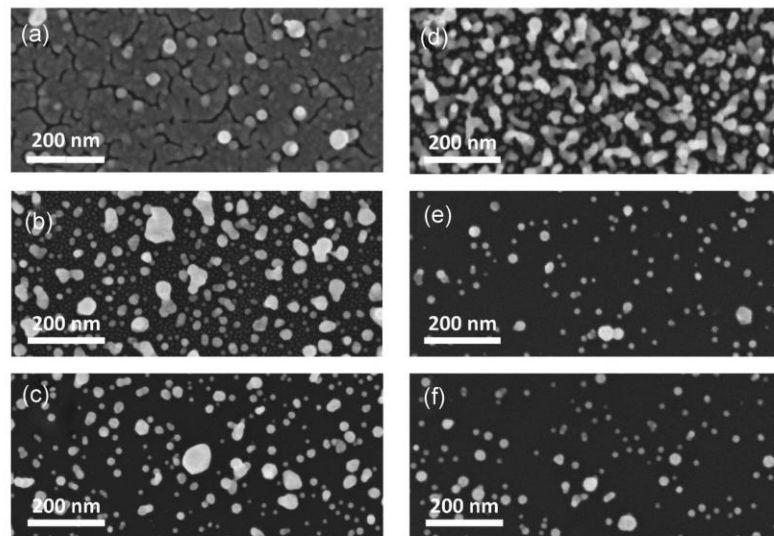


FIGURE 6 SEM images of Ag NPs deposited inside the GAS at different distances from the target ((a) and (d)–20 mm top and rear; (b) and (e)–75 mm top and rear; (c)–115 mm top; (f)–200 mm behind the orifice). The deposition time is 10 s. GAS, gas aggregation cluster source; NPs, nanoparticles

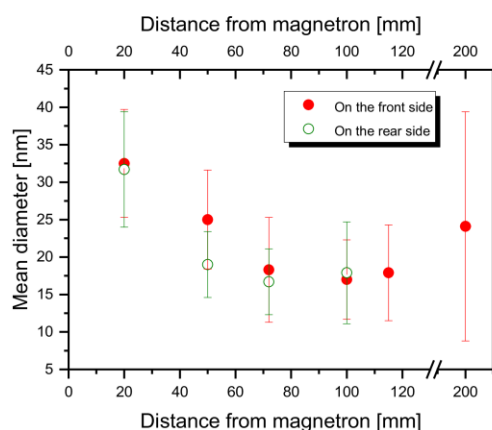


FIGURE 7 Dependence of the NP mean diameter on the distance from the magnetron for the front samples (facing the magnetron) and rear samples (facing the orifice). NP, nanoparticle

irregularly-shaped NPs is probably given by coalescence of smaller NPs which did not suffice to thermalize and remained at the temperature close to the melting point.

At farther distances, the formation of the film is not observed anymore for either of the samples, pointing to a decrease of the atomic metal flux to negligible values. Coalesced NPs can be occasionally observed; however, individual spherical NPs dominate in the samples. This finding agrees with an idea that NPs are born in a liquid state close to the magnetron target, but then undergo phase transition and thermalization via the collisions with atoms of the cold buffer gas.

The size distribution histograms were calculated and they show that the mean NP size decreases from 33 nm to 18 nm with the distance from the target (Figure 7). It should be noted that the NP size stops changing at distances closer to the exit orifice. The phenomenon supports the idea that part of the NPs grow in the capture zone to a larger size but become lost on the walls and on the target surface after reaching the critical size.^[20]

4 | CONCLUSION

LSPR of Ag NPs has been shown to serve as a useful phenomenon for in situ detection of plasmonic NPs during their nucleation, growth, and transport inside the gas aggregation cluster source. A relatively simple arrangement of UV-Vis spectroscopy allows for monitoring of the intensity of the LSPR band and plotting its spatial map in dependence on the position inside the aggregation chamber. It has been shown that a number of Ag NPs originate near the magnetron target and become captured in the central region at the distance of < 10 mm from the target plane.

The capturing leads to an increase of the mean NP size up to 100 nm. These NPs eventually become electrostatically expelled from the capture zone, being redeposited partially back onto the target surface. Another part of the NPs leave the capture zone in an outward direction and travel to the exit orifice with the gas flow. The larger NPs become continuously lost on their way from the magnetron to the exit orifice as witnessed by SEM on the sample deposits. This results in the shift of the size distribution histograms along the aggregation chamber with the mean size decreasing to 24 nm at remote distances. These NPs leave the cluster source and constitute the final deposit in the deposition chamber.

ACKNOWLEDGMENTS

The research was supported by the grant GACR 17-22016S from the Czech Science Foundation and by the Charles University, project GA UK No. 1186217. D.N. and S.A.-O. acknowledge the support from the student grant SVV 260 444/2019 of Univerzita Karlova.

ORCID

Daniil Nikitin <http://orcid.org/0000-0001-7293-0272>
 Jan Hanuš <http://orcid.org/0000-0002-5825-8536>
 Andrei Choukourov <http://orcid.org/0000-0002-0582-5453>

REFERENCES

- [1] H. Haberland, M. Karrais, M. Mall, *Zeitschrift fur Phys. D Atoms, Mol. Clust.* **1991**, 20, 413.
- [2] H. Haberland, M. Karrais, M. Mall, Y. Thurner, *J. Vac. Sci. Technol. A Vacuum, Surfaces, Film* **1992**, 10, 3266.
- [3] R. Rudd, A. Obrusnik, P. Zikán, R. Pratt, C. Hall, P. Murphy, D. Evans, E. Charrault, *Surf. Coatings Technol* **2017**, 314, 125.
- [4] A. Shelemin, O. Kylián, J. Hanus, A. Choukourov, I. Melnichuk, H. Biederman, A. Serov, D. Slavinska, *Vacuum* **2015**, 120, 162.
- [5] A. Choukourov, P. Pleskunov, D. Nikitin, V. Titov, A. Shelemin, M. Vaidulych, A. Kuzminova, P. Solař, J. Hanuš, J. Kousal, O. Kylián, D. Slavinská, H. Biederman, *Bellstein J. Nanotechnol* **2017**, 8, 2002.
- [6] P. Pleskunov, D. Nikitin, R. Tafichuk, A. Shelemin, J. Hanuš, I. Khalakhan, A. Choukourov, *J. Phys. Chem. B* **2018**, 122, 4187.
- [7] D. Llamasa, M. Ruano, L. Martínez, A. Mayoral, E. Roman, M. García-Hernández, Y. Huttel, *Nanoscale* **2014**, 6, 13483.
- [8] Y. Huttel, L. Martínez, A. Mayoral, I. Fernández, *MRS Commun* **2018**, 8, 947.
- [9] C. Binns, *Surf. Sci. Rep.* **2001**, 44.
- [10] I. Shyjumon, M. Gopinadhan, O. Ivanova, M. Quaas, H. Wulff, C. A. Helm, R. Hippler, *Eur. Phys. J. D* **2006**, 37, 409.
- [11] O. Kylián, V. Valeš, O. Polonskyi, J. Pešička, J. Čechvala, P. Solař, A. Choukourov, D. Slavinská, H. Biederman, *Mater. Lett.* **2012**, 79, 229.

- [12] Y. Yan, T. Santaniello, L. G. Bettini, C. Minnai, A. Bellacicca, R. Porotti, I. Denti, G. Faraone, M. Merlini, C. Lenardi, P. Milani, *Adv. Mater.* **2017**, *29*, 1606109.
- [13] J. Vernieres, S. Steinhauer, J. Zhao, A. Chapelle, P. Menini, N. Dufour, R. E. Diaz, K. Nordlund, F. Djurabekova, P. Grammatikopoulos, M. Sowwan, *Adv. Funct. Mater.* **2017**, *27*, 1605328.
- [14] T. Kretková, J. Hanuš, O. Kylián, P. Solař, M. Dopita, M. Cieslar, I. Khalakhan, A. Choukourov, H. Biederman, *J. Phys. D. Appl. Phys.* **2019**, *52*, 205302.
- [15] A. Choukourov, O. Kylián, M. Petr, M. Vaidulych, D. Nikitin, J. Hanuš, A. Artemenko, A. Shelemin, I. Gordeev, Z. Kolská, P. Solař, I. Khalakhan, A. Ryabov, J. Májek, D. Slavínská, H. Biederman, *Nanoscale* **2017**, *9*, 2616.
- [16] D. Nikitin, S. Madkour, P. Pleskunov, R. Tafichuk, A. Shelemin, J. Hanuš, I. Gordeev, E. Sysolyatina, A. Lavrikova, S. Ermolaeva, V. Titov, A. Schönhals, A. Choukourov, *Soft Matter* **2019**, *15*, 2884.
- [17] J. Kousal, O. Polonskyi, O. Kylián, A. Choukourov, A. Artemenko, J. Pešička, D. Slavínská, H. Biederman, *Vacuum* **2013**, *96*, 32.
- [18] L. Zhang, J. Shao, X. Chen, *Vacuum* **2016**, *128*, 137.
- [19] J. Kousal, A. Kolpáková, A. Shelemin, P. Kudrna, M. Tichý, O. Kylián, J. Hanuš, A. Choukourov, H. Biederman, *Plasma Sources Sci. Technol.* **2017**, *26*, 105003.
- [20] J. Kousal, A. Shelemin, M. Schwartzkopf, O. Polonskyi, J. Hanuš, P. Solař, M. Vaidulych, D. Nikitin, P. Pleskunov, Z. Krtouš, T. Strunskus, F. Faupel, S. V. Roth, H. Biederman, A. Choukourov, *Nanoscale* **2018**, *10*, 18275.
- [21] O. Polonskyi, J. W. Abraham, T. Strunskus, M. Bonitz, F. Faupel, *B. Ext. Abstr. ISPC* **2017**, *23*, 590.
- [22] J. Kratochvíl, A. Kuzminova, O. Kylián, H. Biederman, *Surf. Coatings Technol.* **2014**, *275*, 296.

SUPPORTING INFORMATION

Additional supporting information may be found online in the Supporting Information section.

How to cite this article: Nikitin D, Hanuš J, Ali-Ogly S, et al. The evolution of Ag nanoparticles inside a gas aggregation cluster source. *Plasma Process Polym.* 2019;e1900079.

<https://doi.org/10.1002/ppap.201900079>

Supporting Information

The evolution of Ag nanoparticles inside a gas aggregation cluster source

Daniil Nikitin*, Jan Hanuš, Suren Ali-Ogly, Oleksandr Polonskyi, Jonas Drewes, Franz Faupel, Hynek Biederman, Andrei Choukourov

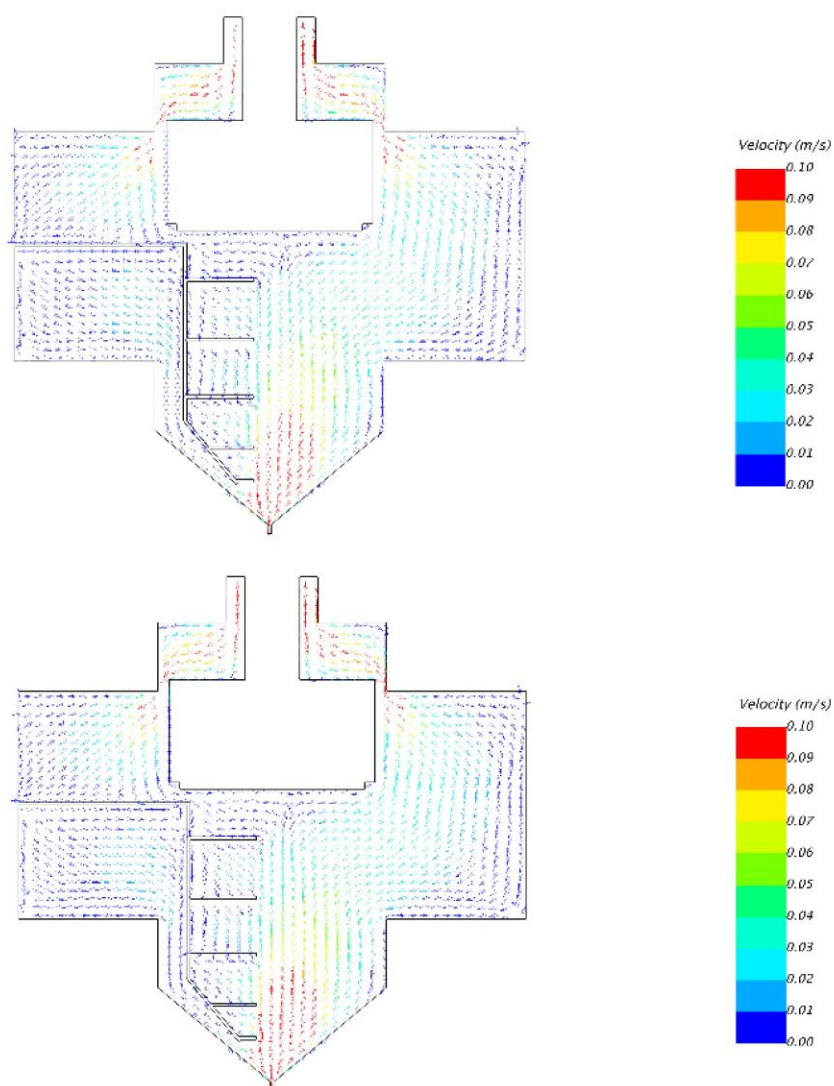


Figure S1. Simulation of the Ar flow within the GAS equipped with a cascade sample holder.

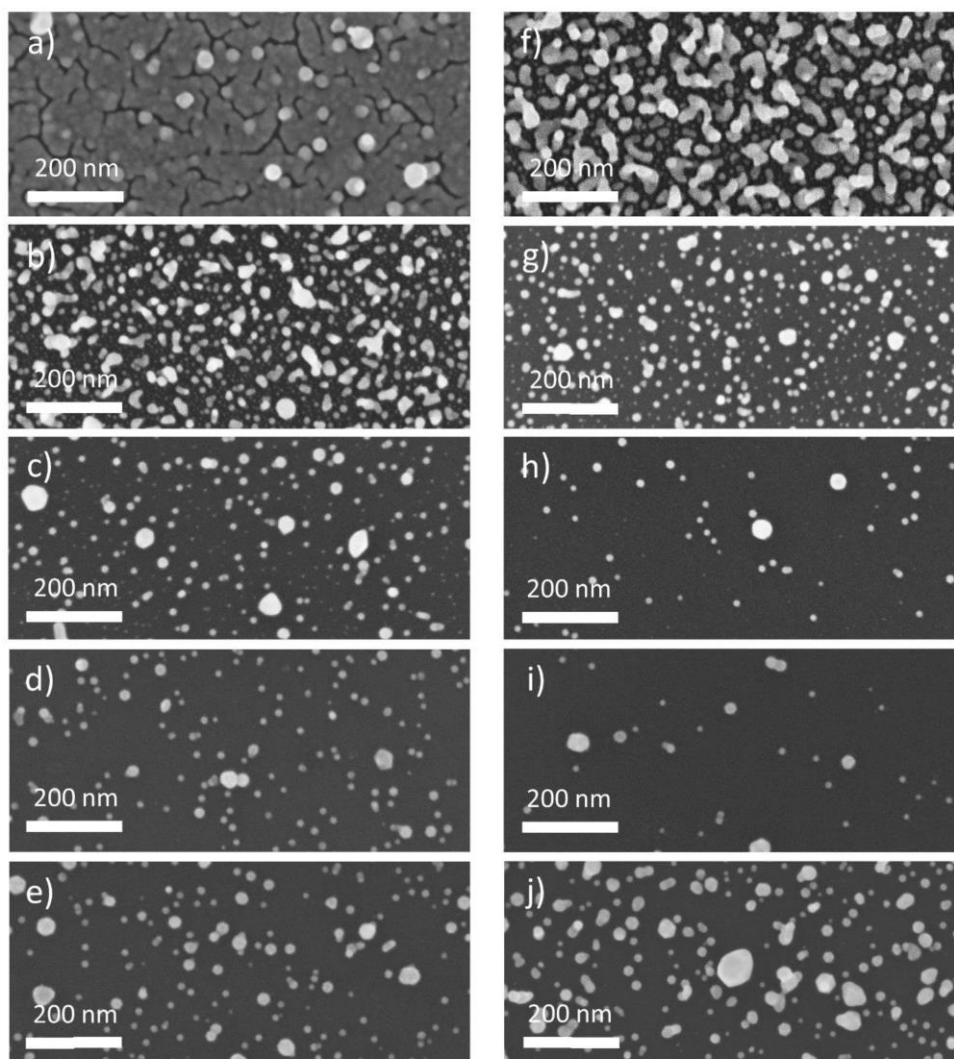


Figure S2. SEM images of Ag NPs measured at all positions: a, f – 20 mm top and rear; b, g – 50 mm top and rear; c, h – 75 mm top and rear; d, i – 100 mm top and rear; e – 115 mm top; j – 200 mm behind the orifice.

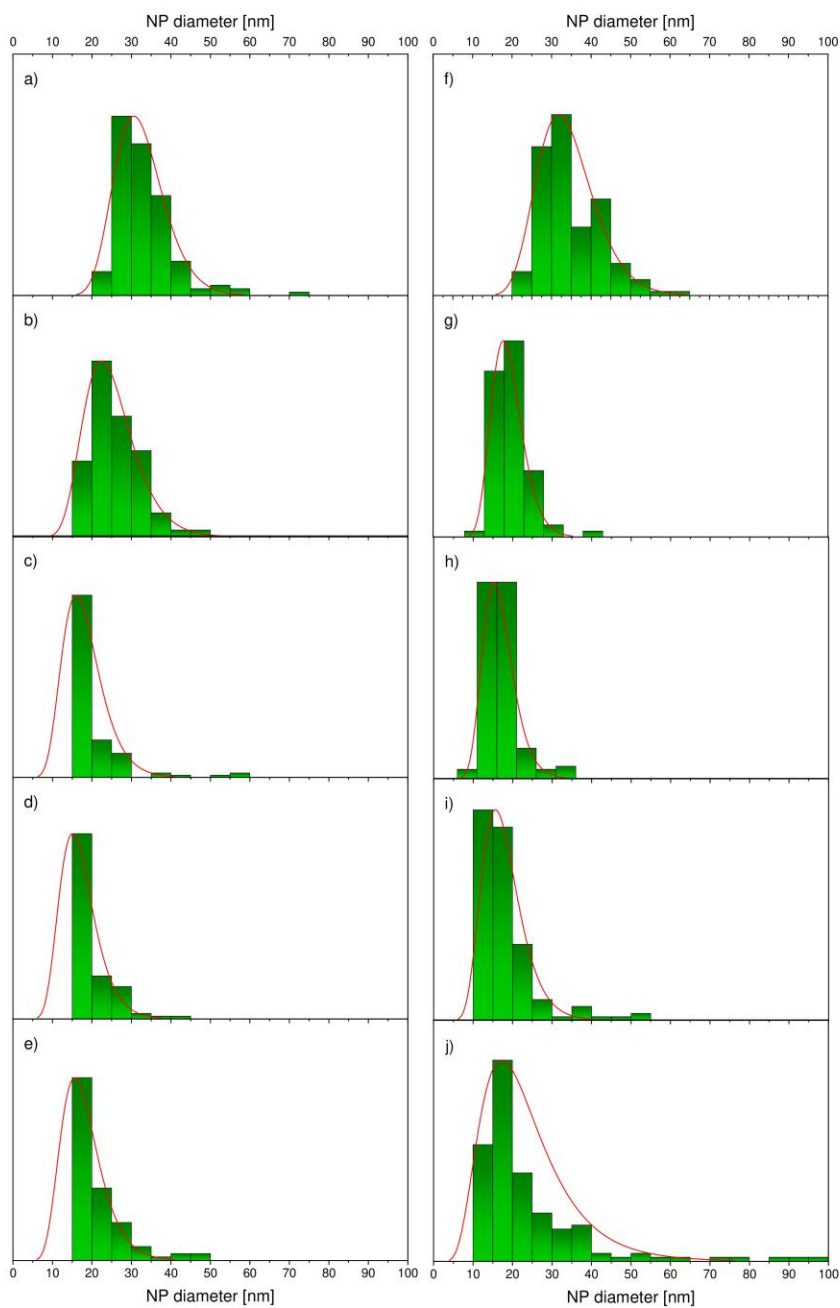


Figure S3. Size distributions corresponding to each position from Figure S2: a, f – 20 mm top and rear; b, g – 50 mm top and rear; c, h – 75 mm top and rear; d, i – 100 mm top and rear; e – 115 mm top; j – 200 mm behind the orifice.

3.4 Publication C: Impact of Argon Flow and Pressure on the Trapping Behavior of Nanoparticles Inside a Gas Aggregation Source

In this publication, the impact of the Ar flow and pressure on the trapping behavior was investigated with the help of UV-Vis spectroscopy, which was successfully used also for the investigations in the Publication B. Additionally, CFD simulations were used to relate the gas velocity distribution to the NP trapping behavior.

One of the first results of the publication is the time dependence of the plasmonic absorption of the NPs during the growth inside the HGAS. It was found by comparing the UV-Vis spectra to simulated extinction cross sections for different NP sizes that the NPs grow up to a diameter of ≈ 70 nm. Nevertheless, these NPs were not found on the samples placed outside the source. This has shown in accordance to the previous publications that NP trapping exists and that larger NPs are more likely trapped than smaller ones. Additionally, the trapping zone of NPs was shifted away from the magnetron and the NP density in the trapping zone was decreasing with increasing gas flow. For higher gas flows no trapping was observed with the UV-Vis spectroscopy. Furthermore, quartz crystal microbalance (QCM) measurements have shown higher deposition rates for higher gas flows. To understand the forces acting on the trapped NPs better, CFD simulations were performed to obtain the gas velocity distribution inside the source. The simulations have shown that regions are existing which show a gas velocity close to 0 m/s. These regions were termed loss regions. It was found that a loss region is present close to the target surface in the central region. This supports that a lot of redeposition takes place at this position. Another loss region is located around the main stream of the gas flow close to the outside walls. The loss regions do not change their location or size, when the gas flow was varied. Therefore, the loss regions can only be influenced by the HGAS geometry.

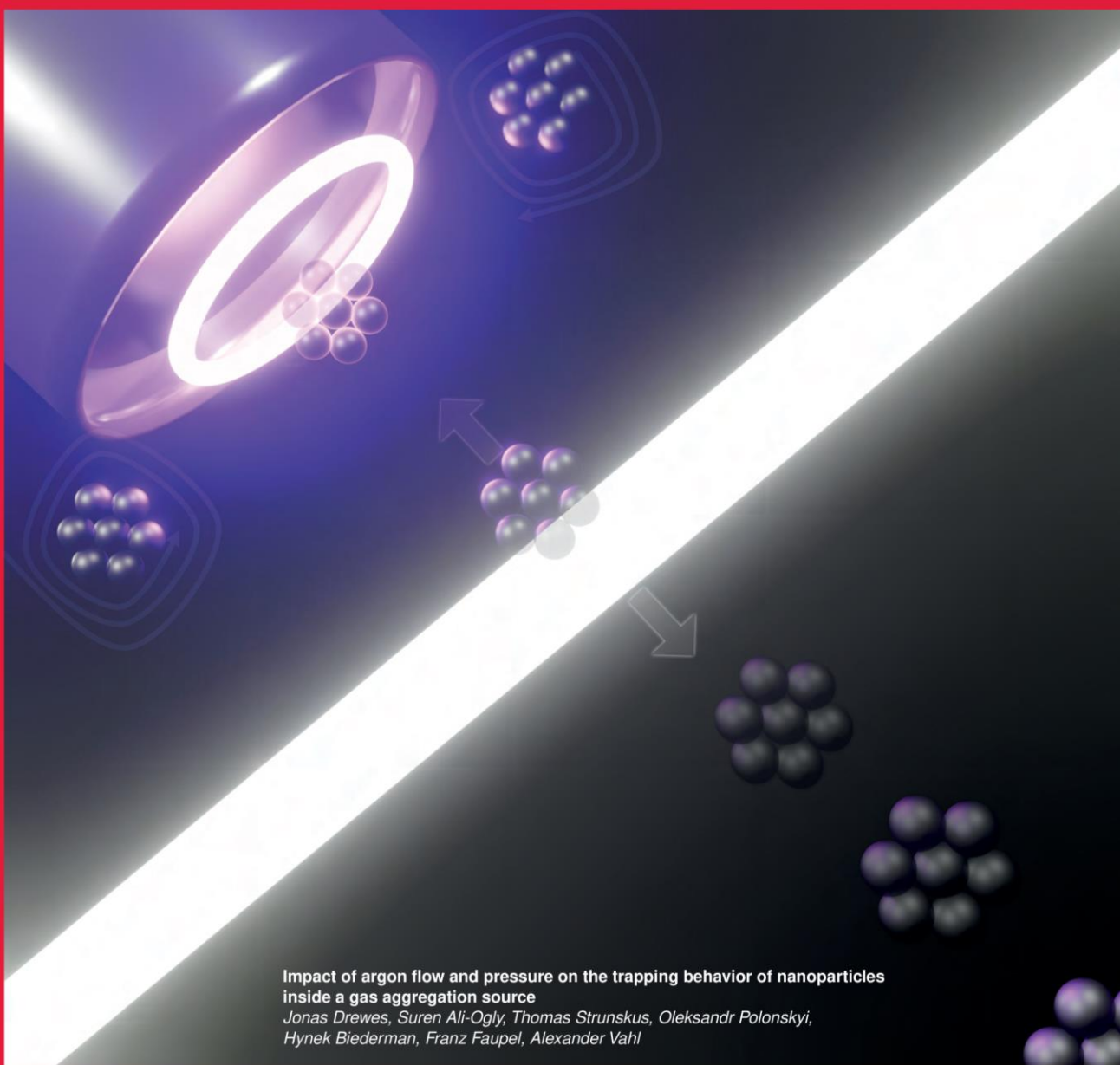
This publication has drawn the attention to the only rarely investigated gas velocity distribution inside the HGAS. It was shown that the velocity distribution has a big impact on the trapping and transport of NPs inside the HGAS. Therefore, the gas flow pattern should be treated as a crucial parameter in the design of future HGAS sources.

The data of this publication was partially obtained during my master thesis at the Chair of Multicomponent Materials at Kiel University. The final interpretation, conceptualization of the manuscript, the conductance of the CFD simulations by our collaboration partner and writing of the manuscript draft was done in the frame work of this doctoral thesis.

This chapter is reprinted from the following publication and was selected as the front cover:

Drewes, J., Ali-Ogly, S., Strunskus, T., Polonskyi, O., Biederman, H., Faupel, F., & Vahl, A. (2022). Impact of argon flow and pressure on the trapping behavior of nanoparticles inside a gas aggregation source. *Plasma Processes and Polymers*, 19(1), 2100125. <https://doi.org/10.1002/ppap.202100125>

PLASMA PROCESSES AND POLYMERS



Impact of argon flow and pressure on the trapping behavior of nanoparticles inside a gas aggregation source

Jonas Drewes, Suren Ali-Ogly, Thomas Strunskus, Oleksandr Polonskyi, Hynek Biederman, Franz Faupel, Alexander Vahl

Editors-in-Chief: Pietro Favia, Bari | Dirk Hegemann, St. Gallen |
Christian Oehr, Stuttgart | Michael R. Wertheimer, Montreal
Founding Editor: Riccardo d'Agostino, Bari †

WILEY-VCH

Received: 5 August 2021 | Revised: 19 September 2021 | Accepted: 11 October 2021

DOI: 10.1002/ppap.202100125

RESEARCH ARTICLE

PLASMA PROCESSES
AND POLYMERS

Impact of argon flow and pressure on the trapping behavior of nanoparticles inside a gas aggregation source

Jonas Drewes¹  | Suren Ali-Ogly²  | Thomas Strunskus¹  |
Oleksandr Polonskyi^{1,3}  | Hynek Biederman²  | Franz Faupel¹  |
Alexander Vahl¹ 

¹Chair of Multicomponent Materials, Institute of Materials Science, Faculty of Engineering, Kiel University, Kiel, Germany

²Department of Macromolecular Physics, Charles University, Prague, Czech Republic

³Department of Chemical Engineering, Engineering II, University of California, Santa Barbara, California, USA

Correspondence

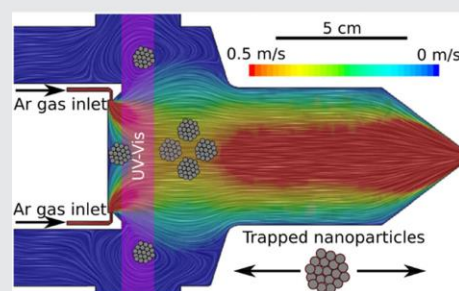
Alexander Vahl, Chair of Multicomponent Materials, Institute of Materials Science, Faculty of Engineering, Kaiserstraße 2, D-24143 Kiel, Germany. Email: alva@tf.uni-kiel.de

Funding information

Deutsche Forschungsgemeinschaft, Grant/Award Number: PO2299/1-1

Abstract

In this study, in situ UV–Vis spectroscopy is used to investigate the growth and transport of nanoparticles inside a gas aggregation source (GAS) dependent on the Ar gas flow and operating pressure. It was found that the nanoparticles were becoming trapped at different positions inside the GAS dependent on the gas flow. Moreover, in situ UV–Vis spectroscopy suggested the presence of large nanoparticles inside the GAS, which were not observed outside. Computational fluid dynamic simulations were performed to study the velocity distribution inside the GAS. Three distinct areas were identified, where nanoparticles can become trapped or lost. The gas flow velocity distribution was found to strongly impact the transport of nanoparticles.



KEYWORDS

computational fluid dynamic simulation, gas aggregation cluster source, gas-phase synthesis, in situ UV–Vis spectroscopy, sputter deposition

1 | INTRODUCTION

Metal nanoparticles (NPs) have received considerable attention over the last decades due to their unique properties in comparison to the properties of bulk metals,

resulting in high application potential in many fields like catalysis,^[1] photocatalysis,^[2–6] optics,^[7] resistive switching,^[8–15] and sensors.^[16–20] In particular, the optical properties of noble-metal NPs are highly interesting due to the presence of localized surface plasmons,^[21] and

Abbreviations: CFD, computational fluid dynamic; DLR, distal loss region; GAS, gas aggregation cluster source; LSPR, localized surface plasmon resonance; NPs, nanoparticles; PLR, proximal loss region; QCM, quartz crystal microbalance; SEM, scanning electron microscopy.

This is an open access article under the terms of the Creative Commons Attribution License, which permits use, distribution and reproduction in any medium, provided the original work is properly cited.

© 2021 The Authors. *Plasma Processes and Polymers* published by Wiley-VCH GmbH.

Plasma Process Polym. 2021;e2100125
https://doi.org/10.1002/ppap.202100125

www.plasma-polymers.com

1 of 11

various applications are possible including molecular fluorescence,^[22] solar cells,^[23] and surface-enhanced Raman spectroscopy.^[24] Furthermore, molecularly labeled NPs that bond specifically to cancer cells were used for selective hyperthermia therapy of cancer cells without harming healthy cells.^[25] Another field of application for noble-metal NPs and especially silver NPs is antibacterial coatings for medicine, construction industry, clothing, and also food packaging.^[26] Here, their high surface-to-volume ratio enables fast ion release, which leads to tailored antibacterial properties.

There are several ways to produce metal NPs using either chemical, biological, or physical approaches. Chemical methods commonly use surfactants, which has the major disadvantage that the NPs created are contaminated by surfactant molecules.^[27] A physical vapor deposition approach to produce NPs is gas-phase synthesis in a “gas aggregation cluster source” (GAS). Many different kinds of GAS have been developed from the early 1970s based on for example, erosion techniques, effusive method, and supersonic jet expansion.^[28–30] In 1992, another physical vapor deposition method for the synthesis of NPs was proposed by Haberland et al.^[31] In this approach, a DC magnetron is used in a GAS, where the sputtered atoms condensate in the gas phase in the presence of inert gas. Henceforth, the abbreviation GAS always stands for a Haberland-type GAS.

In the GAS, the particle size can be tuned by various parameters, including the ratio of sputtering and cooling gases, the addition of molecular gases, the gas flow, the operating pressure in the aggregation volume, magnetron power, and the overall source geometry. All of these parameters influence the underlying processes of cluster formation from the nucleation up to the transport of NPs.^[32] Furthermore, it is commonly reported that the sizes of NPs synthesized with GAS can also be tuned by varying the aggregation length.^[33–36] This supports the common textbook understanding of the NP synthesis inside such GAS. It is known that after a stable nucleus is formed, it can grow while being transported toward the orifice by condensation of sputtered atoms or by coalescence with other nuclei or NPs.^[31,32,37] Regarding the transport of NPs inside the gas, it has been reported many times that the movement of NPs inside a GAS is caused by the drag force from the inert gas.^[31,35,38,39] Nevertheless, recent publications reported the trapping of NPs inside a GAS, indicating that a fraction of NPs is not able to leave the GAS.^[40–42]

To understand the NP growth and transport mentioned above, in situ investigations are necessary. Small-angle X-ray scattering^[40,41] and in situ UV–Vis observations were used to analyze the growth and transport inside the GAS.^[42] These studies reported that

NPs become trapped in the close vicinity of the magnetron due to a complicated interplay between different forces (Figure S1). However, this contradicts the simple theory of NPs linearly growing alongside their paths through the GAS.

In this study, the ongoing processes inside the GAS and the origin of the trapping of NPs inside the GAS are studied in more detail. Therefore, the influence of different Ar flows on the transport and growth of NPs are investigated in situ using UV–Vis spectroscopy. While in recent works the main attention was focused on investigations of trapping at a specific gas flow and pressure,^[40–42] in this study, the impact of different geometrical parameters and gas flows on the trapping behavior inside the GAS is investigated. In particular, this study focuses on the aspects of NP growth and transport in relation to aggregation length and gas flow dynamics.

To determine how the trapping of NPs inside the GAS is influenced by the gas flow, in situ UV–Vis measurements combined with quartz crystal microbalance (QCM) measurements at different magnetron-to-beam distances (M-B distances) are performed (Figure 1). These results are complemented by scanning electron microscopy (SEM) measurements of the synthesized NPs and target surface, profilometer measurements of the target surface, and computational fluid dynamic (CFD) simulations inside the GAS. From these results, we developed a hypothesis on the trapping behavior of NPs in a Haberland-type GAS.

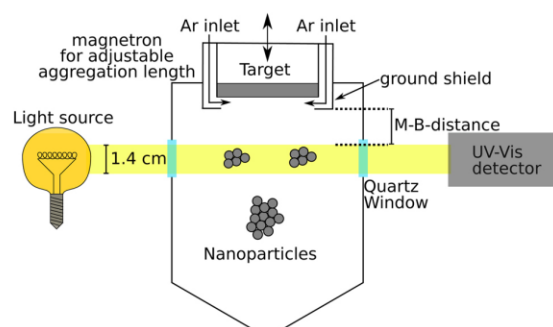


FIGURE 1 Schematic of the experimental setup. The GAS is equipped with a magnetron for adjustable aggregation length. Using this, the M-B distance can be adjusted because the UV–Vis optics is at a fixed position, but the aggregation length of the magnetron can be varied. The light beam of the UV–Vis is 1.4 cm in diameter. The Ar gas inlet is located between the magnetron main body and the ground shield. Hence, the ground shield projects over the magnetron main body, and the Ar gas streams directly over the target surface. GAS, gas aggregation source

2 | EXPERIMENTAL DETAILS

The experiments are performed using a custom-built gas aggregation source equipped with a 2-in. magnetron for adjustable aggregation length (Thin Films Consulting; Ionix) with a 2-in. Ag target (99.99% purity, Kurt J. Lesker). The main vacuum chamber is pumped by a turbo molecular pump (TMU 261, 210 L/s; Pfeiffer) together with a dry scroll vacuum pump (SH-110; Agilent Technologies), and the GAS is connected to the main chamber via an exit orifice (3-mm diameter). The argon gas is injected into the GAS through the magnetron ground shield, allowing for gas delivery directly to the target surface (Figure 1). The flow is controlled using a gas flow controller (1179BX22CM1BV with 200 sccm range; MKS Instruments Deutschland GmbH) and adjusted to 24, 60, 96, and 120 sccm with the corresponding pressures of 49, 113, 177, and 220 Pa inside the GAS. The power supply (MDX 500; Advanced Energy) of the magnetron was operated at 100 W for all experiments. The GAS is equipped with two quartz windows and a UV-Vis spectroscopy setup (Light source: Deuterium/Halogen lamp DH-2000BAL; Detector: Ocean Optics, HR 4000CG-UV-Nir; Ocean Optics). The light beam diameter of the UV-Vis spectroscope is 1.4 cm. To measure the transmission at different M-B distances, the aggregation length was adjusted with the magnetron. The M-B distance of 0 cm corresponds to the closest possible distance between the magnetron and the light beam without cutting the light beam with the ground cap of the magnetron. Since the direct optical emission lines do not contain additional information, these lines were removed to increase the visibility of the plasmonic absorption. As substrates, P-doped, (100)-oriented Si wafer pieces with native oxide (cut to $1 \times 1 \text{ cm}^2$; SiMat) were used. SEM analysis was performed using a Zeiss Ultra Plus microscope.

The flow simulations were conducted using the commercially available software Siemens STAR CCM + 15.04.010 R8. Further details about the CFD simulations can be found in the Supporting Information.

3 | RESULTS AND DISCUSSION

In the first part of the work, the time evolution of the localized surface plasmon resonance (LSPR) of Ag NPs inside the GAS for an Ar flow of 24 sccm and an M-B distance of 3 cm to the target will be exemplarily discussed. In Figure 2a,b, transmittance UV-Vis spectra are shown and presented in two different ways. Figure 2a shows the spectra from 0 to 30 s in 5 s steps as a conventional two-dimensional (2D) plot, where the different

spectra are offset by 5% to increase the visibility of the evolution of the LSPR. The same spectra are also contributing in Figure 2b, where the transmittance is represented by a color bar; on the X-axis, the wavelength is shown, and on the Y-axis, the time is shown. This makes it possible to include all spectra between 0 and 30 s in one plot. With time, the LSPR of the Ag NPs undergoes a strong red shift from ~ 360 to ~ 380 nm, the absorption increases from $\sim 1\%$ to $\sim 9\%$, and also the peak broadens. A red shift together with peak broadening of the LSPR indicates that the NPs are growing over time.^[43,44] In this case, the red shift of the LSPR and the peak broadening are related to the depolarization phenomenon.^[45,46] This observation indicates that the nucleation and growth at the beginning of the NP formation have not reached a stable equilibrium, which is in good agreement with the theory of NP growth inside a GAS.^[32,40–42] After a stable nucleus is formed, it can grow further by condensation of sputtered atoms on the NP surface,^[32] which provides a possible explanation for the observed time evolution in the spectrum.

To estimate the diameter of NPs, extinction cross-sectional area estimations based on the dissertation of Steven J. Oldenburg^[47] are performed. Here, the full vectorial solution to Maxwell's equations is solved without approximation for the problem of light scattering at a homogeneous sphere. The resulting extinction cross-sectional area is a superposition of the absorption cross-sectional area and the scattering cross-sectional area. In this case, only the extinction cross-sectional area is of interest because the UV-Vis measurements only show reduced transmission without differentiation between light scattering and absorption. From these estimations, it turned out that Ag NPs with a diameter of 40 nm have the maximum extinction cross-sectional area at 360 nm, and NPs with a diameter of 70 nm have the maximum extinction cross-sectional area at 380 nm under vacuum conditions and a broader peak (Figure 2c).^[47] The comparison with the UV-Vis data indicates that the NPs in our experiment should have a size of ~ 40 nm in the early growth phase and increase up to ~ 70 nm after ~ 25 s of continuous magnetron operation in GAS. Nevertheless, such large NPs were never observed on the substrate located outside the GAS in front of the orifice. Although the comparison of the UV-Vis data with the estimations in Figure 2c indicates the presence of large NPs up to 70 nm, this does not exclude the presence of smaller NPs because the UV-Vis signal is a superposition of the interaction of the incoming light with several NPs, which may have different sizes. SEM micrographs indicate that the mean diameter of the extracted and deposited NPs is ~ 15 nm and the largest NPs were ~ 35 nm (Figures 2d and S3). This implies that the NPs with diameters larger

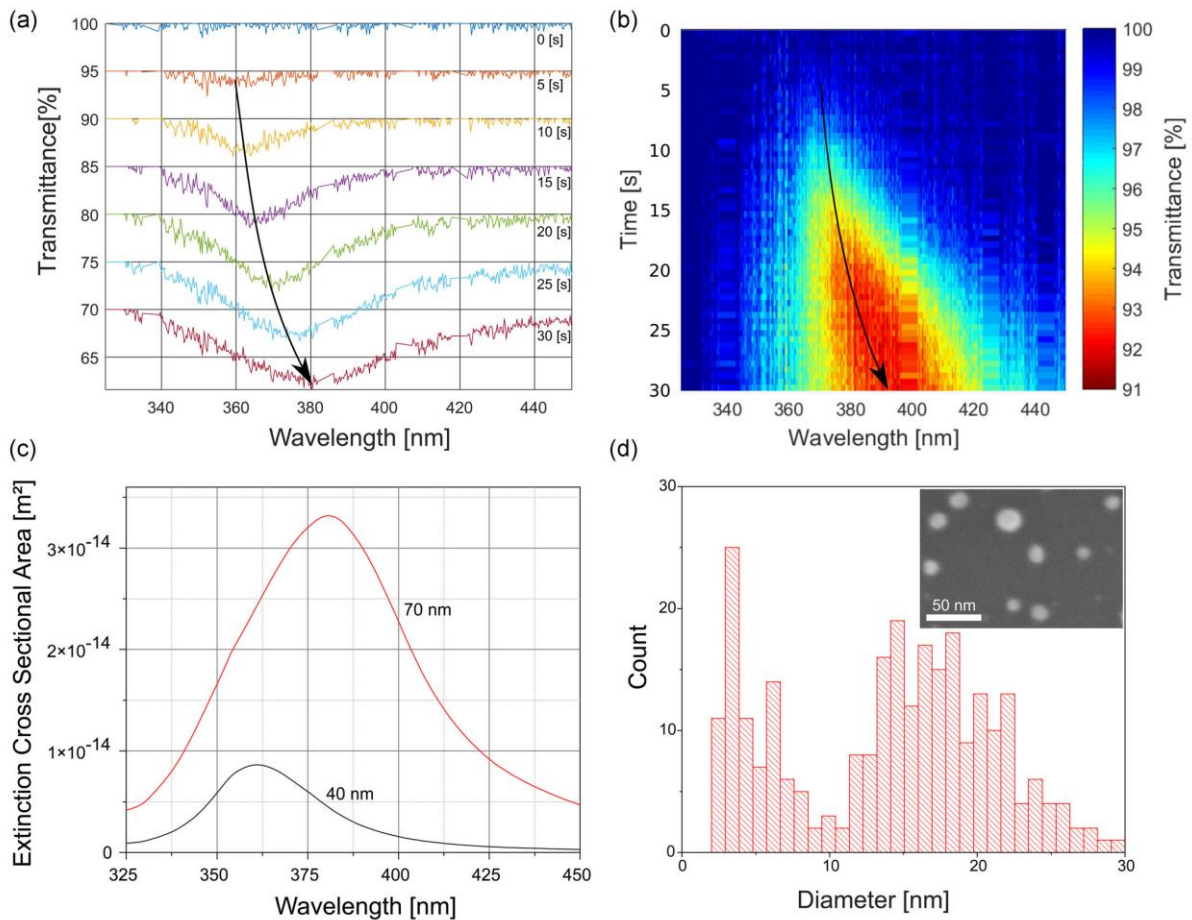


FIGURE 2 UV-Vis spectra showing the time evolution of the LSPR of Ag NPs with a flow of 24 sccm and an M-B distance of 3 cm. The spectra are offset by 5% to increase the visibility of the LSPR. (a) The color map shows the data of (a) together with all other spectra recorded between 0 and 30 s. It can be seen that the LSPR undergoes a red shift over time and the absorption increases, which is related to the growth of NPs and the density of NPs. (b) Estimated extinction cross-sectional areas for NPs with sizes of 40 and 70 nm dependent on the wavelength are shown for comparison with the results of the UV-Vis measurements. (c) The histogram shows the size distribution of NPs deposited on a Si substrate outside the GAS at 24 sccm and an M-B distance of 3 cm. The inset shows an image section of an exemplary SEM image that was considered for the histogram (d). GAS, gas aggregation source; LSPR, localized surface plasmon resonance; NP, nanoparticle; SEM, scanning electron microscopy

than 35 nm, whose presence inside the GAS is predicted based on UV-Vis, can, for some reason, not leave the GAS. Thus, they are either deposited on the inside walls of the GAS apparatus or redeposited onto the target. Considering that the UV-Vis data indicate that large NPs are present in close vicinity to the magnetron, there must be some forces that prevent the NPs from leaving the GAS. Since the UV-Vis light beam passes through the center of the GAS, the NPs would be expected to be transported perfectly by the drag force from the Ar gas outside the GAS. Nevertheless, the phenomenon of large NPs inside GAS that were not able to leave the GAS is known and is referred to as the trapping of NPs.^[40–42]

The observation of an evolving LSPR in the vicinity of the target surface implies that NPs of considerable sizes are formed already close to the target. This is consistent with earlier observations by Kousal et al.^[41] and Shelemin et al.,^[40] who applied synchrotron radiation to perform small-angle X-ray scattering experiments. They found that the NPs grow over time and that large NPs become trapped due to electrostatic force interactions with the charged NPs in close vicinity to the target.

In the second part of this study, NP trapping will be discussed in more detail. To gain an understanding of the location at which the majority of NPs are trapped (i.e., trapping position), the following experiment was

performed: The M-B distance was varied by adjusting the position of the magnetron. In addition, the argon gas flow was varied, which in turn impacted the operating pressure inside the GAS.

Figure 3 shows the UV-Vis spectra for flows of 24 (a) and 60 sccm (b) at different M-B distances at 30 s of magnetron operation. For 24 sccm, it can be clearly seen that the maximum absorption is at an M-B distance of 1 cm. On the other hand, the maximum absorption for a flow of 60 sccm was found at 3 cm. In particular, the observation of a maximum in LSPR in the close vicinity to the target surface is deviating from the common theory of NP growth and transport, which assumes continuous growth of NPs along their transport path.^[32]

Considering that considerable NP growth is already finished in the close vicinity of the target and that the particles do not get lost, the UV-Vis signal must not change when the M-B distance is changed. Assuming that the particles are growing over their whole transport path from the magnetron to the exit orifice, the transmittance in the UV-Vis signal must decrease and the wavelength has to increase. This has to be the case, because with growing size of NPs, the LSPR is red-shifted and broadened, and the extinction cross-sectional area is also increasing (Figure 2c).

This is not the case, and indicates that particles are becoming trapped at different positions, depending on the gas flow and pressure. Accordingly, the common theory of steady nucleation, growth, coalescence, and transport needs to be extended by including the possibility that particles become trapped inside the GAS. In fact, the observations of a maximum in LSPR in the vicinity to the target surface imply that trapping is a highly important component of the overall NP formation process and hence has to be considered in an updated theory.

The data in Figure 3 show that a higher gas flow directly affects the trapping behavior of the NPs in the GAS. The maximum absorption for 24 sccm at an M-B distance of 1 cm is $\sim 24\%$ and that for 60 sccm at an M-B distance of 3 cm is $\sim 6\%$. Since the transmittance is decreased in the same wavelength range, one can assume that the size distributions are also close to each other. This allows the assumption that the absorption is related to the amount of NPs; this means that a significantly smaller amount of NPs becomes trapped with higher gas flows. When the flow is increased to 96 sccm or even up to 120 sccm, almost no absorption due to the LSPR of the Ag NPs can be found (Figure S2). This implies that the higher drag force, which originates from the higher gas flow in combination with higher pressure, can release more of the trapped particles out of the trapping region. This was also proven by QCM measurements (Figure 3c), which have shown an increased deposition rate for increasing flows. The plot shows that for a constant power of 100 W, the deposition rate increases with gas flow from 24 to 120 sccm and is 34 times higher for 120 sccm than for 24 sccm. This indicates that more NPs are released from the GAS, even when the same power was applied to the target.

In a conventional GAS deposition experiment with a fixed exit orifice diameter and pumping rate, any increase in gas flow results in an increase in pressure inside the GAS. This can also change the growth of the NPs. However, the NPs outside the GAS are still in the same diameter range for 60 sccm as for 24 sccm (Figure S3). The fact that the NPs' size distributions for 24 and 60 sccm are close to each other even when the deposition rate for 60 sccm is already reasonably higher than for 24 sccm implies that the increase in drag force is only able to release the smaller NPs out of the "trapping"

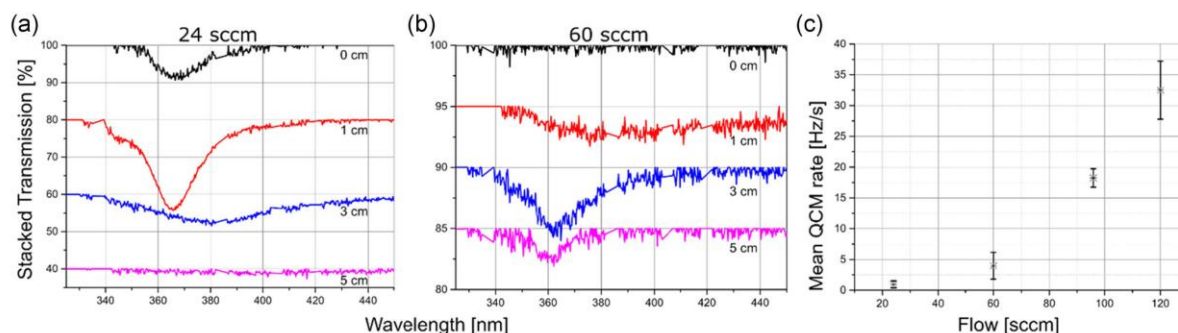


FIGURE 3 UV-Vis spectra at 24 (a) and 60 sccm (b) at different M-B distances after discharge was switched on for 30 s. The spectra have an offset of 20% for 24 sccm and 5% for 60 sccm. It turned out that for 24 sccm, the highest absorption was found 1 cm away from the magnetron, which is referred to as the trapping region. In contrast, the trapping region for 60 sccm was found at 3 cm. Dependence of the deposition rate of Ag NPs on the Ar flow measured with a QCM can be found in (c). Depositions were performed at a constant magnetron power of 100 W. The values are given together with standard deviation error bars. NP, nanoparticle; QCM, quartz crystal microbalance

region because, otherwise, one would expect that also NPs of up to 70 nm or at least 40 nm would be found on the substrate, whose presence was indicated by UV-Vis spectroscopy in the gas phase. To further investigate the "trapping" of NPs and to figure out how big the earlier mentioned forces acting on the NPs are, further research with novel methods has to be conducted. Especially the question why big NPs of up to 70 nm can not escape the GAS but were found with the UV-Vis investigations can only be answered, when the force equilibrium of the NPs is further investigated.

To identify the potential trapping locations inside the GAS, in the third part of the work, CFD simulations were performed using the commercially available software "Siemens STAR CCM+15.04.010 R8." Before discussion of the CFD results, the conditions for trapping or loss of particles have to be defined. In the context of this study, a loss region is indicated by a velocity magnitude of 0 m/s or close to 0 m/s (<0.02 m/s). If an NP is entering a region with a gas velocity close to 0 m/s, the drag force that is forcing the NPs to leave the GAS through the orifice is missing and the NPs will potentially collide with the chamber wall. Therefore, the regions with a gas velocity close to 0 m/s are termed loss regions.

A trapping region is defined as a region with a non-zero velocity and the presence of an additional driving force, which counteracts the drag force and directs the NPs to a stationary trajectory. The NPs in a GAS source can be charged due to the plasma environment and be trapped by a complicated interplay of drag forces from the Ar gas, electromagnetic force, thermophoretic force, gravity, and ion drag force.^[40–42] The forces acting on the NPs are schematically shown in Figure S1.

In Figure 4, the CFD simulation results for 24 sccm at an M-B distance of 0 cm are shown. For all CFD simulations in this study, a linear scale of the velocity was chosen and the range was set from 0 to 0.5 m/s. This was necessary because velocities of up to 100 m/s can be found close to the exit orifice and at the gas inlets. If the linear scale is set to such high values, the visibility of changes in the velocity distribution in the region of interest would be decreased to an unacceptable level. In the Supporting Information, CFD simulations for all flows with a logarithmic scale can be found (Figure S4). Therefore, blue regions are not exactly 0 m/s, but close to 0 m/s, and red regions are 0.5 m/s or higher, which can be seen in Figure S4. Using UV-Vis spectroscopy as a diagnostic approach to determine the NP trapping region, the area under investigation is limited to the beam trajectory of the UV-Vis light source. For a better comparison, the region corresponding to the UV-Vis light beam is also indicated as a yellow bar in the visualization of the CFD simulation. In Figure 4, three different

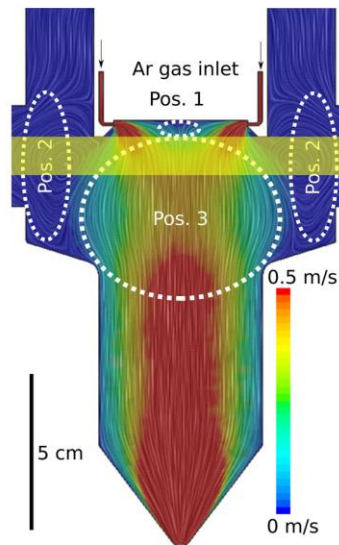


FIGURE 4 An exemplary CFD velocity distribution is shown. Here, the yellow region corresponds to the position of the UV-Vis light beam at an M-B distance 0 cm. Three different positions (Pos.) are shown. Positions 1 and 2 correspond to loss regions and Position 3 corresponds to the trapping region. The flow direction of the gas is indicated by white stream lines. The gas inlet is shown and located between the ground cap and the magnetron. CFD, computational fluid dynamic

positions in the gas stream are shown. Position 1 and Position 2 are loss regions where the velocity magnitude equals nearly 0 m/s (blue regions). To distinguish Position 1 and Position 2 more easily, they are termed the "proximal loss region" (PLR), which is close to the target, and the "distal loss region" (DLR), which is further away from the target. Position 3 indicates the possible trapping region. In the next section, first, the possible PLR and DLR, where the gas velocity is close to 0 m/s, will be discussed.

The PLR is directly in front of the target in the center position and the DLR is left and right from the mainstream of the gas when we depict the GAS in a 2D representation. In a 3D representation, the DLR can be described by a torus with its rotational symmetry axis aligned to the rotational symmetry axis of the target. It is expected that NPs can get lost at both loss regions. The loss of NPs from the PLR region is indicated by the Profilometer and SEM measurements. The profile and the SEM images at the center of the target, which is close to the PLR region, show clearly that material was redeposited there (Figure 5). A profile of 0 μm corresponds to the original target surface height before any deposition was carried out. It is clear that, everywhere, material is redeposited onto the target surface, except at the erosion

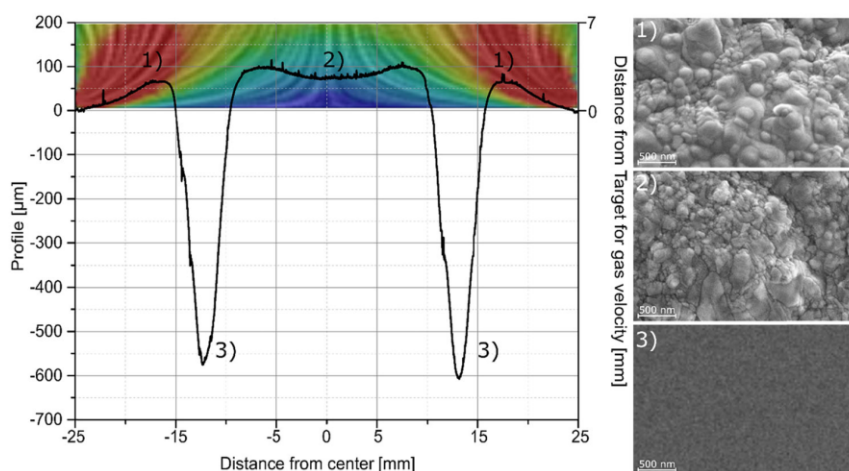


FIGURE 5 Profilometer measurements after target usage and corresponding SEM pictures at different places of the target. CFD velocity distribution above the target is inserted into the profilometer measurement plot. The CFD section shows ~ 7 mm of the velocity distribution above the target. The color bar is identical to Figures 4 and 6 and ranges from 0 (blue) to 0.5 m/s (red). The profile shows less redeposition at the low-velocity region (blue) than at the high-velocity region (red). CFD, computational fluid dynamic; SEM, scanning electron microscopy

zone. The phenomenon of redeposition in GAS sources has been reported many times and is much more pronounced in comparison to conventional thin-film sputter deposition with magnetrons.^[40,42,48] The profile shows that much more material is redeposited onto the center (max. height: ~ 100 nm) of the target than onto the sides of the target (max. height: ~ 67 nm).

The SEM images at the redeposition regions show that the redeposited material consists of NPs but also single atoms can contribute to the redeposition. On the contrary, the SEM micrographs from the erosion zone show a smooth surface, as expected for a sputtered surface. In particular, the increase in the redeposition from the outer edge of the target toward the onset of the erosion zone indicates a strong effect of the gas flow on the redeposition behavior. The CFD simulations have shown that the gas velocity is high at the sides of the target because the gas inlet is located there. On the other hand, the velocity in front of the center of the target is 0 m/s. The profilometer measurements together with the CFD simulations indicate that NPs that are formed in the close vicinity of the target sides are guided into the main Ar gas flow, which prevents redeposition. If the NPs are close to the middle of the target, a considerably higher amount of NPs becomes redeposited in comparison to the sides of the target. The low-velocity area close to the target, despite being mostly shadowed by the ground cap of the magnetron, can still contribute to the UV-Vis spectra of the PLR in the visible region.

The PLR would be visible in the UV-Vis spectra at an M-B distance of 0 cm even when a part of the PLR is

shadowed by the ground cap. This means that for 60 sccm, definitely no particles were found in the visible region for this possible trapping because at an M-B distance of 0 cm, no absorption is visible (Figure 3). On the other hand, for 24 sccm at an M-B distance of 0 cm, absorption was present, which means that NPs are present at that M-B distance. Since the UV-Vis measurement technique obtains data from the cylindrical volume at a specific M-B distance, one obtains information only from the volume and not from specific positions in space. In case of a gas flow of 24 sccm at an M-B distance of 0 cm, the UV-Vis measurement includes the PLR, DLR, and trapping region. The observation of absorption in the corresponding UV-Vis measurement indicates the presence of NPs in either of the PLR, DLR, or trapping regions.

At the DLR, no samples could be placed; therefore, no SEM or profilometer measurements were possible. Nevertheless, after the deposition experiments, the entirety of the inside walls of the GAS showed NP deposits, which proves that NPs are sometimes deposited on walls in loss regions (Figure S5). However, according to the theory of the working principle of a GAS, particles are transported out of the GAS only because of the gas flow. From this point of view, particles can get lost potentially at the PLR and also at the DLR.

In the following section, the influence of changes in the gas flow and the M-B distance on the Ar gas velocity is discussed. Therefore, CFD simulations for 24 and 60 sccm and M-B distances of 0, 1, and 3 cm were conducted, and these are shown in Figure 6. In this figure,

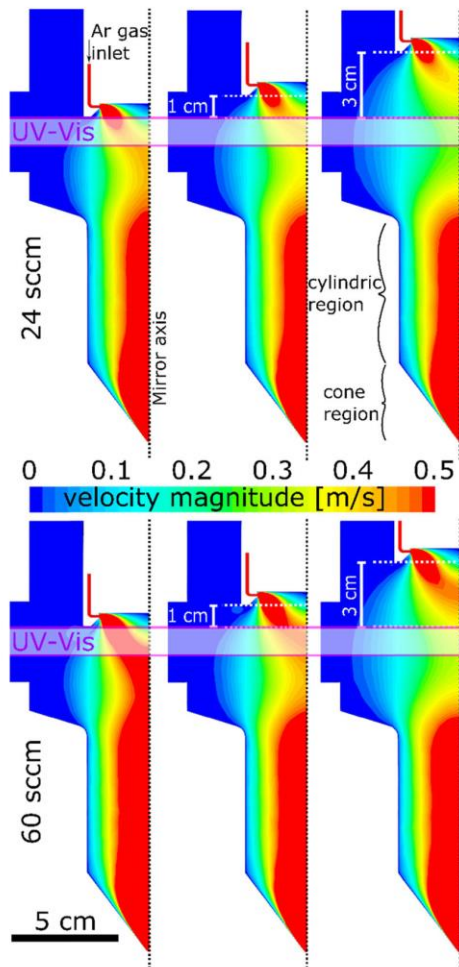


FIGURE 6 CFD flow simulation for 24 (top) and 60 sccm (bottom) and for different M-B distances of 0, 1, and 3 cm from left to right. The black dotted line indicates the mirror axis. The violet beam locates the position and the size of the UV-Vis light beam. The loss regions (blue) are not much affected by changes in gas flow or the M-B distance. An increase in the M-B distance leads to an increase in the low-velocity region in the center of the GAS. On the other hand, an increase in gas flow leads to an increase in the gas velocity everywhere but does not affect the shape of the flow. CFD, computational fluid dynamic; GAS, gas aggregation cluster source

the color code shows the velocity magnitude of the Ar gas atoms inside the GAS, which is restricted to the range 0–0.5 m/s. The borders of the colored regions correspond to the inside walls of the GAS. In total, six different simulations are shown. Each row corresponds to one Ar flow (24 sccm on top and 60 sccm at the bottom) and the resulting pressure (49 and 113 Pa), and each column corresponds to an M-B distance, which is shown in white color. In each GAS simulation, the magnetron is located

on the top and the exit orifice is located on the bottom. The schematic depiction of the UV-Vis light beam indicates the approximate volume from which the UV-Vis spectra are originating. These simulations showed three different behaviors depending on the changed parameters and the regions of interest, which will be described and discussed in the following section (Figures 4 and 6):

- 1) The velocity distributions in the PLR and DLR are not much affected by the change in the gas flow or the changes in the aggregation length. The UV-Vis spectra show that the M-B distance where the particles are trapped changes depending on the gas flow (Figure 3). This indicates that the NPs most probably do not get lost only in the 0 m/s velocity regions (PLR and DLR) inside the GAS because these regions are almost not affected by the change of gas flow. From this point of view, it follows that there must exist a trapping region in the higher velocity regions in the mainstream of the Ar gas inside the GAS as described earlier.
- 2) The trapping region, which is located inside the mainstream of the Ar gas stream, has shown more differences. With an increase in gas flow, the velocity in the center of the GAS is also increasing. This increase, together with the increase of the pressure, increases the drag force on the NPs drastically. Experimentally, this is related to the increased NP deposition rate from Figure 3c found already and is also reflected by the change of the trapping position from 1 cm for 24 sccm to 3 cm for 60 sccm (Figure 3a,b).
- 3) A change in the aggregation length affects the velocity distribution in the trapping region. It turned out that the region close to the magnetron, the cylindrical region, and the cone region (Figure 6) in the GAS remained nearly unaffected. However, the region between the magnetron and the cylindrical region of the GAS with lower velocities is increasing. On this basis, on the one hand, the NPs are transported better at higher gas flows and pressures because they are guided better into the mainstream of Ar by the increased drag force. On the other hand, for lower flows, the drag force is too low to overcome the other forces that are trapping the NPs. However, the UV-Vis results indicated that large NPs are present inside the GAS, but it is unclear why they cannot be deposited onto the substrate. Most probably, the forces related to the plasma, which are trapping the NPs, are higher for larger NPs and cannot be overcome by higher gas flows or they cannot follow the gas stream as good as the small ones, due to their higher mass. More investigations on this topic are needed in the future.

Here, in situ UV–Vis spectroscopy can be an important analytical tool to expand the understanding of trapping and transport.

With the increase in the M-B distance, the aggregation length was also increased, which also slightly increased the size of the resulting NPs (Figure S3). The mean NP size increases with the M-B distance from ~12 to ~17 nm for 24 sccm and from ~12 to ~16 nm for 60 sccm. The CFD simulations showed that with an increase in the aggregation length, not only was the aggregation region increased but also the gas flow was affected. Accordingly, the residence time of the NPs was not only increased because the aggregation zone was increased but also because the gas velocity and therefore the velocity of NP that were not trapped were decreased, which in turn increased the time for the growth of the NPs. The size distributions also showed that a bimodal distribution is much more pronounced with higher gas flow, pressure, and aggregation length. The simulations showed that the diversity in the velocity distribution in the GAS increases with an increase in aggregation length and increase in the gas flow. This may be the reason for the resulting bimodal distributions because the NPs, depending on their path through the GAS, can have very different conditions for growth and transport. The bigger population in the size distribution, which is the group of NPs around the second maximum in the size distribution, can also be a result of coalescence between several NPs of the smaller population. This may be much more probable for the higher gas flows because the deposition rate was much higher and so the probability for coalescence is higher. On the other hand, it has to be pointed out that the actual geometry of the GAS, as well as the magnetron, is of crucial importance. While some magnetrons have a gas inlet between the ground shield and the target, as shown here, others have a gas inlet at a certain place behind the magnetron. Although these instrumental details have not received much attention yet, we want to point out that even small differences in different GAS setups can cause huge differences in the gas flow.

On combining the UV–Vis results, profilometer measurements, and CFD simulation, it was found that forces other than the drag force influence the NPs during their growth and transport because otherwise, no particle trapping would be observed in the trapping region. In addition, the CFD simulations showed that the velocity in the aggregation zone decreased with increasing aggregation length, which increased the residence time of NPs in the GAS in addition to the longer path.

The results indicate that an updated theory for the growth and transport of NPs is urgently required. With a

better understanding of NP growth and transport processes, especially taking the trapping mechanism into account, it would be possible to tailor the sizes of NPs more efficiently. We were able to show that the gas flow and its velocity distribution have a huge impact on the transport of NPs, which should be considered as a more important parameter in the design of future GAS sources. Already during the construction process, CFD simulations can be performed and special attention should be paid to the appearance of low-velocity regions. These regions can be, in some circumstances, useful to tune the size of NPs, if a means for the release of these NPs can also be found. Also, the gas inlet location should be considered as a critical construction part to reduce re-deposition onto the target.

4 | CONCLUSION

In this study, gas flow-related transport phenomena in GAS have been studied and two indications for trapping of NPs are observed. On the one hand, in situ UV–Vis spectroscopy found evidence of a time-dependent red shift and broadening of the LSPR peak, which can be seen as an indication of NP growth. Comparing UV–Vis data to estimated extinction cross sections for differently sized NPs, larger particles are expected to be trapped inside the GAS than those observed in the deposit. By means of UV–Vis measurements and the magnetron for adjustable aggregation length, it has been found that the position of the trapping region inside the GAS can be significantly influenced by different gas flows and pressures.

On the other hand, CFD simulations were conducted to determine the working gas flow pattern. The CFD simulations have shown that the gas flow in the loss regions does not differ much. Therefore, their position is always nearly the same with varying gas flows and pressures. However, the velocity distribution of the gas inside the possible trapping region changed considerably with different aggregation lengths and gas flows. In addition, the velocity distribution close to the target revealed that a loss region (PLR) is present there. This has been confirmed by profilometer measurements (more NP material is redeposited in the center of the target in comparison to the outer side of the target).

Finally, in conclusion, the gas velocity pattern determines, to a huge extent, the transport of NPs inside the GAS and therefore it should be treated as a crucial parameter in the designing process of future gas aggregation cluster sources. This may lead to considerably increased production rates of NPs and thus constitute an important milestone for industrial applications.

ACKNOWLEDGMENTS

This study was financially supported by the German Research Foundation (DFG) via the project PO2299/1-1. The authors would like to thank Stefan Rehders for technical assistance. Special thanks are due to Siemens's official distributor in the Czech Republic, TechSim s.r.o., for providing the license for the CFD software Siemens STAR CCM+.

CONFLICT OF INTERESTS

The authors declare that there are no conflict of interests.

AUTHOR CONTRIBUTIONS

Jonas Drewes, Alexander Vahl, Oleksandr Polonskyi, Thomas Strunskus, and Franz Faupel developed the idea and conceived the initial design of the study. Jonas Drewes, Oleksandr Polonskyi, and Alexander Vahl established the experimental setup. Jonas Drewes performed the Ag NP depositions and recorded UV-Vis data. Jonas Drewes, Alexander Vahl, and Oleksandr Polonskyi analyzed the results. Suren Ali performed the computational fluid dynamic simulations. Jonas Drewes and Alexander Vahl prepared the manuscript draft. Alexander Vahl and Franz Faupel supervised the work of Jonas Drewes. Hynek Biederman supervised the work of Suren Ali. All authors discussed the experimental results and their analysis and revised and approved the manuscript.

DATA AVAILABILITY STATEMENT

The UV-Vis spectra and scanning electron microscopy pictures that support the findings of this study are available from the corresponding author upon reasonable request.

ORCID

Jonas Drewes  <http://orcid.org/0000-0002-8539-1543>

Suren Ali-Ogly  <http://orcid.org/0000-0002-2808-8353>

Thomas Strunskus  <http://orcid.org/0000-0003-3931-5635>

Oleksandr Polonskyi  <http://orcid.org/0000-0001-5013-0944>

Hynek Biederman  <http://orcid.org/0000-0003-4061-8481>

Franz Faupel  <https://orcid.org/0000-0003-3367-1655>

Alexander Vahl  <http://orcid.org/0000-0002-7311-272X>

REFERENCES

- [1] D. Astruc, *Chem. Rev.* **2020**, *120*, 461.
- [2] M. Z. Ghorji, J. Adam, O. C. Aktas, S. Veziroglu, B. B. Shurtleff, T. Strunskus, F. Faupel, O. Polonskyi, A. Hinz, *ACS Appl. Nano Mater.* **2018**, *1*, 3760.
- [3] S. Veziroglu, M. Z. Ghorji, A. L. Obermann, K. Röder, O. Polonskyi, T. Strunskus, F. Faupel, O. C. Aktas, *Phys. Status Solidi A* **2019**, *216*, 1.
- [4] S. Veziroglu, J. Hwang, J. Drewes, I. Barg, J. Shondo, T. Strunskus, O. Polonskyi, F. Faupel, O. C. Aktas, *Mater. Today Chem.* **2020**, *16*, 100251.
- [5] A. Vahl, S. Veziroglu, B. Henkel, T. Strunskus, O. Polonskyi, O. C. Aktas, F. Faupel, *Materials* **2019**, *12*, 2840.
- [6] H. Li, Z. Li, Y. Yu, Y. Ma, W. Yang, F. Wang, X. Yin, X. Wang, *J. Phys. Chem. C* **2017**, *121*, 12071.
- [7] C. Minnai, M. Di Vece, P. Milani, *Nanotechnology* **2017**, *28*, 0.
- [8] C. Minnai, A. Bellacicca, S. A. Brown, P. Milani, *Sci. Rep.* **2017**, *7*, 1.
- [9] M. Mirigliano, D. Decastri, A. Pullia, D. Dellasega, A. Casu, A. Falqui, P. Milani, *Nanotechnology* **2020**, *31*, 234001.
- [10] M. Mirigliano, F. Borghi, A. Podestà, A. Antidormi, L. Colombo, P. Milani, *Nanoscale Adv.* **2019**, *1*, 3119.
- [11] Z. Wang, S. Joshi, S. E. Savel'ev, H. Jiang, R. Midya, P. Lin, M. Hu, N. Ge, J. P. Strachan, Z. Li, Q. Wu, M. Barnell, G. L. Li, H. L. Xin, R. S. Williams, Q. Xia, J. J. Yang, *Nat. Mater.* **2017**, *16*, 101.
- [12] H. Jiang, D. Belkin, S. E. Savel'Ev, S. Lin, Z. Wang, Y. Li, S. Joshi, R. Midya, C. Li, M. Rao, M. Barnell, Q. Wu, J. J. Yang, Q. Xia, *Nat. Commun.* **2017**, *8*, 882.
- [13] B. J. Choi, A. C. Torrezan, K. J. Norris, F. Miao, J. P. Strachan, M. X. Zhang, D. A. A. Ohlberg, N. P. Kobayashi, J. J. Yang, R. S. Williams, *Nano Lett.* **2013**, *13*, 3213.
- [14] S. H. Jo, T. Chang, I. Ebong, B. B. Bhadviya, P. Mazumder, W. Lu, *Nano Lett.* **2010**, *10*, 1297.
- [15] X. B. Yan, J. H. Zhao, S. Liu, Z. Y. Zhou, Q. Liu, J. S. Chen, X. Y. Liu, *Adv. Funct. Mater.* **2018**, *28*, 1.
- [16] V. Postica, A. Vahl, D. Santos-Carballal, T. Dankwort, L. Kienle, M. Hoppe, A. Cadi-Essadek, N. H. De Leeuw, M. I. Terasa, R. Adelung, F. Faupel, O. Lupan, *ACS Appl. Mater. Interfaces* **2019**, *11*, 31452.
- [17] Y. Yong, C. Li, X. Li, T. Li, H. Cui, S. Lv, *J. Phys. Chem. C* **2015**, *119*, 7534.
- [18] S. W. Choi, A. Katoch, G. J. Sun, S. S. Kim, *Sens. Actuators, B* **2013**, *181*, 446.
- [19] F. Fan, J. Zhang, J. Li, N. Zhang, R. R. Hong, X. Deng, P. Tang, D. Li, *Sens. Actuators, B* **2017**, *241*, 895.
- [20] K. Hassan, G. S. Chung, *Sens. Actuators, B* **2017**, *239*, 824.
- [21] S. Enoch, B. Nicolas, A. Adibi, T. W. Hänsch, F. Krausz, B. A. J. Monemar, H. Venghaus, H. Weber, H. Weinfurter, in *Plasmonics* (Eds: S. Enoch, N. Bonod), Springer, Berlin, Heidelberg **2012**.
- [22] P. Anger, P. Bharadwaj, L. Novotny, *Phys. Rev. Lett.* **2006**, *96*, 3.
- [23] H. A. Atwater, A. Polman, *Nat. Mater.* **2010**, *9*, 865.
- [24] H. X. Xu, E. J. Bjerneld, M. Käll, L. Börjesson, *Phys. Rev. Lett.* **1999**, *83*, 4357.
- [25] P. Cherukuri, E. S. Glazer, S. A. Curley, *Adv. Drug Delivery Rev.* **2010**, *62*, 339.
- [26] V. Zaporozhchenko, R. Podschun, U. Schürmann, A. Kulkarni, F. Faupel, *Nanotechnology* **2006**, *17*, 4904.
- [27] X.-F. Zhang, Z.-G. Liu, W. Shen, S. Gurunathan, *Int. J. Mol. Sci.* **2016**, *17*, 1534.
- [28] W. de Heer, *Rev. Mod. Phys.* **1993**, *65*, 611.
- [29] V. N. Popok, E. E. B. Campbell, *Rev. Adv. Mater. Sci.* **2006**, *11*, 19.
- [30] K. Wegner, P. Piseri, H. V. Tafreshi, P. Milani, *J. Phys. D: Appl. Phys.* **2006**, *39*, R439.
- [31] H. Haberland, M. Karrais, M. Mall, Y. Thurner, *J. Vac. Sci. Technol., A* **1992**, *10*, 3266.

- [32] Y. Huttel, *Gas-Phase Synthesis of Nanoparticles*, Wiley-VCH Verlag GmbH & Co. KGaA, Weinheim, Germany **2017**.
- [33] M. Gracia-Pinilla, E. Martínez, G. S. Vidaurri, E. Pérez-Tijerina, *Nanoscale Res. Lett.* **2010**, *5*, 180.
- [34] T. Hihara, K. Sumiyama, *J. Appl. Phys.* **1998**, *84*, 5270.
- [35] S. Pratontep, S. J. Carroll, C. Xirouchaki, M. Streun, R. E. Palmer, *Rev. Sci. Instrum.* **2005**, *76*, 045103.
- [36] M. Hillenkamp, G. Di Domenicantonio, C. Félix, *Rev. Sci. Instrum.* **2006**, *77*, 025104.
- [37] H. Haberland, M. Mall, M. Moseler, Y. Qiang, T. Reiners, Y. Thurner, *J. Vac. Sci. Technol., A* **1994**, *12*, 2925.
- [38] J. Bai, J. P. Wang, *Appl. Phys. Lett.* **2005**, *87*, 1.
- [39] I. Shyumon, M. Gopinadhan, C. A. Helm, B. M. Smirnov, R. Hippler, *Thin Solid Films* **2006**, *500*, 41.
- [40] A. Shelemin, P. Pleskunov, J. Kousal, J. Drewes, J. Hanuš, S. Ali-Ogly, D. Nikitin, P. Solař, J. Kratochvíl, M. Vaidulych, M. Schwartzkopf, O. Kylián, O. Polonskyi, T. Strunskus, F. Faupel, S. V. Roth, H. Biederman, A. Choukourov, *Part. Part. Syst. Character.* **2020**, *37*, 1.
- [41] J. Kousal, A. Shelemin, M. Schwartzkopf, O. Polonskyi, J. Hanuš, P. Solař, M. Vaidulych, D. Nikitin, P. Pleskunov, Z. Krtouš, T. Strunskus, F. Faupel, S. V. Roth, H. Biederman, A. Choukourov, *Nanoscale* **2018**, *10*, 18275.
- [42] D. Nikitin, J. Hanuš, S. Ali-Ogly, O. Polonskyi, J. Drewes, F. Faupel, H. Biederman, A. Choukourov, *Plasma Processes Polym.* **2019**, *16*, 1.
- [43] G. Xu, M. Tazawa, P. Jin, S. Nakao, *Appl. Phys. A: Mater. Sci. Process.* **2005**, *80*, 1535.
- [44] J. J. Mock, M. Barbic, D. R. Smith, D. A. Schultz, S. Schultz, *J. Chem. Phys.* **2002**, *116*, 6755.
- [45] M. Meier, A. Wokaun, *Opt. Lett.* **1983**, *8*, 581.
- [46] P. W. Barber, R. K. Chang, H. Massoudi, *Phys. Rev. Lett.* **1983**, *50*, 997.
- [47] S. J. Oldenburg, *Light Scattering from Gold Nanoshells*, Rice University, Houston, TX, USA **2000**.
- [48] J. Drewes, A. Vahl, N. Carstens, T. Strunskus, O. Polonskyi, F. Faupel, *Plasma Processes Polym.* **2020**, *1*.

SUPPORTING INFORMATION

Additional supporting information may be found in the online version of the article at the publisher's website.

How to cite this article: J. Drewes, S. Ali-Ogly, T. Strunskus, O. Polonskyi, H. Biederman, F. Faupel, A. Vahl, *Plasma Processes Polym.* **2021**, e2100125.
<https://doi.org/10.1002/ppap.202100125>

Supplementary Information to
Impact of argon flow and pressure on the trapping behavior of
nanoparticles inside a gas aggregation source

J. Drewes¹, S. Ali-Ogly², T. Strunskus¹, O. Polonsky^{1,3}, H. Biederman², F. Faupel¹, A. Vahl^{1*}

¹ Institute for Materials Science – Chair for Multicomponent Materials, Faculty of Engineering, Christian-Albrechts-University of Kiel, Kaiserstraße 2, D-24143 Kiel, Germany

² Department of Macromolecular Physics, Faculty of Mathematics and Physics, Charles University, V Holesovickach 2, 18000 Prague, Czech Republic

³ Department of Chemical Engineering, University of California - Santa Barbara, Engineering II, Santa Barbara, CA 93106-5080, United States

Corresponding Author

Dr.-Ing. Alexander Vahl, alva@tf.uni-kiel.de, Institute for Materials Science – Chair for Multicomponent Materials, Faculty of Engineering, Christian-Albrechts-University of Kiel, Kaiserstraße 2, D-24143 Kiel, Germany

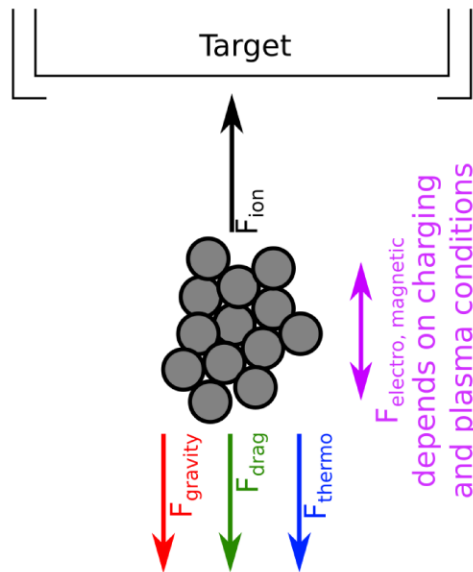


Figure S1: The figure shows possible forces acting on the nanoparticles. The gravitation ($F_{gravity}$), the drag force (F_{drag}) from the Argon gas and the thermophoretic force (F_{thermo}) are pointing in the direction of the orifice. The ion drag force (F_{ion}) is pointing in the target direction. The electromagnetic force ($F_{electro, magnetic}$) can principally act in all direction depending on the charging of the nanoparticles and the plasma environment. An equilibrium of all this forces would cause a trapping of the nanoparticles inside the GAS.

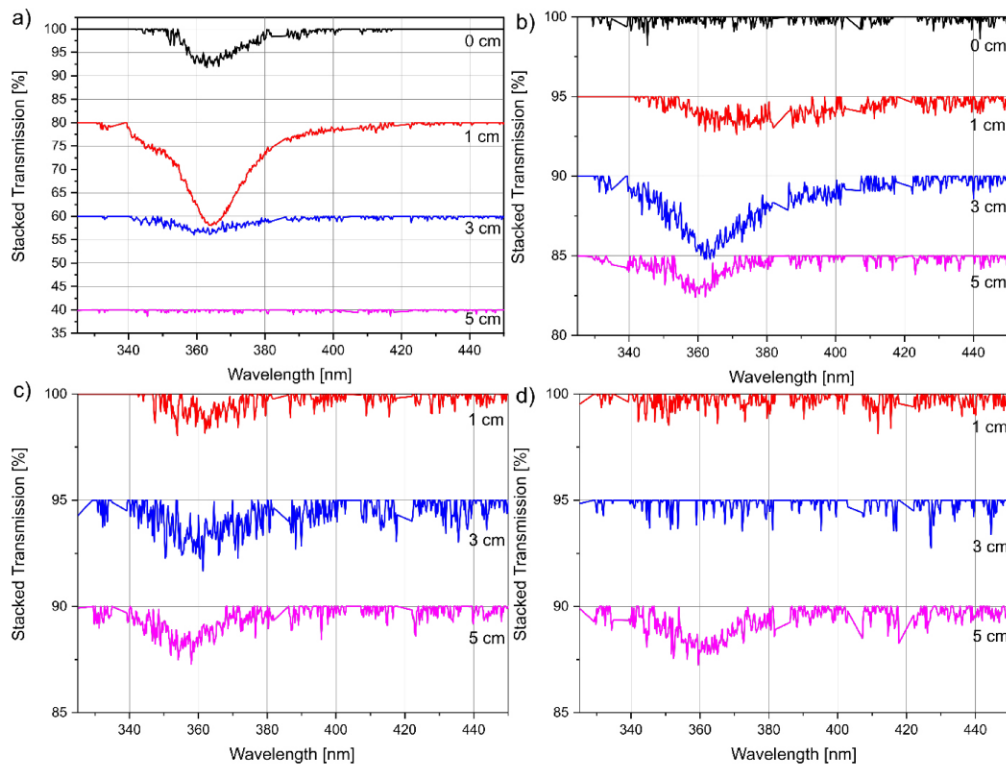


Figure S2: UV-Vis spectra at 24 sccm (a), 60 sccm (b), 96 sccm (c) and 120 sccm (d) at different M-B-distance after discharge was switched on for 10 s. The spectra have an offset of 20 % for 24 sccm and 5 % for 60 sccm, 96 sccm and 120 sccm. It turned out that for 24 sccm the highest absorption was found at 1 cm away from the magnetron which is referred to as "trapping" region. In contrary, the trapping region for 60 sccm was found at 3 cm. For 96 sccm and 120 sccm nearly no absorption could be found. For 0 cm no recording was done, because in pre-experiments was already found that no signal can be found for MDB of 0 cm. Because the deposition rate was much higher for 96 sccm and 120 sccm the deposition time was reduced. So the spectra shown are after 10 s discharge on and not 30 s like in the main body of this manuscript, because the deposition time was reduced in accordance to the QCM rate.

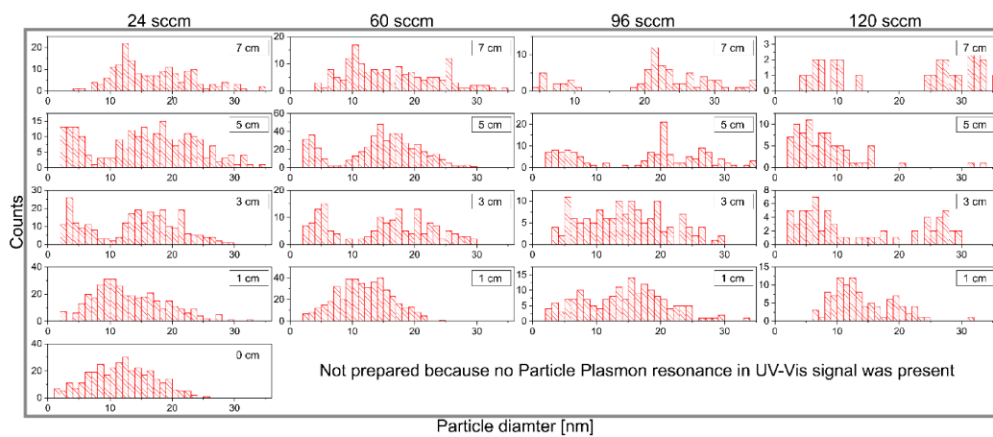


Figure S3: Size distributions of Ag NPs out of SEM images at different M-B-distance and a flow of 24 sccm, 60 sccm, 96 sccm and 120 sccm. The sputter power is 100 W. The different M-B-distance are indicated in the figure.

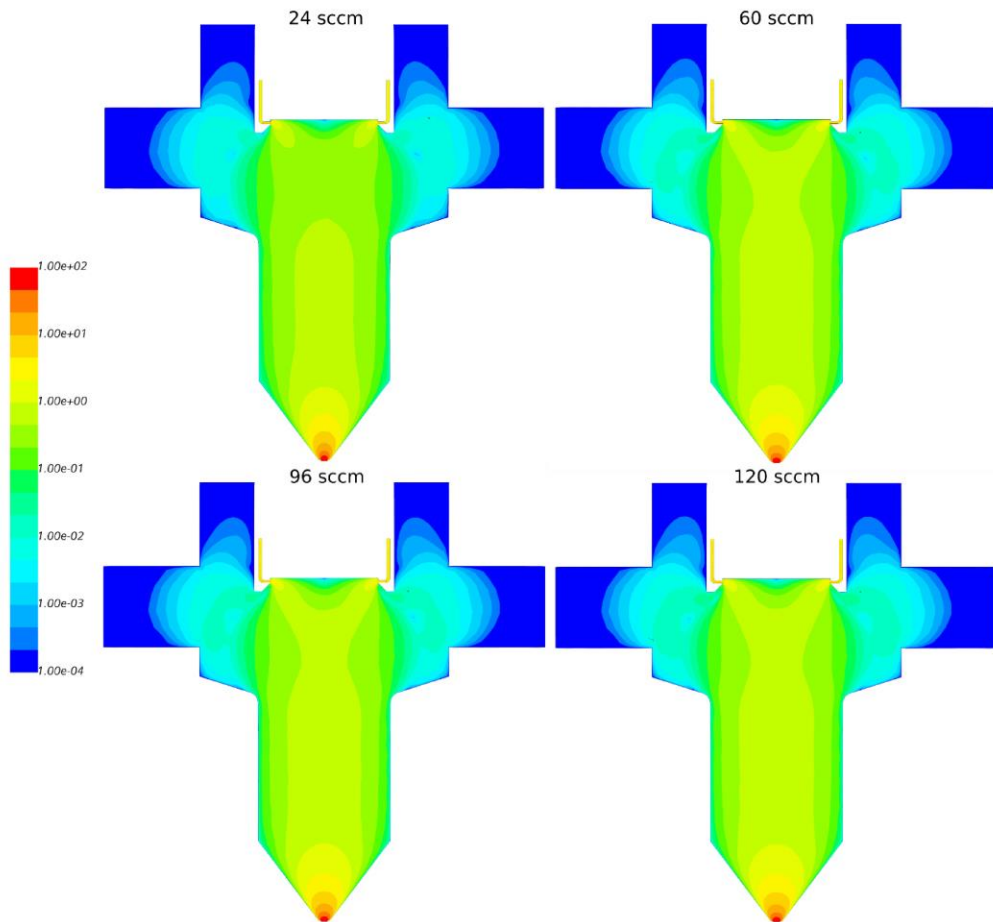


Figure S4: CFD simulations for 24, 60, 96 and 120 sccm at M-B-distance of 0 cm are shown. The velocity scale is set to logarithmic scale in contrary to the shown CFD simulations in the paper. In that representation, the maximum and minimum values of the gas velocity are well visible but nearly no other changes are observable. For that reason, a linear velocity scale with the maximum of 0.5 m/s was chosen in the paper to increase the visibility of changes in the gas flow in the regions of interest.

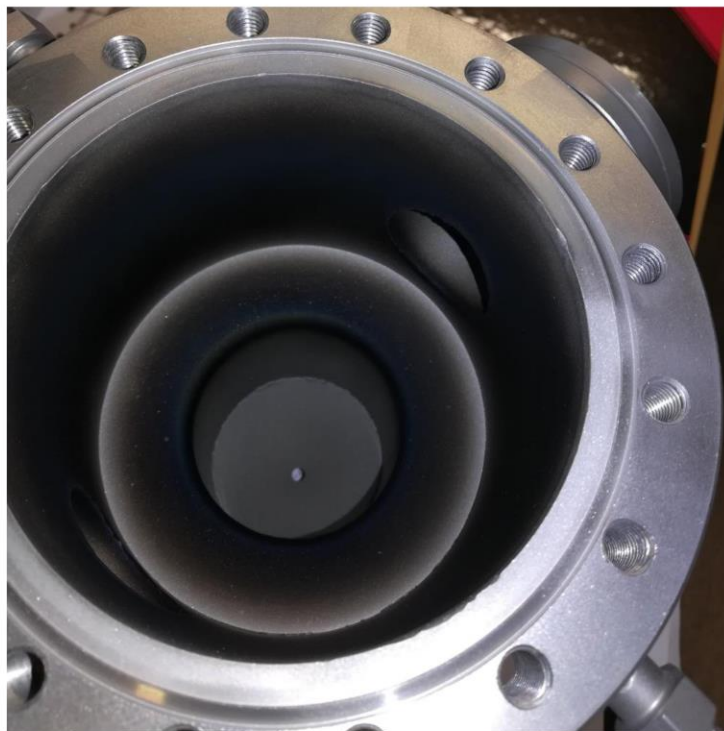


Figure S5: Exemplary photograph of a GAS after long deposition time. A lot of deposition can be found on the chamber walls indicated by black color.

CFD Simulations

In the typical Haberland gas aggregation nanocluster source, nanoparticles are dragged by the flow of the carrier gas in the aggregation volume. Afterwards, nanoparticles extracted from the source through an orifice in to the deposition chamber. The pressure inside the GAS is tens or several hundreds of Pascal. CFD simulation showed that the carrier gas velocity inside the GAS may reach some tens of cm/s. Relatively high pressure and relatively high velocities allows us to treat the carrier gas as viscous laminar flow in the cylindrical part of the cluster source. Under such conditions the nanoparticles have much bigger cross-section than the atoms of the carrier gas and their velocity is equal to the drift velocity of the gas.

Relatively low Knudsen number ($Kn < 0.01$) (see Figure S 7) allows us to treat the carrier gas flow as a continuum and we may solve carrier gas flow motion equation using computational fluid dynamics (CFD). For that purpose, the software Siemens STAR CCM+ 15.04.010 R8 (double precision) was used. In the regions with transitional flow ($0.01 < Kn < 0.1$), we applied corrections, specifically Maxwell slip correction.

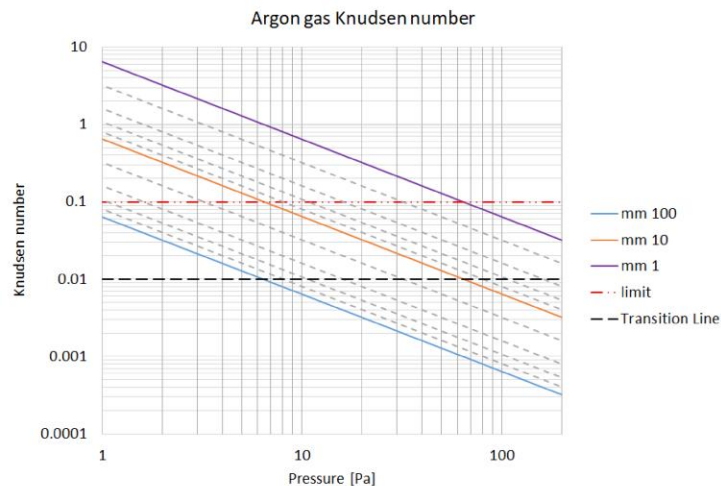


Figure S6: Knudsen number (Kn) diagram. Kn defines if the treated flow obeys continuity law or behaves as free particle motion (molecular flow). Kn is a ratio between mean free path and characteristic length of the geometry. Flow that has $Kn < 0.1$ is assumed to be purely continuous, which is a major portion of the fluid domain in the analysis; $0.01 < Kn < 0.1$ is a transitional flow (correction needed in orifice, inlet channel), $Kn > 0.1$ molecular flow (not used in the simulation)

For CFD analysis, certain assumptions were made:

- Fluid was assumed to be ideal gas and to be compressible
- No slip on the walls were expected, except of the regions with transitional Knudsen number (orifice, deposition chamber, etc.), where Maxwell partial slip model was used
- Flow of the fluid was expected to be laminar
- Polyhedral mesh was produced for this simulation
- No electromagnetic model was used

Referring to the mentioned assumptions, there was decided to use steady state analysis, employing segregated flow solver with 2nd order convection. SIMPLE pressure-velocity (Semi-Implicit Method for Pressure Linked Equations) coupling algorithm was used to solve Navier-Stokes equations.

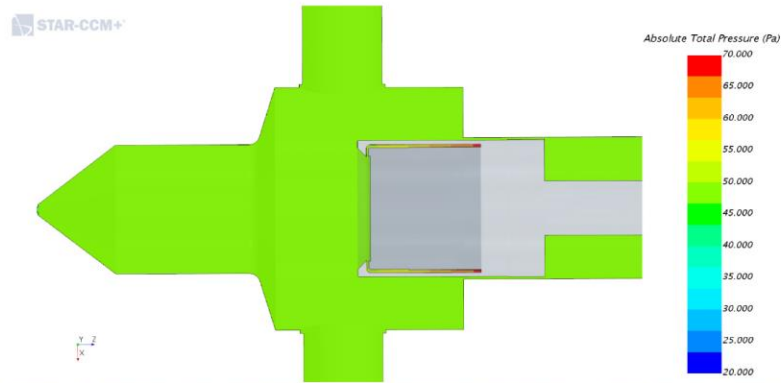


Figure S7: Exemplarily simulated total pressure distribution inside the GAS for Ar flow of 24 sccm.

3.5 Publication D: In-situ Laser Light Scattering for Temporally and Locally Resolved Studies on Nanoparticle Trapping in a Gas Aggregation Source

In this publication, LLS was used the first time successfully to observe the growth and transport of NPs inside a HGAS with good spatial and temporal resolution. Finally, it was possible to detect the NPs with a 2-dimensional resolution, which was impossible with the SAXS and UV-Vis measurements.

The fast growth kinetics were investigated for the middle gas inlet configuration, where the gas inlet is located in the center of the target. Here vortices were observed left and right from the central axis through the HGAS. It was seen that the growth and transport of NPs is far away from equilibrium and the intensity of scattered particles never reaches a constant value. In this work it was observed as well that when the plasma is switched off the trapped NPs are removed immediately. This proves that electro-magnetic forces play a crucial role, although the trapping pattern looks like vortices and must therefore originate at least partially from the gas flow. Additionally, different trapping locations were observed in the dependence of the gas inlet. This observation proved how important the gas flow pattern is, because although all parameters like power, gas flow, pressure and HGAS geometry were kept constant, the gas inlet configuration changes the trapping behavior significantly. QCM and SEM investigations of the deposited NPs have shown that the deposition rate and the size distributions are also affected by the gas inlet configuration.

In comparison to SAXS and UV-Vis spectroscopy, this method was able to give a 2D representation of the NP growth and transport inside the HGAS. The information provided by the LLS method in terms of temporal and spatial resolution could not be obtained by the two other methods used in the previous publications. Nevertheless, LLS cannot provide information about the size and density of NPs, because the intensity depends on both.

Own contributions to this publication are the conceptualization, the conductance of the experiments, data processing and writing of the manuscript.

This chapter is a reprint from the following publication:

Drewes, J., Rehders, S., Strunskus, T., Kersten, H., Faupel, F., & Vahl, A. (2022). In Situ Laser Light Scattering for Temporally and Locally Resolved Studies on Nanoparticle Trapping in a Gas Aggregation Source. *Particle & Particle Systems Characterization*, 2200112. <https://doi.org/10.1002/ppsc.202200112>

In Situ Laser Light Scattering for Temporally and Locally Resolved Studies on Nanoparticle Trapping in a Gas Aggregation Source

Jonas Drewes, Stefan Rehders, Thomas Strunskus, Holger Kersten, Franz Faupel, and Alexander Vahl*

Gas phase synthesis of nanoparticles (NPs) via magnetron sputtering in a gas aggregation source (GAS) has become a well-established method since its conceptualization three decades ago. NP formation is commonly described in terms of nucleation, growth, and transport alongside the gas stream. However, the NP formation and transport involve complex non-equilibrium processes, which are still the subject of investigation. The development of in situ investigation techniques such as UV-Vis spectroscopy and small angle X-ray scattering enabled further insights into the dynamic processes inside the GAS and have recently revealed NP trapping at different distances from the magnetron source. The main drawback of these techniques is their limited spatial resolution. To understand the spatio-temporal behavior of NP trapping, an in situ laser light scattering technique is applied in this study. By this approach, silver NPs are made visible inside the GAS with good spatial and temporal resolution. It is found that the argon gas pressure, as well as different gas inlet configurations, have a strong impact on the trapping behavior of NPs inside the GAS. The different gas inlet configurations not only affect the trapping of NPs, but also the size distribution and deposition rate of NPs.

1. Introduction

Noble metal nanoparticles (NPs) are used in many applications, ranging from catalysis,^[1] photocatalysis,^[2–4] optics,^[5] and resistive switching^[6–11] to sensors.^[12–16] Especially the optical properties are well tunable because they depend strongly on the shape, size, size distribution, and the surrounding medium.^[17,18]


A lot of synthesis methods for NPs are available and range from biological over chemical to physical processes.^[19,20] The most often used strategy is the solution-based chemical synthesis. This approach has the drawback that the synthesized NPs are contaminated with, for example, surfactants.^[19] Physical vapor deposition (PVD) techniques stand out with their extremely high purity of the synthesized NPs. Moreover, it is much easier to produce alloy particles and compound particles with tailored composition.^[21] The PVD

strategies range from surface energy-related self-organization of NPs on solid substrates^[22–25] and in liquids^[26–28] to gas phase synthesis.^[8,29] The gas phase synthesis relies often on so-called gas aggregation sources (GASs). They encompass laser ablation,^[29] pulsed microplasma cluster source,^[8] and magnetron sputtering.^[30] The GAS equipped with a magnetron was firstly developed by Haberland et. al. in 1992. Here a magnetron is operated at comparatively high pressures (typically between some 10 Pa and few 100 Pa) in contrast to normal magnetron sputtering for the preparation of thin films. Due to the higher pressure, the mean free path of the sputtered atoms is shorter, which enables three-body collisions (two sputtered atoms are colliding with one gas atom) and leads to the formation of dimers.^[31] This enables further attachment of sputtered atoms, and the dimers can grow further to clusters and NPs. These NPs are guided by the drag force due to the gas flow outside the GAS into the deposition chamber, where they can be deposited onto various substrates.^[30]

Although the fundamental three-body collision process and consecutive nucleation, growth, coalescence, and transport are well discussed in literature, still not all ongoing processes inside such sources are completely understood. For example, the impact of the gas flow pattern inside a GAS was for a long time only superficially investigated. Nevertheless, previous studies have shown that

J. Drewes, S. Rehders, T. Strunskus, F. Faupel, A. Vahl
 Chair for Multicomponent Materials
 Institute of Materials Science
 Kiel University
 Kaiserstr. 2, D-24143 Kiel, Germany
 E-mail: alva@tf.uni-kiel.de

T. Strunskus, H. Kersten, F. Faupel, A. Vahl
 Kiel Nano
 Surface and Interface Science KiNSIS
 Kiel University
 Christian-Albrechts-Platz 4, D-24118 Kiel, Germany
 H. Kersten
 Chair for Plasma Technology
 Institute of Experimental and Applied Physics
 Kiel University
 Leibnizstr.19, D-24098 Kiel, Germany

 The ORCID identification number(s) for the author(s) of this article can be found under <https://doi.org/10.1002/ppsc.202200112>.

© 2022 The Authors. Particle & Particle Systems Characterization published by Wiley-VCH GmbH. This is an open access article under the terms of the Creative Commons Attribution-NonCommercial License, which permits use, distribution and reproduction in any medium, provided the original work is properly cited and is not used for commercial purposes.

DOI: 10.1002/ppsc.202200112

the gas flow pattern inside a GAS plays a crucial role.^[32–36] For example if low-velocity regions are present inside a GAS, NPs can get lost in the chamber walls or the target.^[36] This effect strongly impacts the material conversion efficiency of a GAS.

To improve the performance of GAS sources, in the last decade several in situ techniques were utilized already to analyze the growth and transport of NPs inside the GAS. Examples are in situ small angle X-ray scattering (SAX)^[37,38] and in situ UV–Vis.^[33,36] Both techniques provided further insights into the dynamic processes inside the GAS and have revealed NP trapping at different distances from the magnetron source. Even though these techniques can provide information about the NP size, the techniques suffer from their low spatial resolution.

Therefore, a technique with good spatial and temporal resolution to investigate the processes inside the GAS is urgently needed. Different laser light scattering (LLS) techniques have been successfully used to investigate NP growth and transport in situ in plasmas but not inside a GAS. Some methods rely on Mie scattering^[39–41] and others on Rayleigh scattering.^[42–45] Mie scattering techniques are Mie ellipsometry, angular-resolved Mie scattering, and 2D imaging Mie ellipsometry. By these methods, NPs of radii between 80–200 nm can be detected, for example, inside a dusty plasma. By evaluation of the polarization also the size distribution of the NPs can be evaluated in situ inside the plasma.^[39–41] The limit for the NP diameter between Mie scattering and Rayleigh scattering is about 1/10 of the wavelength. Because the usual size of NPs which are prepared with a GAS is typically below 50 nm and the wavelength of the applied laser is 532 nm, Mie scattering techniques are not applicable to the GAS.

Therefore, in this study LLS based on Rayleigh scattering has been used. A laser plane through the GAS is created and in a 90° configuration a camera with color filter is mounted to the GAS. The scattered light by the NPs can be detected and so the location of NPs inside the GAS can be observed. In this way the LLS technique was often used in conventional RF dusty plasmas but not in a GAS.^[42–45] Here no information about the size distributions can be found, but other techniques like in situ SAX or in situ UV–Vis can provide this information. However, they cannot provide precise information about the location of NPs. For that reason, LLS can be seen as a complementary tool to understand the ongoing processes inside a GAS.

Here, LLS of Ag NPs will be utilized to extract better spatial information about the trapping positions of NPs inside a custom-built GAS based on a typical design. To study the impact of the Ar gas flow pattern on the NP formation and transport process, three different types of gas inlets are investigated. The results from the LLS for different gas inlets will be complemented by size distributions obtained by scanning electron microscopy (SEM) measurements of the deposited NPs and the measured deposition rates.

2. Experimental Section

2.1. Setup of the Experiment

In typical gas aggregation deposition experiments, the GAS sources have commonly only 4 flanges. In this common

4-flange-setup, one flange was used to attach the magnetron and one flange (on the opposite side) was used for the orifice. Additionally, two ports perpendicular to the main axis of the GAS were used for analytical purposes.^[21,33,37,38,46] Computational fluid dynamic simulations (CFD) have shown that additional ports, which do not taper the cross-section of the GAS, do not significantly influence the gas velocity distribution.^[33,46] Therefore, additional analytical ports were considered uncritical for the growth and transport of NPs. For this study more than two analytical ports were needed, which motivated the choice to build a GAS based on a CF 63 cross with 6 ports (**Figure 1**). On the back-left port, a 2-inch custom-made magnetron was mounted. The design of the magnetron was based on the “Ionix” magnetron series from the company Thin Films Consulting. On one of the ports (front right in **Figure 1a**) a cone with a 3 mm orifice was installed and connected to the deposition chamber. Two other ports of the GAS, which were located directly next to each other, were equipped with glass windows for the optical scattering system. On the remaining ports, the pressure gauge and a blind flange were installed. The deposition chamber was equipped with a QCM (Quartz Crystal Microbalance) and load-lock, which enables fast sample transfer without breaking the vacuum.

The GAS was mounted to the deposition chamber. The orifice connects the GAS and the deposition chamber. The deposition chamber was evacuated by a turbo pump (Pfeiffer, HiPace 60 P) with a scroll fore pump (Edwards, nXDS 6i). The base pressure is in the range of 10^{−7} mbar. The loadlock was equipped with a turbo pump (Pfeiffer, TMU 071 P) with a scroll fore pump (Edwards, nXDS 6i). The gas flow was controlled via mass flow controller (MKS Instruments, 1179BX22CM1BV, 200 sccm range of N₂). The used Ar gas flows are 109.6, 1370, 164.4, 191.8, and 219.2 sccm with the corresponding pressures in the GAS of 118, 141, 163, 183, and 204 Pa, respectively.

The custom-made magnetron enables three different gas inlet configurations. Therefore, the original design of thin Films consulting was professionally overhauled. The three different inlet configurations are shown in **Figure 1b**. The first configuration was termed normal inlet based on the default design of thin Films Consulting. In the normal inlet configuration, the gas was injected into the chamber between the magnetron and the ground cap. The custom-made magnetron used here enables the gas to be injected through the middle of the target. This is called middle inlet. Here the difficulty was to guide the Ar gas between the ground cap and the magnetron and finally under the target through the central bore (5 mm diameter) inside the target. It was important to prevent large stagnation pressures between the magnetron and the ground cap, because this can cause plasma ignition at this undesired point. The bore was closed with a stainless-steel mesh on the same electrical level as the target surface. Otherwise, plasma ignition can take place inside the bore. The third inlet configuration was the behind inlet configuration, which can be often found in literature.^[33,37,38] Here the gas inlet was located somewhere behind the magnetron. Ag was always used as a target material (99.99% purity, Kurt J. Lesker, 2 inch)).

An MDX 500 from Advanced Energy supplies the DC power to the magnetron. It was used in the power regulation mode, which is always set to 300 W.

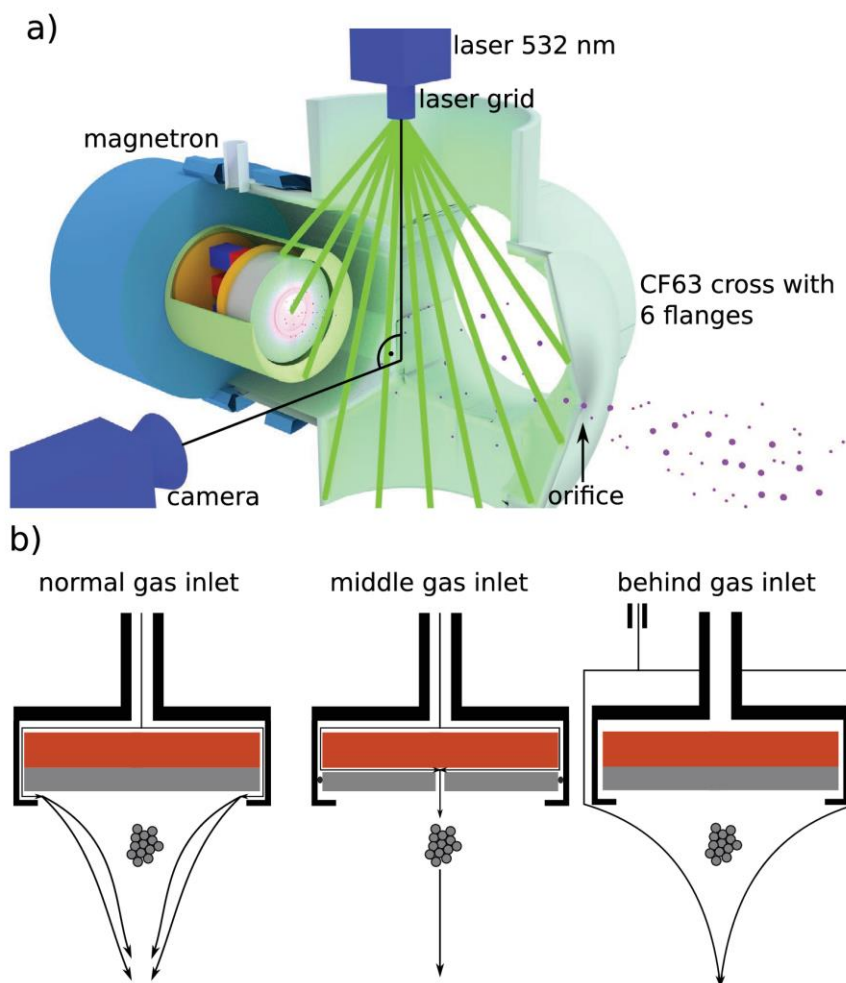


Figure 1. a) Measurement setup for the in situ laser scattering experiments in the GAS. The GAS is based on a CF63 cross with 6 flanges. On the back left flange, the magnetron is mounted. On two side flanges, two windows are mounted. On one window the camera with a color filter for green light is mounted and on the other window the laser. The laser beam is split by a grid so, that the plane from the center of the magnetron to the orifice is illuminated. b) The three different types of gas inlets are shown. For the normal gas inlet, the gas is inserted between the magnetron and the ground cap so that the gas is directed onto the target surface. The middle gas inlet means that the gas is injected through the middle of the target. The third gas inlet configuration is termed behind inlet, which means that the gas is injected somewhere behind the magnetron and the gas flows around the ground cap.

The scattering system consists of a laser with a wavelength of 532 nm with a power of 450 mW (Roitner Laser Technik, RLTMGL-532 1–450 mW) and a CMOS camera (XIMEA, MQ042CG-CM), with a color filter, which transmits light with a wavelength of 532 nm but blocks most of the light with different wavelength, which was generated by the plasma. The framerate of the camera was fixed at 25 frames per s. In front of the laser, a grid was installed which created out of the single beam a laser plane under an opening angle of 30° . The laser and the camera were installed under a 90° angle, and the laser plane includes the center line from the target to the orifice and lies normal to the camera (Figure 1).

For SEM investigations, NPs were deposited inside the vacuum chamber at a distance of 16 cm from the GAS exit

orifice. Here, as substrate material, p-doped, (100) oriented Si wafer pieces with native oxide (cut to $1 \times 1 \text{ cm}^2$, SiMat) were used. The SEM analysis was done with a Zeiss Ultra Plus microscope.

2.2. Image Formation

First, the image formation and the image processing will be described. In general, three different effects were contributing to the recorded raw image of the camera: The reflections of the incident laser light from the chamber walls, the plasma emission, and the scattered light from the NPs. The latter one contains the information about the location of NPs, which was of interest for this study.

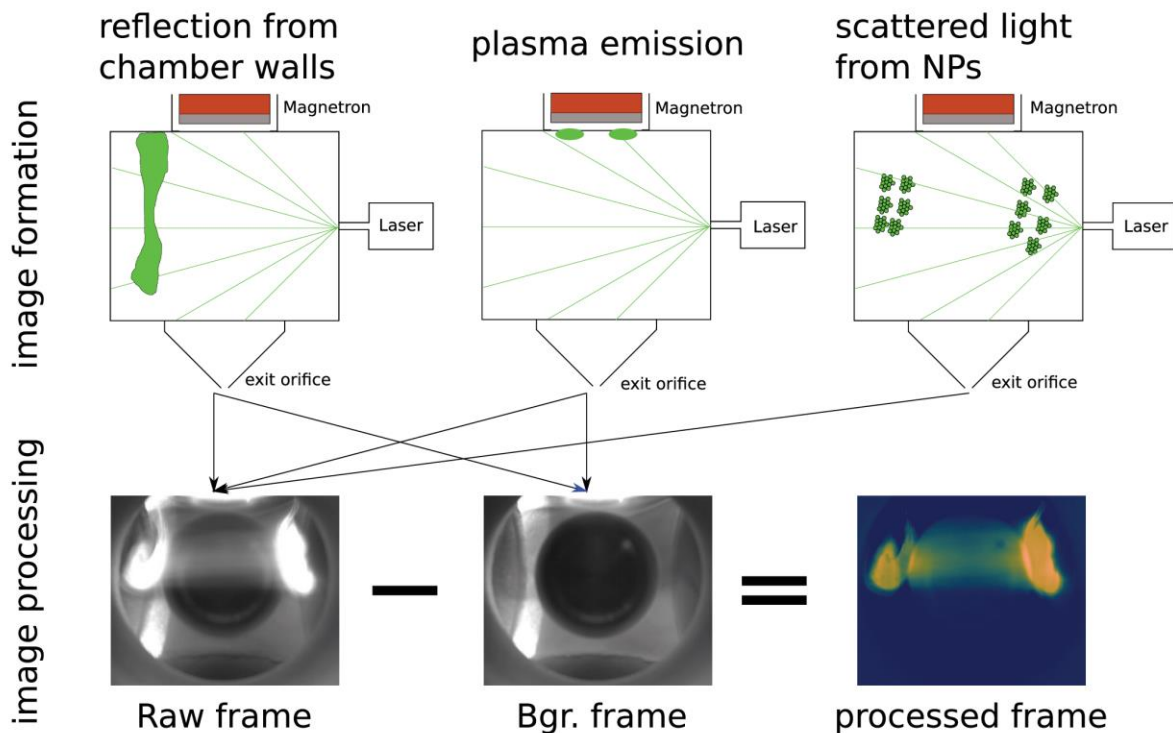


Figure 2. Schematic of image formation and image processing by the Matlab script. In the top row, the three light contributions inside the chamber are shown: Reflection from chamber walls, plasma emission, and the scattered light from NPs. In the bottom row, the video processing by the Matlab script is illustrated. The arrows from the top to the bottom row are visualizing the contributions from the different light sources into the raw frame and the background frame.

Information about the locations of NPs can be obtained due to the Rayleigh scattering phenomenon. The Rayleigh scattering equation tells us that the scattering Intensity (I) depends on the particle size (a), the refractive index of the medium (n_{med}), the intensity of the incident light (I_0), the distance from the scattering object to the detector (d), the wavelength of laser light in vacuum (λ_0), the particle relative refractive index (m), and the test angle (θ):^[47]

$$I = \frac{8\pi^4 a^6 n_{\text{med}}^4 I_0}{d^2 \lambda_0^4} \left| \frac{m^2 - 1}{m^2 + 1} \right|^2 (1 + \cos^2 \theta) \quad (1)$$

For the LLS method, the two most important varying parameters were the particle size and particle density. The scattering equation shows that the scattering intensity depends on particle size to the sixth power. Since this equation gives the scattering intensity for one particle, the scattering intensity depends only linearly on the particle density. The dependence on the size of the NPs and the particle density was important for the interpretation of the LLS images.

The different contributions to the raw image are schematically shown in **Figure 2**. The plasma emission and the reflections from the chamber walls do not contain the desired spatial information about the NPs. Therefore, the videos have to be processed after the experiments before further analysis. The

color filter used in front of the camera already filters out the main portion of the plasma emission but still, a small portion contributes to the image. Since the chamber walls were curved, always some reflected laser light can enter the camera. In the end, the remaining plasma emission and the reflected light from the chamber walls have to be subtracted to obtain the information about the location of the NPs. This was done with a Matlab script and will be described in detail in the next chapter.

2.3. Image Recording and Processing

To extract only the signal of NPs out of the video, a Matlab script was used to subtract the emission and the scattered light from the chamber walls. The procedure was as follows: The camera recording was started prior to the experiment. The program detects the start of the plasma discharge and synchronizes the recording of the camera with the plasma ignition. Half a second after the plasma was ignited a background frame was taken. This frame contains the plasma emission and the reflected light from the chamber walls but no signal from NPs. A previous study has shown that it takes some seconds until NPs were detected inside a GAS.^[36,38] For that reason, half a second was chosen for the background frame. This background frame was subtracted afterwards from the whole video. Then

the program transfers the video into a color plot to increase the visibility in comparison to a mono-colored picture (Figure 2). In addition, the program sums up all pixel values for each frame after the background subtraction. These summed-up values are called cumulative intensity and can be plotted over time to analyze the temporal development of the intensity within one experiment. Furthermore, one can integrate over the whole experimental time to obtain the total intensity of one experiment to compare experiments with each other.

3. Results and Discussion

This study is structured in four different sections. In the first section, the temporal changes in the spatial distribution of NPs inside the GAS will be discussed for one gas inlet configuration with a specific flow. By this example, the dynamic processes inside the GAS will be visualized and discussed. In the second part, the spatial NP distribution inside the GAS

for three different gas inlets and five different gas flows and pressures will be evaluated. The aim is to study the influence of GAS geometries and different gas flow patterns on the trapping behavior of NPs inside the GAS. In the third section, the change in the size distribution of the deposited NPs will be discussed to understand the dependence between the growth processes of NPs and the gas flow pattern. In the last section, the impact of different gas inlets and pressures on the deposition rate will be analyzed to understand the impact of different gas inlets and flows on the efficiency of the NP synthesis.

3.1. Dynamic Processes of NP Formation and Transport

In the first part of this study, an exemplary typical LLS image time series for the middle inlet configuration will be discussed. Figure 3a shows schematically how the magnetron, the laser, and the exit orifice are located in relation to the field of view of the camera. Within this field of view, different features can be

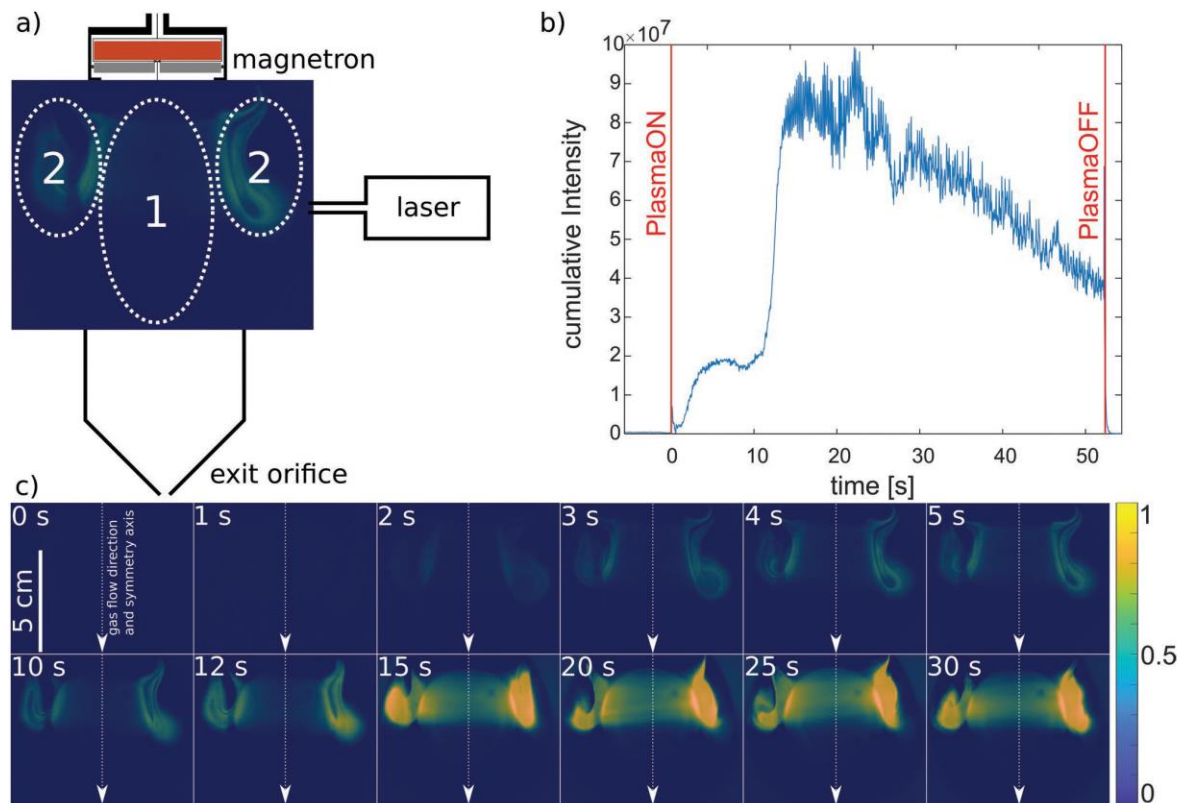


Figure 3. a) Left the position of the magnetron and the orifice are schematically drawn into an exemplary LLS image to clarify where the NPs are in comparison to the magnetron and the orifice. Moreover, three different regions are labeled inside the LLS image. The edge regions (marked as 2) are located left and right and the center region (marked as 1) in the middle of the LLS image. (b) The plot shows on the x-axis the time and on the y-axis the cumulative intensity. The cumulative light intensity is the sum of all pixel values from the whole picture. It first increases until ≈ 7 s before it reaches a local maximum and shortly decreases until ≈ 10 s. Then it increases further until ≈ 15 s and then decreases until the plasma is switched OFF. (c) LLS images for the middle inlet configuration with a pressure of 183 Pa for 0, 1, 2, 3, 4, 5, 10, 12, 15, 20, 25, and 30 s after the plasma is switched on. It is visible, that the intensity is increasing over time, indicating growth of NPs or increasing NP density. The NPs are trapped only in the edge regions of the GAS and it appears to have a vortex-like shape. Additionally, the dotted arrows are indicating the gas flow direction and the symmetry axis of the GAS.

observed. These include the center region in the middle of the picture (marked as 1) and the edge regions left and right in the image (marked as 2). Directly after starting the magnetron discharge, the NP formation process is far away from equilibrium, as at 0 s there are no nuclei or preformed particles in the source. Therefore, the early stages of the gas phase synthesis are particularly interesting to study. For this reason, the time period between 0 and 5 s is depicted in detail in Figure 3c. The time 0 s corresponds to the moment where the plasma is switched on. After 2 s scattered light from the NPs becomes visible and the intensity is increasing up to 15 s. Not only the intensity is increasing over time but also the shape and the dimensions of the trapped NPs in the edge regions are changing. The NP cloud looks like vortexes are present. The vortex behavior is much more visible in the processed videos. Therefore, one video for each inlet configuration can be found in the supporting information. In Figure 3c only at the edge regions, NPs are visible and not in the center regions. Additionally, the image series shows that the growth and transport of NPs inside the gas is a highly dynamic process. Finally, Figure 3b shows the cumulative intensity of the whole LLS image over time. This means that all pixel values of the images are summed up for each frame. This plot indicates also that the processes of NP formation and transport inside the GAS are time-dependent. In the beginning, the cumulative intensity is increasing until ≈ 5 s before it reaches a local maximum and shortly decreases until ≈ 10 s. Then it increases further until ≈ 15 s and then decreases until the plasma is switched off. That the intensity increases, in the beginning, is due to the NP formation and further growth of these NPs, which can be also seen in the LLS images from 0 to 5 s. The decrease is caused by fewer NPs or smaller NPs, respectively. Since the Rayleigh scattering depends strongly on the size of the NPs (to the power of 6) but also on the number of particles, this method cannot distinguish between the impact of size and number of NPs (discussed in detail in Section 2.3). One other reason could be that the NPs are simply moving in and out of the inspected region which is related to the small width of the laser plane. By the example of the time series of LLS images, it is presented how complex the NPs' growth and transport behavior in GAS is. Since prior to the deposition no metal atoms and no NPs are present in the gas phase it will take a certain time until it is possible, that nucleation, cluster growth, and transport of NPs out of the growing region are in a steady state. Perhaps a stable steady state can never be reached, because of the fast kinetics and also increasing temperature of the chamber walls. Nevertheless, the fundamental features of the LLS image stay relatively constant over the whole deposition time, which indicates that the NPs are trapped by an interplay out of drag forces and electromagnetic forces. This is in line with earlier reports on trapping of NPs inside the GAS.^[33,34,36–38]

In these earlier studies, techniques like in situ UV-Vis or in situ SAX were used to analyze the growth and transport of NPs. These techniques average data out of the whole interaction volume of the light beam or X-ray beam. In comparison to these studies, LLS has the distinct advantage, that the signal originates from one two-dimensional plane out of the GAS. This enables the exact localization of NPs inside the GAS although the size and the number of NPs cannot be evaluated. Also, the fact that the cumulative intensity drops down extremely fast

after the switch-off, shows that the NP trapping must be related to electromagnetic forces which are missing when the plasma is switched off. Assuming the NPs are trapped only because of turbulences inside the gas flow, the NPs would still stay in the turbulences when the plasma is switched off because the gas flow is not much affected by the plasma. The fact that the NPs are immediately vanishing when the plasma is switched off indicates trapping due to the interplay of electromagnetic forces and drag force.^[33]

3.2. Impact of Gas Inlet and Gas Flow/Pressure on the NP Trapping Behavior

After having discussed the fundamental features of the dynamic phenomena after starting the gas phase synthesis of NPs, in the following section it will be shown how different gas inlet configurations and different Ar gas flows and pressures will change the trapping behavior of the NPs inside the GAS. Figure 4 shows 15 LLS images taken after 30 s of operation and all with the same discharge power. 30 s were chosen because the gas phase synthesis process approaches an equilibrium, where the relative intensity distribution between the different trapping locations does not change significantly over time. Each row corresponds to one pressure and gas flow, which is increasing from left to right. Each line corresponds to one inlet configuration: first the middle configuration, then the normal inlet configuration, and in the last row the behind configuration. The first point to make is that the intensities for all inlet configurations are increasing with an increase in gas flow/pressure. This can be caused by more efficient NP nucleation at higher pressures which produce more NPs.^[48] One can also distinguish between two different trapping regions. One is located at the edge region and one is located in the center region like it was shown in Figure 3a. For the behind configuration, the NPs are only trapped in the center region, and trapping was only observed for high pressures of 183 and 204 Pa. In contrast to that, the middle configuration shows only trapping at the edge regions, and trapping was observed from 141 to 204 Pa. The normal inlet configuration shows a transition from vortex-like trapping at the edge regions (at lower pressures) towards a superposition of both trapping regions (at higher pressures). From 118 to 163 Pa the NPs are only trapped at the edge regions. For 183 and 204 Pa the normal inlet configuration shows trapping at both locations.

For better visualization of the exact positions of the NP trapping regions, the field of view of the camera is divided into 9 quadrants (Figure 5a). Then the intensities of the quadrants I and III (representative for edge regions) are summed up and divided by the sum of quadrants V and VIII (representative for center region) for each frame (Figure 5b). This is done because the edge trapping regions are always located in the quadrants I and III. The trapping of NPs in the central region is always located in the quadrants V and VIII. Therefore, for the calculation of the ratio of intensities only the quadrants I, III, V, and VIII are considered. In every time bin, 25 sequential frames are taken to calculate the mean intensity values for regions I, III, V, and VII. One bin contains 1 s of time and the bin 1 s, ranges from 0 to 1 s. For each bin, the ratio of intensities is

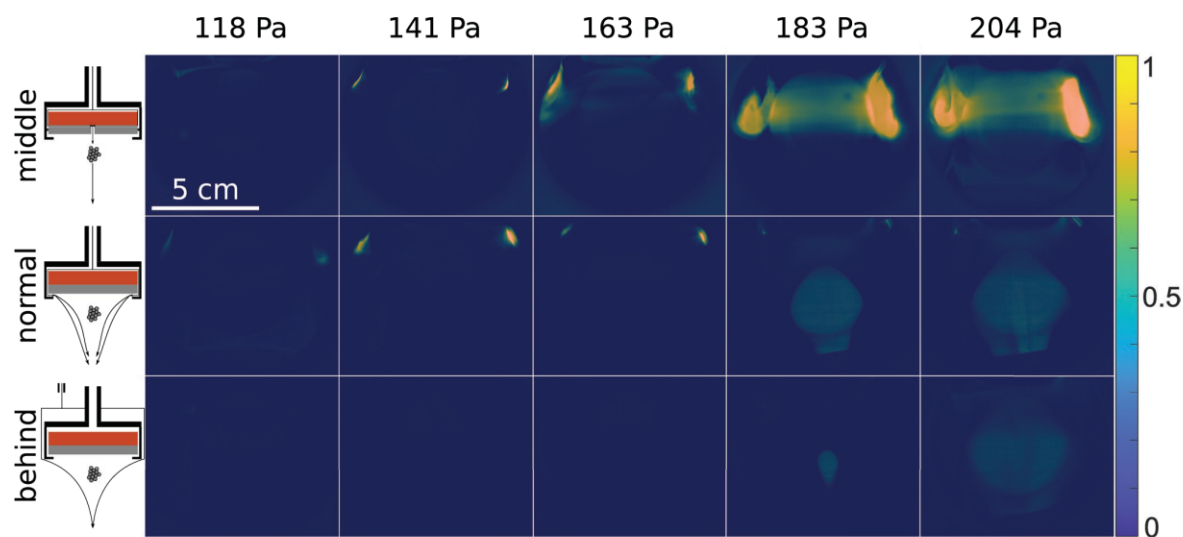


Figure 4. 15 LLS images for different gas inlet configurations and pressures after 30 s of magnetron operation are shown. The pressure is increasing from the left side to the right side. Each row corresponds to one inlet configuration: the first row to the middle inlet, the second to the normal inlet, and the third to the behind inlet. It is visible that for normal configuration NPs are found at the edge regions and also in the center region of the GAS. The middle configuration shows only NP trapping at the edge region. The behind configuration shows NPs only in the center region.

calculated from these mean intensity values. The color scale for the time bins goes from black over red to yellow and represents increasing deposition time. By this method the time dependence of the ratio of intensities becomes visible. If the calculated ratio is clearly smaller than 1, the center regions are dominating. If the ratio is clearly above one, the edge regions are dominating. Assuming that the size distribution of NPs in all quadrants is similar, the ratio gives the information at which position the majority of NPs are located.

Figure 5b shows for the normal configuration, that for a low pressure no clear trend of the location of trapped NPs is present. This is related to the low LLS signal in this experiment. For pressures of 141 and 163 Pa the majority of NPs are clearly located at the edge regions. With increasing time the ratio of intensities increases which shows that more and more NPs are located in the edge regions over time in comparison to the center regions. At higher pressures the trend is different. Here the majority of NPs are trapped at the center region, which is most probably caused by the increasing pressure and flow, which leads to higher drag forces and finally changes the trapping position from the edge regions to the center region.

The behind configuration shows no clear tendency for pressure from 118 to 163 Pa, which is related to the low signal, which can be also seen in Figure 4. For pressures of 183 and 204 Pa the majority of NPs are trapped in the center regions. That no trapping is observed in the behind configuration in the edge regions in contrast to the normal configuration is most probably caused by different gas velocity distribution inside the GAS. CFD simulations have shown, that the velocity is always highest at the inlet and the outlet orifice.^[32–36] In regions, which are not in the direct path between inlet and outlet the velocity is small. For the normal configuration, a low velocity at the edge

regions can be assumed. In contrast to that, the velocity for the behind configuration will be higher. Therefore, less or no trapping is expected for the behind configuration at the edge regions, which the experiments also proved.

For the middle configuration for pressures higher than 141 Pa, the majority of NPs were always at the edge regions. For the lowest pressure of 118 Pa again no clear trend is visible, which is also related to the low LLS signal. The reason for the trapping at the edge regions for this inlet configuration is also explained by the gas velocity distribution. The highest gas velocity is expected in the center of the gas since the gas inlet and outlet are located in the central axis of the GAS. Therefore, trapping in the center is unexpected, as the LLS results have successfully shown.

3.3. Influence of Gas Inlet and Gas Flow/Pressure on the NP Size Distribution

In this part of the study, the influence of gas flow, pressure, and inlet configuration on the size distribution of the deposited NPs will be discussed. It will be shown that the mean diameter of the deposited NPs does not exhibit the same trend for all inlet configurations in dependence on the gas flow/pressure. Figure 6 shows six size distributions with corresponding SEM images as insets. The left column corresponds to a pressure of 118 Pa and the right column to 204 Pa. The first row corresponds to the middle inlet configuration, the second row to the normal configuration, and the last row to the behind inlet configuration. It is important to note that for the middle inlet row, for the normal inlet for a pressure of 204 Pa and for the behind inlet for a pressure of 204 Pa the largest NPs are not visible in the distribution. Their size is shown directly in the SEM

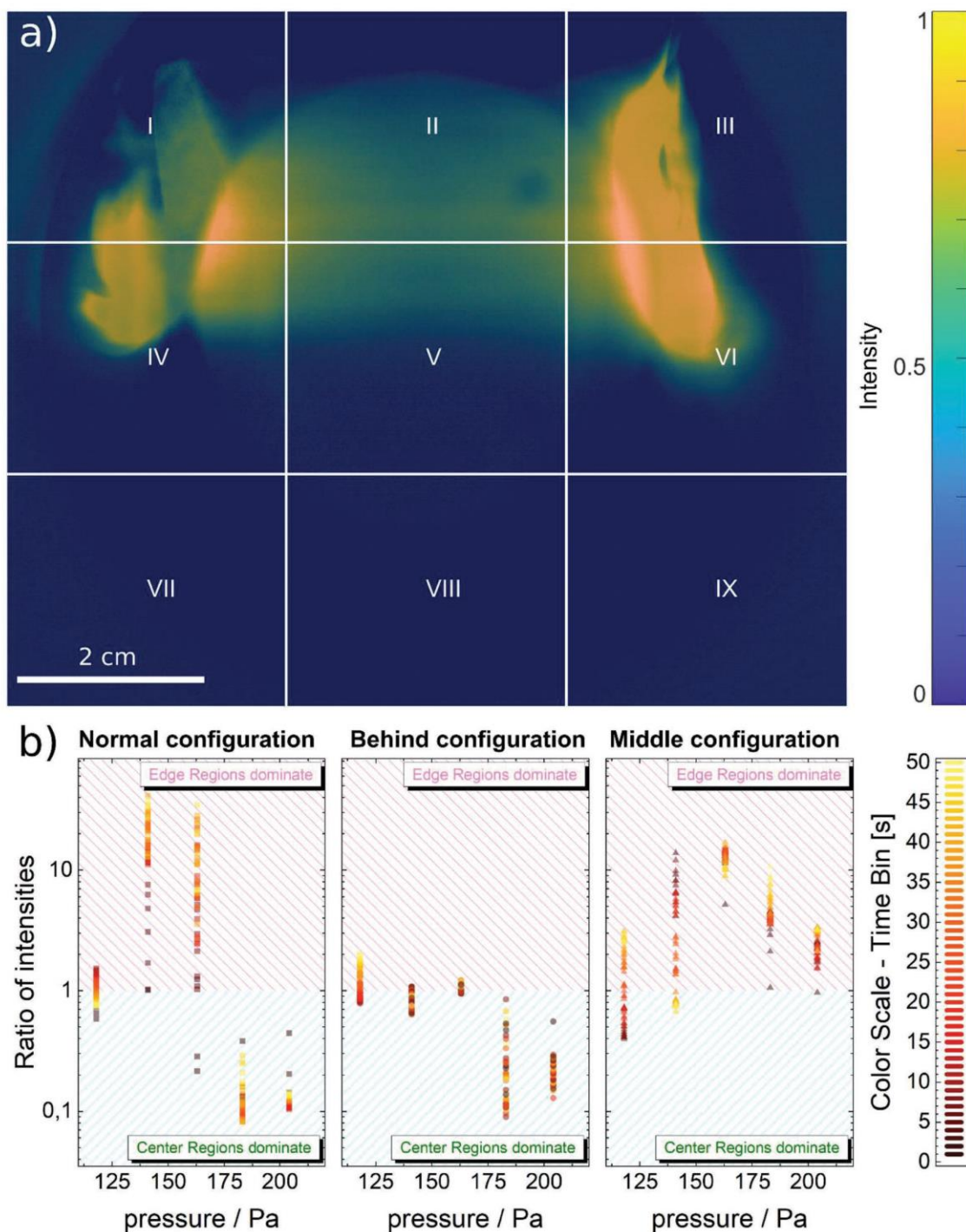


Figure 5. a) Exemplary LLS image for the middle configuration with a pressure of 183 Pa after 30 s of operation. The picture is divided into 9 quadrants. The labeling of the quadrants is important for following calculations. b) The plot shows the ratio of intensities vs. pressure for the three different types of gas inlets. The intensities of the quadrants I and III are summed up and divided by the sum of quadrants V and VIII for each bin. For each bin, the intensities of 25 sequential frames are considered, which corresponds to 1 s. The color scale goes from black (first time bin) over red to yellow and represents an increasing bin number, which is proportional to increasing deposition time (b).

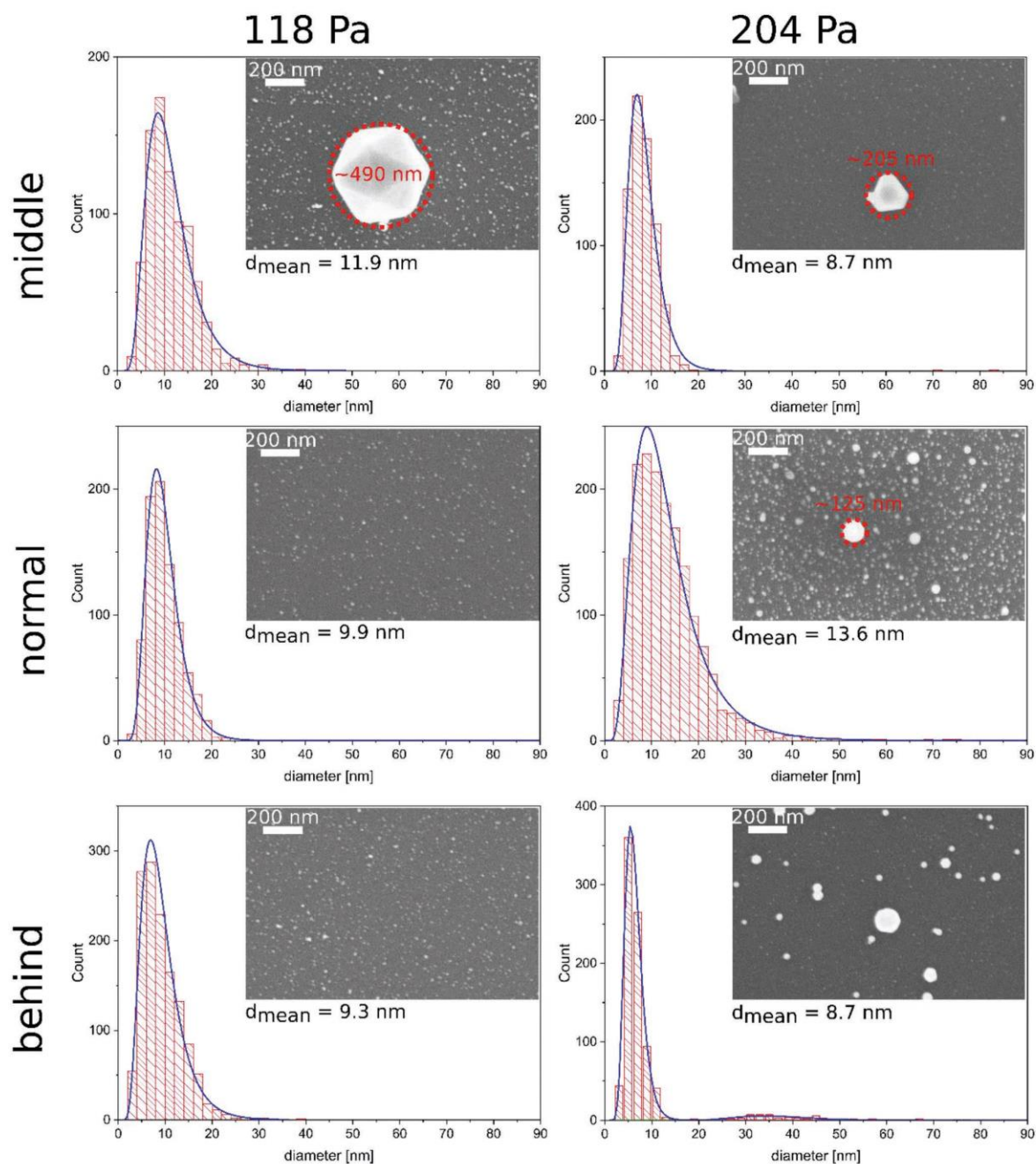


Figure 6. Size distributions and SEM micrographs as insets for two different flows for each type of gas inlet configuration. The left column corresponds to pressure of 118 Pa and the right to 204 Pa. The first row corresponds to the middle gas inlet, the second to the normal gas inlet, and the last one to the behind gas inlet. Additionally, the mean diameter of the size distribution is depicted in the histograms.

pictures because the visibility of the size distributions would be worsened when these particles would be included.

In general, for all gas configurations and pressures log normal distributions are obtained except the behind configura-

tion, which shows a bimodal log normal distribution for a pressure of 204 Pa. All fitting parameters, the mean value, and the fitting function for all size distributions are presented in Table S1 and Equation S1, Supporting Information. When

comparing the mean values of the distributions, the normal configuration shows an increase from 9.9 to 13.6 nm. In contrast to that, the mean for the middle configuration and the behind configuration is decreasing from lower to higher pressure. The mean for the middle configuration decreases from 11.9 to 8.7 nm and for the behind configuration from 9.3 to 8.7 nm.

This behavior of the NPs size is counter-intuitive because one would expect the same trend of the size distribution with increasing flow/pressure for all inlet configurations. This shows once more how important the influence of the gas inlet configuration is. The literature explanation for the flow/pressure dependence on the NPs' size is, that for an increase in Ar flow/pressure the mean NP size and broadness of the distribution is firstly increasing and after a maximum at higher flow decreasing again. This is related to the more effective nucleation with higher pressures in the beginning. At higher flows, the reduced residence time stops the growth of NPs at earlier stages and reduces the probability for coalescence of NPs, which leads to smaller NP sizes.^[49–51] From this explanation one would expect the same trend for all gas inlets, but the results indicate different behaviors for different gas inlets.

Although most of the NPs have a size of around 11.9 nm, the middle inlet configuration additionally shows a pressure of 118 Pa, an NP with a diameter of ≈ 490 nm and for a pressure of 204 Pa, an NP of ≈ 205 nm in the examined region ($20 \mu\text{m}^2$). The shape suggests that these NPs are monocrystalline due to crystalline facets. A diameter of ≈ 490 nm was never produced before in our experiments with normal gas inlets inside a Haberland-type GAS. In the Supporting Information, SEM pictures with lower magnifications are shown (Figure S1, Supporting Information). They show that in the observed region for the middle inlet configuration for a pressure of 118 Pa, indeed, only one NP with a diameter of ≈ 490 nm was found. On the other hand, for a pressure of 204 Pa more NPs with diameters larger than 100 nm were found in the analyzed area.

The different trends in the flow/pressure dependence on the gas inlet position and also the observation of large NPs (greater than 200 nm) for the middle inlet configuration can be explained perhaps with different gas velocity distributions inside the GAS for different gas inlets. CFD simulations in other publications have shown that a broad velocity distribution is present inside the GAS and that also vortex regions can be present. The simulations have also shown that the highest velocity was always found at the inlet and outlet of the gas.^[32–36] Since the gas inlet position was varied, a different gas velocity distribution is expected for all gas inlet configurations. This can cause different release probabilities for the trapped NPs in the GAS.

In the middle configuration, for example, the trapping regions are in the edge regions. Here it is most probably more difficult for NPs to escape and get deposited onto the substrate. It is possible that the larger NPs with diameters above 200 nm are originating from these regions. For the normal and behind configuration one trapping region is in the center. These NPs may escape more often than NPs in the edge regions. Since the residence time of trapped NPs is higher, they have more time to grow. This is perhaps the reason why the size distributions are also showing different trends depending on the gas inlet and

pressure. This potentially also explains the bimodal distribution for the behind inlet at a pressure of 204 Pa. This shows once more how important the gas inlet and fluid dynamics are inside a GAS.

3.4. Impact of Gas Inlet and Gas Flow/Pressure on the Deposition Rate

After the effect of different gas inlets and pressures on the location of trapped NP and their size distributions were discussed in the last section, we will show how the deposition rate is influenced by the different gas inlet geometries and gas flows and pressures. To determine the deposition rate, a QCM is used. The change in the resonance frequency of the QCM crystal is directly proportional to the deposited mass and, therefore, to the mass of deposited NPs. **Figure 7** shows the absolute difference in frequency of the QCM for a deposition of 60 s for all inlet configurations in dependence on the pressure. It is obvious that for all inlet configurations the deposited mass for increasing from 118 to 183 Pa. Up to a pressure of 183 Pa, the behind configuration has a higher deposited mass in comparison to the other configurations. The middle inlet configuration shows the lowest deposited mass in this pressure interval. For 204 Pa all configurations are showing a drastic increase in the deposited mass. The configuration with the highest deposited mass is the middle configuration with 521 Hz, followed by the normal inlet with 212 Hz, followed by the behind inlet with 128 Hz. The general increase of deposition rate with increasing flow and pressure for all configurations can be explained by better NP growth conditions and better NP transport.^[52] But this does not explain why the behind configuration up to a pressure of 183 Pa always shows higher deposition rates than the other configurations. This must be related to less NP trapping for the behind configuration in comparison to the other

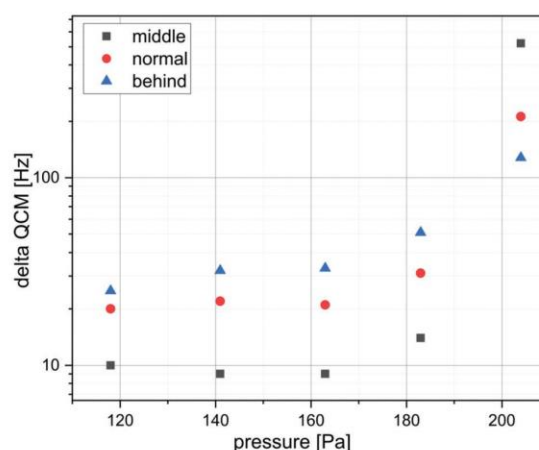


Figure 7. The left plot shows the delta QCM value (absolute difference in frequency after 60 s deposition time) vs. the pressure for all types of inlet configurations. The absolute difference in frequency is directly proportional to the deposited mass. It is obvious that for all inlet configurations the deposited mass is increasing from 118 to 183 Pa. For 204 Pa all configurations are showing a drastic increase in the deposited mass.

configurations, which is in line with the results from the LLS measurements (Section 3.2).

The reason for this behavior can be explained by the gas flow. In the middle configuration, the highest gas velocity can be assumed to be in the center region of the GAS from the inlet to the orifice. On the other hand, the gas velocity at the sides will be much lower. This means that the drag force which can release the particles from the GAS is in the center much higher in comparison to the edge regions. NPs which are located at the edge regions are not efficiently dragged to the orifice in comparison to the NPs in the center. Figure 4 shows clearly that in the middle configuration particles are only trapped at the edge regions and not in the center region.

Comparing this behavior with the behind configuration, the strongest difference is that no NP trapping at the edge regions of the GAS occurs, because in the edge regions the gas velocity, and so the drag force, is higher in relation to the middle inlet (Figure 4). Also, the deposited mass is higher up to 183 Pa for the behind configuration than for the middle configuration (Figure 7). This indicates that trapping is less pronounced in this configuration in comparison to the middle configuration.

The position of the trapping regions for the normal inlet configuration is of interest, too. Up to a pressure of 163 Pa, the NP are predominantly trapped at the sides. For higher pressures, the signal in this trapping region is reduced and a new trapping zone in the bottom center appears. It is clear that due to different GAS inlet configuration, the gas velocity is low at the edges in comparison to the behind configuration. But in the center, the velocity is most probably still lower in comparison to the middle configuration.

At 204 Pa the order of the gas inlets with the maximum deposition rate is changing. Here, the middle inlet shows the highest deposition rate, followed by the normal inlet and then the behind inlet. The middle inlet shows the highest deposition rate, which may be caused by stronger turbulences inside the GAS. This may affect NPs from the edge regions leaving the trapping by too high centrifugal forces, which push them into the central regions where the gas flow guides them to the orifice. This is perhaps also the explanation for the higher deposition rate of the normal inlet in comparison to the behind inlet configuration for a pressure of 204 Pa. Because also for the normal inlet configuration still NP trapping was observed in the edge regions. Interestingly the finding, that the behind configuration showed up to a pressure of 183 Pa always a higher deposition rate in comparison to the normal inlet, is contrary to the findings by Sanzone et. al.^[32] They observed that the deposition rate of Au NPs for a normal configuration was 20 times higher compared to behind inlet even though the sputtering power was roughly 4 times higher for the behind configuration (31 W vs. 8 W). The observed different outcomes can be potentially traced back to differences in the source geometry as well as the applied DC power (300 W in this study compared to 31 or 8 W in the work by Sanzone et. al.). On the one hand, a change in power strongly affects the plasma parameters, which can lead finally to a variation of the trapping forces acting on the NPs. On the other hand, Sanzone et. al. observed a strong increase from 8 to 31 W in the deposition rate for the normal configuration. This indicates that the nucleation process was most probably not extremely efficient at the lower power settings. The

reason could be, that for low power fewer sputtered atoms are present in the aggregation volume, which reduces the probability for three-body collisions. These aspects are expected to severely impact the trapping forces and the nucleation process, which may explain the observed different results. Taken all together, the middle inlet seems to produce more efficient trapping in comparison to the behind and normal inlet. This is caused by different gas velocity distributions inside the GAS. To reduce the amount of trapping it would be beneficial to design an inlet configuration where the gas enters the GAS at the middle inlet and also from behind the magnetron. This would reduce the trapping regions and can increase the overall deposited mass and material conversion efficiency. Additionally, the general source dimension and geometry can potentially be improved with the help of CFD simulations, which aid the prediction of low-velocity regions inside the source during the design process. One option for future improvements could be to decrease the diameter of the source to nearly the diameter of the ground cap of the magnetron. In this case, the development of trapping regions, which were observed in the edge regions would be impeded by the constrained GAS dimensions. This may prevent trapping in these regions, but simultaneously may cause more sputtered atoms to be deposited onto the chamber walls, which in turn would reduce the efficiency of the GAS. Here, CFD simulations combined with experimental tests should allow to find the optimum geometry.

4. Conclusion and Outlook

NP formation and transport inside a GAS are highly dynamic processes. A deeper understanding of the gas phase synthesis in a magnetron-based GAS requires elaborate in situ diagnostic methods. This study demonstrates how LLS can be applied to obtain in situ time-resolved information on the location of NP trapping. In the future, the LLS technique could be improved by light sources with different and smaller wavelengths to estimate the sizes of the trapped NPs. Additionally, more powerful light sources and a better camera, with a high frame rate and a low exposure time, could be used to learn more about the forces acting on the NPs, if the release could be monitored when the plasma is switched off.

Nevertheless, the LLS results have shown that NPs are trapped in different regions inside a GAS. The trapping position and LLS intensity of NPs inside the gas depend strongly on the gas flow and pressure. Additionally, three different gas inlet configurations and their impact on the NP trapping were studied. It turned out, that the location of the gas inlet is the most important parameter, which affects the confinement and the size distribution of NPs. The middle inlet showed the strongest trapping of NPs with a vortex-like behavior. However, the position of the trapping was only at the edge regions, which was also expectable because of the high gas velocity in the center of the source. This indicates that this configuration is perhaps not the most efficient gas inlet configuration for a GAS. Nevertheless, it has also shown how efficiently the gas inlet position can change the trapping behavior and the size distribution of the resulting NPs. Even when only three types of gas inlet locations were investigated in this work, many options

are possible to improve the transport of NPs inside the GAS. Different kinds of inlet configurations can be used to prevent NP trapping or even make use of the trapping to tailor the properties of the resulting NPs. A combination of the LLS technique, together with in situ UV-Vis or in situ SAX and CFD simulations may enable the development of a novel and highly efficient GAS.

Supporting Information

Supporting Information is available from the Wiley Online Library or from the author.

Acknowledgements

Funded by the Deutsche Forschungsgemeinschaft (DFG, German Research Foundation) – Project IDs 411452476; 434434223.
Open access funding enabled and organized by Projekt DEAL.

Conflict of Interest

The authors declare no conflict of interest.

Author Contributions

J.D., A.V., S.R., T.S. H.K., and F.F. developed the idea and conceived the initial design of the study. J.D. and S.R. established the experimental setup and constructed the magnetron with different gas inlets. J.D. performed the Ag NP depositions, recorded the LLS videos, and performed the SEM measurements. J.D. developed the Matlab code for the processing of the LLS videos. J.D. and A.V. analyzed the results and prepared the manuscript draft. A.V. and F.F. supervised the work of J.D. All authors discussed the experimental results and their analysis and revised and approved the manuscript.

Data Availability Statement

The data that support the findings of this study are available from the corresponding author upon reasonable request.

Keywords

dusty plasma, gas aggregation source, gas phase synthesis, in situ laser light scattering, nanoparticles, trapping

Received: June 8, 2022

Revised: July 14, 2022

Published online:

- [1] D. Astruc, *Chem. Rev.* **2020**, *120*, 461.
[2] S. Veziroglu, J. Hwang, J. Drewes, I. Barg, J. Shondo, T. Strunskus, O. Polonskyi, F. Faupel, O. C. Aktas, *Mater. Today Chem.* **2020**, *16*, 100251.
[3] A. Vahl, S. Veziroglu, B. Henkel, T. Strunskus, O. Polonskyi, O. C. Aktas, F. Faupel, *Materials* **2019**, *12*, 2840.

- [4] H. Li, Z. Li, Y. Yu, Y. Ma, W. Yang, F. Wang, X. Yin, X. Wang, *J. Phys. Chem. C* **2017**, *121*, 12071.
[5] C. Minnai, M. di Vece, P. Milani, *Nanotechnology* **2017**, *28*, 355702.
[6] C. Minnai, A. Bellacicca, S. A. Brown, P. Milani, *Sci. Rep.* **2017**, *7*, 7955.
[7] M. Mirigliano, D. Decastri, A. Pullia, D. Dellasega, A. Casu, A. Falqui, P. Milani, *Nanotechnol.* **2020**, *31*, 234001.
[8] M. Mirigliano, F. Borghi, A. Podestà, A. Antidormi, L. Colombo, P. Milani, *Nanoscale Adv.* **2019**, *1*, 3119.
[9] Z. Wang, S. Joshi, Savel'ev, H. Jiang, R. Midya, P. Lin, M. Hu, N. Ge, J. P. Strachan, Z. Li, Q. Wu, M. Barnell, G. L. Li, H. L. Xin, R. S. Williams, Q. Xia, J. J. Yang, *Nat. Mater.* **2017**, *16*, 101.
[10] H. Jiang, D. Belkin, S. E. Savel'Ev, S. Lin, Z. Wang, Y. Li, S. Joshi, R. Midya, C. Li, M. Rao, M. Barnell, Q. Wu, J. J. Yang, Q. Xia, *Nat. Commun.* **2017**, *8*, 882.
[11] B. J. Choi, A. C. Torrezan, K. J. Norris, F. Miao, J. P. Strachan, M. X. Zhang, D. A. A. Ohlberg, N. P. Kobayashi, J. J. Yang, R. S. Williams, *Nano Lett.* **2013**, *13*, 3213.
[12] V. Postica, A. Vahl, D. Santos-Carballal, T. Dankwort, L. Kienle, M. Hoppe, A. Cadi-Essadek, N. H. de Leeuw, M. I. Terasa, R. Adelung, F. Faupel, O. Lupan, *ACS Appl. Mater. Interfaces* **2019**, *11*, 31452.
[13] Y. Yong, C. Li, X. Li, T. Li, H. Cui, S. Lv, *J. Phys. Chem. C* **2015**, *119*, 7534.
[14] S. W. Choi, A. Katoch, G. J. Sun, S. S. Kim, *Sens. Actuators, B* **2013**, *181*, 446.
[15] F. Fan, J. Zhang, J. Li, N. Zhang, R. R. Hong, X. Deng, P. Tang, D. Li, *Sens. Actuators, B* **2017**, *241*, 895.
[16] K. Hassan, G. S. Chung, *Sens. Actuators, B* **2017**, *239*, 824.
[17] R. Ferrando, J. Jellinek, R. L. Johnston, *Chem. Rev.* **2008**, *108*, 845.
[18] B. Choi, H.-H. Lee, S. Jin, S. Chun, S.-H. Kim, *Nanotechnology* **2007**, *18*, 075706.
[19] X.-F. Zhang, Z.-G. Liu, W. Shen, S. Gurunathan, *Int. J. Mol. Sci.* **2016**, *17*, 1534.
[20] S. Gurunathan, K. Kalishwaralal, R. Vaidyanathan, D. Venkataraman, S. R. K. Pandian, J. Muniyandi, N. Hariharan, S. H. Eom, *Colloids Surf., B* **2009**, *74*, 328.
[21] J. Drewes, A. Vahl, N. Carstens, T. Strunskus, O. Polonskyi, F. Faupel, *Plasma Processes Polym.* **2020**, *8*, 1.
[22] N. Alissawi, V. Zaporotchenko, T. Strunskus, I. Kocabas, V. S. K. Chakravadhanula, L. Kienle, D. Garbe-Schönberg, F. Faupel, *Gold Bull.* **2013**, *46*, 3.
[23] M. Petr, O. Kylián, A. Kuzminova, J. Kratochvíl, I. Khalakhan, J. Hanuš, H. Biederman, *Opt. Mater.* **2017**, *64*, 276.
[24] H. T. Beyene, V. S. K. Chakravadhanula, C. Hanisch, M. Elbahri, T. Strunskus, V. Zaporotchenko, L. Kienle, F. Faupel, *J. Mater. Sci.* **2010**, *45*, 5865.
[25] M. Gensch, M. Schwartzkopf, W. Ohm, C. J. Brett, P. Pandit, S. K. Vayalil, L. Bießmann, L. P. Kreuzer, J. Drewes, O. Polonskyi, T. Strunskus, F. Faupel, A. Stierle, P. Müller-Buschbaum, S. v. Roth, *ACS Appl. Mater. Interfaces* **2019**, *11*, 29416.
[26] M. T. Nguyen, T. Yonezawa, *Sci. Technol. Adv. Mater.* **2018**, *19*, 883.
[27] M. T. Nguyen, T. Yonezawa, Y. Wang, T. Tokunaga, *Mater. Lett.* **2016**, *171*, 75.
[28] M. Meischein, M. Fork, A. Ludwig, *Nanomaterials* **2020**, *10*, 525.
[29] S. Vučković, M. Svanqvist, V. N. Popok, *Rev. Sci. Instrum.* **2008**, *79*, 073303.
[30] H. Haberland, M. Karrais, M. Mall, Y. Thurner, *Jourf. Vac. Sci. Technol., A* **1992**, *10*, 3266.
[31] P. Grammatikopoulos, *Curr. Opin. Chem. Eng.* **2019**, *23*, 164.
[32] G. Sanzone, J. Yin, K. Cooke, H. Sun, P. Lievens, *Rev. Sci. Instrum.* **2021**, *92*, 033901.
[33] D. Nikitin, J. Hanuš, S. Ali-Ogly, O. Polonskyi, J. Drewes, F. Faupel, H. Biederman, A. Choukourov, *Plasma Processes Polym.* **2019**, *16*, 1900079.

- [34] D. Nikitin, J. Hanuš, P. Pleskunov, Z. Krtouš, S. Ali-Ogly, R. Tafichuk, K. Biliak, M. Protsak, J. Valter, J. Vyskočil, A. Choukourov, H. Biederman, *Plasma Processes Polym.* **2021**, 16, 1.
- [35] R. Rudd, A. Obrusník, P. Zikán, R. Pratt, C. Hall, P. Murphy, D. Evans, E. Charrault, *Surf. Coat. Technol.* **2016**, 314, 125.
- [36] J. Drewes, S. Ali-Ogly, T. Strunskus, T. Polonskyi, H. Biederman, F. Faupel, A. Vahl, *Plasma Processes Polym.* **2021**, 2100125.
- [37] J. Kousal, A. Shelemin, M. Schwartzkopf, O. Polonskyi, J. Hanuš, P. Solař, M. Vaidulych, D. Nikitin, P. Pleskunov, Z. Krtouš, T. Strunskus, F. Faupel, S. v. Roth, H. Biederman, A. Choukourov, *Nanoscale*. **2018**, 10, 18275.
- [38] A. Shelemin, P. Pleskunov, J. Kousal, J. Drewes, J. Hanuš, S. Ali-Ogly, D. Nikitin, P. Solař, J. Kratochvíl, M. Vaidulych, M. Schwartzkopf, O. Kylián, O. Polonskyi, T. Strunskus, F. Faupel, S. v. Roth, H. Biederman, A. Choukourov, *Part. Part. Syst. Charact.* **2020**, 37, 1900436.
- [39] I. Pilch, F. Greiner, *J. Appl. Phys.* **2017**, 121, 113302.
- [40] F. Greiner, J. Carstensen, N. Köhler, I. Pilch, H. Ketelsen, S. Knist, A. Piel, *Plasma Sources Science, Technology* **2012**, 21, 065005.
- [41] F. Greiner, A. Melzer, B. Tadsen, S. Groth, C. Killer, F. Kirchschrager, F. Wieben, I. Pilch, H. Krüger, D. Block, A. Piel, S. Wolf, *Eur. Phys. J. D* **2018**, 72, 81.
- [42] Y. Qin, U. R. Kortshagen, E. S. Aydil, *J. Phys. D: Appl. Phys.* **2016**, 49, 085203.
- [43] M. Mikikian, M. Cavarroc, L. Couëdel, Y. Tessier, L. Boufendi, *Pure Appl. Chem.* **2010**, 82, 1273.
- [44] Z. Marvi, E. von Wahl, T. Trottenberg, H. Kersten, *J. Appl. Phys.* **2020**, 127, 173301.
- [45] F. M. J. H. van de Wetering, R. J. C. Brooimans, S. Nijdam, J. Beckers, G. M. W. Kroesen, *J. Phys. D: Appl. Phys.* **2015**, 48, 035204.
- [46] J. Drewes, S. Ali-Ogly, T. Strunskus, O. Polonskyi, H. Biederman, F. Faupel, A. Vahl, *Plasma Processes Polym.* **2022**, 19, 2100125.
- [47] C. Z. Huang, J. Ling, J. Wang, in *Elastic Light Scattering Spectrometry*, De Gruyter, Berlin, Boston **2018**, p. 11.
- [48] J. Vernieres, S. Steinhauer, J. Zhao, A. Chapelle, P. Menini, N. Dufour, R. E. Diaz, K. Nordlund, F. Djurabekova, P. Grammatikopoulos, M. Sowwan, *Adv. Funct. Mater.* **2017**, 27, 1605328.
- [49] M. Gracia-Pinilla, E. Martínez, G. S. Vidaurri, E. Pérez-Tijerina, *Nanoscale Res. Lett.* **2010**, 5, 180.
- [50] M. Ganeva, T. Peter, S. Bornholdt, H. Kersten, T. Strunskus, V. Zaporozhchenko, F. Faupel, R. Hippler, *Nanoscale Adv.* **2012**, 52, 881.
- [51] D. Nelli, M. Cerbelaud, R. Ferrando, C. Minnai, *Nanoscale Adv.* **2021**, 3, 836.
- [52] K. T. Batková, S. Haviar, P. Mareš, J. Čapek, *Surf. Coat. Technol.* **2021**, 417, 127196.

Particle

& Particle Systems Characterization

Supporting Information

for *Part. Part. Syst. Charact.*, DOI: 10.1002/ppsc.202200112

In Situ Laser Light Scattering for Temporally and Locally Resolved Studies on Nanoparticle Trapping in a Gas Aggregation Source

*Jonas Drewes, Stefan Rehders, Thomas Strunskus, Holger Kersten, Franz Faupel, and Alexander Vahl**

Supporting information

In-situ laser light scattering for temporally and locally resolved studies on nanoparticle trapping in a gas aggregation source

Jonas Drewes¹, Stefan Rehders¹, Thomas Strunskus^{1,3}, Holger Kersten^{2,3}, Franz Faupel^{1,3}, Alexander Vahl^{1,3*}

¹ Chair for Multicomponent Materials, Institute of Materials Science, Kiel University, Kaiserstr. 2, D-24143 Kiel, Germany

² Chair for Plasma Technology, Institute of Experimental and Applied Physics, Kiel University, Leibnizstr.19, D-24098 Kiel, Germany

³ Kiel Nano, Surface and Interface Science KiNSIS, Kiel University, Christian-Albrechts-Platz 4, D-24118 Kiel, Germany

Exemplary LLS videos:

Video No.	File name	p [Pa]	P [W]	Inlet
1	Behind_183Pa_Ag_Scattering_61.m4v	183	300	Behind
2	Middle_183Pa_Ag_Scattering_33.m4v	183	300	Middle
3	Normal_183Pa_Ag_Scattering_55.m4v	183	300	Normal

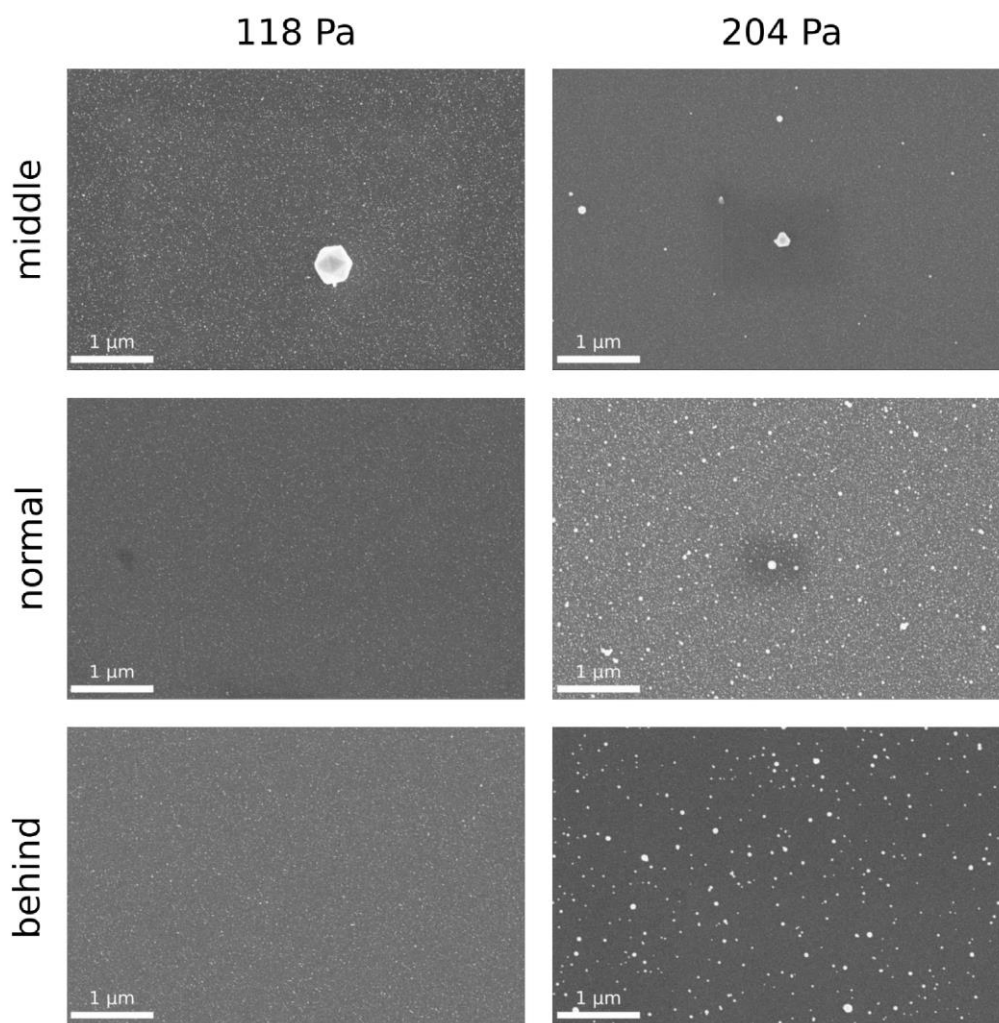


Figure S1: Shown are 6 SEM images for two different flows for each type of gas inlet configuration. The left column corresponds to pressure of 118 Pa and the right to 204 Pa. The first row corresponds to the middle gas inlet, the second to the normal gas inlet and the last one to the behind gas inlet.

Table S1: Mean value and fit parameters for the log normal size distributions for different gas inlets and pressures.

gas inlet	pressure [Pa]	d_{mean} [nm]	y_0	x_c	w	A
Middle	118	11.9	-0.03	10.39	0.43	1704.53
Middle	204	8.7	-0.07	8.07	0.36	1540.56
Normal	118	9.9	-0.01	9.33	0.36	1665.20
Normal	204	13.6	-0.16	12.12	0.55	3449.47
Behind	118	9.3	-0.08	8.36	0.48	2691.49
Behind	204	8.7	0.05	6.00	0.30	1612.91
			0.05	35.80	0.22	108.39

The fit function for the log normal distribution:

$$y = y_0 + \frac{A}{\sqrt{2\pi} w x} \exp\left(\frac{\left(-\ln\frac{x}{x_c}\right)^2}{2 w^2}\right) \quad (S1)$$

3.6 Publication E: Enhancing Composition Control of Alloy Nanoparticles from Gas Aggregation Source by in-operando Optical Emission Spectroscopy

In this study, the effect of redeposition on the alloy composition of NPs in the multicomponent target approach, developed by Vahl et al., was investigated by longer operation of the source in comparison to the study by Vahl et al.

SEM and EDX investigations have shown that after longer operation time of a multicomponent target Au can be found nearly everywhere on the target, although it was only embossed into the erosion trench of a pure Ag target. XPS measurements of the deposited NPs have shown that the Au concentration vs. pressure plot significantly varied to the reported linear dependency by Vahl et. al. But in the study from Vahl et al. the operation time of the HGAS and the number of samples was significantly lower. Since the EDX results have confirmed that a significant amount of Au is redeposited onto the target a new plot was created where the Au concentration is plotted in a 3D plot vs. pressure and target lifetime. This showed a much better correlation. Nevertheless, the target lifetime is not a very useful parameter, because it cannot be actively controlled by the operator. This motivated the measurements of optical emission lines during the experiments. It was possible to calibrate the OES results to XPS measurements to predict the concentration of the following samples.

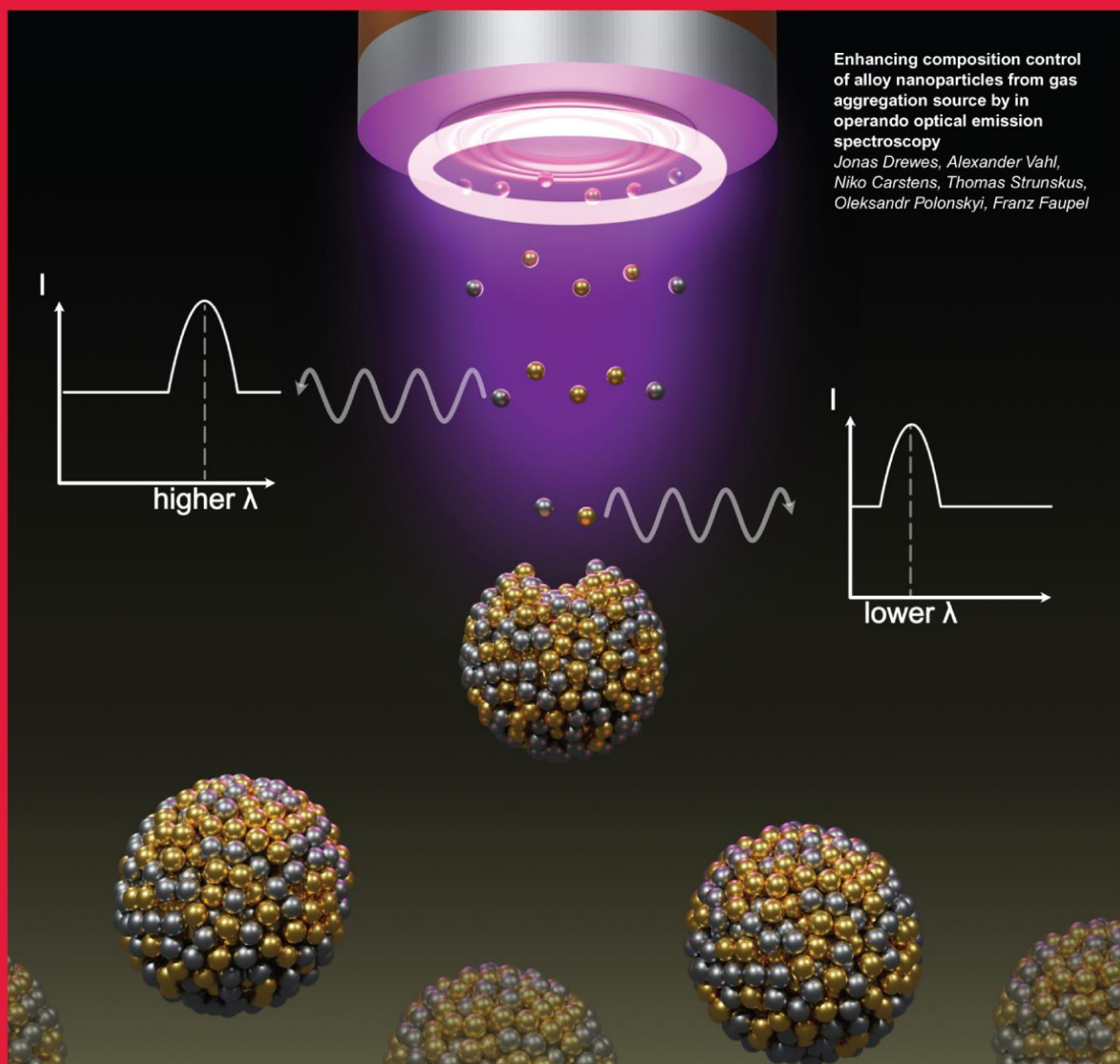
Therefore, in this publication on the one hand the problematic redeposition effect was analyzed, but on the other hand also a suitable solution was presented to predict the composition of the NPs. All in all, it was possible to extend the scope of applications of the HGAS by enhancing the composition control of the multicomponent target approach by in-situ OES.

Own contributions to this publication are the conceptualization, the conductance of the experiments, data processing and writing of the manuscript.

This chapter is reprinted from the following publication and was selected as the front cover:

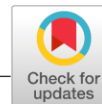
Drewes, J., Vahl, A., Carstens, N., Strunskus, T., Polonskyi, O., & Faupel, F. (2020). Enhancing composition control of alloy nanoparticles from gas aggregation source by in operando optical emission spectroscopy. *Plasma Processes and Polymers, October*, 1–11. <https://doi.org/10.1002/ppap.202000208>

PLASMA PROCESSES AND POLYMERS



Editors-in-Chief: Pietro Favia, Bari | Dirk Hegemann, St. Gallen |
Christian Oehr, Stuttgart | Michael R. Wertheimer, Montreal
Founding Editor: Riccardo d'Agostino, Bari †

WILEY-VCH



FULL PAPER

PLASMA PROCESSES
AND POLYMERS

Enhancing composition control of alloy nanoparticles from gas aggregation source by in operando optical emission spectroscopy

Jonas Drewes¹ | Alexander Vahl¹ | Niko Carstens¹ |
Thomas Strunskus¹ | Oleksandr Polonskyi^{1,2} | Franz Faupel¹

¹Institute for Materials Science–Chair for Multicomponent Materials, Faculty of Engineering, Christian-Albrechts-University of Kiel, Kiel, Germany

²Department of Chemical Engineering, University of California–Santa Barbara, Santa Barbara, California, USA

Correspondence

Oleksandr Polonskyi, Department of Chemical Engineering, University of California–Santa Barbara, Engineering II, Santa Barbara, CA 93106-5080, USA.
Email: polonskyi.oleksandr@gmail.com

Franz Faupel, Institute for Materials Science–Chair for Multicomponent Materials, Faculty of Engineering, Christian-Albrechts-University of Kiel, Kaiserstraße 2, D-24143 Kiel, Germany.
Email: ff@tf.uni-kiel.de

Funding information

Deutsche Forschungsgemeinschaft, Grant/Award Numbers: FOR2093, PO2299/1-1

Abstract

The use of multicomponent targets allows the gas-phase synthesis of a large variety of alloy nanoparticles (NPs) via gas aggregation sources. However, the redeposition of sputtered material impacts the composition of alloy NPs, as demonstrated here for the case of AgAu alloy NPs. To enable NPs with tailored Au fractions, in operando control over the composition of the NPs is in high demand. We suggest the use of optical emission spectroscopy as a versatile diagnostic tool to determine and control the composition of the NPs. A strong correlation between operating pressure, intensity ratio of Ag and Au emission lines, and the obtained NP compositions is observed. This allows precise in operando control of alloy NP composition obtained from multicomponent targets.

KEYWORDS

alloy nanoparticle, gas aggregation cluster source, gas-phase synthesis, in operando optical emission spectroscopy, sputter deposition

1 | INTRODUCTION

Over the last few decades, metal nanoparticles (NPs) have attracted huge attention due to their unique properties resulting from the high surface-to-volume ratio. Their properties can be tuned by size distribution, filling factors, and surrounding media (e.g., in the case of nanocomposites),

which makes them applicable in many fields like catalysis,^[1] photocatalysis,^[2–6] optics,^[7] resistive switching,^[8–15] and sensors.^[16–20] In particular, noble metal alloy NPs with the composition as an additional tunable parameter are nowadays in the focus of researchers in a broad variety of application scenarios. Due to the unique properties of alloy noble metal NPs, especially of AgAu metal NPs, they can be

Abbreviations: GAS, gas aggregation cluster source; NP, nanoparticle; OES, optical emission spectroscopy; SEM, scanning electron microscopy; XPS, X-ray photoelectron spectroscopy.

This is an open access article under the terms of the Creative Commons Attribution License, which permits use, distribution and reproduction in any medium, provided the original work is properly cited.

© 2020 The Authors. *Plasma Processes and Polymers* published by Wiley-VCH GmbH

utilized for different applications, including heterogeneous catalysis (e.g., oxidant-free benzyl alcohol dehydrogenation),^[21] in surface plasmon-enhanced photocatalysis,^[22] in solar cells,^[23] as a potential advanced ink for anticounterfeiting purposes,^[24] and for achieving a stable Ag ion release.^[25] The optical properties of noble metal alloy NPs are also well known,^[26] which are strongly dependent on the shape, size, size distribution, and composition of the NPs. Compared with conventional single-element NPs, the composition of alloy NPs is an additional crucial parameter, which can be used to tailor their performance in the respective application scenario. In this study, we focus on AgAu NPs motivated by recent interest in plasmonic nanocomposites,^[27,28] functional nanocomposites,^[29] solar energy harvesting,^[23] and memristive devices.^[14,30]

Possible synthesis approaches for alloy NPs range from biological over chemical to physical pathways, with solution-based chemical synthesis being the most common approach.^[31,32] Physical vapor deposition (PVD) excels in generating high-purity NPs and does not rely on the utilization of surfactants. A broad variety of PVD-based strategies to produce alloy NPs with control over NP composition has already been employed successfully. These PVD strategies include surface energy-related self-organization of NPs on solid substrates^[25,33–35] and in liquids (i.e., “Sputter into liquids”)^[36–38] as well as gas-phase synthesis. In this study, alloy AgAu NPs are fabricated using a PVD approach known as gas aggregation cluster source (GAS), which was first realized by Haberland in 1992.^[39] In such a GAS, the NP sizes and size distributions are controlled by the magnetron power, gas flow, pressure, and aggregation length.^[40] To produce alloy NPs inside such a GAS, three different ways are possible: the multiple magnetron approach,^[40–44] the single-alloy target approach,^[45–47] and the multi-component target approach.^[48]

Recent approaches with multiple magnetrons in a single GAS apparatus have enabled good control over NP composition, but this approach is costly, needs huge source dimensions, and is experimentally challenging, because interferences between individual magnetrons make the plasma control sometimes difficult.^[40–44] Nevertheless, this method also allows control over the structure, for example, core-shell, core-shell-shell, and so forth. However, it can be sometimes challenging to achieve only alloy particles without core-shell particles, because the magnetrons are separated from each other. Using only one alloy target is also a suitable and simple strategy to synthesize alloy NPs, but controlled adjustment of alloy composition is not possible here.^[45–47]

In a previous work, single magnetron sputtering inside a Haberland-type GAS with multicomponent targets was introduced as a new method to produce NPs with

defined size distribution, high purity, and variable composition, which can be adjusted by the operating pressure in the GAS. In this method, one component is located in the erosion zone of an otherwise pure target, which serves as the second component. A change in pressure impacts the mean free path of Ar ions and, in turn, also influences the size of the erosion zone, which changes in the last consequence, due to the special target geometry, the composition of the produced NPs.^[48]

Despite this simple relation between operating pressure and NP composition,^[48] additional effects have to be considered for long-term depositions. It is known that in a GAS, a significant amount of material can be re-deposited on the target surface,^[49,50] which in the case of a multicomponent target may impact the alloy composition of the NPs. Furthermore, the erosion profile of the target can affect the NPs synthesis in a GAS.^[51]

The deposition characteristics of the gas-phase synthesis of NPs, in general, are varying throughout the target lifetime,^[49–51] which, in particular, is a challenge to be overcome in the case of multicomponent targets. Thus, a reliable in operando diagnostic approach is in high demand to satisfy the necessity of a precise control of the NP composition. In operando approaches are extremely useful to gain an insight into the NP formation process in a GAS, as the finally deposited NPs do not contain full information about any intermediate stages in the gas-phase synthesis. To analyze the growth and transport of NPs in the GAS, several in situ diagnostics, like small-angle X-ray scattering,^[50,52] passive thermal probe, Langmuir probe,^[53] and UV-Vis spectroscopy,^[49] have already been applied successfully. In earlier reports, optical emission spectra (OES) were also successfully utilized to analyze sputter processes^[54–56] or to analyze the oxidation and cluster formation processes in the GAS.^[57]

In this study, the concept of alloy NP deposition by single-target sputtering from a multicomponent target is pursued. Special attention is being paid to the impact of target aging on the composition of AgAu NPs, and a potential approach for in operando control of the NP composition is discussed. In the context of target aging, this study reveals that for the long-term use of multicomponent targets inside a GAS, the composition of alloy NPs is gradually changing toward an enrichment in Au with each subsequent deposition cycle, which could be successfully attributed to redeposition effects. Redeposition is well known for magnetron sputtering. In the general picture, sputtered atoms may be redirected and adsorbed on the target surface due to collisions with gas atoms. The effect of redeposition is especially prominent in a GAS with its typical operational pressure range around 100 Pa, which is significantly higher as compared

with conventional sputter deposition.^[49,50,58,59] Whereas in the case of single-component targets, any redeposition solely changes the target's morphology and has no influence on elemental composition, in the case of alloy targets or multicomponent targets, local changes in composition have also to be considered. Redeposition is well known for pure single-component targets as well as in a GAS.^[49,50] Furthermore, the target erosion profile influences the NPs synthesis and limits the working window in which NPs can be produced.^[51] Due to these target history effects, a precise prediction of NP composition just based on operation pressure, which was suggested in an earlier report,^[48] is impossible for long-term use of a multicomponent target. To account for the immense significance of precise control over NP properties for application purposes, a diagnostic approach to control the NP composition is presented. This approach goes beyond the application of OES as a tool for analysis of discharge characteristics^[54–56] and utilizes a simple UV–Vis setup to record the OES of Ag and Au from the plasma. In this respect, in operando UV–Vis offers the possibility to record OES as well as obtain information on the NP plasmon resonance (PPR) of the NPs. Although the PPR is a great tool to obtain information about the growth and transport of NPs in the GAS (cf. transmission spectra of pure Ag and AgAu NPs in Figures S1 and S2), in this study, OES is presented as an efficient diagnostic tool to determine the composition of AgAu NPs in operando, which has the prospect to be used in future also for active control over the composition by the implementation of a feedback loop.

2 | EXPERIMENTAL SECTION

2.1 | Fabrication of the custom-build multicomponent target

The composite AgAu target was prepared by milling a radially symmetric trench of 3-mm width at the center of the erosion zone of an Ag target (99.99%, 2-inch diameter; Kurt J. Lesker). Three concentric rings of Au wire (99.95%, 1-mm diameter; Alfa Aesar) were put into the trench and embossed into the target. The chosen geometry allows a more effective use of the more costly Au.

2.2 | Deposition and analysis of NPs

The GAS with the deposition chamber was mounted on the transfer chamber of an Omicron XPS system (Omicron full lab). This configuration allows the transfer of the samples to the X-ray photoelectron spectroscopy

(XPS) analytical chamber without exposure to air. The base pressure of the deposition chamber was 1.6×10^{-5} Pa, pumped by a turbomolecular pump (TMU 262; Pfeiffer Vacuum) and a scroll pump (Edwards 6i). The GAS was equipped with a 2" height-adjustable and water-cooled DC magnetron (IX2U_9A327-02; Thin Films Consulting). The height-adjustable magnetron enables to tune the distance between the magnetron and the orifice of the GAS. This distance was kept constant and was only once adjusted, depending on the UV–Vis light beam, which is explained in Section 2.3. The deposition was performed at a DC power of 100 W, and the pressure inside the GAS was randomized for each deposition in a range between 37 and 188 Pa, corresponding to argon flows of 20 and 120 sccm, respectively. MDX 500 from Advanced Energy was used as a power supply and an Apex flow controller (AX-MC-200sccm-D/5M) with 200-sccm range was used for the gas flow regulation. The deposition time was adjusted individually for all samples, because different flows and pressures in the GAS change the deposition rate strongly. The time was set in a way that the surface coverage with NPs was sufficient to obtain reliable XPS spectra. The XPS spectra were evaluated with the software "CasaXPS." Each spectrum was analyzed by four different persons to reduce statistical and systematic errors that could occur, for example, during the background correction of an XPS spectrum. By that approach, we obtained a mean value for the NP composition. The highest and lowest calculated fractions were used as the error of the XPS measurements. Quartz wafers (0.5-mm thickness; Plan Optik) cut into 10×10 mm pieces were used as substrate material. Quartz was chosen, because it would allow ex situ UV–Vis transmission measurements to determine the optical properties. Depending on the selected operating pressure, the resulting NP diameters range from 2 to 30 nm (cf. scanning electron microscopy [SEM] micrographs in Figure S3 and the corresponding histograms of NP diameters in Figure S4).

2.3 | Measurement of OES

As the magnetron was height-adjustable, but the position of the access windows for the UV–Vis was fixed, the height of the magnetron was adjusted in a way that the UV–Vis light beam was in the closest distance to the magnetron without getting cut by the magnetron (Figure S5). The diameter of the light beam was 1.4 cm, and hence the distance between the center of the light beam and the ground cap of the magnetron was 0.7 cm. This position was fixed for all experiments to maintain the same aggregation length for the NPs. The integration

time of the Ocean Optics spectrometer (STS-UV) was set to 25 ms and 40 spectra were averaged, so that every second, one spectrum was collected. After the background was subtracted from the counts, the height of the Ag I (328 nm) and Au I (312 nm) peaks was measured and averaged over the deposition time. The error of the spectrometer is small and can be neglected in comparison to the strong changes of the emission line spectrum induced by experimental parameters like, for example, pressure changes. A suitable error calculation was not possible, because any changes detected could be caused by a variation of an experimental parameter (e.g., change in sputter trench), and should be thus considered as a real signal.

3 | RESULTS AND DISCUSSION

Within this section, it will be discussed that in the context of multicomponent targets with concentric rings at the center of the erosion zone, the redeposition adds another layer of complexity to a reliable determination of alloy NP composition.

In Figure 1a, a photographic image of an AgAu multicomponent target before (left half) and after prolonged deposition (right half) is shown. Whereas in the pristine state before deposition, the Au wires are embedded into a pure Ag target with a seemingly homogenous surface, after the prolonged deposition, two phenomena can be observed. The racetrack (erosion zone) of the target ranges

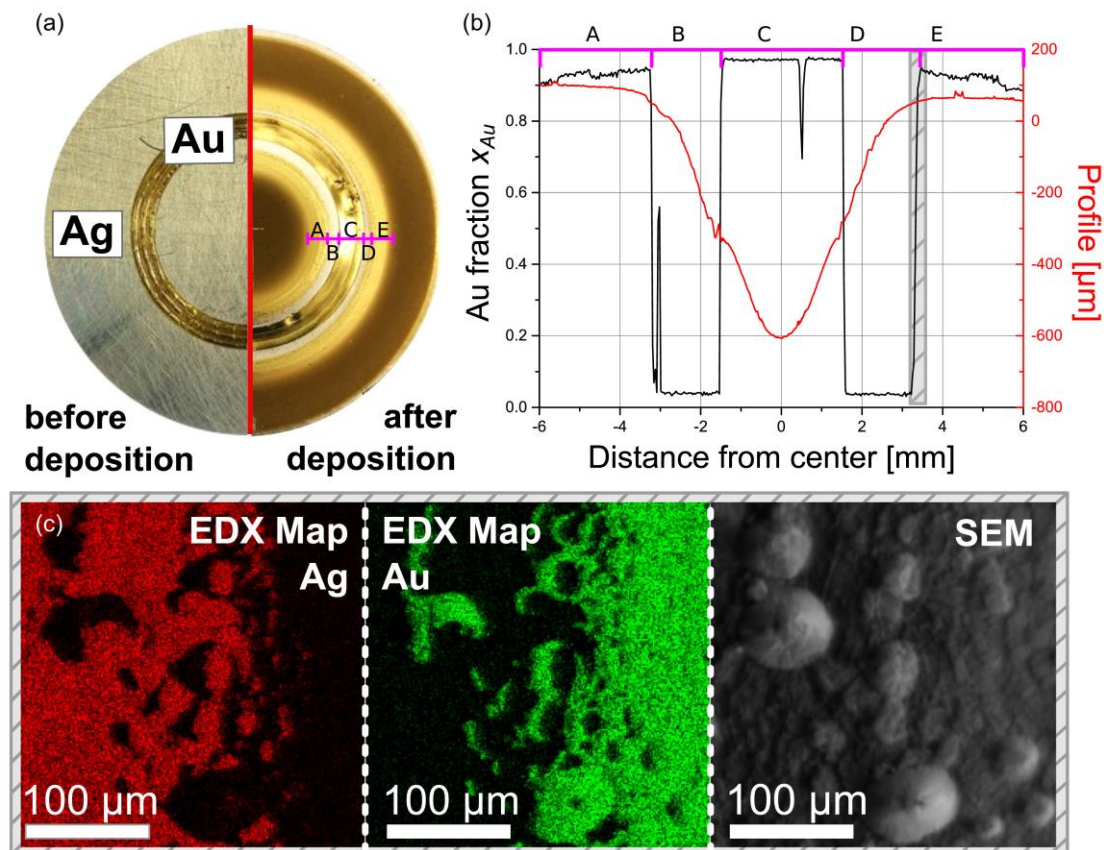


FIGURE 1 (a) A photograph of the target before (left) and after hours of deposition (right). The target surface is clearly enriched with Au after deposition. (b) The EDX line scan and depth profile of the target, as recorded after prolonged deposition, shows a clear transition between the Au wire and Ag target, but also an abrupt transition between the pure Ag target surface and the redeposition area, where the target surface is enriched by Au. The profile is in good agreement with the EDX line scan and shows that the transition region from the erosion zone to the redeposition zone lies exactly at the transition between Ag-rich region and Au-rich region. Here, the racetrack (sputter trench) includes the regions B, C, and D, where the center region (C) corresponds to the position of the embossed Au wires. The outer regions (A and E) correspond to the redeposition area. (c) The EDX map of the transition area between regions D (left) and E (right) shows a sharp transition between almost pure Ag (marked red) and Au (marked green). EDX, energy-dispersive X-ray spectroscopy; SEM, scanning electron microscopy

over the Au wires (region C) and the adjacent regions (B and D). The remaining surface of the target is covered by redeposition of golden and dark golden color. To describe this redeposition effect in more detail, SEM energy-dispersive X-ray spectroscopy (EDX) measurements were performed, and the resulting EDX line profile of a scan over the regions A to E and the depth profile of the target (recorded via profilometry) are depicted in Figure 1b. The line scan shows that the target surface within regions A and E is Au-rich with an Au content of 90 at% and above. Before the deposition, these areas correspond to the pristine Ag target surface. Accordingly, the presence of the high Au content after the deposition indicates that in these areas, there is significant redeposition. The profilometer depth profile implies that the thickness of the deposit within areas A and E is roughly in the order of 64–100 μm . At the center of the erosion zone, in area C, there is another Au-rich region, which corresponds to the embedded Au wires. Adjacent to the wires, areas B and D represent a region of almost pure Ag (Ag content 95 at% and above). There is a sharp transition from the Au-rich region C to the Ag-rich regions B and D, which is expected from the target geometry of the manufactured target before deposition. Interestingly, the transition between the regions A to B and D to E also appears very sharp and narrow in the EDX line scan. This observation indicates that there is a distinct boundary between the regions of redeposition (A and E) and the erosion zone (B–D). To gain further insights into this boundary, EDX elemental maps showing the Ag (red) and Au (green) content, as well as the corresponding SEM micrograph, are shown in

Figure 1c. These measurements were obtained at the interface between regions D and E (as schematically depicted by a grey box in Figure 1b). The EDX maps underline that there is a sharp transition between the Au-rich redeposition region and the Ag-rich part of the erosion zone. In between the Ag-rich erosion zone (left, red) and the Au-rich redeposition zone (right, green), there is an overlap area with a width in the range of 100 μm . Within the overlap area, there are Au-rich and Ag-rich subregions; however, alloy-like smooth transitions are not observed.

To obtain additional information on the redeposition and target surface enrichment with Au, the target surface morphology was investigated by SEM (Figure 2). Besides the target surface Au enrichment effects, the surface morphology also varies across the different areas on the target. Whereas within the erosion zone (regions 3–6), the morphology is smooth and the surface exhibits spherical dome-like structures with a regular distribution, the surface morphology at the redeposited areas is dominated by large, irregular structures with a high number of cracks in between (regions 1–2 and 7–8).

So far, the investigations on the target after prolonged deposition have shown that there is an abrupt transition between the Au-rich redeposition area and the Ag-rich part of the erosion zone. In fact, only within a small region (100- μm width as compared with 6.7-mm width for the overall erosion zone), an overlap of Au-rich and Ag-rich compartments has been observed. However, in the multicomponent target approach, the capability to control NP composition traces back to changes in the

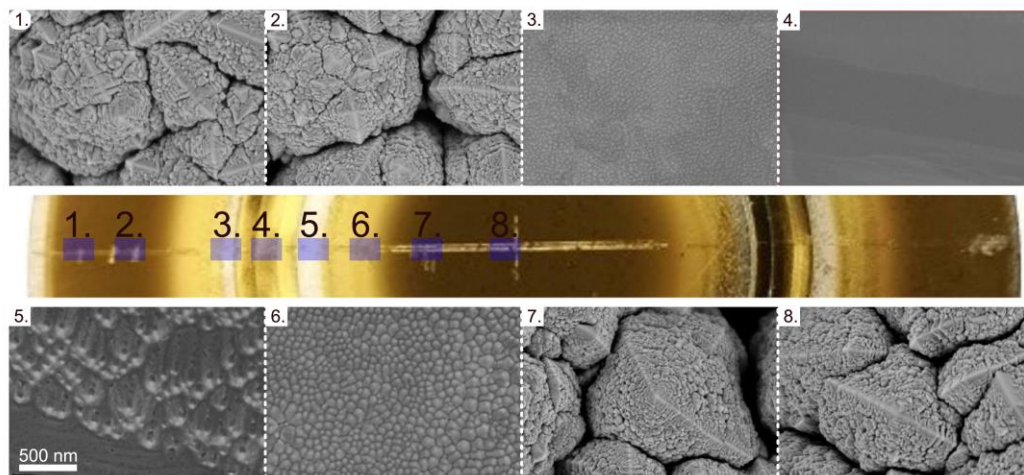


FIGURE 2 Scanning electron microscopy pictures from different positions on the target at the same magnification. The inset numbers show the position on the target from which the pictures are taken. Panels (1 and 2) and (7 and 8) show an interesting pyramid-like structure formed by the redeposition. For regions 3–6, the morphology is smooth and the surface exhibits spherical dome-like structures with a regular distribution

width of the effective erosion zone upon variation of pressure. This suggests that redeposition and target history will also impact the composition range, which can be achieved with the multicomponent target approach. In the following section, the effect of target history on the composition of AgAu NPs will be discussed. Within the range of the experimental aggregation pressure between 37 and 188 Pa, AgAu NPs with a gold fraction (x_{Au}) between 54 and 82 at% were obtained. More deposition details can be found in Section 2.2. The results from a quantification of the Au fraction based on the Au 4d and Ag 3d lines (cf. Figure S6) from the recorded XPS spectra are shown in Figure 3a, where the Au fraction is plotted versus the pressure in the GAS. The plot shows that the linear relation between alloy NPs composition and operating pressure, which was proposed in an earlier work, is not completely sufficient to describe the composition dependence of the AgAu NPs, which is reflected in a rather low linear correlation coefficient of 0.833 (Pearson correlation).^[48] In contrast to the first study by Vahl et al.,^[48] the deposition times were increased drastically and a higher number of individual depositions were investigated. This implies that changes on the target surface due to redeposition also impact the composition of alloy NPs from multicomponent targets in a GAS. To also account for the effect of target aging in terms of redeposition, we incorporated the accumulated deposition time as a measure of target history as a second parameter into a linear regression. Hence, the target history is defined as the sum of all individual deposition times of the experiments as well as the preparation times, where the

discharge was on but the shutter was closed. Using a linear fit with pressure and target history as parameters, the fit (blue line) is in reasonable agreement (correlation coefficient of 0.983) with the composition data from XPS quantification (red bars), as depicted in Figure 3b.

For practical applications, the parameter of target history is not very useful, as it is not obtainable in the experiment itself but only accessible via bookkeeping over every experiment's deposition time. An in operando diagnostic approach, which is capable of directly determining the NPs composition, is highly favorable. Such an approach could also be used to control the NPs composition via a feedback loop, for example, controlling the gas flow. In the following section, in operando optical spectroscopy techniques are discussed as a potential pathway to enable control over NP composition.

Considering the plasmonic properties of noble metal (alloy) NPs, such as AgAu, an in operando monitoring of the plasmon absorption peak by UV-Vis spectroscopy can be applied to obtain information about the NPs.^[49] However, this approach renders very challenging for alloy NPs, due to the extinction coefficient as well as the simultaneous influence of NPs diameter and composition on the plasmon peak's wavelength (Figures S1 and S2).^[60,61] However, by using the identical UV-Vis setup also, direct optical emission lines (OES) from the Ag and Au species in the plasma can be recorded, which consequently makes OES a viable diagnostic approach to be used complementary to in situ UV-Vis. OES has already been reported as a tool to monitor compositional changes

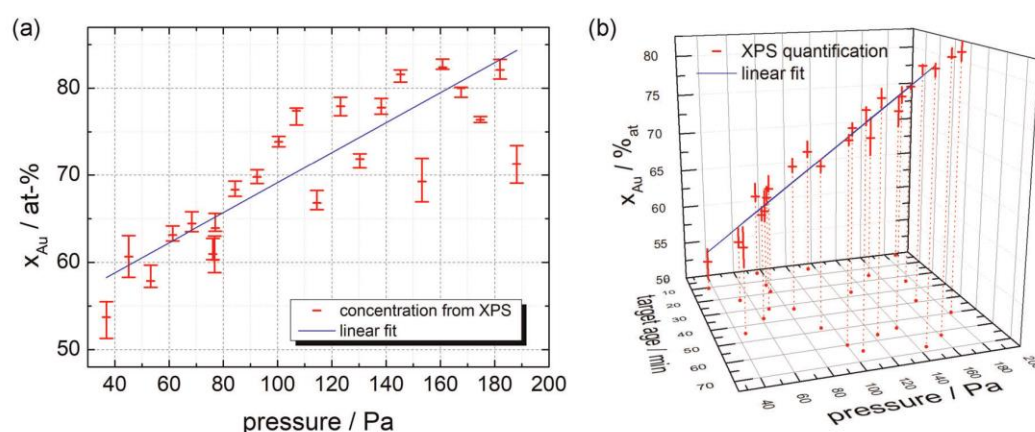


FIGURE 3 Evaluation of the Au fractions of AgAu NPs (x_{Au}) as experimentally obtained from X-ray photoelectron spectroscopy (XPS) quantification. The plot of gold fractions versus operating pressure (a) shows a considerable deviation from the expected simple linear behavior (Pearson correlation coefficient: 0.833),^[41] which indicates that additional parameters impact the resulting composition of the nanoparticles. In this context, the target lifetime (i.e., the cumulative deposition time) correlates with the ongoing change in redeposition. In the 3D plot of the gold fraction versus target lifetime as well as pressure (b), the linear fit shows a reasonable agreement (Pearson correlation coefficient: 0.983)

of thin films in conventional sputter deposition processes.^[54–56,62] The intensity in an OES spectrum is related to the amount of excited atoms of a specific element in the gas phase, and a good correlation between the intensity of optical emission lines and the resulting elemental concentrations in thin films is commonly reported.^[54–56,62] Although in a conventional sputter deposition process, all sputtered atoms that enter the gas phase are contributing to the thin film, the formation of alloy NPs in a gas-phase synthesis adds another layer of complexity. One cannot be sure whether all sputtered atoms of both elements are contributing equally to the formation of NPs. One possibility is that one element preferentially contributes to the cluster growth and more of the other elements get lost on the walls of the GAS. Nevertheless, the intensity of an emission line for a specific element is related to the concentration of this element in the plasma and should correlate with the fraction of this element in the formed NPs. One advantage of using OES is also that different sputter yields of the individual components of the multicomponent target do not play a role, because only already sputtered atoms can contribute to the signal. An exemplary OES spectrum, recorded in operando during a typical alloy NP deposition, is shown in Figure 4a. Within the range from 305 to 345 nm, three optical emission lines corresponding to the elements Ag (indicated by orange color) and Au (indicated by blue color) are observed. We assign the line around 312 nm to the Au I emission line at 312.28 nm and the line around 327 nm to Ag I line at 328.07 nm. These are the most intense lines with the shortest wavelength difference to each other for each element within this range. Both the Au I line at 312 nm and the Ag I line at 328 nm were intense enough to record them over the whole pressure range studied in this study. For further

evaluations, the peak intensities of these lines, $I_{\text{Ag I}}$ and $I_{\text{Au I}}$, were extracted from the spectra.

To underline the effect of redeposition and target aging, we investigated the time evolution of the selected Au I and Ag I emission lines. For this purpose, at first, the target was conditioned by running a deposition at a pressure of 168 Pa, which corresponds to a narrow sputter region (i.e., narrow erosion zone) and yields considerable redeposition. The following deposition is operated at a significantly lower pressure of 45 Pa, which results in a broader sputter region that also covers a part of the redeposited area. In Figure 4b, the time evolution of the peak intensities $I_{\text{Ag I}}$ and $I_{\text{Au I}}$ during the deposition at a pressure of 45 Pa is shown. During the deposition, $I_{\text{Ag I}}$ is increasing, whereas $I_{\text{Au I}}$ is decreasing simultaneously. This change is especially prominent within the initial period of the deposition (with time constant $\tau \sim 47.9$ s) and settles gradually within the final period of the deposition. A similar behavior is observed regularly, if the pressure decreases drastically in comparison to the previous deposition. This is in good agreement with our EDX analysis of the target after the deposition, which showed an abrupt change between Au- and Ag-rich regions. The effect of target history and redeposition is schematically depicted in Figure 4c in terms of the time evolution of the target cross-section. For high pressures, the erosion zone is narrow (indicated in green in Figure 4c) and a lot of Au is redeposited on the target in the vicinity of the erosion zone (indicated in yellow). If in the next deposition, the pressure during the deposition is reduced, the erosion zone will be wider (cyan color) and also a lot of the redeposited material (AgAu) will be sputtered off until the redeposited material is removed from the erosion zone. However, when the target is conditioned by running a deposition at a

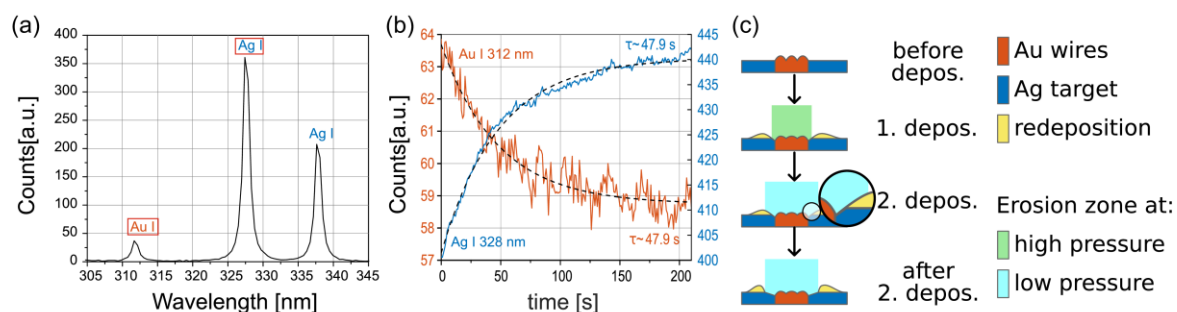


FIGURE 4 Exemplary optical emission spectroscopy during the deposition of AgAu nanoparticles. (a) The peaks in the spectrum can be clearly attributed to the emission lines of the elements Ag (indicated by blue color) and Au (orange), and the two emission lines that are considered for further evaluations are marked with a red rectangle. These two emission lines were selected for further evaluations due to their high intensity as well as a small difference in wavelength. (b) Time evolution of the Au I and Ag I emission lines for an exemplary deposition after a drastic pressure reduction from 168 to 45 Pa. Au I exhibits an exponential decay in the peak intensity over deposition time. This behavior is an effect of target history caused by redeposition, which is schematically sketched in (c)

pressure of 92.4 Pa, this corresponds to a broader sputter region. When afterward the pressure is increased to 182 Pa, which corresponds to a narrow sputter region, nearly no changes in the emission lines over time are visible, because no redeposited material gets sputtered (Figure S7). Before each deposition of NPs, the target was cleaned and conditioned by running the discharge for 60 s, because earlier experiments have shown that this time is sufficient to clean the target and to obtain a stable cluster formation and deposition rate. The cleaning was performed with a closed shutter at the pressure under which the following deposition should be performed, so that no clusters can approach the substrate. However, the effect of target history on the resulting NP composition (Figure 3), as well as the gradual change in I_{AgI} and I_{AuI} , as observed by OES, indicates that the pre-deposition cleaning time was too short to reduce the effect of redeposition and the target got gradually enriched with Au. Nevertheless, also the change in the target geometry over the lifetime due to erosion can possibly influence the composition slightly. The effect of target erosion could not be overcome by longer cleaning times, but the effect of redeposition plays a major role.

However, as OES is able to capture the change of the peak intensities I_{Ag} and I_{Au} in operando, we will elaborate in the following section how OES can be applied as a diagnostic tool to determine the NP composition. In the most general approximation, the peak intensities of the most intensive emission lines for the elements Ag and Au are related to the presence of excited Ag and Au species in the plasma. The amount of excited Ag and Au species in the plasma, in turn, is related to the overall amount of sputtered species from the target. On the basis of the assumption that the NPs form via nucleation, growth, and coalescence from Ag and Au atoms from the gas phase, the composition (in terms of the atomic fraction of Au, x_{Au} in atomic percent) of the resulting NPs can be expressed by Equation (1).

$$x_{Au} \propto \frac{c_{Au} \times \overline{I_{AuI}}}{c_{Au} \times \overline{I_{AuI}} + c_{Ag} \times \overline{I_{AgI}}}, \quad (1)$$

$$\frac{1}{x_{Au}} - 1 \propto c_{rel} \times \frac{\overline{I_{AgI}}}{\overline{I_{AuI}}}; \quad c_{rel} = \frac{c_{Ag}}{c_{Au}}, \quad (2)$$

$$c_{rel} = (c_1 \times p) + c_2, \quad (3)$$

$$\frac{1}{x_{Au}} - 1 \propto c_1 \times p \times \frac{\overline{I_{AgI}}}{\overline{I_{AuI}}} + c_2 \times \frac{\overline{I_{AgI}}}{\overline{I_{AuI}}}. \quad (4)$$

Here, the values of peak intensities of the selected emission lines I_{Au} and I_{Ag} , averaged over the whole deposition time, are representing the amount of excited Au and Ag species in the plasma. Furthermore, coefficients

c_{Au} and c_{Ag} are introduced to take into account the potential differences in the contributions of Ag and Au to the OES signal and to the NP composition. Therefore, the intensity coefficients cover two aspects: On the one hand, the fraction of excited species for Au and Ag depends on the plasma parameters and, on the other hand, the growth process of NPs in the gas-phase synthesis may lead to a different incorporation of Ag and Au into the NPs.

Instead of considering separate intensity coefficients c_{Au} and c_{Ag} , Equation (1) can be simplified by using a relative intensity coefficient c_{rel} (Equation 2).

The plot of $(1/x_{Au}) - 1$ versus $\overline{I_{AgI}}/\overline{I_{AuI}}$ in Figure 5a shows a nonlinear relation, which implies that the coefficient c_{rel} is not readily described by a constant. In contrast, the color scale in Figure 5a indicates that the pressure does impact coefficient c_{rel} . In this context, it is important to mention that with varying pressure inside the GAS, the position and width of the plasma zone are also varying. In addition, the variation of pressure also impacts plasma parameters like electron energy distribution function and electron density. To accommodate any potential effect of pressure, the fitting parameter c_{rel} can be written in a linear approximation (Equation 3), which is used in the following evaluation. Inserting Equation (3) into Equation (2), the empirical fit model is obtained, as shown in Equation (4).

To test the derived fit model, the first four depositions (blue color, calibration) were used to obtain the fit parameters c_1 and c_2 . In the experiment, the parameters for the first four depositions were selected, such that the full pressure range from approximately 37 to 188 Pa is covered. Using these fit parameters as well as the diagnostic quantities pressure p and OES intensities, as shown in Figure 5b, the NP composition can be estimated for the following 19 depositions (red color, test). The fitted NP composition $x_{Au, fit}$ correlates well with the experimentally determined NP composition $x_{Au, XPS}$. The correlation factor (0.970) is very close to the earlier evaluation under application of the target history (0.983), as depicted in Figure 3. However, compared with the target history, the intensity ratio and the operating pressure are easily obtainable by diagnostic approaches, in operando at each timestep of the NP deposition. Thus, OES proved to be a valuable tool to determine the composition of alloy NPs inside a GAS, as soon as a series of reference NP depositions has been analyzed regarding its composition and the fitting parameters have been determined according to the empirical relation described in Equation (4). Within its tested validity range (I_{Ag}/I_{Au} between 3.03 and 9.87; p between 37 and 188 Pa), which is given by the set of AgAu NPs that have been investigated by XPS quantification, the empirical model offers a good

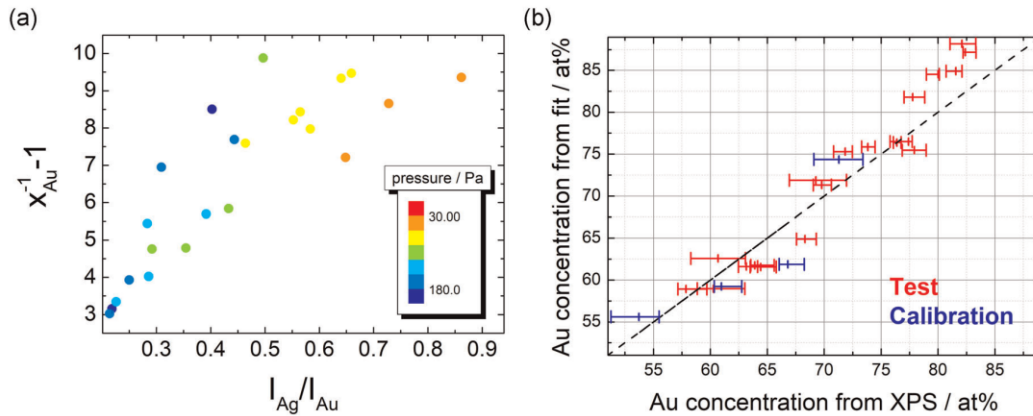


FIGURE 5 The plot of $(1/x_{\text{Au}}) - 1$ versus $\overline{I_{\text{Ag1}}}/\overline{I_{\text{Au1}}}$ in (a) shows a nonlinear relation and indicates that coefficient c_{rel} is not readily described by a constant. The color scale implies that the pressure does impact coefficient c_{rel} . (b) The intensities obtained from in operando optical emission spectroscopy (OES), as well as the operating pressure, are taken into account (Equation 4) from the first four depositions (blue color, calibration). Afterward, the Au fraction can be reasonably predicted for the following 19 depositions only by measuring OES and pressure (red color, test)

estimate of the composition of the AgAu NPs that are just formed at these conditions. The effect of redeposition and target aging, while altering the range of obtainable NP compositions over the lifetime of the target, is here already reasonably covered by the changes in the intensity ratio. After the determination of the fitting parameters, the presented method yields a good basis for in operando control over the alloy composition of NPs.

4 | CONCLUSION

In this study, the gas-phase synthesis via a gas aggregation source with a multicomponent target was applied to fabricate AgAu alloy NPs with an Au fraction ranging from 54 to 82 at%. In this study, on the one hand, the effect of redeposition on the composition of alloy NPs is discussed. It is shown that the multicomponent target was enriched with gold over the course of experiments due to redeposition. The phenomenon of redeposition is well known for pure metallic NP production in a GAS and is related to the higher pressures in comparison to normal sputter deposition. During the compositional analysis of the NPs, we were able to show that composition does not only depend on the pressure in the GAS but also on the cumulative deposition time. The relation between target lifetime and composition is attributed to the gold enrichment of the target due to redeposition. A linear fit incorporating operating pressure and target history (cumulative deposition time) was found to capture the obtained NP compositions well. On the other

hand, a versatile and robust approach for in operando diagnostics is presented. It was demonstrated that for practical applications, an in operando diagnostic approach is highly favorable over using a fitting function based on cumulative deposition time, which is not an intrinsic property of the target. Therefore, we searched for an in operando diagnostic approach, which is able to solve the problem of the target aging. A versatile, robust, and simple diagnostic approach is described by using in operando OES. A good correlation between operating pressure, intensity ratio of Ag and Au emission lines, and the experimentally obtained NP compositions was found. With the addition of in operando OES, it is possible to determine the alloy NPs fraction for a broad variety of alloy systems, which are deposited by a GAS based on magnetron sputtering using the multicomponent target approach. In future, an in operando feedback loop could be implemented, which can measure the pressure and the OES to operate the flow controller in operando according to the composition needs of the operator.

ACKNOWLEDGMENTS

The authors would like to thank Stefan Rehders for technical assistance. This study was financially supported by the German Research Foundation (DFG) via the project PO2299/1-1 and the coordinated effort FOR2093 “Memristive devices for neuronal systems” through project A2. Open Access funding enabled and organized by Projekt DEAL.

CONFLICT OF INTERESTS

The authors declare that there are no conflict of interests.

AUTHOR CONTRIBUTIONS

Jonas Drewes, Alexander Vahl, Oleksandr Polonsky, Thomas Strunskus, and Franz Faupel developed the idea and conceived the initial design of the study. Jonas Drewes, Oleksandr Polonsky, and Alexander Vahl established the experimental setup around the multi-component target approach. Jonas Drewes performed the AgAu NP depositions and recorded XPS and UV-Vis data. Jonas Drewes, Alexander Vahl, Oleksandr Polonsky, and Niko Carstens analyzed the results, including XPS quantification. Alexander Vahl, Jonas Drewes, and Niko Carstens elaborated the multiple regression model and performed correlation analysis. Jonas Drewes and Alexander Vahl prepared the manuscript draft. Franz Faupel supervised the work of Jonas Drewes, Alexander Vahl, and Niko Carstens. All authors have discussed the experimental results and their analysis and revised and approved the manuscript.

DATA AVAILABILITY STATEMENT

The XPS and UV-Vis spectra that support the findings of this study are available from the corresponding author upon reasonable request.

ORCID

Jonas Drewes  <https://orcid.org/0000-0002-8539-1543>

Alexander Vahl  <https://orcid.org/0000-0002-7311-272X>

Thomas Strunskus  <https://orcid.org/0000-0003-3931-5635>

Oleksandr Polonskyi  <https://orcid.org/0000-0001-5013-0944>

Franz Faupel  <https://orcid.org/0000-0003-3367-1655>

REFERENCES

- [1] D. Astruc, *Chem. Rev.* **2020**, *120*, 461.
- [2] M. Z. Ghorri, S. Veziroglu, A. Hinz, B. B. Shurtleff, O. Polonskyi, T. Strunskus, J. Adam, F. Faupel, O. C. Aktas, *Nano Mater.* **2018**, *1*, 3760.
- [3] S. Veziroglu, M. Z. Ghorri, A. L. Obermann, K. Röder, O. Polonskyi, T. Strunskus, F. Faupel, O. C. Aktas, *Mater. Sci.* **2019**, *216*, 1.
- [4] S. Veziroglu, J. Hwang, J. Drewes, I. Barg, J. Shondo, T. Strunskus, O. Polonskyi, F. Faupel, O. C. Aktas, *Mater. Today Chem.* **2020**, *16*, 100251.
- [5] A. Vahl, S. Veziroglu, B. Henkel, T. Strunskus, O. Polonskyi, O. C. Aktas, F. Faupel, *Materials (Basel)* **2019**, *12*, 2840.
- [6] H. Li, Z. Li, Y. Yu, Y. Ma, W. Yang, F. Wang, X. Yin, X. Wang, *J. Phys. Chem. C* **2017**, *121*, 12071.
- [7] C. Minnai, M. Di Vece, P. Milani, *Nanotechnology* **2017**, *28*, 355702.
- [8] C. Minnai, A. Bellacicca, S. A. Brown, P. Milani, *Sci. Rep.* **2017**, *7*, 1.
- [9] M. Mirigliano, D. Decastri, A. Pullia, D. Dellasega, A. Casu, A. Falqui, P. Milani, *Nanotechnology* **2020**, *31*, 234001.
- [10] M. Mirigliano, F. Borghi, A. Podestà, A. Antidormi, L. Colombo, P. Milani, *Nanoscale Adv.* **2019**, *1*, 3119.
- [11] Z. Wang, S. Joshi, S. E. Savel'ev, H. Jiang, R. Midya, P. Lin, M. Hu, N. Ge, J. P. Strachan, Z. Li, Q. Wu, M. Barnell, G. L. Li, H. L. Xin, R. S. Williams, Q. Xia, J. J. Yang, *Nat. Mater.* **2017**, *16*, 101.
- [12] H. Jiang, D. Belkin, S. E. Savel'ev, S. Lin, Z. Wang, Y. Li, S. Joshi, R. Midya, C. Li, M. Rao, M. Barnell, Q. Wu, J. J. Yang, Q. Xia, *Nat. Commun.* **2017**, *8*, 882.
- [13] B. J. Choi, A. C. Torrezan, K. J. Norris, F. Miao, J. P. Strachan, M. X. Zhang, D. A. A. Ohlberg, N. P. Kobayashi, J. J. Yang, R. S. Williams, *Nano Lett.* **2013**, *13*, 3213.
- [14] S. H. Jo, T. Chang, I. Ebong, B. B. Bhadviya, P. Mazumder, W. Lu, *Nano Lett.* **2010**, *10*, 1297.
- [15] X. Yan, J. Zhao, S. Liu, Z. Zhou, Q. Liu, J. Chen, X. Y. Liu, *Adv. Funct. Mater.* **2018**, *28*, 1.
- [16] V. Postica, A. Vahl, D. Santos-Carballal, T. Dankwort, L. Kienle, M. Hoppe, A. Cadi-Essadek, N. H. de Leeuw, M. I. Terasa, R. Adelung, F. Faupel, O. Lupan, *ACS Appl. Mater. Interfaces* **2019**, *11*, 31452.
- [17] Y. Yong, C. Li, X. Li, T. Li, H. Cui, S. Lv, *J. Phys. Chem. C* **2015**, *119*, 7534.
- [18] S. W. Choi, A. Katoch, G. J. Sun, S. S. Kim, *Sens. Actuators, B* **2013**, *181*, 446.
- [19] F. Fan, J. Zhang, J. Li, N. Zhang, R. R. Hong, X. Deng, P. Tang, D. Li, *Sens. Actuators, B* **2017**, *241*, 895.
- [20] K. Hassan, G. S. Chung, *Sens. Actuators, B* **2017**, *239*, 824.
- [21] J. Zheng, J. Qu, H. Lin, Q. Zhang, X. Yuan, Y. Yang, Y. Yuan, *ACS Catal.* **2016**, *6*, 6662.
- [22] W. Hou, S. B. Cronin, *Adv. Funct. Mater.* **2013**, *23*, 1612.
- [23] M. A. Al-Azawi, N. Bidin, M. Bououdina, S. M. Mohammad, *Sol. Energy* **2016**, *126*, 93.
- [24] J. P. Wilcoxon, P. P. Provencio, *J. Am. Chem. Soc.* **2004**, *126*, 6402.
- [25] N. Alissawi, V. Zaporojtchenko, T. Strunskus, I. Kocabas, V. S. K. Chakravadhanula, L. Kienle, D. Garbe-Schönberg, F. Faupel, *Gold Bull.* **2013**, *46*, 3.
- [26] R. Ferrando, J. Jellinek, R. L. Johnston, *Chem. Rev.* **2008**, *108*, 845.
- [27] M. Elbahri, M. K. Hedayati, V. S. Kiran Chakravadhanula, M. Jamali, T. Strunskus, V. Zaporojtchenko, F. Faupel, *Adv. Mater.* **2011**, *23*, 1993.
- [28] M. K. Hedayati, M. Javaherirahim, B. Mozooni, R. Abdelaziz, A. Tavassolizadeh, V. S. K. Chakravadhanula, V. Zaporojtchenko, T. Strunskus, F. Faupel, M. Elbahri, *Adv. Mater.* **2011**, *23*, 5410.
- [29] F. Faupel, V. Zaporojtchenko, T. Strunskus, M. Elbahri, *Adv. Eng. Mater.* **2010**, *12*, 1177.
- [30] A. Vahl, N. Carstens, T. Strunskus, F. Faupel, A. Hassanien, *Sci. Rep.* **2019**, *9*, 1.
- [31] X.-F. Zhang, Z.-G. Liu, W. Shen, S. Gurunathan, *Int. J. Mol. Sci.* **2016**, *17*, 1534.
- [32] S. Gurunathan, K. Kalishwaralal, R. Vaidyanathan, D. Venkataraman, S. R. K. Pandian, J. Muniyandi, N. Hariharan, S. H. Eom, *Colloids Surf., B* **2009**, *74*, 328.
- [33] M. Petr, O. Kylián, A. Kuzminova, J. Kratochvíl, I. Khalakhan, J. Hanuš, H. Biederman, *Opt. Mater. (Amst)* **2017**, *64*, 276.
- [34] H. T. Beyene, V. S. K. Chakravadhanula, C. Hanisch, M. Elbahri, T. Strunskus, V. Zaporojtchenko, L. Kienle, F. Faupel, *J. Mater. Sci.* **2010**, *45*, 5865.

- [35] M. Gensch, M. Schwartzkopf, W. Ohm, C. J. Brett, P. Pandit, S. K. Vayalil, L. Bießmann, L. P. Kreuzer, J. Drewes, O. Polonskyi, T. Strunskus, F. Faupel, A. Stierle, P. Müller-Buschbaum, S. V. Roth, *ACS Appl. Mater. Interfaces* **2019**, *11*, 29416.
- [36] M. T. Nguyen, T. Yonezawa, *Sci. Technol. Adv. Mater.* **2018**, *19*, 883.
- [37] M. T. Nguyen, T. Yonezawa, Y. Wang, T. Tokunaga, *Mater. Lett.* **2016**, *171*, 75.
- [38] M. Meischein, M. Fork, A. Ludwig, *Nanomaterials* **2020**, *10*, 20.
- [39] H. Haberland, M. Karrais, M. Mall, Y. Thurner, *J. Vac. Sci. Technol., A* **1992**, *10*, 3266.
- [40] Y. Huttel, L. Martínez, A. Mayoral, I. Fernández, *MRS Commun.* **2019**, *8*, 947.
- [41] P. Grammatikopoulos, S. Steinhauer, J. Vernieres, V. Singh, M. Sowwan, *Adv. Phys. X* **2016**, *1*, 81.
- [42] P. Solař, J. Hanuš, M. Cieslar, T. Kořutová, K. Škorvánková, O. Kylián, P. Kůš, H. Biederman, *J. Phys. D: Appl. Phys.* **2020**, *53*, 195303.
- [43] Y. Huttel, *Gas-Phase Synthesis of Nanoparticles*, 1st ed., Wiley-VCH Verlag GmbH & Co. KGaA, Weinheim **2017**, p. 79.
- [44] L. Martínez, M. Díaz, E. Román, M. Ruano, P. D. Llamasa, Y. Huttel, *Langmuir* **2012**, *28*, 11241.
- [45] A. Mayoral, L. Martínez, J. M. García-Martín, I. Fernández-Martínez, M. García-Hernández, B. Galiana, C. Ballesteros, Y. Huttel, *Nanotechnology* **2018**, *30*, 065606.
- [46] D. Llamasa Pérez, A. Espinosa, L. Martínez, E. Román, C. Ballesteros, A. Mayoral, M. García-Hernández, Y. Huttel, *J. Phys. Chem. C* **2013**, *117*, 3101.
- [47] A. I. Ayesh, *J. Alloys Compd.* **2018**, *745*, 299.
- [48] A. Vahl, J. Strobel, W. Reichstein, O. Polonskyi, T. Strunskus, L. Kienle, F. Faupel, *Nanotechnology* **2017**, *28*, 175703.
- [49] D. Nikitin, J. Hanuš, S. Ali-Ogly, O. Polonskyi, J. Drewes, F. Faupel, H. Biederman, A. Choukourov, *Plasma. Processes Polym.* **2019**, *16*, 1.
- [50] A. Shelemin, P. Pleskunov, J. Kousal, J. Drewes, J. Hanuš, S. Ali-Ogly, D. Nikitin, P. Solař, J. Kratochvíl, M. Vaidulych, M. Schwartzkopf, O. Kylián, O. Polonskyi, T. Strunskus, F. Faupel, S. V. Roth, H. Biederman, A. Choukourov, *Part. Part. Syst. Charact.* **2020**, *37*, 1.
- [51] A. Rai, A. Mutzke, G. Bandelow, R. Schneider, M. Ganeva, A. V. Pipa, R. Hippler, *Nucl. Instrum. Methods Phys. Res., Sect. B* **2013**, *316*, 6.
- [52] J. Kousal, A. Shelemin, M. Schwartzkopf, O. Polonskyi, J. Hanuš, P. Solař, M. Vaidulych, D. Nikitin, P. Pleskunov, Z. Krtouš, T. Strunskus, F. Faupel, S. V. Roth, H. Biederman, A. Choukourov, *Nanoscale* **2018**, *10*, 18275.
- [53] S. Gauter, F. Haase, P. Solař, O. Kylián, P. Kůš, A. Choukourov, H. Biederman, H. Kersten, *J. Appl. Phys.* **2018**, *124*, 073301.
- [54] A. Raveh, M. Weiss, R. Schneck, *Surf. Coat. Technol.* **1999**, *111*, 263.
- [55] J. Posada, A. Bousquet, M. Jubault, D. Lincot, E. Tomasella, *Plasma Processes Polym.* **2016**, *13*, 997.
- [56] S.-K. Wu, K.-H. Tseng, *Mater. Trans.* **2002**, *43*, 871.
- [57] A. Shelemin, O. Kylián, J. Hanuš, A. Choukourov, I. Melnichuk, A. Serov, D. Slavinská, H. Biederman, *Vacuum* **2015**, *120*, 162.
- [58] S. M. Rossnagel, I. Yang, J. J. Cuomo, *Thin Solid Films* **1991**, *199*, 59.
- [59] D. Depla, *Nucl. Instrum. Methods Phys. Res., Sect. B* **2014**, *328*, 65.
- [60] S. Enoch, B. Nicolas, A. Adibi, T. W. Hänsch, F. Krausz, B. A. J. Monemar, H. Venghaus, H. Weber, H. Weinfurter, *Plasmonics*, Vol. 167 (Eds: S. Enoch, N. Bonod), Springer, Berlin, Heidelberg **2012**.
- [61] S. Link, Z. L. Wang, M. A. El-Sayed, *J. Phys. Chem. B* **1999**, *103*, 3529.
- [62] S. Inoue, H. Uchida, A. Hioki, K. Koterazawa, R. P. Howson, *Thin Solid Films* **1995**, *271*, 15.

SUPPORTING INFORMATION

Additional Supporting Information may be found online in the supporting information tab for this article.

How to cite this article: Drewes J, Vahl A, Carstens N, Strunskus T, Polonskyi O, Faupel F. Enhancing composition control of alloy nanoparticles from gas aggregation source by in operando optical emission spectroscopy. *Plasma Process Polym.* 2020;e2000208. <https://doi.org/10.1002/ppap.202000208>

Supplementary Information to

Enhancing composition control of alloy nanoparticles from gas aggregation source by *in-operando* optical emission spectroscopy

Jonas Drewes¹, Alexander Vahl¹, Niko Carstens¹, Thomas Strunskus¹, Oleksandr Polonskyi^{1,2*},

Franz Faupel^{1*}

¹ Institute for Materials Science – Chair for Multicomponent Materials, Faculty of Engineering, Christian-Albrechts-University of Kiel, Kaiserstraße 2, D-24143 Kiel, Germany

² Department of Chemical Engineering, University of California - Santa Barbara, Engineering II, Santa Barbara, CA 93106-5080, United States

Corresponding Author

* Prof. Dr. Franz Faupel, ff@tf.uni-kiel.de, Institute for Materials Science – Chair for Multicomponent Materials, Faculty of Engineering, Christian-Albrechts-University of Kiel, Kaiserstraße 2, D-24143 Kiel, Germany

* Dr. Oleksandr Polonskyi, polonskyi.oleksandr@gmail.com, Department of Chemical Engineering, University of California - Santa Barbara, Engineering II, Santa Barbara, CA 93106-5080, United States

In-situ particle plasmon resonance

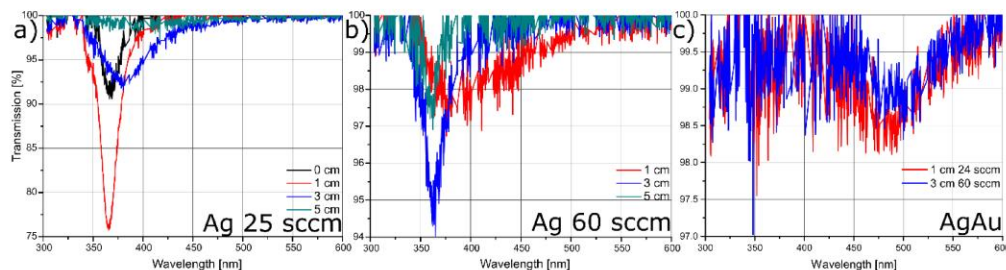


Figure S1: In-Situ UV-Vis transmission spectra for different flow conditions and recorded at different distances to the magnetron after the discharge was running for 30 s. In a) and b) spectra for Ag NPs are shown and in c) for AgAu NPs. The legends are showing the different distances to magnetron and for c) also the Ar flow conditions. In a) one can see that the plasmon resonance is located around 370 nm. In c) spectra for AgAu NPs are measured at the same conditions where the maximum absorption was found for pure Ag NPs. Here the plasmon resonance is located around 480 nm but the absorption is much lower compared to the pure Ag NPs at the same conditions.

In Figure S1 a and b the in-situ UV-Vis transmission spectra of pure Ag NPs inside the GAS for different Ar flows are shown and for each flow spectra at different distances are recorded. The particle plasmon resonance (PPR) is located around 370 nm which is in good agreement with literature values. More interesting is that the strongest absorption is found at 1cm (~25 % absorption) distance from the magnetron for 25 sccm (45.1 Pa), Ar flow but for 60 sccm (100.4 Pa) Ar flow the maximum absorption is at 3 cm (~6 % absorption). This shows that the concentration of NPs in the GAS varies in height and also depends on the flow. Figure S1 c) shows the spectra for AgAu NPs measured under the same conditions, like the pure Ag NPs with the strongest absorption. It is well known that the particle plasmon resonance of alloy NPs is located in between the resonance of the pure NPs depending on their concentrations. Hence the particle plasmon resonance of Au is around 525 nm and of Ag around 370 nm the resonance of AgAu NPs is found in between this values, which is in good agreement with the expected shift from the XPS measurements. The XPS measurements have shown for 25 sccm a Au fraction of ~61 at% and for 60 sccm ~74 at%. This means that the PPR for 60 sccm should be redshifted in comparison to 25 sccm. Even when the signal is really noisy this trend is observable. Assuming that the NP formation does not differ that much between Ag and AgAu NPs these spectra are proving that the PPR absorption is reduced by alloying, which causes less absorption for the same amount of NPs.

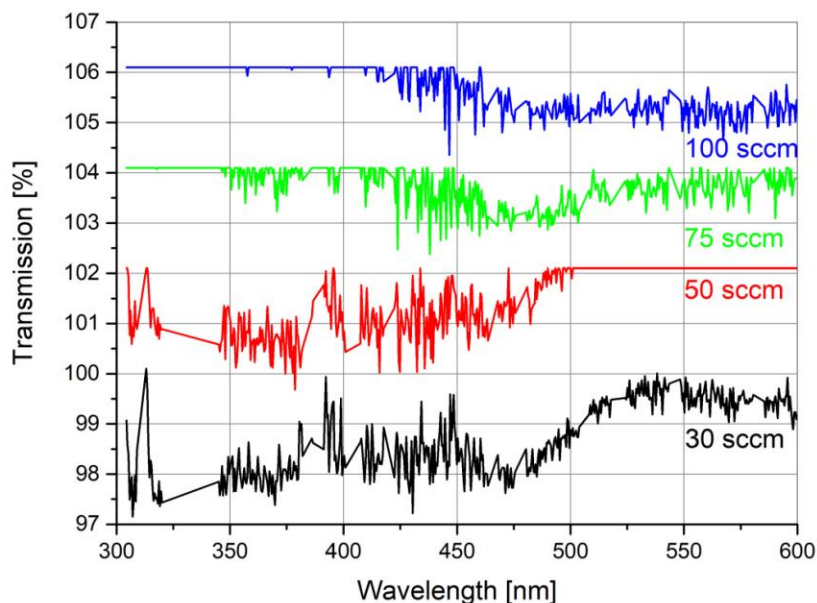


Figure S2: In-situ UV-Vis Transmission spectra of AgAu NPs at different Ar flows and pressures after the discharge was running for 30 s. The spectra have an offset of 2 %. The most intensive emission lines and all data points higher than 100% are removed and the residual data points are linearly connected. The particle plasmon resonance is redshifted from low to high pressures which is in good agreement with the XPS data, which are showing increasing gold content with increasing pressure

Figure S2 shows absorption spectra for AgAu NPs obtained by four different flows at the closest possible distance to the magnetron. The PPR is located in between the PPR of pure Ag and Au NPs. The PPR undergoes a redshift with increasing flow / pressure which is in good agreement with the XPS data, since the gold concentration is increasing with increasing flow.

Nevertheless the absorption is weak compared to pure Ag NPs and the noise plays a more important role, if the absorption is reduced that much.. Since the PPR is also size dependent a specific determination of the composition is impossible, except the size distribution and particle density is known. Although our paper about the in-situ UV-Vis diagnostic about Ag NPs has shown that it is possible to see the growth and transport of NPs in the GAS with this approach, it has also shown that the particles are trapped at different positions in the GAS[1,2]. Hence in our experiments the magnetron was adjusted in a way that the emission lines are most intense and not the absorption related to the NPs, that explains why we have seen only weak absorption in our experiments.

Nevertheless it is helpful to use in-situ UV-Vis and not only record the OES because the signal is still good enough to see if the NP formation is working. This approach works of course only with noble metal NPs which are undergoing particle plasmon resonance. The strength of the emission lines do not depend on the PPR, why our approach with the OES for the in-situ composition determination, is much better suitable.

SEM Analysis of the target

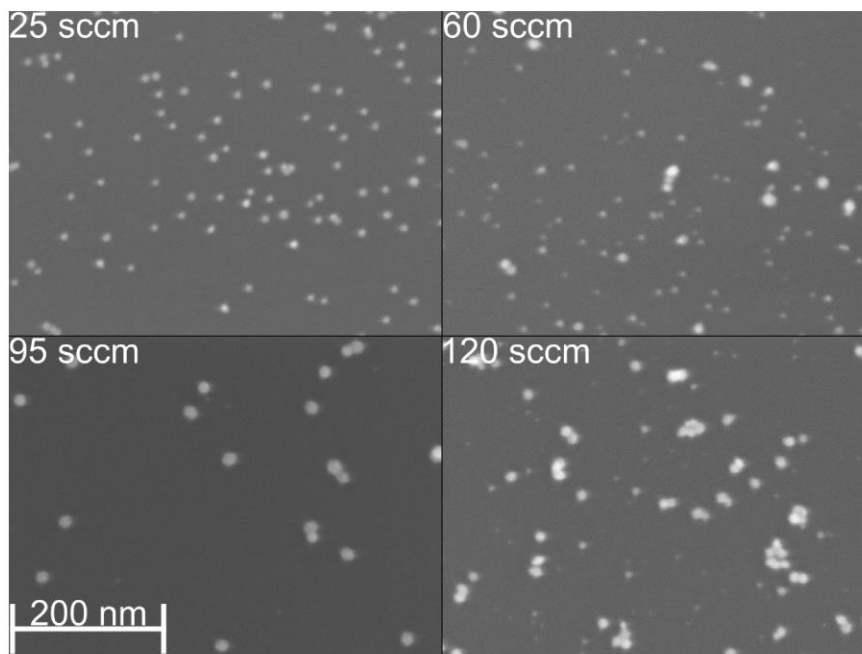


Figure S3: SEM images of four different AgAu NPs samples deposited with a power of 100 W and different flows. Top left 25 sccm (45.1 Pa), top right 60 sccm (100.4 Pa), bottom left 95 sccm (153.2 Pa) and bottom right 120 sccm (188.1 Pa).

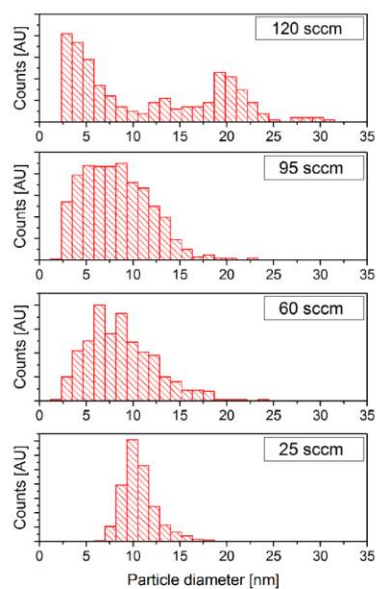


Figure S4: Size distribution of four different AgAu NPs sample deposited with a power of 100 W and different flows. From top to bottom with flows of 120 sccm (188.1 Pa), 95 sccm (153.2 Pa), 60 sccm (100.4 Pa) and 25 sccm (45.1 Pa).

Setup of the system

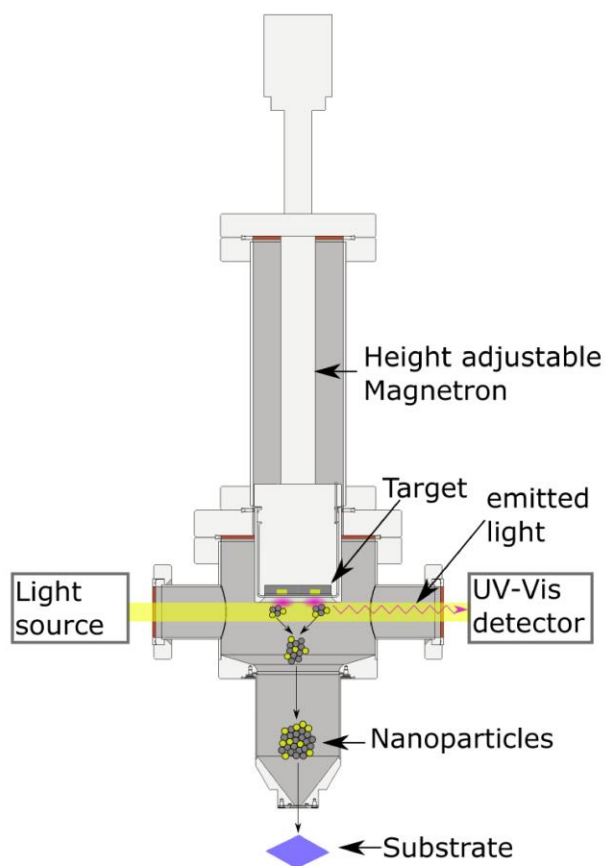


Figure S5: Schematic of the gas aggregation source with mounted UV-Vis setup and a schematic of the cluster formation.

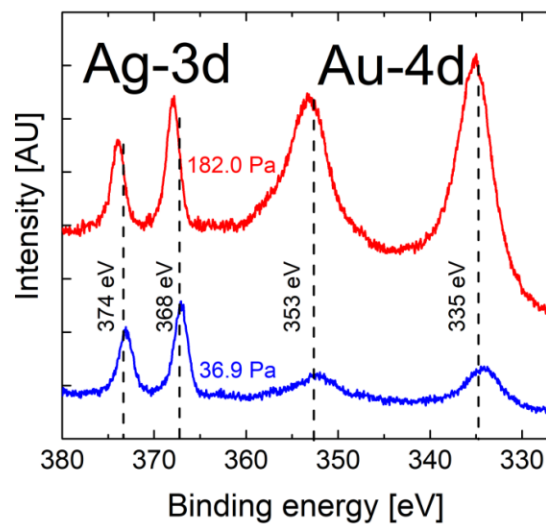
XPS Analysis

Figure S6: Exemplary XPS spectra of the Ag-3d and Au-4d peaks for AuAg nanoparticles deposited at two different pressures. The red curve shows the high resolution spectra for 182.0 Pa and the blue curve for 36.9 Pa. One can see directly that the Au concentration is much higher for 182.0 Pa than for 36.9 Pa.

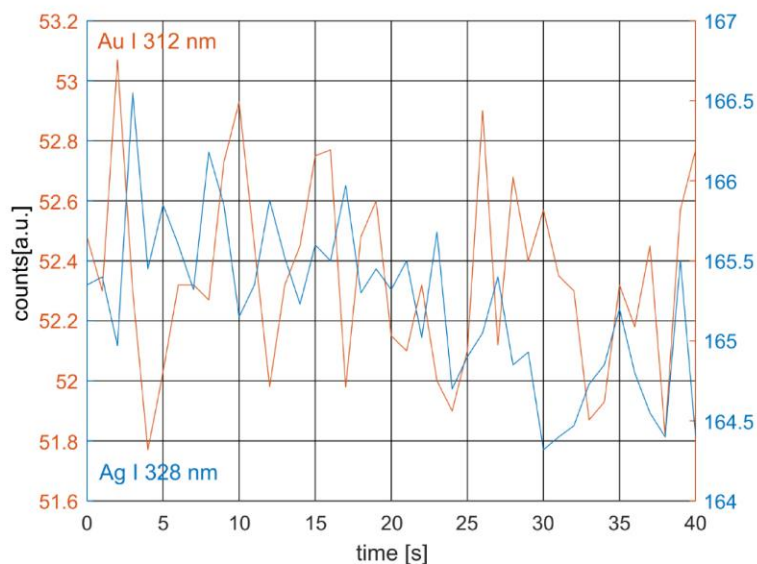
Time evolution of emission intensity

Figure 7: The time evolution of the emission intensities of the Au and Ag line are shown. The target was conditioned by running a deposition at a pressure of 92.4 Pa prior to the experiments which corresponds to broader sputter region and afterwards the pressure is increased to 182 Pa which corresponds to a narrow region, nearly no changes in the emission lines over time are visible because no redeposited material get sputtered.

References

- [1] Shelemin A, Pleskunov P, Kousal J, Drewes J, Hanuš J, Ali-Ogly S, Nikitin D, Solař P, Kratochvíl J, Vaidulych M, Schwartzkopf M, Kylián O, Polonskyi O, Strunskus T, Faupel F, Roth S V., Biederman H and Choukourov A 2020 Nucleation and Growth of Magnetron-Sputtered Ag Nanoparticles as Witnessed by Time-Resolved Small Angle X-Ray Scattering *Part. Part. Syst. Charact.* **37** 1–11
- [2] Nikitin D, Hanuš J, Ali-Ogly S, Polonskyi O, Drewes J, Faupel F, Biederman H and Choukourov A 2019 The evolution of Ag nanoparticles inside a gas aggregation cluster source *Plasma Process. Polym.* **16** 1–7
- [3] Kousal J, Shelemin A, Schwartzkopf M, Polonskyi O, Hanuš J, Solař P, Vaidulych M, Nikitin D, Pleskunov P, Krtouš Z, Strunskus T, Faupel F, Roth S V., Biederman H and Choukourov A 2018 Magnetron-sputtered copper nanoparticles: lost in gas aggregation and found by in situ X-ray scattering *Nanoscale* **10** 18275–81

3.7 Publication F: A Novel Method for the Synthesis of Core-Shell Nanoparticles for Functional Applications Based on the Long-Term Confinement in a Radio Frequency Plasma

In this study, a novel method for the production of core-shell NPs is presented. First, Ag NPs are produced with a HGAS and then these NPs are confined and coated in a secondary RF discharge. Other groups have produced core-shell NPs also by a combination of a HGAS and secondary sputtering process. But there the NP coating thickness depends on the time of flight through the coating region. In our approach, the NPs are confined inside the RF discharge and can be held there for extremely long durations. The confinement as well as the coating process were monitored by in-situ FTIR measurements and in-situ UV-Vis spectroscopy.

In the first part of the publication, it was proven with in-situ UV-Vis measurements that the Ag NPs can be confined and trapped inside the second RF-discharge for 1 h without the loss of NPs. Since the absorption of the LSPR was stable for the measurement time of 1 h, it is expected that the NPs can be trapped for even longer time scales. In the second part of the study, the coating of the Ag NPs was performed by injecting silane (SiH₄) into the RF discharge. The UV-Vis measurements have shown that the LSPR red-shifts during the whole coating time as long as silane is injected into the discharge. This was attributed to the formation of a silicon dioxide shell around the NPs. The FTIR measurements have shown increasing absorption due to the Si-O-Si bonds during the coating process which also confirmed the shell formation. Additionally, samples were extracted out of the RF discharge for different coating times. These samples were measured with a TEM and also EDX measurements were performed. It turned out that the Ag NPs are not homogeneously coated for a coating time of 5 min, but the coating became homogeneous for a deposition time of 10 min. The EDX measurements have also shown a nonlinear trend of the silicon content in relation to the coating time. Unfortunately, it could not be clarified without further research why the growth is inhomogeneous.

In summary, a novel production method for core-shell NPs was demonstrated. The very fast development of this approach was only possible because of the in-situ diagnostic methods, which enabled to find stable confinement and coating conditions without the extraction and ex-situ analysis of samples. This is a perfect example which shows how in-situ diagnostics can be used to speed up the process development. Furthermore, the in-situ diagnostics could be used in this publication to demonstrate the high degree of process control. In the future, diverse types of core-shell NPs can be produced by this method as long as the cores can be produced by the HGAS and a suitable precursor is available for the desired shell material. Even multiple shells are possible.

Own contributions were the development of a new HGAS for this setup and the execution of UV-Vis measurements. The writing of the manuscript and the interpretation of data was done together with equal contributions from me and Oguz Han Asnaz.

This chapter is a reprint from the following publication:

Asnaz, O. H., **Drewes, J.**, Elis, M., Strunskus, T., Greiner, F., Polonskyi, O., Faupel, F., Kienle, L., Vahl, A., & Benedikt, J. (2023). A novel method for the synthesis of core-shell nanoparticles for functional applications based on long-term confinement in a radio frequency plasma. *Nanoscale Advances*. <https://doi.org/10.1039/D2NA00806H>



Cite this: DOI: 10.1039/d2na00806h

A novel method for the synthesis of core–shell nanoparticles for functional applications based on long-term confinement in a radio frequency plasma†

Oguz Han Asnaz,^{†a} Jonas Drewes,^{†b} Marie Elis,^c Thomas Strunskus,^{†bd} Franko Greiner,^{†ad} Oleksandr Polonskyi,^{†§b} Franz Faupel,^{†bd} Lorenz Kienle,^{†cd} Alexander Vahl^{†*bd} and Jan Benedikt^{†*ad}

A novel combined setup of a Haberland type gas aggregation source and a secondary radio frequency discharge is used to generate, confine, and coat nanoparticles over much longer time scales than traditional in-flight treatment. The process is precisely monitored using localized surface plasmon resonance and Fourier-transform infrared spectroscopy as *in situ* diagnostics. They indicate that both untreated and treated particles can be confined for extended time periods (at least one hour) with minimal losses. During the entire confinement time, the particle sizes do not show considerable alterations, enabling multiple well-defined modifications of the seed nanoparticles in this synthesis approach. The approach is demonstrated by generating Ag@SiO₂ nanoparticles with a well-defined surface coating. The *in situ* diagnostics provide insights into the growth kinetics of the applied coating and are linked to the coating properties by using *ex situ* transmission electron microscopy and energy dispersive X-ray spectroscopy. Surface coating is shown to occur in two phases: first, singular seeds appear on the particle surface which then grow to cover the entire particle surface over 3 to 5 minutes. Afterwards, deposition occurs *via* surface growth which coincides with lower deposition rates. Our setup offers full control for various treatment options, which is demonstrated by coating the nanoparticles with a SiO₂ layer followed by the etching of the part of the applied coating using hydrogen. Thus, complex multi-step nanofabrication, *e.g.*, using different monomers, as well as very large coating thicknesses is possible.

Received 14th November 2022
Accepted 19th December 2022

DOI: 10.1039/d2na00806h
rsc.li/nanoscale-advances

1 Introduction

Over the last few decades, noble metal nanoparticles (NPs) attracted the attention of many researchers because of their unique properties in comparison to their bulk counterparts. These properties gave rise to various fields of applications such as photocatalysis,^{1–5} optics,⁶ resistive switching,^{7–13} and

sensors.^{14–18} The optical properties originating from the presence of localized surface plasmons¹⁹ open up applications in the fields of, *e.g.*, surface-enhanced Raman spectroscopy,²⁰ solar cells,²¹ and absorber layers for solar thermal collectors.²² Furthermore, noble metal NPs and especially Ag NPs show antibacterial properties because their high surface-to-volume ratio enables fast ion release.²³ Fine control over the ion release rate of Ag NPs is of high importance for applications like antibacterial coatings in medicine, construction industry, clothing, or food packaging. This can be achieved *via* the incorporation of Ag NPs into a polymer matrix, *e.g.*, PTFE, PMMA, or PA6 as the ion release rate depends on the matrix material as well as on its thickness.^{24–26} The optical properties of Ag NPs are also tunable by changing the surrounding dielectric medium, because the localized surface plasmon resonance depends on the dielectric constant of the surrounding medium.²⁷ Therefore, a precise control over the matrix properties and its thickness is critical to tune the ion release, antimicrobial, and optical properties.

^aInstitute of Experimental and Applied Physics, Kiel University, Leibnizstr. 19, D-24098 Kiel, Germany. E-mail: benedikt@physik.uni-kiel.de

^bChair for Multicomponent Materials, Institute of Materials Science, Kiel University, Kaiserstr. 2, D-24143 Kiel, Germany. E-mail: alva@tf.uni-kiel.de

^cChair for Synthesis and Real Structure, Institute of Materials Science, Kiel University, Kaiserstr. 2, D-24143 Kiel, Germany

^dKiel Nano, Surface and Interface Science KiNSIS, Kiel University, Christian-Albrechts-Platz 4, D-24118 Kiel, Germany

† Electronic supplementary information (ESI) available. See DOI: <https://doi.org/10.1039/d2na00806h>

‡ These authors contributed equally to this work.

§ Currently at: Department of Chemical Engineering, Engineering II, University of California–Santa Barbara, Santa Barbara, CA 93106, United States.



The inter-particle distance is an additional important parameter to tune the optical properties of absorber layers,²⁸ which is usually difficult to tune when the NPs and the matrix are synthesized at the same time or after each other on a substrate. In such cases, core-shell NPs are interesting building blocks, as a precise control of their coating thickness comes with control over the inter-core distance once the particles are closely packed. Ag@SiO₂ NPs (Ag core and SiO₂ shell) exhibit interesting optical²⁹ and antibacterial properties.³⁰ Ag@SiO₂ core-shell NPs can be synthesized by different methods. For the core, Ag NPs can be synthesized by chemical, physical, or biological methods.³¹ A chemical way is, *e.g.*, the reduction of silver nitrate with hydrazine. In order to form Ag@SiO₂ core-shell NPs, the Stöber method³² can be applied to coat the Ag NPs.³⁰ Such methods have the drawback that the produced particles are in solution and it can be difficult to remove all chemicals from the NPs to obtain high purity.

One particularly versatile approach to fabricate highly pure noble metal nanoparticles without the need for any surfactant is a magnetron-based, Haberland-type gas aggregation source (GAS).³³ A Haberland type GAS consists of a vacuum chamber equipped with a magnetron. The chamber is connected to a deposition chamber *via* a small orifice with a diameter in the range of millimeters. Due to the orifice the pressure in the GAS is in the order of tens to hundreds of pascals, which is high in comparison to conventional sputtering devices for the formation of thin films. The sputtered atoms can form NPs in the gas phase due to the high pressure and are then transported to the deposition chamber by the drag force of the sputtering gas.

GASs have also been successfully used to create core-shell NPs. Huttel *et al.*³⁴ use multiple magnetrons in the gas aggregation volume and tailor the distance between each magnetron and the exit orifice to create binary or ternary core-shell NPs. This approach however is limited by the time of flight of the particles and the length of the aggregation zone and is mostly used for metal@metal nanoparticles. In a second approach by Ahadi *et al.*³⁵ and Kylián *et al.*,³⁶ the Haberland type GAS is combined with a secondary direct current (DC) magnetron discharge to synthesize pure NPs in the GAS and then coat them prior to deposition in the second discharge with a shell material. The achievable coating thickness is limited by the maximum power, which can be applied to the target and the residence times defined by the strength of the gas flow. Investigations by Solař *et al.*³⁷ on the exit velocity of NPs have shown that for typical operating conditions even mean velocities of up to 93 m s⁻¹ are possible. Therefore, special experimental measures have to be taken in order to increase the residence time of the particles in the secondary coating region, *e.g.*, by injecting additional argon gas. Moreover, the fabrication of complex core-shell particles involving several layers is not possible.

In this paper, we will present a combination of a Haberland type GAS together with a secondary radio frequency (RF) plasma discharge, in which Ag NPs are trapped for a secondary coating process with SiO₂. This setup circumvents the limitations of in-flight coating, as the trapped particles can be treated over much longer time scales and even over multiple processing steps

independent of their synthesis parameters. On these time scales, *in situ* diagnostics become powerful tools for very fine control of the particle properties. Using both localized surface plasmon resonance (LSPR) and Fourier-transform infrared spectroscopy (FTIR) allows for creating core-shell particles with a defined composition and thickness specifically designed for their application. We will compare the two diagnostic methods focusing on the insight into particle properties they offer. To provide a ground truth for the *in situ* diagnostics, we are extracting particles and using transmission electron microscopy (TEM) and energy dispersive X-ray spectroscopy (EDX) as an *ex situ* measurement.

2 Experimental setup and diagnostics

2.1 Experimental setup

The experimental setup shown in Fig. 1 is a modular vacuum deposition setup consisting of two fundamental components: a gas aggregation source (GAS) that generates metal NPs and an RF plasma trapping setup, which holds them for further

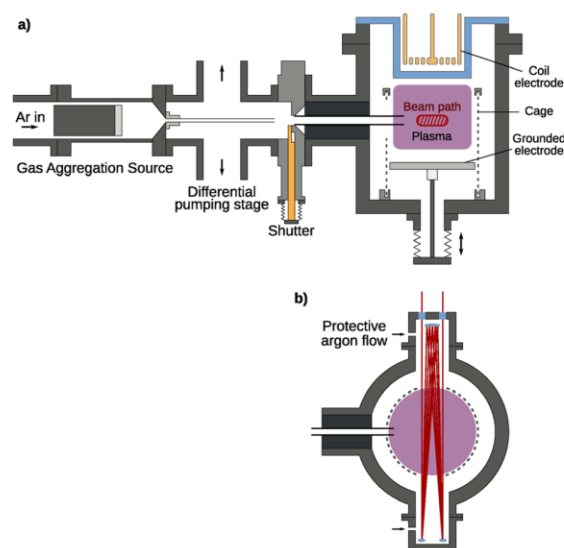


Fig. 1 (a) Side view of the experimental setup combining a gas aggregation source (GAS) with a secondary treatment plasma setup for long-term confinement. Particles are generated at the GAS at a higher pressure, creating a flow directed through the feed pipe to the differential pumping stage. Here, the buffer gas is pumped away symmetrically to minimize the loss of particles. The particles then flow through a second feed pipe through a shutter system directly into the treatment plasma volume, where charging effects ensure their confinement. While a coil electrode is used for the option of an inductively coupled plasma, in this work it is only used in a capacitively coupled mode. The plasma volume is surrounded by a grounded cage for better confinement through higher electric fields. The hatched area in red represents the IR/UV-vis beam area oriented perpendicular to the sketch plane. (b) Top view of the treatment plasma chamber. The IR/UV-vis beam path is shown in red. Argon is let in through the marked nozzles to create a protective gas flow for the white cell mirrors.



treatment. The GAS is a custom-build Haberland type gas aggregation source connected to the treatment plasma setup via a differential pumping stage. The source was equipped with a 2-inch height-adjustable and water-cooled DC magnetron (IX2U-9A327-02; Thin Films Consulting). The height-adjustable magnetron enables the tuning of the aggregation length, *i.e.*, the distance between the magnetron and the orifice of the GAS. This distance was kept constant for all experiments. The deposition was performed with a flow of 160 sccm Ar, which corresponds to a pressure of about 170 Pa in the GAS. An MDX 500 from Advanced Energy was used as a power supply and was operated in the power regulation mode with a power of 100 W. An MKS flow controller (GE50 A) with a 500 sccm range was used for the gas flow regulation. To keep the operating pressure of the GAS and treatment plasma independent of each other, a differential pumping stage is used to remove a large portion of the buffer gas. By pumping symmetrically from top and bottom, the resulting deflection of the particle stream is minimized. Additionally, the particles are guided with a feed pipe up to a distance of 10 mm in front of the aperture, keeping the particle stream focused and maximizing transfer into the next stage. At this point, a shutter allows for interrupting the particle stream and sealing the treatment plasma from the rest of the setup, if necessary. Finally, using a second feed pipe, the particles are injected directly into the plasma volume where charging effects and the resulting electric field forces ensure confinement of the particles.

The treatment plasma consists of a grounded bottom electrode on a linear movement stage with a 142 mm diameter. The upper electrode is a copper coil with 2×3 windings driven with a Dressler Cesar 133 RF generator providing a power of up to 150 W at 13.56 MHz at its middle contact behind a borosilicate glass cylinder, enabling both inductively coupled (ICP) and capacitively coupled plasma (CCP) operation. For this experiment, the CCP mode was used exclusively as the higher energy density of the ICP mode disintegrates the silver particles very quickly, seen as emission lines in the optical emission spectrum. Around the plasma volume, a grounded wire mesh with a 1 mm wire diameter and 3 mm spacing is used to improve particle confinement using high electric fields in the resulting plasma sheath. In the mesh, openings are cut for the feed pipe, for a multi-pass IR/UV-vis beam path, and for particle extraction. Additionally, a gas inlet for different reactive gases is present at the treatment plasma chamber. Different MKS flow controllers (GE50 A) are connected to control the precursor flow. The flow controller for the SiH_4/Ar mixture with 0.01% SiH_4 has a range of 200 sccm. Additionally, flow controllers with a range of 10 sccm are present for H_2 and O_2 .

FTIR and UV-vis spectra are always recorded *in situ* in the treatment plasma chamber (see Fig. 1) using a multi-pass beam setup consisting of a white cell (neoplas control GmbH) for up to 20 passes, increasing the optical path through the plasma volume to $z_{\text{IR}} = 20 \times 142 \text{ mm} = 2.8 \text{ m}$ for the IR beam and $z_{\text{UV-vis}} = 4 \times 142 \text{ mm} = 0.6 \text{ m}$ for the UV-vis setup. The beam path crosses a region of about 10 mm height and 40 mm width. To prevent deposition on the multi-pass cell and the windows, Ar gas was injected at both sides of the multi-pass cell. The Ar flow

was controlled with an MKS flow controller (GE50 A) with a range of 50 sccm and was set to 30 sccm. The Ar gas flow is shared by both gas inlets at both sides of the multi-pass cell. For IR-spectrometric monitoring, a commercial FTIR spectrometer (Bruker VERTEX 80v) is used with a liquid-nitrogen-cooled DLaTGS detector. This setup has been previously used for monitoring the growth and treatment of hydrogenated amorphous carbon (a-C:H) NPs generated from C_2H_2 precursors.³⁸ UV-vis spectrometry is performed using a deuterium-halogen light source (Ocean Optics DH-2000-BAL) and a spectrometer (Ocean Optics USB4000).

Particle extraction is realized with a load-lock setup bringing in a 10 mm \times 10 mm silicon wafer piece clamped underneath a stainless steel metal plate with a circular cutout. By applying a short 200 ms pulse of 170 V to the metal plate using a Keithley SourceMeter 2400, particles are accelerated towards the sample holder and stick to the silicon wafer for further *ex situ* analysis. With the chamber being operated only in the high vacuum range and residual air coming in through the load-lock, there is enough residual oxygen in the system when using a gas mixture of 0.01% SiH_4 in Ar for SiO_2 coating without active addition of oxygen.

For transmission electron microscopy (TEM) analysis, the nanoparticles were scratched off the silicon substrate with a scalpel and transferred onto a copper grid with a carbon lacey coating (Plano GmbH). Bright field imaging as well as selected area electron diffraction (SAED) were performed with a FEI Tecnai F30 STwin G^2 with 300 kV acceleration voltage. For energy dispersive X-ray (EDX) spectroscopy, the microscope is equipped with a Si/Li detector (EDAX System). The EDX spectroscopy data were processed with ES Vision (version 4.0.173).

2.2 Experimental procedure

In this chapter, the general experimental procedure will be described in detail:

1. The system is pumped down with a turbo molecular pump down to a pressure of 10^{-5} Pa. Then the valve to the turbo pump is closed.
2. Rough pumps for the differential pumping stage and the rough pump of the treatment plasma chamber are started.
3. The Ar flow for the GAS (160 sccm) and the multi-pass cell (30 sccm) are activated and the valves of the rough pumps are opened. The pressure in the GAS, at the differential pumping stage, and in the treatment plasma chamber stabilizes at values of about 170 Pa, 16 Pa and 11 Pa respectively.
4. The CCP Plasma is switched on with an RF power of 188 W and a reflected power of 88 W.
5. The UV-vis or the FTIR spectrometer respectively starts recording along the line of sight through the treatment plasma chamber.
6. The power supply for the magnetron of the GAS is switched on with 100 W usually for 10 s which starts the synthesis and injection of Ag NPs into the treatment plasma. Only for the long-term confinement in Fig. 2 an on-time of 60 s is used.
7. The flow of the SiH_4 mixture (0.01% in Ar) is set to 20 sccm and the Ar flow through the multi-pass cell is reduced to 10



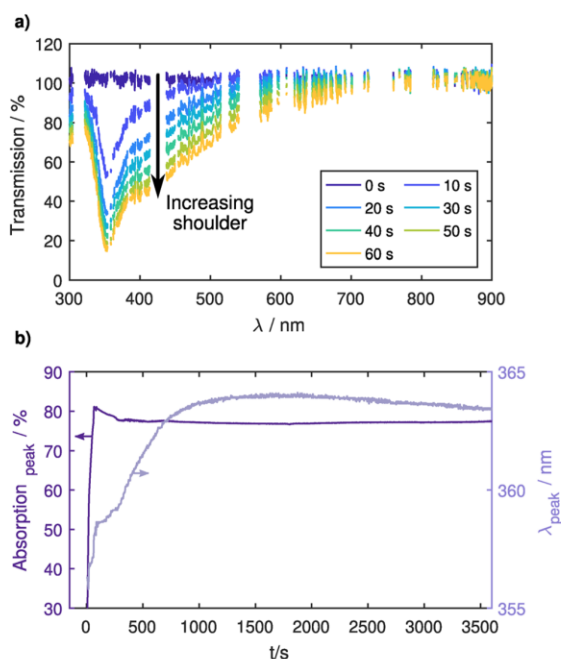


Fig. 2 (a) *In situ* UV-vis transmission spectra for 7 different times during the NP injection. 0 s corresponds to the plasma ignition in the GAS. At 60 s the injection of Ag NPs is stopped. Plasma emission lines were removed from the spectra. (b) Long-term measurement of injected Ag NPs, which are trapped for 1 h in the CCP plasma. The peak position λ_{peak} corresponds to the wavelength of the minimum in the transmission spectrum.

scm to keep the pressures constant. This flow creates precursor densities below the critical point for silicon NP formation from silane precursors, which was confirmed with prior FTIR measurements in the absence of silver NPs.

8. Once the desired coating times of 1, 3, 5 and 10 min are reached, the precursor flow is switched off by setting the flow controller to 0 scm to stop the coating procedure.

9. In the case of extraction, after a short waiting time, the NPs are extracted by opening the load lock and moving the extraction unit close to the plasma. After the voltage pulse (170 V and 200 ms) is applied, the extraction unit is moved back into the load lock, which is then closed again.

10. Plasma and spectrometers are switched off.

3 Results

3.1 Long-term confinement of uncoated Ag NPs

Fig. 2a shows several UV-vis transmission spectra during the injection process. Here, plasma emission lines were excluded from the spectrum using a reference spectrum taken before the injection. The main peak ≈ 355 nm of the localized surface plasmon resonance (LSPR) of the Ag NPs can exhibit a red shift both for an increase in the NP size^{39–41} and for a surrounding dielectric with a dielectric constant greater than unity.^{27,42,43} In Fig. 2b, the position of the main peak only shows a small red

shift of 9 nm over one hour of confinement. This is unlikely to come from a particle size increase due to agglomeration, as the particles are charged in the plasma environment and repulse each other. It is more likely that the presence of trace amounts of oxygen causes an oxidation of the particle surface, effectively changing the surface dielectric constant and thereby causing the slight red shift. Therefore, this measurement can be assumed as a reference measurement for an unperturbed system without the usage of any precursor gas. The shift in the LSPR is relatively small and still allows the detection of a shift of the LSPR related to an additional coating of the Ag NPs, which will be shown in the next section.

Looking at the absorption strength of the LSPR, a strong increase can be seen during particle injection coming from the increase in NP density. This increase is followed by a slight decrease of about 5% in the first minutes of confinement after which it stays very constant for the remainder of the experiment, indicating that the NPs are well confined in the CCP plasma. The small decrease also points towards oxidation, as the oxide layer would effectively decrease the plasmonically active diameter of the NP. After the CCP plasma is switched off, the transmission over the entire spectral range goes back to its initial value, showing that no NPs are deposited on mirrors or windows in the optical path (see Fig. 1 in the ESI†).

Additionally, Fig. 2a shows a change in the peak shape. For longer injection times a shoulder appears at higher wavelengths, which also stays after the injection is stopped. This might stem from the coupling of LSPRs of multiple NPs. If plasmonic NPs approach each other to a close distance of around 30 nm or smaller, the LSPRs can couple which causes additional resonances at higher wavelengths.²⁸ Assuming an average particle diameter of 20 nm and resulting LSPR cross section⁴⁴ of $\sigma_{\text{LSPR}} = 2 \times 10^3 \text{ nm}^2$ at the peak, we can use the UV-vis spectrum to calculate a particle number density of $n \approx 10^{15} \text{ m}^{-3}$. This is in the same order of magnitude as the electron density and therefore leads to a strong electron depletion.^{45,46} Particles are not being charged to their theoretical capacitive limit determined by orbital motion limited (OML) theory, but rather only carry very few elementary charges that fluctuate stochastically. While the average inter-particle spacing at this density is about 5 μm , this reduction of repulsive forces leads to a wide spacing distribution and particles regularly come close enough for plasmonic coupling or even agglomeration to occur. For the following investigations of coating of trapped NPs, the injection time was limited to 10 s to lower particle densities and thereby avoid plasmonic coupling phenomena.

3.2 *In situ* coating and *in situ* diagnostics of coating thickness

Ag NPs were injected into the CCP plasma for treatment. Different SiH_4 exposure durations were applied to control the thickness of the dielectric shell around the Ag NPs. The recorded UV-vis spectra can be seen in Fig. 3a. Over time, the main absorption peak shifts towards higher wavelengths due to the LSPR from the Ag NPs together with a general increase in overall absorption, which is in line with the literature.^{27,42,43} Interestingly, a shoulder



Paper

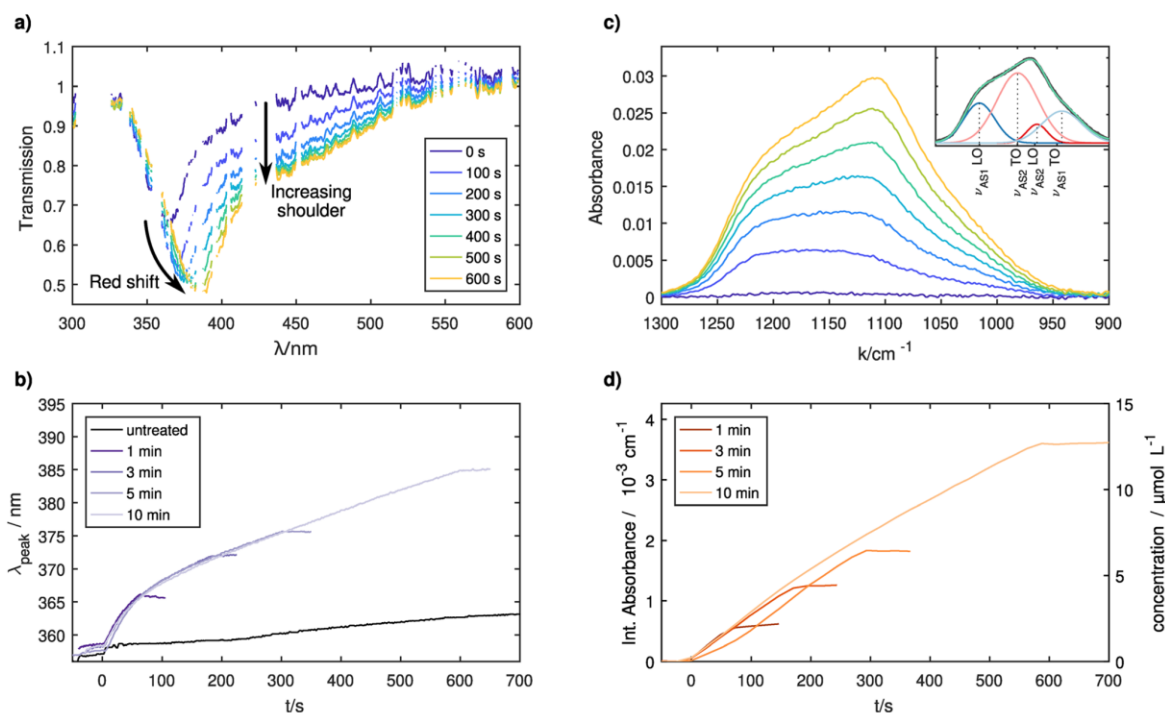


Fig. 3 (a) UV-vis absorption spectrum showing a LSPR peak shift. The starting time $t = 0$ s corresponds to the start of the coating treatment. Plasma emission lines were removed from the spectrum. (b) Time evolution of the LSPR peak position for four different treatment durations. (c) FTIR absorption spectrum with the inset showing a decomposition of the Si–O–Si asymmetric stretching absorption and the sum of fits. (d) Time evolution of the integrated absorbance and calculated Si–O–Si concentration in the plasma volume for four different treatment durations.

at higher wavelengths becomes stronger with increasing coating times similar to the results for high particle densities reported in the previous section. Therefore, it can be assumed that the LSPRs of different NPs are coupled to each other in the coated case. The addition of silane as an electronegative gas lowers the free electron density further,⁴⁷ thereby lowering the average inter-particle spacing. The agglomeration of coated particles could also lead to the observed increased shoulder as even after agglomeration the plasmonically active cores are electrically separated by their shells. SEM pictures have shown that some agglomerates are present on the samples (see Fig. 2 in the ESI†), yet it is unclear if these agglomerates are formed in the CCP plasma or during the deposition. Another study has also shown that agglomerates can be formed already inside the GAS.⁴⁸ Nevertheless, these agglomerates from the GAS would not affect the LSPR during the coating period, as the GAS is switched off prior to the coating step. Further investigations would be necessary to determine whether agglomeration occurs in the treatment plasma.

Fig. 3b shows the time evolution of the main LSPR peak for four separate treatments, differing from each other only in the total coating time. Values smaller than 0 s correspond to the pure Ag NPs before the SiH₄ was injected into the chamber. The reproducibility of the experiment is very good, with the only visible difference between the curves being the different points at which the SiH₄ gas flow was turned off. In general, prior to the treatment no significant changes are visible, which is expected

and was shown in the previous section. Once the treatment starts at 0 s, all curves show a strong redshift of the LSPR peak position. Nevertheless, the trend is not linear. The slope decreases until ≈ 150 s, after which the LSPR shift shows a linear dependency on the coating time until the SiH₄ flow is switched off. The general redshift of the LSPR is explained by the coating of the NPs with a dielectric medium, whereas the change in the slope is more difficult to explain. It is known that for thin coatings, the LSPR shift shows a linear dependence on the layer thickness. For thicker coatings, the slope of the LSPR decreases at some point before an asymptotic limit is reached and the LSPR position does not change anymore with increasing thickness. This is explained by the limited distance to which the local electromagnetic field extends from the surface of the silver NP into the coating.²⁷ In this study, the behavior is different indicating that most probably the coating thickness is not increasing linearly with time or that the coating of the NPs inside the CCP plasma is not homogeneous.

In situ FTIR experiments were additionally conducted to differentiate between these options. A quantitative analysis of the infrared absorption spectrum yields atomic Si densities for the absorbing Si–O–Si bonds. The Si–O–Si asymmetric stretching (ν_{AS}) vibration in the 1300–900 cm⁻¹ range splits up into four separate lines. The first splitting occurs due to the AS motion of two adjacent oxygen atoms being possible either in-phase (ν_{AS1}) or shifted 180° (ν_{AS2}). Furthermore, the stretching



Nanoscale Advances

Table 1 Used parameters for Gaussian line fits. Wavenumbers were selected based on ref. 50

Excitation mode	$\tilde{\nu}/\text{cm}^{-1}$	σ/cm^{-1}
ν_{AS1} LO	1208 ± 13	40
ν_{AS2} TO	1129 ± 12	40
ν_{AS2} LO	1098 ± 11	15
ν_{AS1} TO	1025 ± 90	50

motion is possible in longitudinal optical (LO) and transversal optical (TO) modes, which are coupled through long-range Coulomb interactions leading to a second splitting.⁴⁹ The positions and full width half maxima (FWHM) of these lines are fitted following Fidalgo *et al.*⁵⁰ and Kirk⁴⁹ using bounds given in Table 1 (see also Fig. 3 in the ESI†). An example decomposition can be seen as an inset of Fig. 3c.

We obtain the absolute concentrations of Si in our observed volume, by further considering the absorption intensities of the Si–O–Si asymmetric stretching modes,⁵¹ see Fig. 3d. The reproducibility of the subsequent experiments is similarly good as in the previously described UV-Vis measurements with only one treatment (5 minutes, shown in yellow) showing a slightly delayed onset of the silicon layer growth. This indicates that as the chamber was cleaned using an O₂ plasma before the five minute treatment (first treatment of the measurement series), the initial chamber conditions have an influence on the growth rate of the coating. A detailed look at the 10 minute treatment (see Fig. 4), which was done last in the series of experiments, shows that the first 150 seconds of treatment show a higher rate of growth of about $0.23 \mu\text{mol L}^{-1} \text{s}^{-1}$, whereas afterwards a rate of $0.17 \mu\text{mol L}^{-1} \text{s}^{-1}$ is measured.

In Fig. 5, the long-term effects of confinement are shown for slightly coated particles, as uncoated Ag particles are not visible in the measured IR spectral range. The measurement shows that after 90 s of coating, some slight increase continues in the first 500 s likely due to residual precursors being used up and

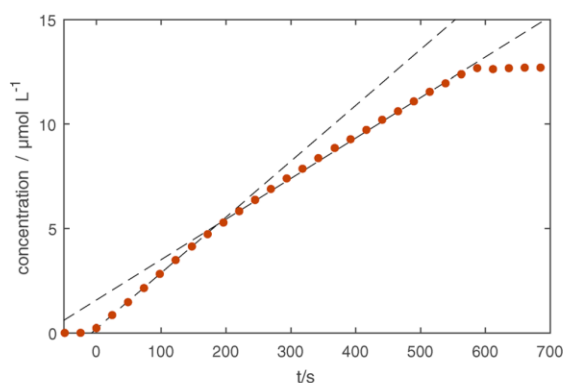


Fig. 4 Total concentration of Si determined through fitting the four Si–O–Si stretching modes in the IR spectrum. The growth rate changes after about 150 seconds from $0.23 \mu\text{mol L}^{-1} \text{s}^{-1}$ to $0.17 \mu\text{mol L}^{-1} \text{s}^{-1}$ and is indicated with dashed lines.

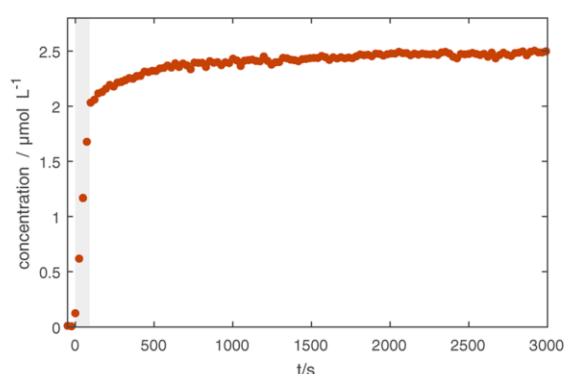


Fig. 5 Prolonged argon plasma treatment of SiO₂-coated Ag NPs. The particles have been generated in the GAS and coated using silane injection for 90 s (marked in grey) followed by an hour-long confinement. Gas pressure: 11 Pa, CCP power: 100 W, and argon flow: 30 sccm.

some slight effects of the plasma treatment. Afterwards, no further changes are seen. This and supplementary TEM measurements (see Fig. 4 in the ESI†) show that it is possible to confine the particles for tens of minutes without damaging the coating, opening up possibilities for various treatments.

3.3 *In situ* observation of coating and etching of the coating

Finally, coating and etching experiments have been conducted using both UV-vis and IR monitoring one after the other. In this last section, the reliability of the particle coating and confinement will be shown.

Here, Ag NPs were injected into the treatment chamber, coated with SiO₂ for 200 s and then etched using H₂. Fig. 6 shows the FTIR and UV-vis results of the coating and etching experiments, measuring both the Si–O–Si concentration and LSPR peak position. Looking at the change in the LSPR peak position, a significant red shift is seen due to the coating process in the first 200 s as discussed in the previous section. Similarly, the IR absorption shows a linear increase of Si–O–Si bonds indicating linear growth of SiO₂ on the surface. When the SiH₄ flow was switched off at 200 s the IR absorption stops increasing except for slight continuing growth while the remaining precursors in the chamber are used up. In contrast, the LSPR shows a continuing red shift albeit at a slower rate than before the SiH₄ flow was switched off. At 250 s, H₂ gas was injected into the treatment plasma chamber with a flow of 1 sccm. Here, the LSPR peak shows an immediate blue shift due to the H₂ etching, with a decreasing rate over time that is also seen in the IR absorption. This indicates that the etching reactions become slower over time, probably due to the decreasing surface area of the particles. When the H₂ flow is switched off, the IR absorption stays constant at its new level, while the LSPR peak position shifts towards longer wavelengths.

While the IR absorption is mainly dependent on the Si–O–Si concentration in the NP shell, the LSPR is also influenced by other particle properties such as charge⁵² and temperature.⁵³



Paper

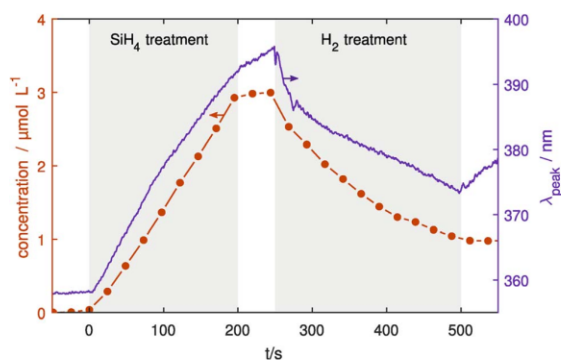


Fig. 6 Deposition and etching experiment with SiO₂ coated Ag NPs. Ag NPs were injected into the treatment chamber, coated using SiH₄ and subsequently etched using H₂ (both marked in grey). This procedure was done once with UV-vis measuring the LSPR peak position (right axis) and once with FTIR monitoring measuring the Si–O–Si concentration (left axis). The increase and decrease in coating can be clearly seen in both methods.

Changing the gas composition especially with electronegative gasses like SiH₄ and H₂ can significantly affect the electron density and temperature in the plasma which determines particle charge. Furthermore, it also affects the processes leading to selective particle heating for example through recombination of ions or hydrogen atoms on the particle surface.⁵⁴ Additional plasma diagnostics would be necessary to separate these effects from the influence of the coating thickness.

3.4 Ex situ TEM and EDX investigations

After the *in situ* UV-vis and FTIR results were presented, transmission electron microscopy (TEM) and energy-dispersive X-ray spectroscopy (EDX) investigations of the extracted NPs will be discussed to confirm the conclusions reached. Fig. 7a–d show TEM pictures for NPs with different coating times. For coating times up to 5 min the Ag NPs are not homogeneously coated, but SiO₂ particles are segregating at the surface of the Ag NPs. For 1 min some NPs seem to be completely uncoated and other NPs are only partially coated. For coating times of 3 and 5 min some NPs seem to be completely coated and others appear to be only partially coated. On the other hand for 10 min coating time, the NPs are homogeneously coated with a coating thickness of around 6 nm. This growth behavior of the coating on the Ag NPs is schematically shown in Fig. 7e–h.

This observation supports our claims in the *in situ* UV-vis and FTIR measurements, where at around 150 s several changes of optical properties were observed, indicating the closure of a previously inhomogeneous coating. There are many possible explanations for this initial inhomogeneity, one of which are different reaction cross sections for the primary attachment of SiO₂ on the Ag surface, the SiO₂ growth along the interface between uncoated and coated Ag surfaces, and the surface growth on top of a Si layer. This could lead to different growth mechanisms becoming energetically favorable over time

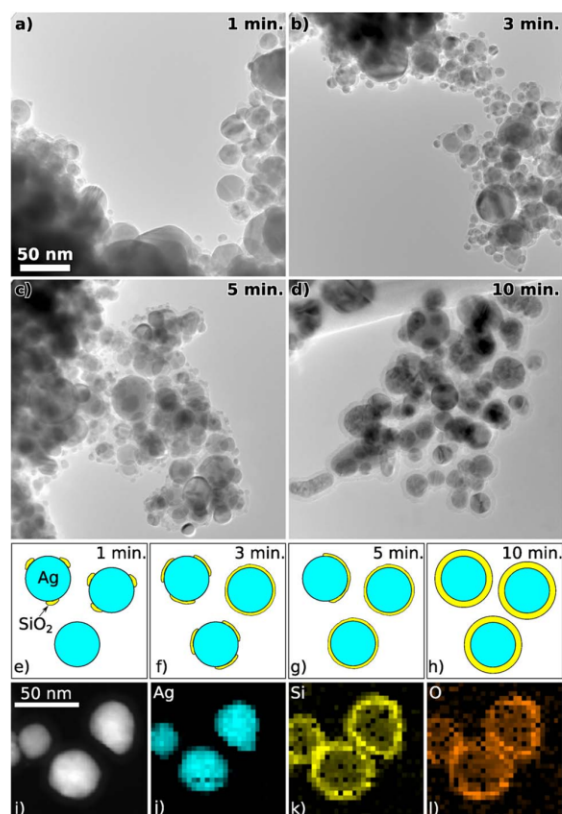


Fig. 7 TEM micrographs for different coating times. It is visible that the NPs are not homogeneously coated for 1 to 5 min. After 10 min the coating looks homogeneous (a–d). The growth of the coating on the Ag NPs is schematically shown (e–h). Additionally, an EDX map is shown for a sample with a coating time of 10 min, which shows that the particles have an Ag core and a SiO_x shell (i–l).

and cause an inhomogeneous initial growth (so-called island growth mechanism). With our novel setup capable of confining the NPs for hours, the longer treatment times necessary to reach a well-defined homogeneous coating are easily possible.

While the NPs are seen as agglomerates on the TEM images, the particles have been scratched off the Si substrates and were transferred onto TEM grids. This procedure is known to cause particle agglomerations. Yet, particle agglomerates were also seen on SEM images (see Fig. 2 in the ESI†), which makes it unclear whether this agglomeration already occurred during confinement in the plasma, as possibly indicated by the coupling of LSPRs seen in an absorption shoulder at higher wavelengths described in an earlier section.

To analyze the coating composition, EDX measurements were performed on the samples. A STEM high angle annular dark field micrograph and the corresponding elemental EDX maps can be seen in Fig. 7i–l. The Ag core and surrounding shell out of Si and O are very well visible. To give a statistically relevant impression of the Si concentration in the samples, multiple TEM EDX spectra were acquired from samples with



Nanoscale Advances

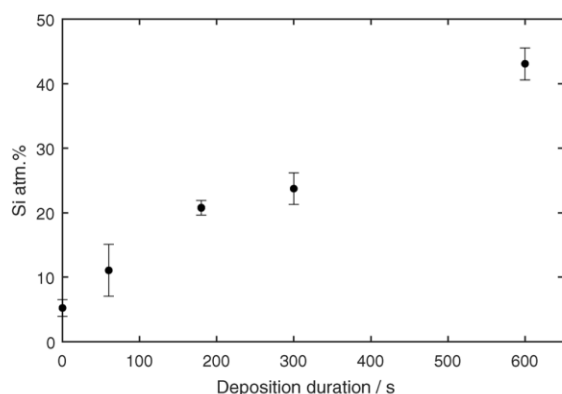


Fig. 8 Atomic concentration of Si measured with EDX during TEM measurements for extracted Ag@SiO₂ NPs with different coating times. Ten different areas of the TEM grid were used for statistical analysis. Only silver and silicon were taken into account to minimize the influence of oxidation after extraction and the background carbon support on the TEM grid.

coating times 1, 3, 5 and 10 min. The exact stoichiometry was not shown because SiO_x was most probably further oxidized as the samples were in contact with air. Nevertheless, the atomic concentrations of Ag and Si were measured, and are shown in Fig. 8. The Si concentration increases steeper from 1 min to 3 min in comparison to the slope from 3 min to 10 min. This is in agreement with the *in situ* FTIR and UV-vis measurements, where different slopes were found from 0 s to 150 s in comparison to 150 s to 600 s.

4 Conclusions

In this work, we have presented a setup capable of confining nanoparticles over very long time scales, which allows a high degree of freedom in the coating process with an additional high degree of process control through *in situ* diagnostics. This has been demonstrated by creating Ag@SiO₂ core-shell NPs for functional applications. Using a Haberland-type GAS, Ag NPs with diameters between 5 and 60 nm have been prepared and subsequently confined in a secondary RF plasma for further plasma treatment. Both UV-vis and FTIR spectroscopy diagnostics have been shown to measure the growth of the SiO₂ shell very sensitively, allowing for fine tuning of the particle properties towards a specific application. For UV-vis, a red shift of the LSPR peak as well as an increase of its absorption strength was observed increasing with the shell size. Similarly, in the FTIR spectrum, the addition of Si–O–Si on the NP surface is seen as an increase in vibrational absorption of lines in the region from 1300–950 cm⁻¹. These findings have been confirmed using *ex situ* TEM and EDX analysis, showing a partial surface coverage for short coating times with a full shell forming after about 5 min. The homogeneity of the coating process could be improved by varying the parameters of the treatment plasma such as plasma power. Here, further particle number density measurements, *e.g.* by using extinction measurements, are

necessary to differentiate between changes in the plasma environment and the coating process.

As GASs are very versatile nanoparticle sources, different metal types, alloys, inorganic compounds, and even polymers can be used as a target to create NPs of various materials. It was shown that it is possible to coat NPs and confine them over an hour without any significant losses of NPs from the treatment plasma. The limits of the confining plasma are only reached when NPs grow to sizes on the micrometer scale, where the gravitational force becomes relevant as it scales with $\propto r^3$ and pushes particles into the lower sheath of the plasma. Our setup overcomes the limitations of in-flight coating and enables various forms of treatment even in multi-step processes demonstrated here through the controlled growth and subsequent etching of an applied coating. This opens up many possibilities for finely tuned particle preparation even of complex core-shell nanoparticles with multiple shells for future applications. One can even imagine creating NPs with a shell with a compositional gradient consisting of different materials, simply by adjusting the reactive gas injection accordingly.

Conflicts of interest

There are no conflicts to declare.

Acknowledgements

The authors thank the German Research Foundation (DFG, project 411452476, and project KI 1263/21-1) for financial support. We also thank the German Academic Exchange Service (DAAD) for the support through the project 57449433.

Notes and references

- M. Z. Ghorri, J. Adam, O. C. Aktas, S. Veziroglu, B. B. Shurtleff, T. Strunskus, F. Faupel, O. Polonskyi and A. Hinz, *ACS Appl. Nano Mater.*, 2018, **1**, 3760–3764.
- S. Veziroglu, M. Z. Ghorri, A. L. Obermann, K. Röder, O. Polonskyi, T. Strunskus, F. Faupel and O. C. Aktas, *Phys. Status Solidi A*, 2019, **216**, 1–6.
- S. Veziroglu, M. Ullrich, M. Hussain, J. Drewes, J. Shondo, T. Strunskus, J. Adam, F. Faupel and O. Cenk, *Surf. Coat. Technol.*, 2020, **389**, 125613.
- A. Vahl, S. Veziroglu, B. Henkel, T. Strunskus, O. Polonskyi, O. C. Aktas and F. Faupel, *Materials (Basel)*, 2019, **12**, 2840.
- H. Li, Z. Li, Y. Yu, Y. Ma, W. Yang, F. Wang, X. Yin and X. Wang, *J. Phys. Chem. C*, 2017, **121**, 12071–12079.
- C. Minnai, M. Di Vece and P. Milani, *Nanotechnology*, 2017, **28**, 0–8.
- C. Minnai, A. Bellacicca, S. A. Brown and P. Milani, *Sci. Rep.*, 2017, **7**, 1–8.
- M. Mirigliano, D. Decastri, A. Pullia, D. Dellasega, A. Casu, A. Falqui and P. Milani, *Nanotechnology*, 2020, **31**, 234001.
- M. Mirigliano, F. Borghi, A. Podestà, A. Antidormi, L. Colombo and P. Milani, *Nanoscale Adv.*, 2019, **1**, 3119–3130.



- 10 Z. Wang, S. Joshi, S. E. Savel'ev, H. Jiang, R. Midya, P. Lin, M. Hu, N. Ge, J. P. Strachan, Z. Li, Q. Wu, M. Barnell, G. L. Li, H. L. Xin, R. S. Williams, Q. Xia and J. J. Yang, *Nat. Mater.*, 2017, **16**, 101–108.
- 11 H. Jiang, D. Belkin, S. E. Savel'ev, S. Lin, Z. Wang, Y. Li, S. Joshi, R. Midya, C. Li, M. Rao, M. Barnell, Q. Wu, J. J. Yang and Q. Xia, *Nat. Commun.*, 2017, **8**, 882.
- 12 X. B. Yan, J. H. Zhao, S. Liu, Z. Y. Zhou, Q. Liu, J. S. Chen and X. Y. Liu, *Adv. Funct. Mater.*, 2018, **28**, 1–9.
- 13 A. Vahl, N. Carstens, T. Strunskus, F. Faupel and A. Hassani, *Sci. Rep.*, 2019, **9**(1), 17367.
- 14 V. Postica, A. Vahl, D. Santos-Carballal, T. Dankwort, L. Kienle, M. Hoppe, A. Cadi-Essadek, N. H. De Leeuw, M. I. Terasa, R. Adelung, F. Faupel and O. Lupan, *ACS Appl. Mater. Interfaces*, 2019, **11**, 31452–31466.
- 15 Y. Yong, C. Li, X. Li, T. Li, H. Cui and S. Lv, *J. Phys. Chem. C*, 2015, **119**, 7534–7540.
- 16 S. W. Choi, A. Katoch, G. J. Sun and S. S. Kim, *Sens. Actuators, B*, 2013, **181**, 446–453.
- 17 F. Fan, J. Zhang, J. Li, N. Zhang, R. R. Hong, X. Deng, P. Tang and D. Li, *Sens. Actuators, B*, 2017, **241**, 895–903.
- 18 K. Hassan and G. S. Chung, *Sens. Actuators, B*, 2017, **239**, 824–833.
- 19 S. Enoch, B. Nicolas, A. Adibi, T. W. Hänsch, F. Krausz, B. A. J. Monemar, H. Venghaus, H. Weber and H. Weinfurter, *Plasmonics*, Springer Berlin Heidelberg, Berlin, Heidelberg, 2012, vol. 167.
- 20 H. X. Xu, E. J. Bjerneld, M. Käll and L. Börjesson, *Phys. Rev. Lett.*, 1999, **83**, 4357–4360.
- 21 H. A. Atwater and A. Polman, *Nat. Mater.*, 2010, **9**, 865.
- 22 N. Perdana, J. Drewes, F. Pohl, A. Vahl, T. Strunskus, M. Elbahri, C. Rockstuhl and F. Faupel, *Micro Nano Eng.*, 2022, **16**, 100154.
- 23 V. Zaporozhchenko, R. Podschun, U. Schürmann, A. Kulkarni and F. Faupel, *Nanotechnology*, 2006, **17**, 4904–4908.
- 24 N. Alissawi, V. Zaporozhchenko, T. Strunskus, T. Hrkac, I. Kocabas, B. Erkartal, V. S. K. Chakravadhanula, L. Kienle, G. Grundmeier, D. Garbe-Schönberg and F. Faupel, *J. Nanopart. Res.*, 2012, **14**, 928.
- 25 C. Damm and H. Münstedt, *Appl. Phys. A: Mater. Sci. Process.*, 2008, **91**, 479–486.
- 26 C. Damm, H. Münstedt and A. Rösch, *J. Mater. Sci.*, 2007, **42**, 6067–6073.
- 27 D. D. Evanoff, R. L. White and G. Chumanov, *J. Phys. Chem. B*, 2004, **108**, 1522–1524.
- 28 P. K. Jain and M. A. El-Sayed, *Chem. Phys. Lett.*, 2010, **487**, 153–164.
- 29 M. Lismont, C. A. Páez and L. Dreesen, *J. Colloid Interface Sci.*, 2015, **447**, 40–49.
- 30 J. Alimunnisa, K. Ravichandran and K. S. Meena, *J. Mol. Liq.*, 2017, **231**, 281–287.
- 31 X.-F. Zhang, Z.-G. Liu, W. Shen and S. Gurunathan, *Int. J. Mol. Sci.*, 2016, **17**, 1534.
- 32 W. Stöber, A. Fink and E. Bohn, *J. Colloid Interface Sci.*, 1968, **26**, 62–69.
- 33 H. Haberland, M. Karrais, M. Mall and Y. Thurner, *J. Vac. Sci. Technol., A*, 1992, **10**, 3266–3271.
- 34 Y. Huttel, L. Martínez, A. Mayoral and I. Fernández, *MRS Commun.*, 2018, **8**, 947–954.
- 35 A. M. Ahadi, H. Libenská, T. Košutová, M. Cieslar, V. Červenková, D. Prokop, M. Dopita, H. Biederman and J. Hanuš, *J. Phys. D: Appl. Phys.*, 2022, **55**, 215201.
- 36 O. Kylián, R. Štefaníková, A. Kuzminova, J. Hanuš, P. Solař, P. Kúš, M. Cieslar and H. Biederman, *Plasma Phys. Controlled Fusion*, 2020, **62**, 014005.
- 37 P. Solař, J. Kousal, J. Hanuš, K. Škorvánková, A. Kuzminova and O. Kylián, *Sci. Rep.*, 2021, **11**(1), 6415.
- 38 O. H. Asnaz, N. Kohlmann, H. Folger, F. Greiner and J. Benedikt, *Plasma Processes Polym.*, 2022, e2100190.
- 39 G. Xu, M. Tazawa, P. Jin and S. Nakao, *Appl. Phys. A: Mater. Sci. Process.*, 2005, **80**, 1535–1540.
- 40 J. J. Mock, M. Barbic, D. R. Smith, D. A. Schultz and S. Schultz, *J. Chem. Phys.*, 2002, **116**, 6755–6759.
- 41 J. Drewes, S. Ali-Ogly, T. Strunskus, O. Polonskyi, H. Biederman, F. Faupel and V. Alexander, *Plasma Processes Polym.*, 2021, **19**, 2100125.
- 42 N. G. Bastús, J. Piella and V. Puentes, *Langmuir*, 2016, **32**, 290–300.
- 43 H. Shen, G. Lu, T. Zhang, J. Liu, Y. Gu, P. Perriat, M. Martini, O. Tillement and Q. Gong, *Nanotechnology*, 2013, **24**, 285502.
- 44 S. J. Oldenburg, PhD. thesis, Rice Univ., Houston, TX, USA, 2000.
- 45 O. Havnes, C. K. Goertz, G. E. Morfill, E. Grün and W. Ip, *J. Geophys. Res.*, 1987, **92**, 2281.
- 46 A. Petersen, O. H. Asnaz, B. Tadsen and F. Greiner, *Commun. Phys.*, 2022, **5**, 308.
- 47 C. B. Fleddermann, J. H. Beberman, J. T. Verdeyen, C. B. Fleddermann, J. H. Beberman, G. Hebner, L. J. Overzet and J. T. Verdeyen, *J. Appl. Phys.*, 1985, **58**, 1344–1348.
- 48 D. Nelli, M. Cerbelaud, R. Ferrando and C. Minnai, *Nanoscale Adv.*, 2021, **3**, 836–846.
- 49 C. T. Kirk, *Phys. Rev. B*, 1988, **38**, 1255.
- 50 A. Fidalgo and L. M. Ilharco, *J. Non-Cryst. Solids*, 2001, **283**, 144–154.
- 51 A. Zamchiy, E. Baranov, I. Merkulova, S. Khmel and E. Maximovskiy, *J. Non-Cryst. Solids*, 2019, **518**, 43–50.
- 52 M. Zapata Herrera, J. Aizpurua, A. K. Kazansky and A. G. Borisov, *Langmuir*, 2016, **32**, 2829–2840.
- 53 O. A. Yeshchenko, I. M. Dmitruk, A. A. Alexeenko, A. V. Kotko, J. Verdál and A. O. Pinchuk, *Plasmonics*, 2012, **7**, 685–694.
- 54 L. Mangolini and U. Kortshagen, *Phys. Rev. E: Stat., Nonlinear, Soft Matter Phys.*, 2009, **79**, 1–8.



Electronic Supplementary Material (ESI) for Nanoscale Advances.
This journal is © The Royal Society of Chemistry 2023

Supplementary Information

A novel method for the synthesis of core-shell nanoparticles for functional applications based on the long-term confinement in a radio frequency plasma

Oguz Han Asnaz,^{1,*} Jonas Drewes,^{2,*} Marie Elis,³ Thomas Strunskus,^{2,4} Franko Greiner,^{1,4} Oleksandr Polonskyi,^{2,#} Franz Faupel,^{2,4} Lorenz Kienle,^{3,4} Alexander Vahl,^{2,4,a} and Jan Benedikt^{1,4,b}

^a E-mail: alva@tf.uni-kiel.de

^b E-mail: benedikt@physik.uni-kiel.de

* These authors contributed equally to this work

currently at: Dept. of Chemical Engineering, Engineering II, University of California - Santa Barbara, Santa Barbara, CA 93106, United States

¹ Institute of Experimental and Applied Physics, Kiel University, Leibnizstr. 19, D-24098 Kiel, Germany

² Chair for Multicomponent Materials, Institute of Materials Science, Kiel University, Kaiserstr. 2, D-24143 Kiel, Germany

³ Chair for Synthesis and Real Structure, Institute of Materials Science, Kiel University, Kaiserstr. 2, D-24143 Kiel, Germany

⁴ Kiel Nano, Surface and Interface Science KiNSIS, Kiel University, Christian-Albrechts-Platz 4, D-24118 Kiel, Germany

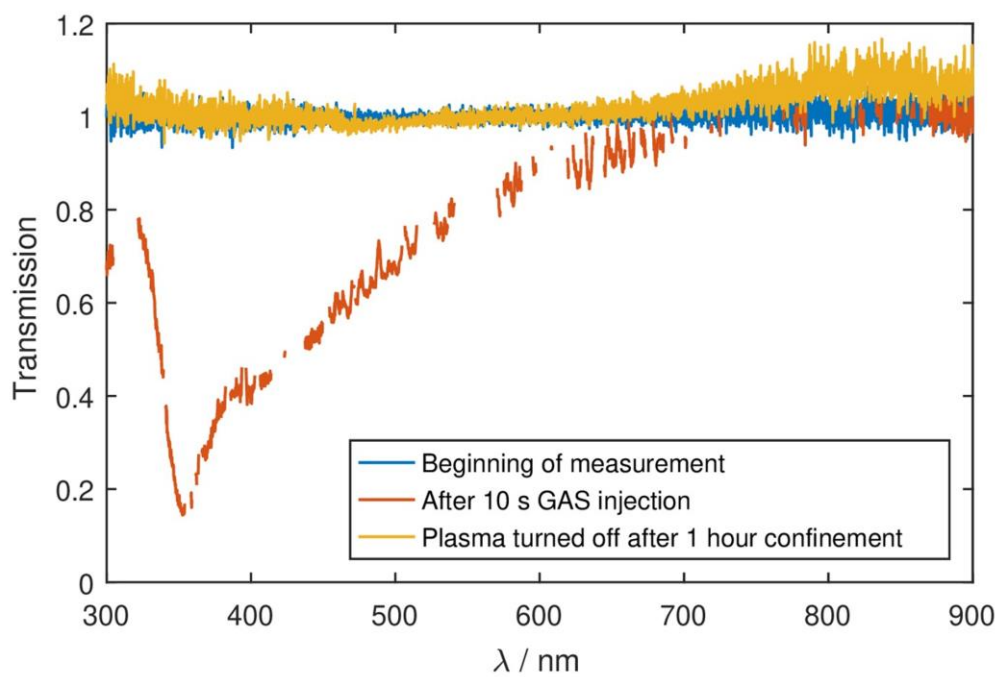


Fig. 1: UV-Vis spectrum of LSPR comparing signal before, during, and after 1 hour of particle confinement. In the spectrum during particle confinement, plasma emission lines have been filtered out. The difference between the first and last spectrum comes from a slight drift of the used light source over time.

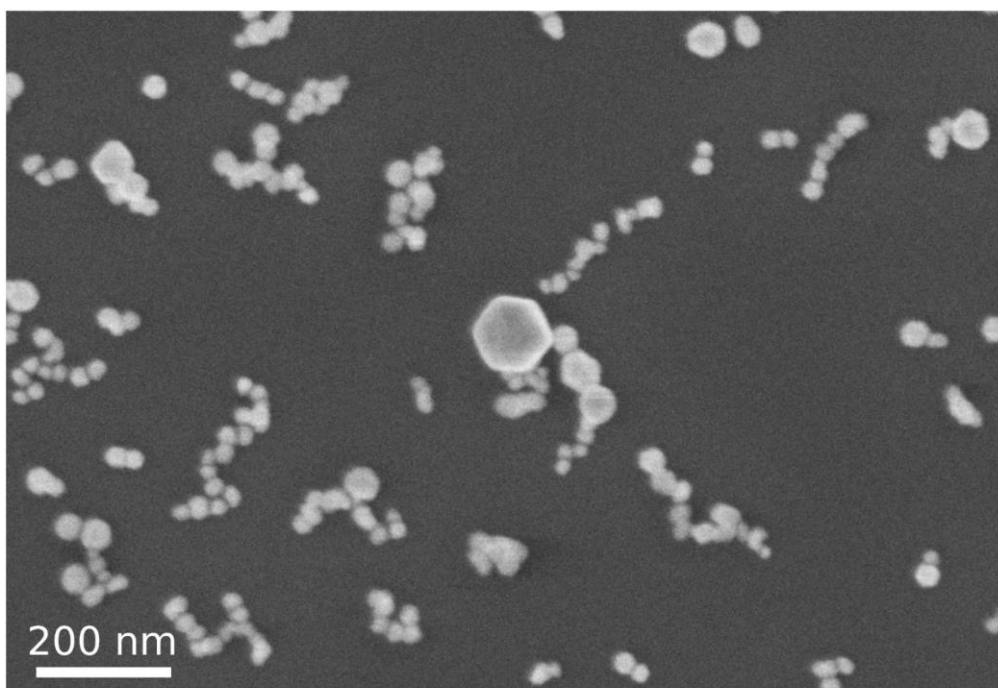


Fig. 2: SEM image of deposited Ag NPs coated for 3 min with SiH₄. Well visible are agglomerates of NPs. It is unclear if the NPs agglomerate during the synthesis or on the substrate during the extraction.

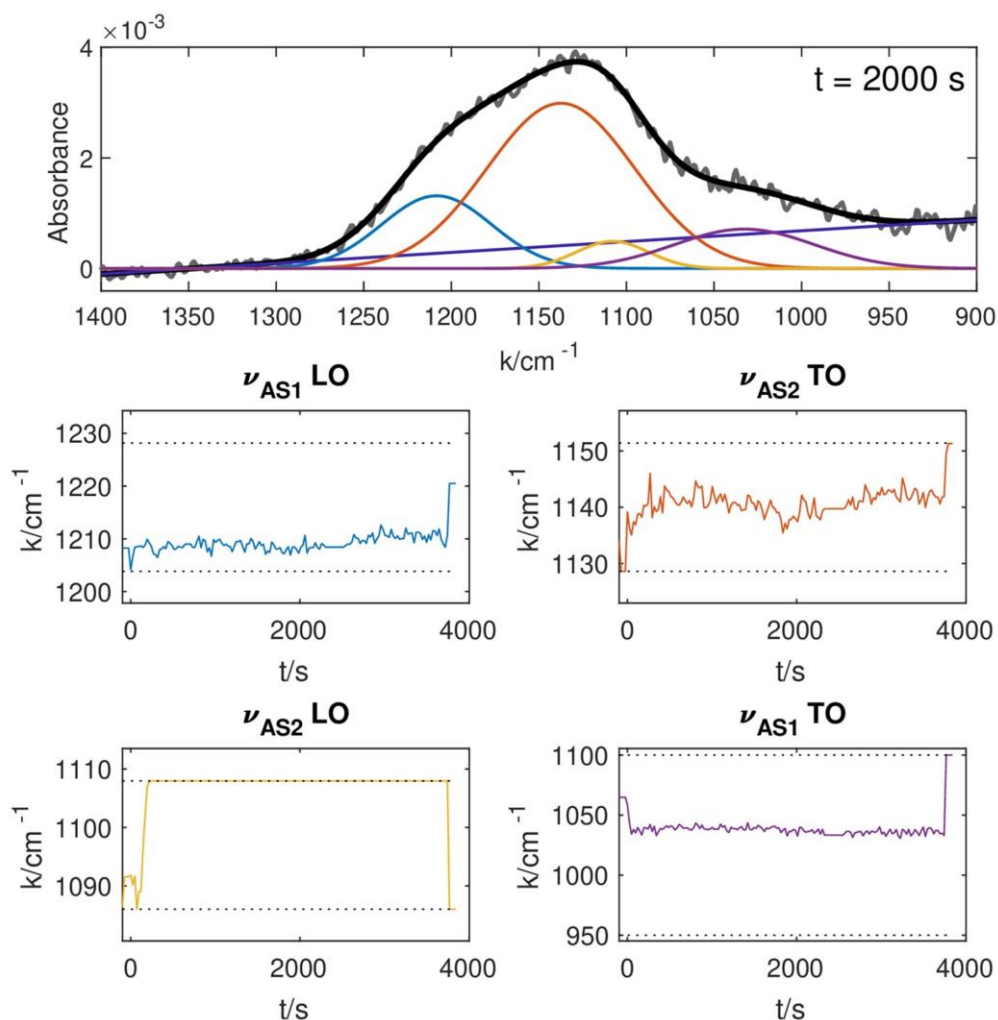


Fig. 3 Top: Decomposition of FTIR spectrum at 2000 s of a long-term confinement measurement into its four constituting vibrational lines. Bottom: Time evolution of fitted peak positions for each line with lower and upper bounds indicated with dotted lines. For ν_{AS2} we were unable to find parameters avoiding reaching the upper bound.

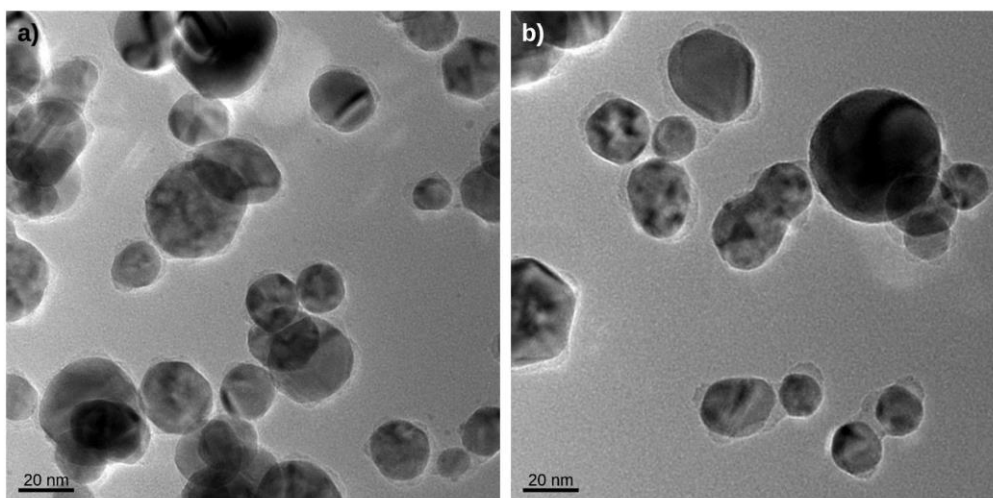


Fig. 4: TEM images of particles after 90 s of silicon coating using SiH_4 . a) Extracted immediately after coating. b) Extracted after an hour of Ar plasma treatment after coating. No significant effect of the plasma treatment can be seen.


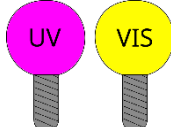

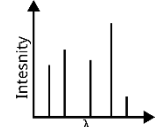
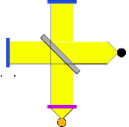
4 Conclusion

In this chapter it will be concluded, how the results of this thesis were able to contribute to increase the fundamental understanding of the HGAS and to extend the scope of applications of the HGAS. Therefore, the three different sub-questions will be answered first and then the main research question.

1) Which in-situ diagnostic techniques can be utilized to investigate the growth, transport and functionalization of Ag NPs inside and outside the HGAS to increase the understanding of the method?

In this thesis, different in-situ diagnostic methods were used. It was possible to investigate the growth, transport and functionalization inside the HGAS. From these results, a lot of knowledge is gained about the dynamic processes inside the HGAS, e.g. trapping of NPs, the formation of vortices and periodic expelling from the capture zone. All methods have in common that they use photons to obtain information about the particles or atomic species in the plasma in a non-invasive way. However, all these methods have different advantages and disadvantages which are summarized in table 1. The SAXS technique provides good information about the size distribution and the density of NPs, but it has the drawback of only 1-dimensional resolution. Furthermore, SAXS measurements at a synchrotron cannot be performed routinely because of the limited accessibility. The UV-Vis technique has the advantage that it is more accessible than a synchrotron, but it provides only 1-dimensional resolution as well. The LLS technique can provide 2-dimensional resolution which helps a lot to understand the dynamic processes inside the HGAS, e.g. formation of vortices and influence of gas inlet. But the LLS technique provides no information about the size distribution and the density of NPs. It turned out that the best solution for further investigations of the processes inside the HGAS is the combination of the LLS technique with either the UV-Vis or the SAXS method.

Table 1: Advantages and disadvantages of different in-situ diagnostics techniques which were used in this thesis.

	SAXS 	UV-Vis 	LLS 	OES 	FTIR 
Detection of NPs	✓	✓	✓	N/A	✓
Spatial resolution	1-D	1-D	2-D	N/A	1-D
Size of NPs	✓	✓	✗	N/A	✗
Independent of material	✓	✗	✓	N/A	✗
Composition of NPs	✗	Alloy NPs with LSPR	✗	✓	Depends on bonding type
Handling and accessibility	Difficult	Good	Good	Good	Medium
Functionalization by, e.g. coating	Needs complex model	✓	✗	✗	✓

Furthermore, OES was used to monitor composition changes during the synthesis of AgAu alloy NPs. The method can predict the resulting composition in-situ after a calibration with XPS samples. Therefore, the redeposition issue of the multicomponent target approach is solved by in-situ OES which substantially increases the reliability of the approach.

Additionally, the functionalization of Ag NPs with a coating of SiO₂ was monitored successfully with UV-Vis spectroscopy and in-situ FTIR outside the HGAS in an RF plasma. Here the in-situ diagnostic methods demonstrate their strength in the acceleration of the experimental work. The in-situ UV-Vis measurements allow to quickly find the optimum gas flow and discharge conditions to successfully confine the NPs in the RF discharge. Without the in-situ UV-Vis, for each parameter set an SEM sample would be necessary to see if the confinement is successful. Thanks to the in-situ diagnostic this is not necessary and the in-situ FTIR enables also to detect that the coating with the desired chemical species is achieved.

All in all, five in-situ diagnostic methods were used to investigate the processes inside the HGAS and outside. In combination, the various in-situ methods allow deep insights into the transport and growth of the NPs. These studies confirm that growth and transport are highly dynamic and connected. Contrary to general understanding in the literature, it is not the case that the particles are transported in a direct path from the magnetron to the orifice and grow steadily along this path. Rather, there are regions in which the particles are trapped or lost. This depends on the gas velocity distribution and the electromagnetic forces of the plasma. Therefore, this knowledge can help to develop new HGAS sources with an increased deposition rate and reliability.

2) Which known and unknown parameters can be used to increase the efficiency of the NP synthesis inside the HGAS?

The influence of the gas flow and pressure on the trapping of NPs inside the HGAS was investigated. The performed CFD simulations have shown that loss regions with a gas velocity close to 0 m/s are present in the HGAS geometry used. Therefore, the efficiency or deposition rate could be potentially increased by the development of a HGAS which does not show low velocity regions to drag the NPs more efficiently outside the HGAS. This development must be assisted by CFD simulations. Additionally, the study about LLS has shown that also the gas inlet location has a drastic influence on the trapping and the efficiency of the HGAS. Also, here CFD simulations can be used to find new types of gas inlets at different locations inside the HGAS which form a homogeneous gas velocity distribution without low velocity regions. Since in all studies a quick release of the trapped NPs was found when the plasma was switched off, also pulsed sputtering can be an option to reduce the trapping of NPs.

In conclusion, this thesis has drawn the attention to the geometry of the HGAS, because this and the gas inlet position have the strongest impact on the gas velocity distribution. Therefore, the most important parameter for optimization is the HGAS design. Furthermore, this finding explains why contradictory trends for the impact of the power on the NP size-distribution were observed. Since no standard HGAS is existing, all results in the literature are only hardly comparable, because the gas flow patterns and gas inlets are often extremely different.

3) How is it possible to functionalize NPs inside and outside the HGAS to extend the scope of applications of the HGAS?

The multicomponent target approach is a known technique for the fabrication of functional alloy NPs. This approach is only compatible with the HGAS, because in this synthesis technique the pressure can be varied in a broad range. However, several of the here presented publications have shown that redeposition often occurs on the target. Therefore, there is the danger of redeposition affecting the

composition of the resulting alloy NPs. It was shown that a lot of Au was redeposited onto regions where prior to the usage only pure Ag was found. Also, the deposited alloy AgAu NPs have shown that the composition depends not only on the operating pressure but also on the target lifetime. Therefore, the redeposition severely influences the synthesis of alloy NPs in this approach. Nevertheless, OES is able to solve this issue, because it can be potentially used in a feedback loop which actively controls the pressure to reach a desired composition. Therefore, it can be concluded that the multicomponent target approach in combination with OES is able to fabricate functional alloy NPs with tailored composition in a cost-effective way. The possibility to tailor the composition of alloy NPs in-situ with high precision is a big advantage of the HGAS over other synthesis approaches.

Another way to functionalize pure NPs is to coat them to produce core-shell NPs. In the literature some in-flight methods are known where NPs are coated with an additional magnetron either inside or outside a HGAS. The problem of these techniques is the limited shell thickness which can be achieved. In this thesis it is shown that a combination of a HGAS and a RF discharge is able to hold Ag NPs for an extended time period. The combination with a second RF-discharge is only possible, because the HGAS is a vacuum compatible NP synthesis method. This is a big advantage over other NP synthesis approaches, e.g. chemical processes. The targeted trapping of NPs inside the RF discharge enables the introduction of a precursor gas like silane to coat the Ag NPs with a shell of SiO₂. This approach can be used to tailor, e.g. the optical properties of the NPs. In comparison to the in-flight treatment approach the maximum achievable shell thickness can be increased drastically. Even though no limit for the coating thickness was found in the publication, from dusty-plasma experiments it is known that even particles in the μm range can be hold inside a plasma. Therefore, it is expected that the NPs can be also coated with a theoretical shell thickness in the μm range if this is desired.

How can the fundamental understanding of the HGAS be increased to extend the scope of applications of the HGAS?

In summary, the results have shown that the current theory of a linear growth of NPs during the way from the magnetron to the orifice is too much simplified. Trapping of NPs was detected with diverse in-situ diagnostics confirming that the current description of growth and transport inside a HGAS needs to be revised. If the HGAS should be applied in the future for industrial applications, a high deposition rate, a high conversion of target material into NPs and outstanding properties of NPs must be achieved. Therefore, the control of the trapping of NPs is essential for further improvement of the HGAS. The trapping and the loss of NPs depends strongly on the gas velocity distribution. The velocity distribution depends, on the one hand, on the HGAS geometry shown by CFD simulations. On the other hand, the gas velocity distribution depends strongly on the gas inlet location shown experimentally with the LLS technique. With this knowledge in the future a HGAS design could be developed with a high velocity distribution everywhere inside the HGAS. This could avoid trapping and loss of NPs enabling the industrial use of the HGAS.

To achieve outstanding properties of NPs, synthesis methods enabling functionalization are extremely important. Two methods to produce functional NPs were improved or developed which have many benefits over other synthesis methods for functional NPs. One is the synthesis of alloy NPs with in-situ composition tuning and monitoring. The other is the synthesis of core-shell NPs with a combination of a HGAS and an RF-discharge. No other synthesis methods are available which are vacuum compatible and produce NPs with high purity, tailored composition and a tailored shell thickness. Especially the tailoring of shell thickness in a broad range and the option to produce multiple shells or shells with gradients was not possible with a HGAS before. This is a perfect example showing how an increased

fundamental understanding of the HGAS together with in-situ diagnostics help to extend the scope of applications of the HGAS.

Although, in this thesis the understanding of the growth, transport and trapping of NPs inside the HGAS is significantly increased, more research has to be done to fully understand how the trapping of NPs works in detail. Especially, the forces acting on the NPs must be identified in detail and their strength has to be investigated. Therefore, a combination of plasma diagnostics, in-situ NP diagnostics and simulations will be needed to fully understand the trapping behavior. In the next chapter as an outlook different experiments are suggested to further increase the understanding of the HGAS and the efficiency of the HGAS. After the processes inside the HGAS are completely understood, the trapping can be either avoided or maybe exploited to increase the size of NPs up to a desired diameter. Furthermore, if the trapping, the loss of NPs by redeposition onto the target or the walls and the loss of sputtered atoms can be significantly decreased, the HGAS can be efficiently used for mass production of functional NPs with a high purity and unique properties.

5 Outlook

To further extend the understanding of the processes inside the HGAS the following experiments are suggested:

Combination of UV-VIS or SAXS with LLS measurements

For the LLS technique it was not possible to determine the size and density of NPs, because the Rayleigh scattering intensity depends on the size and density simultaneously. It would be interesting to establish a setup in which UV-Vis spectroscopy or SAXS measurements can be performed simultaneously together with LLS. This would combine the advantages of both techniques and could be used to determine the size and density of NPs in different regions with a good spatial resolution.

Horizontal vs. vertical alignment of the HGAS

To learn more about the strength of the different forces acting on the trapped NPs, it would be interesting to perform LLS on a HGAS which is once aligned horizontal and once vertical. If all working parameters are the same in both alignments, all forces would stay constant except the gravitational force. If the NPs which were observed with the LLS technique have a size in the order of hundreds of nm, this could influence the position of the trapped NPs. In combination with CFD simulations, the strength of the different forces acting on the NPs could may be better explored.

Simulation of the formation and trapping of NPs

In addition, further simulations, which incorporate not only the gas velocity but also the sputtering process, the NP formation and the forces acting on the NPs, would be a great way to further explore the processes inside the HGAS. Such simulations could be now validated with a broad variety of in-situ diagnostics which were presented inside this thesis.

Combination of plasma diagnostics with LLS measurements

As a last point, plasma diagnostics like Langmuir probe measurements could be performed simultaneously with LLS or other techniques to get an idea about the electron temperature, electron density and electric potential in the trapping regions. This could increase the knowledge about the trapping forces originating from the plasma. Nevertheless, the measurement itself can also disturb the gas flow pattern and the NP growth and transport. Therefore, it is important to use LLS simultaneously to see the impact of the probe onto the trapping of the NPs.

To further increase the efficiency of the HGAS the following experiments are suggested:

Pulsed DC Power

Trapping of NPs inside the HGAS is in principle unwanted, unless it can be controlled. For some applications it would be interesting to grow NPs much larger than, e.g. 20 nm. Their trapping could be helpful if it can be controlled and if the NPs can be deposited. Therefore, it would be interesting to use a pulsed DC power supply, because the studies have shown that trapped particles are released instantaneously if the plasma is switched off. During such pulsing experiments LLS or UV-Vis spectroscopy could be used to see the influence of different frequencies and duty cycles on the trapping behavior.

Complex gas inlet design

To reduce the loss of material inside the HGAS and to increase the efficiency of the HGAS, different gas inlet designs can potentially help to achieve this. One could imagine to create a double-walled HGAS where the gas is injected through the double wall and the magnetron. If the double wall would be equipped everywhere with a high density of tiny holes in a well-defined and homogeneous pattern, the gas velocity at the inner wall of the HGAS would be high and no loss regions should exist. The design should be assisted by CFD simulations. Nevertheless, also the growth process has to be optimized, because only NPs are effectively dragged by the gas. Single atoms could be still deposited onto the wall. Therefore, also the growth conditions have to be optimized in a way that nearly all atoms are incorporated into NPs.

Mesh on potential

Another possibility to reduce the loss of NPs to the chamber walls could be to insert a biased stainless-steel mesh close to the outside walls. Since some NPs are charged, these charged NPs could be pushed into the central region of the HGAS where the drag force is high enough to guide them outside. This could potentially increase the efficiency and deposition rate of the HGAS. But one has to be careful that the potential on the mesh does not impact the plasma at the magnetron too much.

The knowledge from this thesis together with these suggested experiments can substantially help to make the HGAS an efficient tool for the production of NPs with a broad variety of applications.

6 List of Figures

Figure 2-1: Demands on an ideal nanoparticle deposition process.	5
Figure 2-2: Different NP synthesis methods ranging from biological (green) over chemical (orange) to physical processes (blue).[46]	6
Figure 2-3: Different kinds of cluster sources.	7
Figure 2-4: Schematic cross section of a planar magnetron. Shown are the target, the ground cap, the gas inlet, the permanent magnets and the water cooling. Additionally, the sputtering process and the ionization process are schematically depicted. The figure is reprinted from the book from Huttel et al. [47].	9
Figure 2-5: Schematic of a HGAS and the growth of NPs. The HGAS consists of a height adjustable magnetron with an Ar inlet, diagnostic ports for in-situ investigations and an orifice, which is connected to the deposition chamber. Important is that the pressure in the HGAS (p_1) is much higher than in the deposition chamber (p_2). The 6 steps sputtering, nuclei formation, condensation, coalescence, sintering, transport & deposition are also shown.	10
Figure 2-6: Working parameters of the HGAS which are affecting the size and the deposition rate of the resulting NPs.	13
Figure 2-7: Shown are the forces acting on dust particles for the parameters: $\rho d = 1500 \text{ kg/m}^3$, $Te = 2 \text{ eV}$, $\phi fl = -4 \text{ V}$, $E = 1000 \text{ V/m}$, $ni = 1015 \text{ m}^{-3}$, $v_{th,n} = v_{th,i} = 400 \text{ m/s}$, $\nabla Tn = 200 \text{ K/m}$, $kn = 0.016 \text{ kg m s}^{-3} \text{ (Ar)}$. The figure is reprinted from [62].....	18
Figure 2-8: The plot on the left side shows the dispersion curve of the bulk plasmon (green-dashed line) and surface plasmon polariton (blue-dashed line). Additionally, the curve of light in vacuum is displayed (black-solid line). The red dots and red-dashed lines show schematically the additional momentum, which is needed for effective coupling. On the top right, a schematic drawing of a propagating surface plasmon polariton is shown together with a plot for the electric field strength in dependence to the distance to the interface. On the bottom right, the schematic drawing of the surface charge density of a localized surface plasmon together with the electric field strength plot in dependence to the distance to the center of the particle is shown. The figure is reprinted from [65].....	19
Figure 2-9: Roadmap for CFD simulations [70].	23
Figure 2-10: The five different in-situ diagnostic methods used are named and shown with their attributed pictogram. From left to right the pictograms for small angle X-ray scattering (SAXS), UV-Vis spectroscopy (UV-Vis), laser light scattering (LLS), optical emission spectroscopy (OES) and Fourier transform infrared spectroscopy (FTIR) are shown.	24
Figure 2-11: Experimental setup of the SAXS measurements at DESY. The path of the X-ray beam through the HGAS, the SAXS scattering at the NPs and the X-ray detection at the detector is shown. Additionally, the resulting scattering intensity vs. q plot for Ag NPs inside the HGAS is shown. The Figure is reprinted from [79].	27
Figure 2-12: Schematic representation of the LLS setup on the HGAS. The setup consists of a magnetron, a CF63 cross with 6 flanges, an orifice, a laser, a laser grid and a camera. The figure is reprinted from [38].	29
Figure 2-13: Schematic representation of a Michelson interferometer.	30
Figure 2-14: Interaction volume of the primary electron beam. The different regions are indicating the origin of detectable electrons and photons. Secondary and Auger electrons are escaping only close to the sample surface. Backscattered electrons are originating from a deeper volume than the secondary or Auger electrons. X-rays are also able to leave the sample from even deeper regions.[50]	32
Figure 2-15: Working principle of an XPS measurement system.	34

Figure 3-1: Schematic of the structure of the thesis. On the top is the main research question, which was structured into three sub-questions. The arrows from the sub-questions to the publications are indicating which publications have partially answered which sub-questions. The publications are connected also with arrows to show how the publications are connected. 38

7 Bibliography

- [1] Astruc D 2020 Introduction: Nanoparticles in Catalysis *Chem Rev* **120** 461–3
- [2] Ghori M Z, Adam J, Aktas O C, Veziroglu S, Shurtleff B B, Strunskus T, Faupel F, Polonskyi O and Hinz A 2018 Role of UV Plasmonics in the Photocatalytic Performance of TiO₂ Decorated with Aluminum Nanoparticles *ACS Appl Nano Mater* **1** 3760–4
- [3] Veziroglu S, Ghori M Z, Obermann A L, Röder K, Polonskyi O, Strunskus T, Faupel F and Aktas O C 2019 Ag Nanoparticles Decorated TiO₂ Thin Films with Enhanced Photocatalytic Activity *Physica Status Solidi (A) Applications and Materials Science* **216** 1–6
- [4] Veziroglu S, Hwang J, Drewes J, Barg I, Shondo J, Strunskus T, Polonskyi O, Faupel F and Aktas O C 2020 PdO nanoparticles decorated TiO₂ film with enhanced photocatalytic and self-cleaning properties *Mater Today Chem* **16**
- [5] Vahl A, Veziroglu S, Henkel B, Strunskus T, Polonskyi O, Aktas O C and Faupel F 2019 Pathways to Tailor Photocatalytic Performance of TiO₂ Thin Films Deposited by Reactive Magnetron Sputtering *Materials* **12** 2840
- [6] Li H, Li Z, Yu Y, Ma Y, Yang W, Wang F, Yin X and Wang X 2017 Surface-Plasmon-Resonance-Enhanced Photoelectrochemical Water Splitting from Au-Nanoparticle-Decorated 3D TiO₂ Nanorod Architectures *Journal of Physical Chemistry C* **121** 12071–9
- [7] Minnai C, Bellacicca A, Brown S A and Milani P 2017 Facile fabrication of complex networks of memristive devices *Sci Rep* **7** 1–8
- [8] Mirigliano M, Decastri D, Pullia A, Dellasega D, Casu A, Falqui A and Milani P 2020 Complex electrical spiking activity in resistive switching nanostructured Au two-terminal devices *Nanotechnology* **31**
- [9] Mirigliano M, Borghi F, Podestà A, Antidormi A, Colombo L and Milani P 2019 Non-ohmic behavior and resistive switching of Au cluster-assembled films beyond the percolation threshold *Nanoscale Adv* **1** 3119–30
- [10] Wang Z, Joshi S, Savel'ev S E, Jiang H, Midya R, Lin P, Hu M, Ge N, Strachan J P, Li Z, Wu Q, Barnell M, Li G L, Xin H L, Williams R S, Xia Q and Yang J J 2017 Memristors with diffusive dynamics as synaptic emulators for neuromorphic computing *Nat Mater* **16** 101–8
- [11] Jiang H, Belkin D, Savel'Ev S E, Lin S, Wang Z, Li Y, Joshi S, Midya R, Li C, Rao M, Barnell M, Wu Q, Yang J J and Xia Q 2017 A novel true random number generator based on a stochastic diffusive memristor *Nat Commun* **8**
- [12] Choi B J, Torrezan A C, Norris K J, Miao F, Strachan J P, Zhang M X, Ohlberg D A A, Kobayashi N P, Yang J J and Williams R S 2013 Electrical performance and scalability of Pt dispersed SiO₂ nanometallic resistance switch *Nano Lett* **13** 3213–7

- [13] Minnai C, di Vece M and Milani P 2017 Mechanical-optical-electro modulation by stretching a polymer-metal nanocomposite *Nanotechnology* **28** 0–8
- [14] Postica V, Vahl A, Santos-Carballal D, Dankwort T, Kienle L, Hoppe M, Cadi-Essadek A, de Leeuw N H, Terasa M I, Adelung R, Faupel F and Lupan O 2019 Tuning ZnO Sensors Reactivity toward Volatile Organic Compounds via Ag Doping and Nanoparticle Functionalization *ACS Appl Mater Interfaces* **11** 31452–66
- [15] Yong Y, Li C, Li X, Li T, Cui H and Lv S 2015 Ag₇Au₆ cluster as a potential gas sensor for CO, HCN, and NO detection *Journal of Physical Chemistry C* **119** 7534–40
- [16] Choi S W, Katoch A, Sun G J and Kim S S 2013 Bimetallic Pd/Pt nanoparticle-functionalized SnO₂ nanowires for fast response and recovery to NO₂ *Sens Actuators B Chem* **181** 446–53
- [17] Fan F, Zhang J, Li J, Zhang N, Hong R R, Deng X, Tang P and Li D 2017 Hydrogen sensing properties of Pt-Au bimetallic nanoparticles loaded on ZnO nanorods *Sens Actuators B Chem* **241** 895–903
- [18] Hassan K and Chung G S 2017 Catalytically activated quantum-size Pt/Pd bimetallic core–shell nanoparticles decorated on ZnO nanorod clusters for accelerated hydrogen gas detection *Sens Actuators B Chem* **239** 824–33
- [19] Perdana N, Drewes J, Pohl F, Vahl A, Strunskus T, Elbahri M, Rockstuhl C and Faupel F 2022 A thin-film broadband perfect absorber based on plasmonic copper nanoparticles *Micro and Nano Engineering* **16** 100154
- [20] Heer W de 1993 The physics of simple metal clusters: experimental aspects and simple models *Rev Mod Phys* **65** 611–76
- [21] Popok V N and Campbell E E B 2006 Beams of atomic clusters: Effects on impact with solids *Reviews on Advanced Materials Science* **11** 19–45
- [22] Wegner K, Piseri P, Tafreshi H V and Milani P 2006 Cluster beam deposition: A tool for nanoscale science and technology *J Phys D Appl Phys* **39**
- [23] Haberland H, Karrais M, Mall M and Thurner Y 1992 Thin films from energetic cluster impact: A feasibility study *Journal of Vacuum Science & Technology A: Vacuum, Surfaces, and Films* **10** 3266–71
- [24] Grammatikopoulos P 2019 Atomistic modeling of the nucleation and growth of pure and hybrid nanoparticles by cluster beam deposition *Curr Opin Chem Eng* **23** 164–73
- [25] Nelli D, Cerbelaud M, Ferrando R and Minnai C 2021 Tuning the coalescence degree in the growth of Pt-Pd nanoalloys *Nanoscale Adv* **3** 836–46
- [26] Liu C, Zhang L, Zhang S, Liu F, Wang G and Han M 2020 Influence of discharge power on the size of the Pd cluster generated with a magnetron plasma gas aggregation cluster source *Vacuum* **179**
- [27] Straňák V, Block S, Drache S, Hubička Z, Helm C A, Jastrabík L, Tichý M and Hippler R 2011 Size-controlled formation of Cu nanoclusters in pulsed magnetron sputtering system *Surf Coat Technol* **205** 2755–62

- [28] Polonskyi O, Solař P, Kylián O, Drábik M, Artemenko A, Kousal J, Hanuš J, Pešička J, Matolínová I, Kolíbalová E, Slavínská D and Biederman H 2012 Nanocomposite metal/plasma polymer films prepared by means of gas aggregation cluster source *Thin Solid Films* vol 520 pp 4155–62
- [29] Gracia-Pinilla M, Martínez E, Vidaurri G S and Pérez-Tijerina E 2010 Deposition of Size-Selected Cu Nanoparticles by Inert Gas Condensation *Nanoscale Res Lett* **5** 180–8
- [30] Hihara T and Sumiyama K 1998 Formation and size control of a Ni cluster by plasma gas condensation *J Appl Phys* **84** 5270–6
- [31] Pratontep S, Carroll S J, Xirouchaki C, Streun M and Palmer R E 2005 Size-selected cluster beam source based on radio frequency magnetron plasma sputtering and gas condensation *Review of Scientific Instruments* **76**
- [32] Hillenkamp M, di Domenicantonio G and Félix C 2006 Monodispersed metal clusters in solid matrices: A new experimental setup *Review of Scientific Instruments* **77**
- [33] Kousal J, Shelemin A, Schwartzkopf M, Polonskyi O, Hanuš J, Solař P, Vaidulych M, Nikitin D, Pleskunov P, Krtouš Z, Strunskus T, Faupel F, Roth S v., Biederman H and Choukourov A 2018 Magnetron-sputtered copper nanoparticles: lost in gas aggregation and found by in situ X-ray scattering *Nanoscale* **10** 18275–81
- [34] Sanzone G, Yin J and Sun H 2021 Scaling up of cluster beam deposition technology for catalysis application 1–20
- [35] Shelemin A, Pleskunov P, Kousal J, Drewes J, Hanuš J, Ali-Ogly S, Nikitin D, Solař P, Kratochvíl J, Vaidulych M, Schwartzkopf M, Kylián O, Polonskyi O, Strunskus T, Faupel F, Roth S v., Biederman H and Choukourov A 2020 Nucleation and Growth of Magnetron-Sputtered Ag Nanoparticles as Witnessed by Time-Resolved Small Angle X-Ray Scattering *Particle & Particle Systems Characterization* **37** 1900436
- [36] Drewes J, Ali-Ogly S, Strunskus T, Polonskyi O, Biederman H, Faupel F and Vahl A 2022 Impact of argon flow and pressure on the trapping behavior of nanoparticles inside a gas aggregation source *Plasma Processes and Polymers* **19** 2100125
- [37] Nikitin D, Hanuš J, Ali-Ogly S, Polonskyi O, Drewes J, Faupel F, Biederman H and Choukourov A 2019 The evolution of Ag nanoparticles inside a gas aggregation cluster source *Plasma Processes and Polymers* **16** 1900079
- [38] Drewes J, Rehders S, Strunskus T, Kersten H, Faupel F and Vahl A 2022 In Situ Laser Light Scattering for Temporally and Locally Resolved Studies on Nanoparticle Trapping in a Gas Aggregation Source *Particle & Particle Systems Characterization* 2200112
- [39] Vahl A, Strobel J, Reichstein W, Polonskyi O, Strunskus T, Kienle L and Faupel F 2017 Single target sputter deposition of alloy nanoparticles with adjustable composition via a gas aggregation cluster source *Nanotechnology* **28** 175703
- [40] Drewes J, Vahl A, Carstens N, Strunskus T, Polonskyi O and Faupel F 2020 Enhancing composition control of alloy nanoparticles from gas aggregation source by in operando optical emission spectroscopy *Plasma Processes and Polymers* 1–11

Bibliography

- [41] Asnaz O H, Drewes J, Elis M, Strunskus T, Greiner F, Polonskyi O, Faupel F, Kienle L, Vahl A and Benedikt J 2023 A novel method for the synthesis of core–shell nanoparticles for functional applications based on long-term confinement in a radio frequency plasma *Nanoscale Adv*
- [42] Hansen S F, Larsen B H, Olsen S I and Baun A 2007 Categorization framework to aid hazard identification of nanomaterials *Nanotoxicology* **1** 243–50
- [43] Zhang X-F, Liu Z-G, Shen W and Gurunathan S 2016 Silver Nanoparticles: Synthesis, Characterization, Properties, Applications, and Therapeutic Approaches *Int J Mol Sci* **17** 1534
- [44] Gurunathan S, Kalishwaralal K, Vaidyanathan R, Venkataraman D, Pandian S R K, Muniyandi J, Hariharan N and Eom S H 2009 Biosynthesis, purification and characterization of silver nanoparticles using *Escherichia coli* *Colloids Surf B Biointerfaces* **74** 328–35
- [45] Rane A V, Kanny K, Abitha V K and Thomas S 2018 *Methods for Synthesis of Nanoparticles and Fabrication of Nanocomposites* (Elsevier Ltd.)
- [46] Rane A V, Kanny K, Abitha V K and Thomas S 2018 *Methods for Synthesis of Nanoparticles and Fabrication of Nanocomposites* *Synthesis of Inorganic Nanomaterials* (Elsevier) pp 121–39
- [47] Huttel Y 2017 *Gas-Phase Synthesis of Nanoparticles* (Wiley-VCH Verlag GmbH & Co. KGaA)
- [48] Binns C 2008 Chapter 3 Production of Nanoparticles on Supports Using Gas-Phase Deposition and MBE *Handbook of Metal Physics* vol 5 pp 49–71
- [49] Larsen R A, Neoh S K and Herschbach D R 1974 Seeded supersonic alkali atom beams *Review of Scientific Instruments* **45** 1511–6
- [50] Sattler K, Mühlbach J and Recknagel E 1980 Generation of Metal Clusters Containing from 2 to 500 Atoms *Phys Rev Lett* **45** 821–4
- [51] Dietz T G, Duncan M A, Powers D E and Smalley R E 1981 Laser production of supersonic metal cluster beams *J Chem Phys* **74** 6511–2
- [52] Barborini E, Piseri P and Milani P 1999 A pulsed microplasma source of high intensity supersonic carbon cluster beams *J Phys D Appl Phys* **32** L105–9
- [53] Siekmann H R, Lüder Ch, Faehrmann J, Lutz H O and Meiwes-Broer K H 1991 The pulsed arc cluster ion source (PACIS) *Zeitschrift für Physik D Atoms, Molecules and Clusters* **20** 417–20
- [54] Smith D L 1995 *Thin-Film Deposition Principles and Practice* (McGraw Hill Professional)
- [55] Ohring M 2001 *The Materials Science of Thin Films* (Academic Press)
- [56] Huttel Y, Martínez L, Mayoral A and Fernández I 2018 Gas-phase synthesis of nanoparticles: Present status and perspectives *MRS Commun* **8** 947–54
- [57] Haberland H, Mall M, Moseler M, Qiang Y, Reiners T and Thurner Y 1994 Filling of micron-sized contact holes with copper by energetic cluster impact *Journal of Vacuum Science & Technology A: Vacuum, Surfaces, and Films* **12** 2925–2930
- [58] Shyjumon I, Gopinadhan M, Ivanova O, Quaas M, Wulff H, Helm C A and Hippler R 2006 Structural deformation, melting point and lattice parameter studies of size selected silver clusters *European Physical Journal D* **37** 409–15

- [59] Sun J and Simon S L 2007 The melting behavior of aluminum nanoparticles *Thermochim Acta* **463** 32–40
- [60] Jiang A, Awasthi N, Kolmogorov A N, Setyawan W, Börjesson A, Bolton K, Harutyunyan A R and Curtarolo S 2007 Theoretical study of the thermal behavior of free and alumina-supported Fe-C nanoparticles *Phys Rev B Condens Matter Mater Phys* **75**
- [61] Kashtanov P v., Smirnov B M and Hippler R 2007 Magnetron plasma and nanotechnology *Physics-Uspokhi* **50** 455
- [62] Batková, Kozák T, Haviar S, Mareš P and Čapek J 2021 Effect of exit-orifice diameter on Cu nanoparticles produced by gas-aggregation source *Surf Coat Technol* **417**
- [63] Khojasteh M and Kresin V v. 2017 Influence of source parameters on the growth of metal nanoparticles by sputter-gas-aggregation *Appl Nanosci* **7** 875–83
- [64] Drache S, Stranak V, Berg F, Hubicka Z, Tichy M, Helm C A and Hippler R 2014 Pulsed gas aggregation for improved nanocluster growth and flux *Physica Status Solidi (A) Applications and Materials Science* **211** 1189–93
- [65] Ganeva M, Pipa A V and Hippler R 2012 The influence of target erosion on the mass spectra of clusters formed in the planar DC magnetron sputtering source *Surf Coat Technol* **213** 41–7
- [66] Piel A 2017 *Plasma Physics* (Cham: Springer International Publishing)
- [67] Melzer A 2019 *Physics of Dusty Plasmas* vol 962 (Cham: Springer International Publishing)
- [68] Samsonov D, Zhdanov S, Morfill G and Steinberg V 2003 Levitation and agglomeration of magnetic grains in a complex (dusty) plasma with magnetic field *New J Phys* **5** 24–24
- [69] Barnes M S, Keller J H, Forster J C, O'Neill J A and Coultas D K 1992 Transport of dust particles in glow-discharge plasmas *Phys Rev Lett* **68** 313–6
- [70] Enoch S, Nicolas B, Adibi A, Hänsch T W, Krausz F, Monemar B A J, Venghaus H, Weber H and Weinfurter H 2012 *Plasmonics* vol 167, ed S Enoch and N Bonod (Berlin, Heidelberg: Springer Berlin Heidelberg)
- [71] Kelly K L, Coronado E, Zhao L L and Schatz G C 2003 The Optical Properties of Metal Nanoparticles: The Influence of Size, Shape, and Dielectric Environment *J Phys Chem B* **107** 668–77
- [72] Jain P K and El-Sayed M A 2010 Plasmonic coupling in noble metal nanostructures *Chem Phys Lett* **487** 153–64
- [73] Maier S A 2007 *Plasmonics: Fundamentals and Applications* (New York: Springer Science+Buisness Media LLC)
- [74] Mie G 1908 Beiträge zur Optik trüber Medien, speziell kolloidaler Metallösungen *Ann Phys* **330** 377–445
- [75] Andersson B 2011 *Computational fluid dynamics for engineers* (Cambridge University Press)
- [76] Owen T 2000 *Fundamentals of modern UV-visible spectroscopy* (Agilent Technologies)

- [77] Raveh A, Weiss M and Schneck R 1999 Optical emission spectroscopy as a tool for designing and controlling the deposition of graded TiAlN layers by ECR-assisted reactive RF sputtering *Surf Coat Technol* **111** 263–8
- [78] Posada J, Bousquet A, Jubault M, Lincot D and Tomasella E 2016 In Situ Monitoring of Cu(In_{1-x}Ga_x)Se₂ Composition and Target Poisoning by Real Time Optical Emission Spectroscopy During Deposition From a Hybrid Sputtering/Evaporation Process *Plasma Processes and Polymers* **13** 997–1007
- [79] Wu S and Tseng K 2002 Composition Control of R.F.-Sputtered Ni₂MnGa Thin Films Using Optical Emission Spectroscopy *Mater Trans* **43** 871–5
- [80] Drewes J, Vahl A, Carstens N, Strunskus T, Polonskyi O and Faupel F 2020 Enhancing composition control of alloy nanoparticles from gas aggregation source by in operando optical emission spectroscopy *Plasma Processes and Polymers* 1–11
- [81] Nelis T and Payling R 2003 *Glow Discharge Optical Emission Spectroscopy A Practical Guide* (Cambridge : The Royal Society of Chemistry)
- [82] Krumrey M 2019 Small angle x-ray scattering (SAXS) *Characterization of Nanoparticles: Measurement Processes for Nanoparticles* (Elsevier) pp 173–83
- [83] Shelemin A, Pleskunov P, Kousal J, Drewes J, Hanuš J, Ali-Ogly S, Nikitin D, Solař P, Kratochvíl J, Vaidulych M, Schwartzkopf M, Kylián O, Polonskyi O, Strunskus T, Faupel F, Roth S v., Biederman H and Choukourov A 2020 Nucleation and Growth of Magnetron-Sputtered Ag Nanoparticles as Witnessed by Time-Resolved Small Angle X-Ray Scattering *Particle and Particle Systems Characterization* **37** 1–11
- [84] Guinier A, Walker C B, York N and Wiley J 1955 *SMALL-ANGLE SCATTERING OF X-RAYS GERARD FOURNET Translation by* (John Wiley & Sons)
- [85] Ilavský J and Jemian P R 2009 Irena: Tool suite for modeling and analysis of small-angle scattering *J Appl Crystallogr* **42** 347–53
- [86] Qin Y, Kortshagen U R and Aydil E S 2016 Laser light scattering from silicon particles generated in an argon diluted silane plasma *J Phys D Appl Phys* **49**
- [87] Mikikian M, Cavarroc M, Couédel L, Tessier Y and Boufendi L 2010 Dust particles in low-pressure plasmas: Formation and induced phenomena *Pure and Applied Chemistry* vol 82 pp 1273–82
- [88] Marvi Z, von Wahl E, Trottenberg T and Kersten H 2020 Spatiotemporal sampling of growing nanoparticles in an acetylene plasma *J Appl Phys* **127**
- [89] van de Wetering F M J H, Brooimans R J C, Nijdam S, Beckers J and Kroesen G M W 2015 Fast and interrupted expansion in cyclic void growth in dusty plasma *J Phys D Appl Phys* **48** 035204
- [90] Pilch I and Greiner F 2017 Diagnostics of void expansion during cyclic growth and formation of layered nanoparticle clouds *J Appl Phys* **121**
- [91] Greiner F, Carstensen J, Köhler N, Pilch I, Ketelsen H, Knist S and Piel A 2012 Imaging Mie ellipsometry: Dynamics of nanodust clouds in an argon-acetylene plasma *Plasma Sources Sci Technol* **21**

Bibliography

- [92] Greiner F, Melzer A, Tadsen B, Groth S, Killer C, Kirchschrager F, Wieben F, Pilch I, Krüger H, Block D, Piel A and Wolf S 2018 Diagnostics and characterization of nanodust and nanodusty plasmas *European Physical Journal D* **72**
- [93] Ling J and Wang J 2018 *Elastic Light Scattering Spectrometry* (De Gruyter)
- [94] Griffiths P R and de Haseth J A 2007 *Fourier Transform Infrared Spectrometry Second Edition* (New Jersey: John Wiley & Sons, Inc.)
- [95] Reimer L 1998 *Scanning Electron Microscopy* vol 45 (Berlin, Heidelberg: Springer Berlin Heidelberg)
- [96] Williams D B and Carter C B 2009 *Transmission Electron Microscopy* (Boston, MA: Springer US)
- [97] Hofmann S 2013 *Auger- and X-Ray Photoelectron Spectroscopy in Materials Science* vol 49 (Berlin, Heidelberg: Springer Berlin Heidelberg)
- [98] Moulder J F, Stickle W F, Sobol P E and Bomben K D 1992 *Handbook of X-ray Photoelectron Spectroscopy* ed J Chastain (Perking-Elmer Corporation)
- [99] Kramida A, Ralchenko Yu, Reader J and (2019) N A T 2019 NIST Atomic Spectra Database

8 Declaration of Authorship

In this chapter the own contributions to the publications forming this cumulative dissertation are given. The own contributions are divided into three factors: Conceptualization (C), sample preparation (S), collection and processing of data (D), interpretation of data (I) and writing of the manuscript (M). The level of contribution is divided into: Low, medium and high. The full citation for the Publications A-F can be found in chapter “Publications in the Context of this Thesis” or the corresponding sub-chapter in Chapter 3.

Publication	C	S	D	I	M
Publication A	Low	Low	High	Medium	Low
Publication B	Medium	Low	Medium	Medium	Low
Publication C	High	High	High	High	High
Publication D	High	High	High	High	High
Publication E	High	High	High	High	High
Publication F	High	High	High	High	High